

Syracuse University

**SURFACE**

---

Dissertations - ALL

SURFACE

---

December 2019

## **NOVEL SHAPE MEMORY AND MULTI-SHAPE MEMORY POLYMERS FOR BIOMATERIAL APPLICATIONS**

Shelby Lois Buffington  
*Syracuse University*

Follow this and additional works at: <https://surface.syr.edu/etd>



Part of the [Engineering Commons](#)

---

### **Recommended Citation**

Buffington, Shelby Lois, "NOVEL SHAPE MEMORY AND MULTI-SHAPE MEMORY POLYMERS FOR BIOMATERIAL APPLICATIONS" (2019). *Dissertations - ALL*. 1112.  
<https://surface.syr.edu/etd/1112>

This Dissertation is brought to you for free and open access by the SURFACE at SURFACE. It has been accepted for inclusion in Dissertations - ALL by an authorized administrator of SURFACE. For more information, please contact [surface@syr.edu](mailto:surface@syr.edu).

## Abstract

Biomaterial platforms have been used to probe how cells respond to chemical, topographical or mechanical changes in their environments. However, these traditionally static biomaterial platforms have not enabled the study of how cells respond to dynamic changes in their environment. Driven by a need to better understand cell behavior and its role in disease, development and tissue regeneration recent efforts have focused on designing dynamic biomaterial platforms to better mimic a cell's natural environment. In this work, advanced shape memory polymers (SMPs) that respond to non-thermal triggers and multi-shape memory materials capable of multiple topographical transitions were developed for advanced active cell culture platforms.

The first part of this dissertation describes the fabrication and application of an enzymatically triggered SMP, which changed its shape in response to enzymatic degradation (Chapter 2). This was achieved by combining an enzymatically stable fiber and an enzymatically vulnerable fiber. Upon degradation of the enzymatically vulnerable fiber, the enzymatically stable fiber was allowed to relax back to its original conformation, thus driving shape recovery back to the original shape. Both the enzymatically triggered SMP and the process of enzymatic shape recovery were shown to be cytocompatible.

The second part of this dissertation describes the fabrication and application of visible-light triggered SMPs (Chapter 3). To design this material platform, methacrylated graphene oxide was copolymerized with *tert*-butyl acrylate, a material previously used in active cell culture SMP platforms. Upon exposure to white light, the graphene oxide absorbs the light energy through photoexcitation and then transmits that energy as heat to the SMP. This heats the

SMP above its glass transition temperature triggering recovery back to the original shape. In addition, visible-light triggered SMPs demonstrated localized recovery which would enable us to study cell behavioral changes as they crossed topographical boundaries.

Next, this dissertation describes the development of a real-time cell tracking algorithm that could acquire images, segment and link cells between frames and analyze cell migration behavior during a live time-lapse experiment (Chapter 4). The structure of this algorithm is discussed and one of the eight imaging modes is demonstrated during a live cell experiment.

Finally, this dissertation describes utilizing multi-shape memory composites to generate complex topographies. First, a wrinkling platform is discussed that forms double or complex wrinkle patterns along the surface of triple shape polymeric composites (Chapter 5). Second, a novel quadruple shape memory composite that displays quadruple surface shape memory is developed and discussed (Chapter 6).

Overall, this work furthers the experimental applications of SMPs as active cell culture platforms to study cell-material interactions in dynamic environments. It is expected that this work will enable new experiments probing cell mechanobiology.

**NOVEL SHAPE MEMORY AND MULTI-SHAPE MEMORY POLYMERS FOR  
BIOMATERIAL APPLICATIONS**

By

Shelby L. Buffington

B.S. Biomedical Engineering, Texas A&M University, 2012

DISSERTATION

Submitted in partial fulfillment of the requirements for  
the degree of Doctor of Philosophy in *Bioengineering*

Syracuse University  
December 2019



**Copyright © Shelby L. Buffington 2019**

**All Rights Reserved**

*To all the women in STEM who have come before me,  
I wouldn't be here if not for your efforts*

*And to all my friends, family and past mentors. I would not be successful without all of your  
support.*

## Acknowledgments

First, I'd like to thank my advisors, Professors Patrick T. Mather and James H. Henderson for their patience, support, and guidance over these past six years. I have been one of the lucky few who have had direct support for my entire time here and that is due in no small part to their efforts. A special thank you to Dr. Henderson for focusing on my professional development, particularly as it relates to time management and communication. I know I still have a lot of improvements to make, but I'm at least on my way.

I would like to thank my committee members, Prof. Lisa Manning, Prof. Pranav Soman, Prof. Ian Hosein, Prof. Radhakrishna "Suresh" Sureshkumar, Prof. Mary-Beth Monroe for taking the time to review my dissertation.

I want to thank Dr. Richard Baker and Dr. Megan Brasch who were my first mentors when I arrived at Syracuse. I would also like to thank my collaborators Dr. Ian Hosein, and Dr. Saied Biria who provided expertise and equipment toward some of my work.

My sincere thanks go out to all past and current members of the Henderson Lab and Mather Research Group with whom I have had the privilege of working. I would like to acknowledge all of the undergraduate students I have worked with: Justine Paul, Mark Macios, Derek Loh, Stephen Benn, Benjamin Posnick, Bence Kotis, Phil Mohun, Jose Waimin, Jakub Kochanowski, Leila Hart and Johnson Agyapong. I am also thankful for all the behind the scene hard work and support of the administrative staff at Syracuse, especially Karen Low, Lynore De La Rosa, Jason Markel, and Eric Finkelstein. This work would not have been possible without your efforts.

I also would not be here without the support of some of my past mentors, especially Prof. Elizabeth Cosgriff-Hernandez, Prof. Jenny Robinson, Dr. Lloyd Colegrove, Dr. Brenda Colegrove, and Dr. Birgit Braun. You were among my first mentors in research and without the opportunities and guidance you provided early on I would have chosen a very different career path.

To the current Henderson Ph.D. lab members: Paul Chando, Katy Pieri, Alex Jannini, Michelle Pede, and Fred Donelson – I know you’ll make it too. As difficult as the long nights and weekends are I know that each of you will make it to the finish line. Also thank you to my friends who have supported me in Syracuse, especially Monica Ripp, Kyle Bishop, Alex Jannini, Scott Bassler and Micheal Wilkinson. Hanging out with you has always been fun. Lastly, thank you for the love and support of my family. I would not be half the person I am without you.

# Table of Contents

## Contents

<b>List of Tables</b> .....	xv
<b>List of Schemes</b> .....	xvii
<b>List of Figures</b> .....	xxi
<b>Chapter 1: Introduction</b> .....	1xxxviii
1.1 Biomaterials, Tissue Engineering, and Cell Mechanobiology .....	1
1.2 Biomaterials to Probe Cell-Material Interactions .....	4
1.2.1 Probing Cell Responses to Chemical Signals .....	4
1.2.2 Probing Cell Responses to Topographical Signals .....	5
1.2.3 Probing Cell Responses to Stiffness .....	6
1.3 Stimuli Responsive Materials as Biomaterials .....	7
1.3.1 Stimuli Responsive Materials .....	8
1.3.2 Shape Memory Polymers .....	9
1.3.3 Tools for Analyzing Cell Data Sets .....	12
1.4 Dissertation Scope .....	13
1.5 References .....	15
<b>Chapter 2: Enzymatically Triggered Shape Memory Polymers</b> .....	29
2.1 Synopsis .....	29
2.2 Introduction .....	29

2.3 Experimental Methods .....	31
2.3.1 Materials .....	31
2.3.2 Fabrication .....	32
2.3.3 Thermal Analysis .....	34
2.3.4 Shape Memory Characterization.....	35
2.3.5. Bulk Enzymatic Shape Recovery.....	36
2.3.6 Cell Culture Experiments.....	38
2.4 Results.....	40
2.4.1 Fabrication .....	40
2.4.2 Thermal Analysis .....	40
2.4.3 Shape Memory Characterization.....	41
2.4.4 Bulk Enzymatic Shape Recovery.....	42
2.4.5 Cell Culture Experiments.....	44
2.5 Discussion.....	45
2.6 Conclusions and Future Work .....	48
2.7 Acknowledgements.....	48
2.8 References.....	75
<b>Chapter 3: Light-Triggered Shape Memory Polymers .....</b>	<b>79</b>
3.1 Synopsis .....	79
3.2 Introduction.....	79

3.3 Experimental Section .....	80
3.3.1 Materials .....	80
3.3.2 Light Triggered Shape Memory Polymer Fabrication.....	81
3.3.3 Thermal Characterization.....	82
3.3.4 Shape Memory Analysis .....	83
3.3.5 Localized Light-Based Triggering of Shape Recovery .....	84
3.3.6 Cell Culture.....	85
3.4 Results.....	86
3.4.1 Light Triggered Shape Memory Polymer Fabrication.....	86
3.4.2 Thermal Characterization.....	86
3.4.3 Shape Memory Analysis .....	87
3.4.4 Localized Light-Based Triggering of Shape Recovery .....	88
3.4.5 Cell Cytocompatibility to Material Chemistry and to Light-Triggered Shape Recovery .....	89
3.5 Discussion.....	90
3.6 Conclusions and Future Work .....	91
3.7 Acknowledgements.....	91
3.8 References.....	109
<b>Chapter 4: Development of a Real-Time Cell Tracking Algorithm.....</b>	<b>111</b>
4.1 Synopsis .....	111

4.2 Introduction.....	111
4.3 Development and Methodology of the Real-Time ACTIVE Tracking Algorithm.....	113
4.3.1 Post-Processing ACTIVE Platform.....	113
4.3.2 Real-Time Modification.....	114
4.4 Demonstrating the Accuracy of RT-ACTIVE.....	116
4.4.1 Multi-Position RT-ACTIVE Time-Lapse Microscopy .....	116
4.4.2 Processing Time and Accuracy Validation.....	117
4.5 Discussion.....	118
4.6 Conclusions and Future Work .....	118
4.7 Acknowledgments.....	119
4.8 References.....	129
<b>Chapter 5: Generating Complex Wrinkle Patterns Using Triple Shape Memory Polymers</b>	
.....	133
5.1 Synopsis .....	133
5.2 Introduction.....	133
5.3 Materials and Methods.....	136
5.3.1 Materials .....	136
5.3.2 Preparation of Triple Shape Polymeric Composites.....	137
5.3.3 Thermal Characterization.....	137
5.3.4 Triple Shape Memory Behavior.....	138



5.3.5 Programming Triple Shape Polymeric Composites to Make Complex Wrinkle Patterns	139
5.3.6 Sample Recovery and Imaging Protocol	141
5.3.7 Characterizing Wrinkled Surfaces	141
5.4 Results	143
5.4.1 Preparation of Triple Shape Memory Composites	143
5.4.2 Thermal Characterization	144
5.4.3 Triple Shape Memory Behavior	144
5.4.4 Generating Complex Wrinkle Patterns	145
5.5 Discussion	147
5.6 Conclusions and Future Work	150
5.7 Acknowledgements	150
5.8 References	173
<b>Chapter 6: Development of Quadruple Shape Memory Composites</b>	<b>178</b>
6.1 Synopsis	178
6.2 Introduction	178
6.3 Experimental Methods	182
6.3.1 Materials	182
6.3.2. Fabrication of Composite Materials	182
6.3.3 Thermal Characterization	184

6.3.4 Wide Angle X-ray Scattering.....	185
6.3.5 Scanning Electron Microscopy .....	186
6.3.5 Shape Memory Analysis .....	186
6.3.6 Macro Quadruple Shape Memory Demonstration.....	187
6.3.7 Quadruple Shape Surface Shape Memory Demonstration .....	187
6.4 Results.....	188
6.4.1. Fabrication of Composite Materials.....	188
6.4.2 Thermal Characterization.....	189
6.4.3 Wide Angle X-ray Scattering.....	190
6.4.4 Scanning Electron Microscopy .....	191
6.4.5 Shape Memory Analysis .....	191
6.4.6 Macro Quadruple Shape Memory Demonstration.....	192
6.4.7 Quadruple Shape Surface Shape Memory Demonstration .....	193
6.5 Discussion.....	194
6.6 Conclusions and Future Work .....	196
6.7 Acknowledgments.....	197
6.8 References.....	209
<b>Chapter 7: Conclusions and Future Work .....</b>	<b>214</b>
7.1 Overall Conclusions.....	214
7.2 Recommendations for Future Work.....	217

7.2.1 Demonstrating Cell-Triggered Recovery of Enzymatically Triggered SMPs .....	217
7.2.2 Improving the Design of Enzymatically Triggered SMPs.....	218
7.2.3 Physiologically Relevant Multi-Shape Memory Material .....	219
7.2.4 Reversible Light-Triggered SMPs for Active Cell Culture Experiments .....	220
7.3 References.....	223
VITA.....	i

# List of Tables

**Table 2-1.** Measured thermal transitions. For the analyzed temperature range, Pellethane controls demonstrated only a  $T_g$ , at approximately  $-20\text{ }^\circ\text{C}$ , while PCL controls showed only a  $T_m$ , at approximately  $56\text{ }^\circ\text{C}$ . Fiber composites demonstrated both thermal transitions, and the heat of melting of the PCL melt transition was used to quantify the %PCL content in the fiber composites.....49

**Table 2-2.** Calculated fixing ratios for all materials by cycle. PCL is not shown, because the material yields during shape memory testing. All units are %.....50

**Table 2-3.** Calculated recovery ratios for all materials by cycle. PCL is not shown, because the material yields during shape memory testing. All units are %.....51

**Table 3-1.** Measured thermal transitions with varying monomer and cross-linking concentrations. In general, there was an increase in the measured  $T_g$  with increasing BenA and TEGDMA concentration.....93

**Table 3-2.** Measured thermal transitions at different monomer and m-GO concentrations at a fixed cross-linking concentration of 10% TEGDMA. Little change in the  $T_g$  of the SMP films was observed with different m-GO content however all compositions tested showed a higher  $T_g$  than the pure SMP materials.....94

**Table 3-3.** Calculated fixing and recovery ratios for both thermal and light shape memory cycles. Both thermal and light shape memory showed excellent fixing capabilities. However, the light recovery ratio was lower. We believe this is due to some of the light being blocked by the metal clamps of the DMA.....95

**Table 6-1.** The measured thermal transitions and % compositions of all composite materials.  
[a]  $^\circ\text{C}$  [b] %.....198

**Table 6-2.** The fixing and recovery ratios for the 4SM composite cycled through three separate QSMCs.....199

## List of Schemes

**Scheme 2-1.** The strategy used to achieve enzymatic shape memory fiber composites. Fiber composites composed of poly( $\epsilon$ -caprolactone) (PCL) (red) and Pellethane (black) are heated and stretched above the  $T_m$  of PCL to program the samples. The composites are then cooled to fix the temporary shape, putting the Pellethane in an entropically unfavorable state. In this state, the Pellethane applies a compressive force to the PCL, as the Pellethane tries to recover back to its original shape but is resisted by the PCL crystallites that hold the temporary shape. Exposure to the enzyme lipase degrades the PCL portion of the fiber composite. As the PCL degrades, the force resisting the Pellethane is gradually removed and the Pellethane acts as an entropic spring to return back to its original conformation, recovering the permanent shape of the composite.....52

**Scheme 2-2.** The custom electrospinning apparatus used in the present study. A metallic mandrel with variable rotational speed is suspended above an electrically insulating platform. A separate metallic frame is placed over the platform to suspend a translator as well as protective Plexiglas to isolate the interior environment. Attached at the bottom of both translator arms are electrical connection points for the needle tips, which dispense the polymer solution. Syringe pumps (not shown) dispense the polymer solution through the tubing, which connect the syringes to the electrical connections on the translator arms.....53

**Scheme 4-1.** ACTIVE executes four major tasks: (A-E) nuclear segmentation, (F) nuclear linking, (G) cell division and merging event post-processing, and (H-K) individual and collective cell motility analysis. (A) Cells were stained with Hoechst 33342 and imaged for 24 h; (B) image subsections exhibited variable intensity in nuclear staining. (C) Individual frames were first

processed using a bandpass filter and (D) contour profiles were established based on fluctuations in nuclear intensity. (E) Single peak contours were fit with an ellipse at half-height, denoting cell identification. Multi-peak intensity profiles were tagged as either a division or merging event and reevaluated for accuracy during post-processing. (F-i) Once segmentation was complete, cell identification tags were established and (F-ii) cell track information was linked between consecutive frames. (G-i) Post tracking, cell-cell interaction events were identified, (G-ii) processed using a custom cost function, and (G-iii) track information was updated. Motility behavior was then characterized using different analysis metrics such as (H) decomposed mean-squared displacement, (I) velocity-autocorrelation, (J) diffusion plots and (K) final cell locations rotated by the principal axis of the gyration tensor. Adapted with permission from R.M. Baker, M.E.Brasch, M.L. Manning and J.H. Henderson, *Journal of The Royal Society Interface*, **2014**, 11, 20140386. Copyright © The Royal Society 2014.....120

**Scheme 4-2.** A map showing the program structure of the real-time ACTIVE modification. First, the experimental parameters from the input GUIs are loaded and the variables for tracking are initialized. The code then goes into two large loops that loop the core functions of ACTIVE through every experimental time point and position (a maximum of three). Briefly, the code will go through and sequentially: capture and process images (only if scope controls are enabled), conduct segmentation, conduct linking, conduct post-processing corrections, choose or continue to follow a cell (only if single-cell tracking is enabled), move microscope so the cell is centered (only if single-cell tracking is enabled), conduct real-time calculation of tracking metrics, and plot and display real-time cell tracks and tracking metrics. The code then iterates through the number of specified positions (from one to three) and then iterates over the number of specified time points.....122

**Scheme 5-1.** Fabrication schematic for making TSPCs. The epoxy components were first mixed in a beaker until well mixed. The mixture was then poured over an electrospun fiber mat of PCL and placed against a piece of clean and smooth glass. The material was rolled to get some excess epoxy out of the fibers and ensure good contact with the glass. This ensured that one side of the material was atomically smooth like the glass. The epoxy was then cured against the glass at 40 °C for 48 hours to partially cure the epoxy to hold the fiber morphology of the PCL in the composite material. The temperature was then increased to 60 °C to ensure complete cure of the epoxy.....151

**Scheme 5-2.** Schematic of how to program the TSPCs to generate complex or double wrinkle patterns. First, a large strip of the material is heated to 70 C, above the Tm of the PCL component and strained to either 10, 15 or 20% strain. The strip is then cooled and cut into smaller sections either parallel to the original stretch direction, or perpendicular (depicted here). The smaller strips are then heated to 49 C and strained a second time to program in the second strain. The samples are then coated with a thin layer of gold and triggered to recover, forming wrinkle patterns.....152

**Scheme 6-1.** Process to make 4SMCs. 1) PIPS precursor is prepared by heating a solution of NGDE, DGEBA, and PMMA at 80 °C until all materials formed a homogenous solution. 2) JD230 cross-linker is then added and the solution was cooled to 50 °C. 3) PCL web is separately prepared by electrospinning rotating collector drum. 4) The PIPS precursor solution (green) is then imbibed into the web (black). 5) Upon cure, the PMMA and epoxy phase separate, creating a three-phase solid of PMMA, epoxy, and PCL.....200





## List of Figures

**Figure 2-1.** A comparison of the fiber morphologies of fiber composites and material controls (left) immediately after electrospinning and (right) immediately after the heat treatment used to recover residual strain programmed during the electrospinning process. The Pellethane fibers showed no noticeable morphological changes due to heat treatment and no noticeable shrinking. The 20:80 PCL:Pellethane showed fiber morphologies both before and after heat treatment. The 50:50 PCL:Pellethane showed a fiber morphology after electrospinning but showed a film morphology after heat treatment due to the melting of the PCL. The PCL control also transitioned from a fiber morphology before heat treatment to a film morphology after heat treatment. Scale bar is 10  $\mu\text{m}$ .....54

**Figure 2-2.** Thermal gravimetric analysis (TGA) analysis of fiber composites and controls. The poly( $\epsilon$ -caprolactone) (PCL) control (brown) showed a single-step degradation, while the Pellethane control (black) showed a two-step degradation. The fiber composites all showed a two-step degradation, similar to the Pellethane, although it should be noted that the second step of the Pellethane occludes the single PCL step. Due to this occlusion, dynamic scanning calorimetry, not TGA, was used to assess sample compositions.....55

**Figure 2-3.** Differential scanning calorimetry (DSC) thermograms of all dual spun materials ordered in order of increasing poly( $\epsilon$ -caprolactone) (PCL) content. Increasing PCL content resulted in a large exotherm for the PCL melt transition but did not result in shifting of the  $T_m$  of PCL. This exotherm at approximately 56  $^{\circ}\text{C}$  was used to calculate the predicted incorporation of PCL during the electrospinning process, and only fiber mats within 5% of the predicted PCL content were used in subsequent experiments. DSC traces are in order of increasing PCL content,

from top to bottom: Pellethane, 20:80 PCL:Pellethane, 30:70 PCL:Pellethane, 40:60 PCL:Pellethane, 50:50 PCL:Pellethane, and PCL. ....56

**Figure 2-4.** Dynamic mechanical analysis (DMA) curves of fiber composites and control showing (top) storage modulus and (bottom) tan delta traces. Peaks in tan delta traces correspond to changes in the storage modulus. There is a  $T_g$  for Pellethane at approximately  $-20\text{ }^\circ\text{C}$ , a  $T_m$  for poly( $\epsilon$ -caprolactone) (PCL) at  $56\text{ }^\circ\text{C}$ , and a  $T_m$  for Pellethane at approximately  $160\text{ }^\circ\text{C}$ . The ideal range for shape memory behavior would be above the  $T_g$  of Pellethane, so the material is in its elastic region, but below the  $T_m$  of Pellethane, to hold the permanent shape. The  $T_m$  of PCL then acts as the triggering transition that holds the temporary shape.....57

**Figure 2-5.** Thermal shape memory cycles. A) Pure Pellethane showed a fixing ration ( $R_f$ ) of 54% and a recovery ratio ( $R_r$ ) of 87%. B) The 20:80 PCL:Pellethane fiber composite showed an  $R_f$  of 93.5% and an  $R_r$  of 85.1%. C) The 30:70 PCL:Pellethane fiber composite showed an  $R_f$  of 94.45% and an  $R_r$  of 86.3%. D) The 40:60 PCL:Pellethane fiber composite showed an  $R_f$  of 95.2% and an  $R_r$  of 89.8%. E) The 50:50 PCL:Pellethane fiber composite showed an  $R_f$  of 97.5% and an  $R_r$  of 83.2%. F) Pure PCL yielded during the first stretch of the first cycle and is not reported. One shape memory cycle comprises the following steps: starting at the asterisk, the sample is heated to  $60\text{ }^\circ\text{C}$ , and then the force is ramped to stretch the sample; the sample is then cooled to  $0\text{ }^\circ\text{C}$  and unloaded; the sample is then heated back to  $60\text{ }^\circ\text{C}$  to measure recovery. This cycle was completed three times with cycles 1, 2, and 3 shown in black, light gray, and dark gray, respectively.....58

**Figure 2-6.** Enzyme-triggered shape recovery over 7 days. The  $0.5\text{ mg/mL}$  condition (A) is the only condition for which fiber composites showed measurable, significant sample recovery. The  $0.1\text{ mg/mL}$  (B) and  $0.05\text{ mg/mL}$  (C) conditions showed no measurable sample recovery. The

PBS control (D) showed no strain changes for any groups, including the PCL control, over the course of the 7-day experiment. For all conditions, the fiber composites (20:80 and 50:50 PCL:Pellethane) showed a significantly different length compared to Pellethane controls, except for days 5-7 in the 0.5 mg/mL condition. \* and bar indicate the three time points for which the strain of fiber composites was no longer statistically different from that of the Pellethane controls ( $P>0.05$ ), indicating sample recovery. For all groups, the value at day 0 is the mean programmed strain of all 21 samples (3 replicates  $\times$  7 time points), and the value at each subsequent time point is the mean of the 3 samples collected at that time point. ....59

**Figure 2-7.** Macroscopic view of enzymatic recovery. Pictures of samples were taken before and after programming and after being exposed to 0.5 mg/mL lipase solution over the course of 7 days. The Pellethane, 20:80 PCL:Pellethane, 50:50 PCL:Pellethane and PCL are shown in order from left to right. After programming, the Pellethane showed no shape fixing and no measured change in length over the 7-day incubation. In contrast, both fiber composites fixed a temporary shape and then contracted over the course of 7 days. The PCL control fixed a temporary shape and then degraded fully instead of changing shape. The glare in 20:80 samples from days 1 through 7 is due to covering glass used to position the samples during imaging. The scale bar is 10 mm. ....60

**Figure 2-8.** Mass change during degradation. Significant mass loss was observed for the PCL film in all conditions: (A) 0.5 mg/mL lipase; (B) 0.1 mg/mL lipase; (C) 0.05 mg/mL lipase; and (D) PBS (0 mg/mL lipase)). All other samples exhibited no measurable mass loss.....61

**Figure 2-9.** Heat of crystallinity of hydrated 50:50 PCL:Pellethane fiber composites immediately following exposure to lipase. The heat of crystallinity of the PCL, as measured by differential scanning calorimetry (DSC), decreases over the course of degradation experiments, indicating

that the PCL crystal structure is being broken up. The data also suggest that the water present in the sample interferes with the re-crystallization of PCL, resulting in the crystallization being lower for the second heat compared to the first heat.....62

**Figure 2-10.** SEM micrographs of 50:50 PCL:Pellethane incubated in 0.5 mg/mL of lipase. Morphological analysis shows changes in sample morphology indicative of PCL degradation (A-D) at the surface and (E-H) in cross-section of 50:50 PCL:Pellethane fiber composites for day 0, 1, 3, 7, respectively. Day 0 shows the 50:50 fiber composite after heat treatment but before any strain programming or enzymatic recovery. Scale bar is 10  $\mu\text{m}$ . Results for both fiber composites (20:80 and 50:50 PCL:Pellethane) and for the PCL controls under all incubation conditions (0.5 mg/mL, 0.1 mg/mL, and 0.05 mg/mL lipase and PBS) are available in Figs. S6 through S9).....63

**Figure 2-11.** SEM images of Pellethane and fiber composites as samples are incubated in a solution with 0.5 mg/mL of Lipase. Fiber composites go from a fiber-film morphology to a pure fiber morphology over the course of experiments. Pellethane, 20:80 PCL:Pellethane, 50:50 PCL:Pellethane are shown in row A, B and C, respectively. Scale bar is 10  $\mu\text{m}$ .....64

**Figure 2-12.** SEM images of Pellethane and fiber composites as samples are incubated in a solution with 0.1 mg/mL of Lipase. Fiber composites go from a fiber-film morphology to a pure fiber morphology over the course of experiments. Pellethane, 20:80 PCL:Pellethane, 50:50 PCL:Pellethane are shown in row A, B and C, respectively. Scale bar is 10  $\mu\text{m}$ .....65

**Figure 2-13.** SEM images of Pellethane and fiber composites as samples are incubated in a solution with 0.05 mg/mL of Lipase. Fiber composites go from a fiber-film morphology to a pure

fiber morphology over the course of experiments. Pellethane, 20:80 PCL:Pellethane, 50:50 PCL:Pellethane are shown in row A, B and C, respectively. Scale bar is 10  $\mu\text{m}$ .....66

**Figure 2-14.** SEM images of Pellethane and fiber composites as exposed to PBS over a course of 7 days. Samples showed no changes in sample morphology. Pellethane, 20:80 PCL:Pellethane, 50:50 PCL:Pellethane are shown in row A, B and C, respectively. Scale bar is 10  $\mu\text{m}$ .....67

**Figure 2-15.** Cell viability of C3H/10T1/2 cells cultured directly on fiber composite and non-composite control samples in the absence of lipase. No significant differences were found between any groups ( $P>0.05$ ), and viability was  $>75\%$  for all groups. Groups are Pellethane control, PCL control, compressed PCL Film control, 20:80 PCL:Pellethane fiber composite, 50:50 PCL:Pellethane fiber composite, and tissue culture polystyrene control. ....68

**Figure 2-16.** Representative micrographs of C3H/10T1/2 cells cultured directly on fiber composite and non-composite control samples in the absence of lipase. Live cells are shown in green and dead cells are shown in red. Groups are Pellethane control, PCL control, compressed PCL Film control, 20:80 PCL:Pellethane fiber composite, 50:50 PCL:Pellethane fiber composite, and tissue culture polystyrene control. Scale bar is 100  $\mu\text{m}$ .....69

**Figure 2-17.** Cell numbers of C3H/10T1/2 cells cultured directly on fiber composite and non-composite control samples in the absence of lipase. Groups are Pellethane control, PCL control, compressed PCL Film control, 20:80 PCL:Pellethane fiber composite, 50:50 PCL:Pellethane fiber composite, and tissue culture polystyrene control. \*\* and \*\*\* indicate material groups that are significantly different than TCPS control at 48 and 72 h, respectively.....70

**Figure 2-18.** Cell viability of C3H/10T1/2 cells cultured directly on fiber composite and non-composite control samples in (left) a lipase-free control medium or (right) the presence of 0.5

mg/mL lipase. No significant differences were found between any groups ( $P>0.05$ ), and viability was  $>75\%$  for all groups. Groups are Pellethane control, compressed PCL Film control, 20:80 PCL:Pellethane fiber composite, 50:50 PCL:Pellethane fiber composite, and tissue culture polystyrene control.....71

**Figure 2-19.** Representative micrographs of C3HT101/2 cells cultured directly on fiber composite and non-composite control samples in the absence of lipase (control for cells studied in Fig. S13). Live cells are shown in green and dead cells are shown in red. Groups are Pellethane control, PCL control, compressed PCL Film control, 20:80 PCL:Pellethane fiber composite, 50:50 PCL:Pellethane fiber composite, and tissue culture polystyrene control. Scale bar is 100  $\mu\text{m}$ . .....72

**Figure 2-20.** Representative micrographs of C3H/10T1/2 cells cultured directly on fiber composite and non-composite control samples in the presence of 0.5 mg/mL lipase. Live cells are shown in green and dead cells are shown in red. Groups are Pellethane control, PCL control, compressed PCL Film control, 20:80 PCL:Pellethane fiber composite, 50:50 PCL:Pellethane fiber composite, and tissue culture polystyrene control. Scale bar is 100  $\mu\text{m}$ .....73

**Figure 2-21.** Cell numbers of C3H/10T1/2 cells cultured directly on fiber composite and non-composite control samples in the (left) absence or (right) presence of lipase. Groups are Pellethane control, compressed PCL Film control, 20:80 PCL:Pellethane fiber composite, 50:50 PCL:Pellethane fiber composite, and tissue culture polystyrene control. \*, \*\*, and \*\*\* indicate material groups that are significantly different than TCPS control at 24, 48, and 72 h, respectively.....74

**Figure 3-1.** DSC scans of SMP films of different monomer and cross-linker compositions. In general,  $T_g$  increased from 49.7 °C (100tBA 1wt% TEGDMA) to a maximum of 61 °C (100BenA 10 wt% TEGDMA) with increasing BenA and TEGDMA content. However, the broadness of the  $T_g$  also increased with BenA content which would broaden the recovery event of SMP films.....96

**Figure 3-2.** DSC scans of the SMP films with different levels of graphene oxide embedded in the material using 10 wt% TEGDMA as the cross-linker. The amount m-GO content appears to have no effect on the overall  $T_g$  of the SMP system, however all SMP films showed a higher  $T_g$  compared to base films. This is compared to the pure tBA systems which showed the lowest  $T_g$  but the sharpest.....97

**Figure 3-3.** Thermal shape memory cycles of A) 100tBA 10% TEGDMA 0 wt% m-GO, B) 100tBA 10% TEGDMA 0.5wt% m-GO, C) 100tBA 10% TEGDMA 1wt% m-GO and D) 100tBA 10% TEGDMA 2.5wt% m-GO. All compositions showed excellent shape fixing and recovery ability as well as a sharp recovery event. ....98

**Figure 3-4.** Light shape memory graphs. On the left is the thermal programming of the sample before light exposure and on the right is the visible light-triggered recovery. Where the 0.5wt m-GO samples showed strong shape fixing ability it showed no measurable visible light triggered recovery, likely due to the wt% of the m-GO being too low. Both the 1 wt% and 2.5 wt% m-GO samples showed excellent shape fixing and recovery abilities with the 1 wt% m-GO sample demonstrating the highest shape recovery ability.....99



**Figure 3-5.** Demonstration of visible-light triggering of SMPs. The materials are first thermally programmed by heating to 80 °C and then deformed into the temporary shape of a “C”. The SMP is then exposed to white light and recovers back to its original shape.....100

**Figure 3-6.** To create nano-wrinkles along the surface of SMPs, materials are first thermally programmed to 10% strain. The samples were then sputter coated with gold and triggered to recover. Upon recovery the SMP places a compressive strain along the surface of the material causing the gold coating to buckle and form nano-wrinkle patterns. Scale bar is 10 μm.....101

**Figure 3-7.** Wrinkle patterns formed along the surface of light triggered SMPs that are both thermally and visible-light triggered. No noticeable difference in the wrinkle pattern can be observed.....102

**Figure 3-8.** Since the light exposure can be spatially controlled, the SMPs can be locally recovered creating areas with a wrinkled topography (Left) and areas with a flat topography (Right). As can be seen in the figure the boundary between the wrinkled and non-wrinkled areas of the sample is very sharp. Scale bar is 20 μm.....103

**Figure 3-9.** The average viability of C3H10T1/2 cells cultured on the surface of programmed and coated SMPs. The viability for the 24 h time points were lower than the 48 h time points but this is potentially due to the sample floating during experiments versus material cytotoxicity..104

**Figure 3-10.** Representative cell micrographs of C3H10T1/2 cells cultured on the surface of gold coated SMPs. Live cells are shown in green and dead cells are shown in red. Scale bar is 100 μm. Groups are the TCPS live control, 0.5wt% m-GO, 1 wt% m-GO and 2.5 wt% m-GO. The SMP composition was set to 100tBA 10wt% TEGDMA for this study.....105

**Figure 3-11.** Cell viability of C3H10T1/2 cells cultured directly on programmed and coated SMP films exposed to white light for either 30 s, 1 min, or 2 min. The live control was cells grown on a TCPS well plate. The highest viability was observed for the 30 s of exposure, but material recovery was not observed until at least 1 min of exposure in the sample containing 1 wt% or 2.5 wt% m-GO. However, the samples exposed to 2 mins of white light exposure showed poor viability potentially due to hyperthermic cytotoxicity.....106

**Figure 3-12.** Representative micrographs of C3H10T1/2 cells cultured directly on programmed and coated SMP films exposed to either 30 s, 1 min or 2 min of white light. Cell number decreased with increased exposure with very few cells present on the samples exposed to 2 min of white light. The samples showing the highest viability were those cultured on 0.5 wt% m-GO which did not show any material recovery. In addition, samples exposed to 30 s of white light exposure showed a high viability but also did not show any material recovery. Scale bar is 100  $\mu\text{m}$ .....107

**Figure 4-1.** The GUI for the real-time *ACTIVE* tracking code. Users are given the same input parameters from the original version of *ACTIVE*. Users then specific a data file name and choose which tracking options they want to have turned on. The code can be run in 8 different combinations depending on the structure of the experiments. First, the code can be run in “Microscope” or “Image Stack”. Image stack disables the microscope control functions and the code will instead feed images in from an image stack one frame at a time. Second, the user will specify between “single-cell” and “multi-cell”. Single-cell will trigger RT-*ACTIVE* to pick a single cell and follow it over the course of an experiment. Multi-cell will have RT-*ACTIVE* stay in a single location and track the cells entering and exiting the frame. Finally, the user needs to specify between “Single-Position” and “Multi-Position”. Single-position means RT-*ACTIVE*

will only track a single spot or cell while multi-position will allow the user to specify up to three locations. It should be noted that if the scope mode is enabled RT-ACTIVE will read these locations from the position list loaded into  $\mu$ Manager.....123

**Figure 4-2.** The cell tracks (top) and gyration tensor (bottom) for position 1 of the first Multi-Position experiment.....125

**Frame 4-3.** The measured processing time for the full tracking and analysis of a 288-frame test stack. The conditions tested were: Image stack (IS), multi-cell mode (MC), single position (SP) while running no analysis, the radius of gyration analysis, the mean-squared displacement analysis or both the mean squared displacement and the radius of gyration. As expected, the processing time increased as the frame number increased. In addition, the analysis functions increased the processing time as well.....126

**Figure 4-4.** An overlay of the generated cell tracks created using ImageJ. The cell tracks generated by the RT-ACTIVE are shown in green and the tracks generated by the original version of ACTIVE is shown in red. Where the tracks overlap, the image is yellow. Upon close inspection one can see the overlap between the two cell tracking images is not perfect.....127

**Figure 4-5.** An overlay of the generated cell tracks created using ImageJ. The cell tracks generated by the RT-ACTIVE position 1 are shown in green and the tracks generated by the RT-ACTIVE position 2 is shown in red. No differences in cell tracks were observed.....128

**Figure 5-1.** An example DSC trace of a TSMC showing two distinct thermal transitions per composite. The  $T_g$  of the epoxy was carefully controlled by controlling the composition of the epoxy monomers and selected so that the  $T_g$  was high enough to prevent recovery during gold

coating but low enough to ensure good separation between the  $T_g$  of the epoxy and the  $T_m$  of the PCL. Specifically, a  $T_g$  of 45-48 °C was target for the epoxy monomers.....153

**Figure 5-2.** A DMA sweep showing the temperature dependence of the modulus of the TSPCs. The storage modulus trace shows a small separation between the two transitions, while the tan delta shows a secondary hump, indicating two separate mechanical transitions.....154

**Figure 5-3.** An example triple shape memory cycle (TSMC). The dog bone sample is first heated to 80 °C and stretched to program a strain into the PCL phase of the sample. The temperature is then cooled to 0 °C to crystallize the PCL and fix the first temporary shape. The temperature is then increased to 50 °C and strained again to program a temporary shape into the epoxy phase of the material. The material is then cooled to 0 °C to fix the second temporary shape and the force removed. The sample is then heated at a continuous rate to capture the recovery event. The epoxy and PCL showed a fixing ratio of 91.4% and 93.3%, respectively and a recovery ratio of 84.2% and 88.7%, respectively.....155

**Figure 5-4.** AFM micrographs of the TSPC surfaces after coating the samples with gold but prior to any recovery steps for the biaxially programmed samples. The surfaces all showed no sinusoidal wrinkle patterns and were all very flat. Scale bar is 10  $\mu\text{m}$ .....156

**Figure 5-5.** AFM micrographs of the TSPC surfaces after coating the samples with gold but prior to any recovery steps for the uniaxially programmed samples. The surfaces all showed no sinusoidal wrinkle patterns and were all very flat. Scale bar is 10  $\mu\text{m}$ .....157

**Figure 5-6.** AFM micrographs of the TSPC surfaces after the first recovery step at 50 C for the biaxially programmed samples with the 2D-FFT shown in the upper right-hand corner. As the epoxy recovered its strain the gold surface buckled forming wrinkle patterns along the surface of

the materials. As this occurred the 2DFFT scans developed are bar bell shape indicating the presence of a sinusoidal pattern on the surface. The samples with no epoxy strain programmed in did not show any wrinkle pattern formations as expected. The wavelength of the epoxy wrinkles actually increased with increasing PCL strain, indicating the presence of some cross-talk between the programmed strains. The 15% epoxy strain for the 15% PCL samples is not present as it recovered prematurely. Scale bar is 10  $\mu\text{m}$ .....158

**Figure 5-7.** Graphs showing the average roughness, wavelength and relative amplitude of the wrinkle patterns formed after the first 50 C recovery of the biaxially programmed samples. The 20% PCL samples showed a small increasing trend in the average roughness while the other samples showed little change as the strain increased overtime. The average wavelength of the wrinkle patterns increased with increasing PCL strain stain and showed no trend in increasing epoxy strain. The amplitude of the developed wrinkles showed no noticeable trend.....159

**Figure 5-8.** AFM micrographs of the TSPC surfaces after the first recovery step at 50 C for the biaxially programmed samples with the 2D-FFT shown in the upper right-hand corner. As the epoxy recovered its strain the gold surface buckled forming wrinkle patterns along the surface of the materials. As this occurred the 2DFFT scans developed are bar bell shape indicating the presence of a sinusoidal pattern on the surface. The samples with no epoxy strain programmed in did not show any wrinkle pattern formations as expected. The wavelength of the epoxy wrinkles actually increased with increasing PCL strain, indicating the presence of some cross-talk between the programmed strains. The 15% epoxy strain for the 15% PCL samples is not present as it recovered prematurely. Scale bar is 10  $\mu\text{m}$ .....160

**Figure 5-9.** Graphs showing the average roughness, wavelength and relative amplitude of the wrinkle patterns formed after the first 50 °C recovery of the uniaxially programmed samples. No

noticeable trend in the surface roughness was observed with the strain of the materials. The average wavelength of the wrinkle patterns remained the same as the epoxy strain increased, except of the samples programmed with 15% PCL strain, which showed a general decreasing trend. The relative amplitude of all the samples showed no general trend except for the samples programmed with 20% PCL strain which showed a decreasing trend in the amplitude.....162

**Figure 5-10.** AFM micrographs of the TSPC surfaces after the second recovery step at 60 °C for the biaxially programmed samples with the 2D-FFT shown in the upper right-hand corner. For the samples with no epoxy strain, a perpendicular wrinkle pattern formed along the surface as the PCL recovered its strain. As this occurred the 2DFFT scans developed are bar bell shape in an up-down direction indicating the presence of a sinusoidal pattern on the surface. For the samples were the epoxy wrinkles had already formed, the PCL recovery caused an additional wrinkle pattern to form along the surface, but only for those samples with a small amount of epoxy strain. The double wrinkle patterns showed a double bar-bell shape in their 2DFFT scans, indicating that two sinusoidal patterns existed. The 15% epoxy strain for the 15% PCL samples is not present as it recovered prematurely. Scale bar is 10 μm.....163

**Figure 5-11.** Graphs showing the average roughness, wavelength and relative amplitude of the wrinkle patterns formed after the second 60 °C recovery of the biaxially programmed samples. No noticeable trend in the surface roughness was observed with the strain of the materials. The average wavelength of the samples increased with programmed PCL strain but remained constant with increasing epoxy strain. The wavelength of the wrinkles formed by the PCL was on average higher than the wavelength of the wrinkles formed by the epoxy recovery. The amplitude of the wrinkles remained similar for all epoxy strain groups, however the amplitude of the PCL wrinkles showed a decreasing trend with increasing epoxy strain.....165

**Figure 5-12.** AFM micrographs of the TSPC surfaces after the second recovery step at 60 °C for the uniaxially programmed samples with the 2D-FFT shown in the upper right-hand corner. For the samples with no epoxy strain, a wrinkle pattern with the recovery of the PCL, and in some cases showed a double nature, despite there being no biaxially programmed strain. The samples with epoxy wrinkles pre formed showed a decrease in the wavelength of the wrinkle patterns compared to the patterns formed at 50 °C. Scale bar is 10 μm.....166

**Figure 5-13.** Graphs showing the average roughness, wavelength and relative amplitude of the wrinkle patterns formed after the second 60 °C recovery of the uniaxially programmed samples. No noticeable trend in the surface roughness was observed with the strain of the materials. The average wavelength of the samples increased with programmed PCL strain but remained constant with increasing epoxy strain. The wavelength of the wrinkles formed by the PCL was on average higher than the wavelength of the wrinkles formed by the epoxy recovery. The amplitude of the wrinkles remained similar for all epoxy strain groups, however the amplitude of the PCL wrinkles showed a decreasing trend with increasing epoxy strain.....167

**Figure 5-14.** AFM micrographs of the TSPC surfaces after the 1 step recovery 60 °C for the biaxially programmed samples with the 2D-FFT shown in the upper right-hand corner. This allowed for both strains to recover at approximately the same time, although there would still be a lag between the recovery for the PCL compared to the epoxy due to the temperature difference). For the samples with no epoxy strain, a perpendicular wrinkle pattern formed along the surface as the PCL recovered its strain. As this occurred the 2DFFT scans developed are bar bell shape in an up-down direction indicating the presence of a sinusoidal pattern on the surface. Similar to above the samples with a large amount of the PCL strain did show some double wrinkle patterns forming, likely due to a Possoin effect. For samples with both epoxy and PCL

strain programmed in you saw the formation of various wrinkle patterns. In the case where the epoxy strain is high compared to the PCL strain, only the orthogonal wrinkle patterns are observable, however as the PCL strain increases the formation of double wrinkle patterns is evident. In the case of 15% epoxy strain, only the orthogonal wrinkle pattern was observed. The double wrinkle patterns showed a double bar-bell shape in their 2DFFT scans, indicating that two sinusoidal patterns existed. The 15% epoxy strain for the 15% PCL samples is not present as it recovered prematurely. Scale bar is 10  $\mu\text{m}$ .....168

**Figure 5-15.** Graphs showing the average roughness, wavelength and relative amplitude of the wrinkle patterns formed for the 1-step recovery at 60 °C for the biaxially programmed samples. No noticeable trend in the surface roughness was observed with the strain of the materials. The average wavelength of the samples increased with programmed PCL strain but remained constant with increasing epoxy strain. The wavelength of the wrinkles formed by the PCL was on average higher than the wavelength of the wrinkles formed by the epoxy recovery and increased with increasing epoxy strain. The amplitude of the wrinkles remained similar for all epoxy strain groups, however the amplitude of the PCL wrinkles showed a decreasing trend with increasing epoxy strain.....170

**Figure 5-16.** AFM micrographs of the TSPC surfaces after the 1 step recovery at 60 °C for the uniaxially programmed samples with the 2D-FFT shown in the upper right-hand corner. For the samples with no epoxy strain, a wrinkle pattern with the recovery of the PCL, and in some cases showed a double nature, despite there being no biaxially programmed strain; likely due to a Possion effect since the modulus of the composite would be lower for the PCL recovery since the epoxy is already rubbery. Scale bar is 10  $\mu\text{m}$ .....171



**Figure 5-17.** Graphs showing the average roughness, wavelength and relative amplitude of the wrinkle patterns formed after the second 60 °C recovery of the uniaxially programmed samples. No noticeable trend in the surface roughness was observed with the strain of the materials. The average wavelength of the samples increased with programmed PCL strain but remained constant with increasing epoxy strain. The wavelength of the wrinkles formed by the PCL was on average higher than the wavelength of the wrinkles formed by the epoxy recovery. The amplitude of the wrinkles remained similar for all epoxy strain groups, however the amplitude of the PCL wrinkles showed a decreasing trend with increasing epoxy strain.....172

**Figure 6-1.** The images on the left are of epoxy liquids prior to cure. The top image is a pure epoxy resin and the bottom is a PIPS solution. After cure, the epoxy resin remained optically clear (shown top right) and the PIPS precursor solution became optically opaque (bottom right), indicating that phase separation had occurred. Scale Bar is 10 mm.....201

**Figure 6-2.** DSC thermograms (2nd heating) of 4SMCs, triple shape composite controls and material controls. Epoxy matrix, PCL and PMMA controls are shown in black, red and green respectively. The epoxy/PMMA PIPS composite and epoxy/PCL TSPC controls are shown in blue and purple, respectively. The 4SMC is shown in red. The dashed lines are scaled up by a factor of 7 to make the PMMA Tg visible in the DSC traces, since the corresponding DSC signal was very small compared to the other thermal transitions. The heating rate was 10 °C/min for all samples.....202

**Figure 6-3.** The DMA results for all material composites and an epoxy control. The top graph shows the temperature dependence of the storage modulus while the bottom shows the loss modulus. The thermal-mechanical transition of the PMMA was clearly visible in PMMA containing composite materials. The heating rate for all tests was 2 °C/min.....203

**Figure 6-4.** The Wide-Angle X-ray Diffraction of all control samples and composites. A) The intensity versus diffraction angle for all tested materials B) The WAXS scattering patterns for all materials.....204

**Figure 6-5.** SEM of the composite materials and epoxy control. Images A, C, E, and G are representative images of the top surfaces of the epoxy control, epoxy/PCL triple shape composite, epoxy/PMMA PIPS composite and 4SMC, respectively. Images B, D, F, H show the cross section of the epoxy control, epoxy/PCL triple shape composite, epoxy/PMMA PIPS composite and 4SMC, respectively. Scale bar is 10  $\mu\text{m}$ .....205

**Figure 6-6.** Shape memory characterization of epoxy matrix control and all composite materials. Graph A shows the 1 WSMC for the epoxy control matrix. In all graphs the asterisk denotes that starting point. Graph B and C show the triple shape memory cycles for the TSPC control and the PIPS composite control, respectively. Graph D, E and F are QSMCs programming different amounts of strain into each phase of the material. D: Equal amounts of strain were programmed into the composites and then recovered under continuous heating. E: More strain was programmed into the PCL phase of the material. F: More strain was programmed into the PMMA phase of the material. Step 1, 3, and 6 are stretching and programming strain into the PMMA, PCL and Epoxy phase respectively. Step 2, 4 and 7 were cooling steps with fixing of strain into the PMMA, PCL and epoxy phases, respectively. Steps 8, 9 and 10 show the recovery of the Epoxy, PCL and PMMA phases, respectively, under continuous heating. Step 5 was heating above the glass transition of the epoxy after cooling to a low temperature to fix the strain in the PCL.....206

**Figure 6-7.** Macro SM Demonstration. I) shows an animation of the desired programmed shapes. II) Shows the programmed shapes in the 4SMCI. III) Shows the shapes fixed into the material

by the desired material phase. IV) Shows the recovery of the 4SMCs the shape transitions from flat, to an S to a U to flat again, effectively demonstrating 4 distinct shapes. The scale bar shown in each image represents 10 mm.....207

**Figure 6-8.** Surface Shape Memory Demonstration. A) Fully programmed disk with three separate patterns programmed on top of each other in the three separate material phases. B) 4SMC surface after allowing the epoxy to recover and the vertical lines fixed into the matrix recovered. C) 4SMC surface after triggering the PCL phase to recover and the horizontal lines recovered. D) 4SMC surface after triggering the PMMA to recover, returning the disk to its original shape. Scale Bar is 1 mm.....208

**Figure 7-1.** Top) SEM micrographs of the fiber orientation before triggering and after incubating in a solution of PBS and varying concentrations of lipase for 24 hours. Scale bar 10  $\mu\text{m}$ . Middle) 2DFFT azimuthal scans of the SEM micrographs. As the fibers become for aligned a bimodal distribution becomes apparent indicating fiber alignment. Bottom) Cell micrographs of fixed cells cultured on the surface of enzymatic SMPs while the material recovers its aligned fiber architecture. Scale bar 50  $\mu\text{m}$ .....221

# Chapter 1: Introduction

## 1.1 Biomaterials, Tissue Engineering, and Cell Mechanobiology

Biomaterials are materials that can function as a whole or as a part of a device to treat, assist, repair or replace a tissue, organ, or function of the body.<sup>1</sup> Common biomaterials include metals, such as titanium (dental implants, hip implants), cobalt-chromium (hip implants), or stainless steel (stents), and polymers, such as silicon (contact lenses, intraocular lenses, breast implants), cotton (gauze and surgical dressing), polyglycolic acid (sutures), Teflon (vascular shunts), or super glue (wound closures).<sup>1</sup> Recent trends in the development of biomaterials, particularly transplantable materials, have been focused on matching the mechanical properties of the surrounding tissue such as in the development of brain probes that transition from stiff to soft after implantation to modulate the immune response<sup>2</sup> or vascular stents that match the elasticity of arteries and veins.<sup>3,4</sup> By matching the material properties of the surrounding tissue, researchers hope to improve the biocompatibility of synthetic biomaterials.<sup>5</sup>

A critical property on which biomaterials are frequently evaluated is biocompatibility, the ability of a material to perform a function with a host response that is appropriate to the intended application.<sup>1</sup> Traditionally, the gold standard for biocompatibility has been bioinertness or a lack of response from the host. As a result, most biocompatibility tests focus on characterizing biological and chemical inertness.<sup>6</sup> A consequence, however, is that such tests do not reveal the extent to which cells and tissues respond to the mechanical environment presented by a biomaterial, wherein differences in stiffness or surface patterning can generate undesired responses. For example, the compliance mismatch between a cardiac stent and native vasculature

can lead to restenosis—reclosure—of the artery and subsequent device failure.<sup>3</sup> Similarly, metal joint replacements can cause stress shielding leading to subsequent bone loss and a loosening of the implant.<sup>7</sup> Such responses occur because cells and tissues can respond not only to the chemical properties of a material but also to the mechanical properties of that material. In fact, when a material is implanted in the body, three things occur simultaneously: a perturbation of the mechanical environment, a perturbation of the chemical environment, and an absorption of macromolecules into the environment.<sup>6</sup> The perturbation in the mechanical environment is sensed by cells through a process called mechanotransduction, in which mechanical stimuli are converted to biochemical responses.<sup>8</sup> Mechanical stress contributes to the clinical presentation of many important diseases including, asthma, osteoporosis, atherosclerosis, diabetes, and stroke.<sup>9,10</sup> Mechanotransduction plays an important role in cellular biochemistry and can be altered by changes in cell mechanics extracellular matrix structure, or by the deregulation of the molecular mechanisms by which cells sense mechanical signals. Mechanotransduction processes have been recently reviewed for smooth muscle,<sup>11</sup> epithelial tissue,<sup>12</sup> endothelial tissue,<sup>13</sup> osteocytes,<sup>13</sup> and pulmonary tissue<sup>14</sup> and the mechanobiology of diseases has also been reviewed.<sup>9</sup>

Tissue engineering is defined as the creation of new tissue by the deliberate and controlled stimulation of selected target cells through a systematic combination of molecular and mechanical signals. Tissue engineering strategies are developed through the combination of a material scaffolds, or templates, bioactive molecular cues, and host or donor cells and have been successfully implemented in skin and bladder applications. In tissue engineering applications the role of the biomaterial is much more complex, and mechanical stiffness, chemical composition, and material degradation can all direct the formation of new tissue. Due to the complexity of the

situation, it is becoming increasingly important to understand how cells interact with materials, both mechanically and chemically to continue developing new materials and devices to treat injuries and disease. For instance, Zlaty and colleagues were able to develop a neural implant that induced less of an inflammatory response by using a material that would soften over time.<sup>15</sup> As such, the probe was stiff to allow for easy implantation but would soften to match the native mechanical stiffness of the surrounding tissue, thus mitigating the inflammatory response and increasing the lifetime of the probe. In addition to improving the function of implanted medical devices, advanced biomaterials are also helping researchers study cell mechanobiology and behavior. However, due to the difficulty with studying disease processes in vitro researchers have been developing more advanced biomaterial platforms that can better mimic the mechanical transitions that occur during disease. For example, Liu et al. developed a dynamically stiffening hydrogel that stiffened over the course of cell experiments to better mimic the process of tumor cell development.<sup>16</sup> They showed that encapsulation in stiffer hydrogels enhanced the expression of genes relevant to myofibroblastic activation in pancreatic stromal cells, an important process in the development of pancreatic cancer.

It is clear that cell mechanobiology has important implications in the progression of diseases and biomaterials have emerged as powerful platforms to study how cells fundamentally sense their environment. The following sections highlight some of the key work and findings on probing how cells respond to static biomaterial platforms and then transition to the key findings using dynamic biomaterial platforms to study how cells respond to dynamic changes in their environment. It then ends with a summary of the work shown in this dissertation.

## 1.2 Biomaterials to Probe Cell-Material Interactions

Study of the response of mammalian cells to their chemical, mechanical, or electrical environment has typically been assessed using culture on a static material substrate specifically designed to probe a single aspect of the environment of a cell, with glass and tissue culture polystyrene being the most widely used static substrate materials. Although these inert materials can provide valuable snapshots of cell behaviors, their stasis does not recapitulate the complex *in vivo* environment. As such, researchers have been developing increasingly complex biomaterial platforms by precisely controlling material chemistry (both bulk and surface), topographical patterns, and mechanical stiffness. The following sections highlight key work in understanding how cells respond to the surface chemistry, topographical patterns and material stiffness using biomaterials as experimental platforms.

### 1.2.1 Probing Cell Responses to Chemical Signals

A variety of biomaterial platforms have been developed to probe how cells respond to the surface chemistry (or the proteins absorbed on a synthetic surface) to which cells are attached. For example, Paleeck et al. coated glass slides with various concentrations of fibronectin and measured the velocity of CHO-B2 cells with different levels of integrin and binding affinities.<sup>17</sup> They found that cell migration increased with increasing fibronectin content to an optimal concentration. At higher concentrations of fibronectin, migration began to decrease due to stronger cellular binding with the surface. Cell migration speed on fibronectin pattern has also been explored by others.<sup>18,19</sup> Similar findings were noted regarding material hydrophobicity, with cells displaying equally poor attachment to materials showing either a high hydrophobicity or high hydrophilicity.<sup>20</sup> As a result, an optimum hydrophilicity point for cell attachment was identified.

Surface patterning has also been used to confine cells and force them into pre-determined shapes. For example, Chen and colleagues printed adhesive islands of fibronectin ranging in size from 3 to 50  $\mu\text{m}$  and found that culturing cells on the smaller patterns caused cells to transition from a state of growth to a state of apoptosis.<sup>21</sup> Additionally, Peng et al. observed that growing cells on patterns of different shapes can impact cell fate. For example, human mesenchymal stem cells grown on round patterns tended to differentiate into fat cells while cells grown on hexagonal or star patterns tended to differentiate into bone cells.<sup>22</sup> These findings led to the postulate these differences in differentiation occur because the cellular actin cytoskeleton is much stiffer when growing on shapes with sharp corners compared to more rounded shapes.

### 1.2.2 Probing Cell Responses to Topographical Signals

*In vivo*, the extracellular matrix (ECM) consists of nano-scale features that direct cell migration, morphology, adhesion, and orientation through a phenomenon called contact guidance. Disruptions of the ECM can ultimately lead to disease states such as stroke<sup>9</sup> or other disorders like Alzheimer's.<sup>23</sup> A recent review on mechanobiology and disease gives a partial summary of diseases that present as abnormal mechanotransduction and whether that abnormal transduction is due to changes in cell mechanics, alterations in tissue structure or deregulation of mechanochemical conversion.<sup>9</sup> For instance, breast cancer cells directly remodel ECM filaments from a random orientation to a radially oriented to promote tumor cell invasion and metastasis.

24-26

Biomaterial platforms with well-controlled surface or fiber topographies have been developed to investigate the impacts of different topographical patterns on cell behavior to elucidate the mechanisms by which cells respond to their native ECM. Many studies with nano-grooved surfaces have shown that most cell types will align in the direction of



nanotopography<sup>27,28</sup> and migrate along the direction of the surface pattern.<sup>29,30</sup> For instance, Bettinger et al. demonstrated the alignment behavior of endothelial cells using a polydimethylsiloxane (PDMS) platform that had a nano-grated pattern along the surface.<sup>27,31</sup> Similarly, Teixeira et al. showed that human corneal epithelial cells align parallel to nano-gratings with ridge widths ranging from 70-1900 nm and groove depths of 150 and 600 nm. In addition, they found that cell alignment was more sensitive to groove depth than pitch.<sup>28</sup> However, in a follow-up study using different serum conditions, they found that the cells aligned orthogonal on nano-scale gratings and transitioned to parallel alignment when cultured on topography at the micron scale.<sup>32</sup> Furthermore, Yim et al. found that nano-grating topography (without the presence of neurogenic induction medium) promoted the upregulation of neurogenic differentiation markers in mesenchymal stem cells.<sup>33</sup> Micro-patterns resulted in less up-regulation of neurogenic factors, indicating that the differentiation process was more sensitive to nano-topographies for this cell type.

### 1.2.3 Probing Cell Responses to Stiffness

As discussed above, it is well established that mechanical stiffness is a key factor in designing biomaterials for medical devices and current design methods attempt to match the native tissue stiffness. The stiffness of tissues in the human body ranges from 0.1 kPa for brain tissue to 2 GPa for cortical bone and current research has shown that cells are sensitive to the stiffness of materials in this native range. Pelham and Wang were the first to show that cells actively respond to the stiffness of materials.<sup>34</sup> Specifically, they found that cells cultured on soft substrates ( $E \sim 1$  kPa) resulted in less cell spreading and less stable focal adhesions while cells cultured on stiffer substrates ( $E \sim 70$  kPa) resulted in more cell spreading and more stable focal adhesions. In addition, when 3T3 fibroblasts were seeded onto a platform with a gradient in the

material stiffness, the cell migrated toward the stiffer side of the material, a phenomenon later called durotaxis.<sup>35</sup> Cell responses to stiffness were later shown to be highly dependent on the cell type and cell density. For instance, neutrophils are insensitive to stiffness, while fibroblasts and epithelial cells require a substrate stiffness of greater than 2 kPa to form actin stress fibers.<sup>36</sup> Further, Engler showed that stiffness plays an important role in cell differentiation, with human mesenchymal stem cells (hMSCs) seeded on soft substrates (0.1-1 kPa) expressing neurogenic factors, cells seeded on intermediately stiff substrates (8-17 kPa) expressing myogenic factors and cells seeded on stiff substrates (25-40 kPa) expressing osteogenic factors.<sup>37</sup> Gilbert et al. showed that cells cultured on soft substrates that mimicked the stiffness of natural muscle ( $E = 12$  kPa) retained their stemness compared to cells cultured on the much stiffer polystyrene control.<sup>38</sup> In summary, cells actively sense and respond to the stiffness of their environment which can play a key role in the biocompatibility of biomaterials.

### 1.3 Stimuli-Responsive Materials as Biomaterials

Despite the substantial work that has been performed using static biomaterial platforms to understand how cells respond to their environment, these platforms do not capture the dynamic environment a cell interacts within the human body. As such, researchers have been developing dynamic platforms to assess how cells respond to changes in their environments. For example, Lam et al. developed a PDMS platform that, after plasma oxidation, formed wrinkles with attached viable cells by applying an external compressive force. The reversible topography was able to repeatedly align and unaligned the adhered C2C12 mouse myoblasts.<sup>39</sup> Similarly, Guvendiren and Burdick used a similar PDMS platform to reversibly align and unaligned hMSCs for up to 8 cycles and found that as hMSCs approach confluence their ability to dynamically re-align diminished.<sup>40</sup> In addition, they stretched the PDMS substrate biaxially to

form double wrinkle patterns and showed that hMCSs would align to the complex topography in a cross-stitch pattern. Following this, the need for smart instructive materials for use as biomaterials and tissue engineering platforms has led to the growing development of smart materials that can respond to their environment.

### 1.3.1 Stimuli-Responsive Materials

Stimuli-responsive materials are an emerging class of materials that respond to their environment by changing their physical and/or chemical properties.<sup>41–44</sup> Stimuli-responsive polymers (or smart polymers) have been designed to respond to a variety of stimuli such as pH,<sup>45</sup> temperature,<sup>46</sup> mechanical force, the presence of small molecules and biomolecules,<sup>16,47–49</sup> and electric/magnetic fields.<sup>50–52</sup> These materials have found several applications in medicine as sensors and biosensors,<sup>41,42</sup> targeted and controlled drug delivery platforms,<sup>41–43</sup> or chemo-mechanical actuators.<sup>51,53–55</sup> For instance, poly(N-isopropyl acrylamide) (pNIPAm) is a stimuli-responsive polymer that has a lower critical solubility (LCST) that is responsive to temperature.<sup>44,46</sup> At temperatures below its LCST, pNIPAm is in a solvated state (or swollen) and transitions to desolvated (compact coil) as it's heated above the LCST. This response has been used to design sensors and a smart cell culture platform by Sutton and colleagues. Stimuli-responsive polymers that respond to enzymes and glucose have also been reported, enabling the materials to respond directly to biological activity.<sup>16,47,56</sup>

Recently, work has been done on developing dynamically stiffening hydrogels that can dynamically alter their stiffness in response to either secondary cross-linking or light. For example, Guvendiren and Burdick seeded hMSCs on a dynamically stiffening substrate and showed that as the hydrogel stiffened hMSCs increased their total cell area (the sum of the area occupied by all cells) from 500 to 3000  $\mu\text{m}^2$  over the course of several hours.<sup>57</sup> In addition,

dynamic stiffening also impacted cell differentiation behavior with cells cultured on hydrogels that were stiffened on day one or day three differentiation into osteogenic cell types while hMSCs cultured on hydrogels stiffened later showed adipogenic differentiation. In addition, material stiffness has shown to play a key role in the inflammatory response of brain probes.<sup>2</sup>

### 1.3.2 Shape Memory Polymers

Shape memory polymers (SMPs) are a special class of stimuli-responsive materials that can transition from a temporary (learned) shape to a permanent (memorized) shape in response to an external stimulus.<sup>58–60</sup> This behavior requires two components: a memory component that can be in the form of physical or chemical cross-links, crystalline domains, or interpenetrating networks; and a shape fixing component that stems from either vitrification, crystallization, liquid crystal transitions, reversible molecular cross-linking, and supramolecular association.<sup>61</sup> SMPs can be triggered to change shape by a variety of mechanisms including light,<sup>62–66</sup> electricity,<sup>50,67,68</sup> water,<sup>69</sup> magnetism,<sup>52,70</sup> and ultrasound,<sup>71</sup> although the most common triggering mechanism is heat.<sup>60,61,72</sup> In a typical shape memory cycle, the material is first heated above the transition temperature, which is usually a glass transition ( $T_g$ ) or a melt transition ( $T_m$ ). A force is then applied to stretch the sample to the desired strain and then held while the temperature is cooled to below the transition temperature, thereby fixing the temporary shape. The force is then removed and the sample remains in its temporary shape. The sample is then heated above the transition temperature, and the memory component acts as an entropic spring to drive the material to recover back to its original shape.

Due to their versatility, SMPs have been proposed for a variety of applications in aerospace devices,<sup>73</sup> smart textiles,<sup>74,51</sup> biomedical devices,<sup>60,75,76</sup> microsensors and actuators,<sup>39,53,77,78</sup> and other applications. SMPs are reviewed here for the interested

reader.<sup>59,61,79,80</sup> In addition, SMPs exhibiting unique properties such as anisotropy,<sup>81</sup> soft actuation,<sup>82</sup> light emission,<sup>83</sup> reconfigurable shapes,<sup>84</sup> and self-healing<sup>85</sup> have also been developed. Typically, an SMP is only capable of fixing one shape and of transitioning to that memorized shape once, but multi-shape memory materials and reversible SMPs have been developed to address this limitation. Multi-shape memory materials are capable of transitioning between two or more temporary shapes, generally through the use of sequential transition temperatures.<sup>86-88</sup> Reversible SMPs, or actuators, are capable of reversibly switching between the temporary shape and the permanent shape over a large number of cycles.<sup>89</sup>

SMPs have currently been deployed in several FDA approved medical devices. The first example of an FDA approved SMP biomaterial in a medical device was the self-closing suture<sup>90</sup> and FDA approval has since been given to devices in aneurysm treatment<sup>91</sup> and ACL fixation.<sup>5,60</sup> In addition to medical device applications, SMPs have also emerged as powerful research platforms to probe how cells respond to dynamic changes in their environment.

As described above, a variety of stimuli-responsive materials are used to probe how cells respond to dynamic changes in their environment, however, SMPs have the advantage of being able to provide a very precise mechanical stimulus at a predetermined point. The first attempt to design a cytocompatible SMP in both material chemistry and shape transition was unsuccessful due to the high triggering temperature needed to trigger material recovery, which killed the attached cells.<sup>92</sup> Subsequently, work by our group<sup>93,94</sup> and then by Ashby<sup>95</sup> and colleagues led to the first cytocompatible SMPs in both material chemistry and shape change phenomena by making a material with a transition temperature close to body temperature and dubbed these platforms as active cell culture platforms. Where other platforms with transition temperatures close to body temperature had been designed before, these studies were the first that showed this

recovery in the presence of cells. Subsequently other two-dimensional and three-dimensional active cell culture platforms were developed,<sup>77,96</sup> thus creating materials that could be used to study how cell behavior is impacted by dynamic perturbations. To date these SMPs have been used to study cell morphology,<sup>93,95-101</sup> cell differentiation,<sup>102-105</sup> cell motility<sup>106-108</sup> and to control bacteria films.<sup>109</sup> Our group's first work in this area involved the design of an SMP platform that could transition from a flat topography to a grooved topography.<sup>93</sup> In response, cells dynamically altered their morphology from a random to an aligned morphology. This finding was later replicated by Ashby and colleagues<sup>95</sup> and Ebara and colleagues.<sup>97</sup> In addition, work in our group subsequently demonstrated that changes in SMP fiber alignment either induced cancer cells to migrate in a polarized or non-polarized manner and that cells migrating in a polarized manner showed faster cell migration behavior.<sup>106</sup> Adding to this work culture on 2D cell platforms has been shown to increase both osteogenic<sup>104</sup> and myogenic differentiation<sup>102</sup> capabilities. In addition, we showed that differentiation behavior was preserved on 3D cell culture platforms.<sup>104</sup>

However, the main limitations of these past active cell culture platforms were (1) the need to culture at temperatures lower than body temperature (37 °C) prior to the induced shape change and (2) the ability to demonstrate only one shape change. To address these limitations Ebara and colleagues have developed active cell culture platforms that can be triggered by NIR light, thus limiting the need for culture at lower temperatures.<sup>66</sup> To address the second limitation of current SMPs, Gong and colleagues developed an active cell culture platform whose recovery could be precisely controlled by designing a Poly( $\epsilon$ -caprolactone) (PCL) based system with a broad  $T_m$ .<sup>102</sup> The broad  $T_m$  of PCL allowed them to slowly trigger the material recovery, which subjected the cells to multiple recovery events. However, there is still an overall need for more

advanced material platforms to enable additional *in vitro* cell studies to better elucidate how dynamic mechanical changes change cell behavior.

### 1.3.3 Tools for Analyzing Cell Data Sets

With the development of increasingly dynamic cell culture platforms, a need has arisen of new approaches in tracking cell migration behavior. The ability to track cells during cell migration experiments has been identified as an important challenge in understanding essential biological phenomena such as cell developmental processes, tissue repair, and disease progression.<sup>110,111</sup> However, the gold standard for cell tracking is still manual tracking which is very time-intensive and often limits the time-scale and size of cell experiments. To address this limitation, efforts have focused on designing cell tracking algorithms capable of automatically tracking cell tracks over long time scales. Early attempts at designing these tracking codes varied widely in their ability to identify cells frame to frame, sort interaction points for dense cells, and precisely analyze natural cell proliferation.<sup>110</sup> To address some of these limitations, our group in collaboration with that of M. Lisa Manning developed an automated contour-based cell tracking algorithm. To do this, *ACTIVE* (Automated contour-based tracking of *in vitro* environment) first segments nuclear-stained images by fitting an ellipse to the stained cell nuclei and then identifies and links cells through the image stack, thereby generating long-timescale cell migration data. This powerful analytical tool has already been used to show how cells migrate on isotropic vs anisotropic surfaces,<sup>107</sup> how bacteria migration responds to stiffness,<sup>112</sup> how cell organelles reorganize during migratory changes,<sup>113</sup> and identifying potential mechanisms of cell migration kinetics.<sup>114</sup> However, in its current form *ACTIVE* can only analyze a cell experiment once the experiment is completed and future experiments would benefit from the development of a processing method that can analyze data sets in real-time.

## 1.4 Dissertation Scope

This dissertation advances the state of the art of SMPs for generating complex topographical transitions and of SMPs as active cell culture platforms to study cell mechanobiology. In particular, we first designed multi-shape memory composites capable of learning multiple shapes and thus transition between a multitude of topographical surfaces. Second, we designed active cell culture platforms that do not require a temperature change to trigger shape recovery by designing both enzymatically and light-responsive SMP platforms. A chapter overview is discussed below.

The current chapter (Chapter 1) provides an overview of the current state of SMPs and their potential applications in biomaterials, tissue engineering, and dynamic experiments studying cell mechanobiology. Chapters 2 through 5 focus on the development of novel SMPs to create active cell culture platforms that do not require a temperature change to recover. Chapter 2 develops the first example of an SMP that responds to enzymatic activity, enabling for the first time the potential for an SMP to respond directly to cell behavior. Chapter 3 focuses on the development of a novel light-triggered SMP by cross-linking methacrylated graphene into the SMP film. Chapter 4 focuses on the development of a real-time contour-based tracking code to enable both analysis of cell migration behavior in real-time and the development of a semi-autonomous feedback loop by combining this real-time tracking code with a light triggerable SMP.

Chapters 5 and 6 both focus on generating complex topographies using multi-shape memory composites. Specifically, Chapter 5 applies the system developed by Yang and colleagues<sup>99</sup> to a triple-shape memory composite developed by Luo and colleges,<sup>115</sup> thereby enabling the generation of complex, or double wrinkle, patterns. Chapter 6 develops quadruple



shape memory composites that are capable of quadruple surface shape memory or showing 4 unique surface topographical patterns.

The studied work fell under the following goals:

Goal 1: *To create and understand the first enzymatically triggered shape memory polymers.*

Questions: does enzyme concentration impact the rate of material recovery? How does this change with material composition? On what time scale does this recovery occur and what are the kinetics of it?

Goal 2: *To develop a fast-acting light activated shape memory polymer for isothermal active cell culture experiments.* Questions: How fast can light-triggered recovery occur? How does this time scale relate to the concentration of particles and the power of the light? Is there a resolution limit on how precise localized recovery can be induced?

Goal 3: *To develop a real-time cell tracking algorithm to later be used in the development of semi-autonomous feedback loops between SMPs, cultured cells and ACTIVE analysis.*

Questions: How efficiently can ACTIVE analyze real-time imaging?

Goal 4: *To both generate and understand complex wrinkle patterns on the surface of triple shape memory composites.* Questions: Is there cross-talk between the two material phases? Is there an

ideal ratio between the programmed strains to create double wrinkle patterns? Does the recovery profile impact the formation of these patterns?

Goal 5: *To design the first demonstrated example of a quadruple shape memory composite capable of quadruple shape memory behavior.* Questions: Is there cross-talk between the material phases? Does programming more strain in one portion of the composite impact shape memory behavior? How clear are multiple topographical transitions?

## 1.5 References

1. Ratner, B. D., Hoffman, A. S., Schoen, F. J., & Lemons, J. E. *Biomaterials science: an introduction to materials in medicine.* (2004).
2. Bedell, H. W. *et al.* Understanding the Effects of Both CD14-Mediated Innate Immunity and Device/Tissue Mechanical Mismatch in the Neuroinflammatory Response to Intracortical Microelectrodes. *Front. Neurosci.* (2018). doi:10.3389/fnins.2018.00772
3. Nezarati, R. M., Eifert, M. B., Dempsey, D. K. & Cosgriff-Hernandez, E. Electrospun vascular grafts with improved compliance matching to native vessels. *J. Biomed. Mater. Res. - Part B Appl. Biomater.* (2015). doi:10.1002/jbm.b.33201
4. Berry, J. L. *et al.* Hemodynamics and wall mechanics of a compliance matching stent: In vitro and in vivo analysis. *J. Vasc. Interv. Radiol.* (2002). doi:10.1016/S1051-0443(07)60015-3
5. Mazza, E. & Ehret, A. E. Mechanical biocompatibility of highly deformable biomedical

- materials. *Journal of the Mechanical Behavior of Biomedical Materials* (2015).  
doi:10.1016/j.jmbbm.2015.03.023
6. Williams, D. F. Biocompatibility Pathways in Tissue-Engineering Templates. *Engineering* (2018). doi:10.1016/j.eng.2018.03.007
  7. Summer, D. & Galante, J. Determinants of Stress Shielding: Design Versus Materials Versus Interface. *Clin. Orthop. Relat. Res.* (1991).
  8. Ingber, D. E. Cellular mechanotransduction: putting all the pieces together again. *FASEB J.* (2006). doi:10.1096/fj.05-5424rev
  9. Ingber, D. E. Mechanobiology and diseases of mechanotransduction. *Ann. Med.* 1–14 (2003). doi:10.1080/07853890310016333
  10. Barnes, J. M., Przybyla, L. & Weaver, V. M. Tissue mechanics regulate brain development, homeostasis and disease. *Comment. Spec. ISSUE 3D CELL Biol.* (2017). doi:10.1242/jcs.191742
  11. Hill, M. A. & Potocnik, S. Invited Review: Arteriolar smooth muscle mechanotransduction: Ca<sup>2+</sup> signaling pathways underlying myogenic reactivity. *Artic. J. Appl. Physiol.* (2001). doi:10.1152/jappl.2001.91.2.973
  12. Wang, J. *et al.* An updated review of mechanotransduction in skin disorders: Transcriptional regulators, ion channels, and microRNAs. *Cellular and Molecular Life Sciences* (2015). doi:10.1007/s00018-015-1853-y
  13. Weinbaum, S., Duan, Y., Thi, M. M. & You, L. An integrative review of mechanotransduction in endothelial, epithelial (renal) and dendritic cells (osteocytes).

*Cellular and Molecular Bioengineering* (2011). doi:10.1007/s12195-011-0179-6

14. Spieth, P. M. *et al.* Mechanotransduction in the lungs. *Minerva Anesthesiol.* **80**, 933–41 (2014).
15. Zátonyi, A. *et al.* A softening laminar electrode for recording single unit activity from the rat hippocampus. *Sci. Rep.* (2019). doi:10.1038/s41598-019-39835-6
16. Liu, H. Y. *et al.* Enzyme-mediated stiffening hydrogels for probing activation of pancreatic stellate cells. *Acta Biomater.* (2017). doi:10.1016/j.actbio.2016.10.027
17. Palecek, S. P. S. P. *et al.* Integrin – ligand binding properties govern cell migration speed through cell – substratum adhesiveness Total synthesis of the potential anticancer vaccine KH-1 adenocarcinoma antigen Integrin – ligand binding properties govern cell migration speed through. *Nature* **388**, 537–540 (1997).
18. Huttenlocher, A., Ginsberg, M. H. & Horwitz, A. F. Modulation of Cell Migration by Integrin-mediated Cytoskeletal Linkages and Ligand-binding Affinity. doi:10.1083/jcb.134.6.1551
19. Maheshwari, G., Wells, A., Griffith, L. G. & Lauffenburger, D. A. *Biophysical Integration of Effects of Epidermal Growth Factor and Fibronectin on Fibroblast Migration.* (1999). doi:10.1016/S0006-3495(99)77435-7
20. Bacakova, L., Filova, E., Parizek, M., Ruml, T. & Svorcik, V. Modulation of cell adhesion, proliferation and differentiation on materials designed for body implants. (2011). doi:10.1016/j.biotechadv.2011.06.004
21. Chen, C. S., Mrksich, M., Huang, S., Whitesides, G. M. & Ingber, D. E. Micropatterned

- Surfaces for Control of Cell Shape, Position, and Function. *Biotechnol. Prog.* **14**, 356–363 (1998).
22. Peng, R., Yao, X. & Ding, J. Effect of cell anisotropy on differentiation of stem cells on micropatterned surfaces through the controlled single cell adhesion. (2011). doi:10.1016/j.biomaterials.2011.07.035
  23. Lepelletier, F. X., Mann, D. M. A., Robinson, A. C., Pinteaux, E. & Boutin, H. Early changes in extracellular matrix in Alzheimer's disease. *Neuropathol. Appl. Neurobiol.* (2017). doi:10.1111/nan.12295
  24. Goetz, J. G. *et al.* Biomechanical remodeling of the microenvironment by stromal caveolin-1 favors tumor invasion and metastasis. *Cell* (2011). doi:10.1016/j.cell.2011.05.040
  25. Provenzano, P. P., Inman, D. R., Eliceiri, K. W., Trier, S. M. & Keely, P. J. Contact guidance mediated three-dimensional cell migration is regulated by Rho/ROCK-dependent matrix reorganization. *Biophys. J.* (2008). doi:10.1529/biophysj.108.133116
  26. Lyons, T. R. *et al.* Postpartum mammary gland involution drives progression of ductal carcinoma in situ through collagen and COX-2. *Nat. Med.* (2011). doi:10.1038/nm.2416
  27. Bettinger, C. J., Zhang, Z., Gerecht, S., Borenstein, J. T. & Langer, R. Enhancement of in vitro capillary tube formation by substrate nanotopography. *Adv. Mater.* (2008). doi:10.1002/adma.200702487
  28. Teixeira, A., Abrams, G., Bertics, P. J., Murphy, C. J. & Nealey, P. F. Epithelial contact guidance on well-defined micro- and nanostructured substrates. *J. Cell Sci.* (2003).

doi:10.1242/jcs.00383

29. Wang, X., Ohlin, C. A., Lu, Q. & Hu, J. Cell directional migration and oriented division on three-dimensional laser-induced periodic surface structures on polystyrene. *Biomaterials* (2008). doi:10.1016/j.biomaterials.2007.12.047
30. Ann Dalton, B. *et al.* Modulation of epithelial tissue and cell migration by microgrooves. *J. Biomed. Mater. Res.* (2001). doi:10.1002/1097-4636(200108)56:2<195::AID-JBM1084>3.0.CO;2-7
31. Bettinger, C. J., Langer, R. & Borenstein, J. T. Engineering substrate topography at the Micro- and nanoscale to control cell function. *Angewandte Chemie - International Edition* (2009). doi:10.1002/anie.200805179
32. Teixeira, A. I. *et al.* The effect of environmental factors on the response of human corneal epithelial cells to nanoscale substrate topography. *Biomaterials* (2006). doi:10.1016/j.biomaterials.2006.01.044
33. Yim, E. K. F., Pang, S. W. & Leong, K. W. Synthetic nanostructures inducing differentiation of human mesenchymal stem cells into neuronal lineage. *Exp. Cell Res.* (2007). doi:10.1016/j.yexcr.2007.02.031
34. Wang Pelham, Robert J, Y.-L. Cell locomotion and focal adhesions are regulated by substrate flexibility. *Natl. Acad. Sci.* (1997). doi:10.1073/pnas.94.25.13661
35. Lo, C. M., Wang, H. B., Dembo, M. & Wang, Y. L. Cell movement is guided by the rigidity of the substrate. *Biophys. J.* (2000). doi:10.1016/S0006-3495(00)76279-5
36. Yeung, T. *et al.* Effects of substrate stiffness on cell morphology, cytoskeletal structure,

- and adhesion. *Cell Motil. Cytoskeleton* (2005). doi:10.1002/cm.20041
37. Engler, A. J., Sen, S., Sweeney, H. L. & Discher, D. E. Matrix elasticity directs stem cell lineage specification. *Cell* (2006). doi:10.1016/j.cell.2006.06.044
  38. Gilbert, P. M. *et al.* Substrate elasticity regulates skeletal muscle stem cell self-renewal in culture. *Science* (80-. ). (2010). doi:10.1126/science.1191035
  39. Lam, M. T., Clem, W. C. & Takayama, S. Reversible on-demand cell alignment using reconfigurable microtopography. doi:10.1016/j.biomaterials.2007.12.010
  40. Guvendiren, M. & Burdick, J. A. Stem Cell Response to Spatially and Temporally Displayed and Reversible Surface Topography. *Adv. Healthc. Mater.* **2**, 155–164 (2013).
  41. Stuart, M. A. C. *et al.* Emerging applications of stimuli-responsive polymer materials. *Nat. Mater.* **9**, 101–113 (2010).
  42. Wei, M., Gao, Y., Li, X. & Serpe, M. J. Stimuli-responsive polymers and their applications. *Polym. Chem.* **8**, 127–143 (2017).
  43. Wang, Y., Byrne, J. D., Napier, M. E. & DeSimone, J. M. Engineering nanomedicines using stimuli-responsive biomaterials. *Adv. Drug Deliv. Rev.* **64**, 1021–1030 (2012).
  44. Theato, P., Sumerlin, B. S., O'reilly, R. K. & Epp, T. H. Stimuli responsive materials. *Chem. Soc. Rev.* **42**, 7055–7056 (2013).
  45. Zhang, S. *et al.* A pH-responsive supramolecular polymer gel as an enteric elastomer for use in gastric devices. *Nat. Mater.* **14**, 1065–1071 (2015).
  46. Takezawa, T., Mori, Y. & Yoshizato, K. Cell culture on a thermo-responsive polymer surface. *Nat. Biotechnol.* (1990). doi:10.1038/nbt0990-854

47. Mart, R. J., Osborne, R. D., Stevens, M. M. & Ulijn, R. V. Peptide-based stimuli-responsive biomaterials. *Soft Matter* **2**, 822 (2006).
48. Zelzer, M. *et al.* Phosphatase responsive peptide surfaces. *J. Mater. Chem.* **22**, 12229 (2012).
49. Phillips, D. J., Wilde, M., Greco, F. & Gibson, M. I. Enzymatically Triggered, Isothermally Responsive Polymers: Reprogramming Poly(oligoethylene glycols) To Respond to Phosphatase. *Biomacromolecules* **16**, 3256–3264 (2015).
50. Frewin, C. L. *et al.* Electrical Properties of Thiol-ene-based Shape Memory Polymers Intended for Flexible Electronics. *Polymers (Basel)*. (2019). doi:10.3390/polym11050902
51. Hu, J., Meng, H., Li, G. & Ibekwe, S. I. A review of stimuli-responsive polymers for smart textile applications. *Smart Materials and Structures* (2012). doi:10.1088/0964-1726/21/5/053001
52. Herrera-posada, S. *et al.* Magneto-responsive liquid crystalline elastomer nanocomposites as potential candidates for dynamic cell culture substrates. *Mater. Sci. Eng. C* **65**, 369–378 (2016).
53. Andrianesis, K. & Tzes, A. Development and Control of a Multifunctional Prosthetic Hand with Shape Memory Alloy Actuators. *J. Intell. Robot. Syst. Theory Appl.* (2015). doi:10.1007/s10846-014-0061-6
54. Gao, F., Deng, H. & Zhang, Y. Hybrid actuator combining shape memory alloy with DC motor for prosthetic fingers. *Sensors Actuators, A Phys.* (2015). doi:10.1016/j.sna.2014.11.025



55. Guo, Q. *et al.* Entanglement-Based Thermoplastic Shape Memory Polymeric Particles with Photothermal Actuation for Biomedical Applications. *ACS Appl. Mater. Interfaces* **10**, (2018).
56. Liu, H. Y., Korc, M. & Lin, C. C. Biomimetic and enzyme-responsive dynamic hydrogels for studying cell-matrix interactions in pancreatic ductal adenocarcinoma. *Biomaterials* **160**, 24–36 (2018).
57. Guvendiren, M. & Burdick, J. A. Stiffening hydrogels to probe short- and long-term cellular responses to dynamic mechanics. *Nat. Commun.* (2012).  
doi:10.1038/ncomms1792
58. Lendlein, A. & Kelch, S. Shape-Memory Polymers. *Angew. Chemie Int. Ed.* **41**, 2034 (2002).
59. Chan, B. Q. Y. *et al.* Recent Advances in Shape Memory Soft Materials for Biomedical Applications. *ACS Applied Materials and Interfaces* **8**, (2016).
60. Small IV, W., Singhal, P., Wilson, T. S. & Maitland, D. J. Biomedical applications of thermally activated shape memory polymers. *J. Mater. Chem.* **20**, 3356–3366 (2010).
61. Liu, C., Qin, H. & Mather, P. T. Review of progress in shape-memory polymers. *J. Mater. Chem.* **17**, 1543 (2007).
62. Jiang, H. Y., Kelch, S. & Lendlein, A. Polymers Move in Response to Light. *Adv. Mater.* **18**, 1471–1475 (2006).
63. Lendlein, A., Jiang, H., Jünger, O. & Langer, R. Light-induced shape-memory polymers. *Nature* **434**, 879–882 (2005).

64. Hribar, K., Metter, R., Ifkovits, J., Troxler, T. & Burdick, J. Light-Induced Temperature Transitions in Biodegradable Polymer and Nanorod Composites. *Small* **5**, 1830–1834 (2009).
65. Maitland, D. J. *et al.* Prototype laser-activated shape memory polymer foam device for embolic treatment of aneurysms. *J. Biomed. Opt.* **12**, 30504 (2007).
66. Shou, Q., Uto, K., Lin, W. C., Aoyagi, T. & Ebara, M. Near-infrared-irradiation-induced remote activation of surface shape-memory to direct cell orientations. *Macromol. Chem. Phys.* **215**, 2473–2481 (2014).
67. Kai, D. *et al.* Biocompatible electrically conductive nanofibers from inorganic-organic shape memory polymers. *Colloids Surfaces B Biointerfaces* **148**, 557–565 (2016).
68. Luo, X. & Mather, P. T. Conductive shape memory nanocomposites for high speed electrical actuation. doi:10.1039/c001295e
69. Gu, X. & Mather, P. T. Water-triggered shape memory of multiblock thermoplastic polyurethanes (TPUs)<sup>3</sup>. **3**, (2013).
70. Zhang, F. H. *et al.* Remote, fast actuation of programmable multiple shape memory composites by magnetic fields. *J. Mater. Chem. C* **3**, 11290–11293 (2015).
71. Li, G., Fei, G., Xia, H., Han, J. & Zhao, Y. Spatial and temporal control of shape memory polymers and simultaneous drug release using high intensity focused ultrasound. *J. Mater. Chem.* **22**, 7692 (2012).
72. Dogan, S. K., Boyacioglu, S., Kodal, M., Gokce, O. & Ozkoc, G. Thermally induced shape memory behavior, enzymatic degradation and biocompatibility of PLA/TPU blends:

- 'Effects of compatibilization'. *J. Mech. Behav. Biomed. Mater.* **71**, 349–361 (2017).
73. Liu, Y., Du, H., Liu, L. & Leng, J. Shape memory polymers and their composites in aerospace applications: A review. *Smart Mater. Struct.* (2014). doi:10.1088/0964-1726/23/2/023001
74. Hu, J. & Chen, S. A review of actively moving polymers in textile applications. *J. Mater. Chem.* (2010). doi:10.1039/b922872a
75. Senatov, F. S. *et al.* Shape memory effect in 3D-printed scaffolds for self-fitting implants. *Eur. Polym. J.* **93**, 222–231 (2017).
76. Biswas, A., Singh, A. P., Rana, D., Aswal, V. K. & Maiti, P. Biodegradable toughened nanohybrid shape memory polymer for smart biomedical applications. *Nanoscale* **10**, 9917–9934 (2018).
77. Baker, R. M., Henderson, J. H. & Mather, P. T. Shape memory poly( $\epsilon$ -caprolactone)-copoly(ethylene glycol) foams with body temperature triggering and two-way actuation. *J. Mater. Chem. B* **1**, 4916 (2013).
78. Fan, J. & Li, G. High performance and tunable artificial muscle based on two-way shape memory polymer. *RSC Adv.* **7**, 1127–1136 (2017).
79. Lendlein, A., Behl, M., Hiebl, B. & Wischke, C. Shape-memory polymers as a technology platform for biomedical applications. *Expert Rev. Med. Devices* **7**, 357–379 (2010).
80. Hager, M. D., Bode, S., Weber, C. & Schubert, U. S. Shape memory polymers: Past, present and future developments. *Prog. Polym. Sci.* **49–50**, 3–33 (2015).
81. Rodriguez, E. D. *et al.* Anisotropic Shape-Memory Elastomeric Composites: Fabrication

- and Testing. doi:10.1002/macp.201300086
82. Torbati, A. H. & Mather, P. T. A hydrogel-forming liquid crystalline elastomer exhibiting soft shape memory. *J. Polym. Sci. Part B Polym. Phys.* **54**, 38–52 (2016).
  83. Torbati, A. H., Mather, R. T., Reeder, J. E. & Mather, P. T. Fabrication of a light-emitting shape memory polymeric web containing indocyanine green. doi:10.1002/jbm.b.33107
  84. Lawton, M. I. *et al.* Anhydride-Based Reconfigurable Shape Memory Elastomers. *ACS Macro Lett.* **5**, 203–207 (2016).
  85. Rodriguez, E. D., Luo, X. & Mather, P. T. Linear/Network Poly( $\epsilon$ -caprolactone) Blends Exhibiting Shape Memory Assisted Self-Healing (SMASH). doi:10.1021/am101012c
  86. Zhao, Q., Behl, M. & Lendlein, A. Shape-memory polymers with multiple transitions: complex actively moving polymers. *Soft Matter* **9**, 1744–1755 (2013).
  87. Behl, M., Razzaq, M. Y. & Lendlein, A. Multifunctional Shape-Memory Polymers. *Adv. Mater.* **22**, 3388–3410 (2010).
  88. Liu, T. *et al.* Stimulus methods of multi-functional shape memory polymer nanocomposites: A review. *Compos. Part A Appl. Sci. Manuf.* **100**, 20–30 (2017).
  89. Westbrook, K. K. *et al.* Two-way reversible shape memory effects in a free-standing polymer composite. *Smart Mater. Struct.* **20**, (2011).
  90. Lendlein, A. & Langer, R. Biodegradable, elastic shape-memory polymers for potential biomedical applications. *Science* **296**, 1673–6 (2002).
  91. Maitland, D. J. *et al.* Prototype laser-activated shape memory polymer foam device for embolic treatment of aneurysms. *J. Biomed. Opt.* **12**, 30504 (2007).

92. Neuss, S. *et al.* The use of a shape-memory poly( $\epsilon$ -caprolactone)dimethacrylate network as a tissue engineering scaffold. *Biomaterials* **30**, 1697–1705 (2009).
93. Davis, K. A., Burke, K. A., Mather, P. T. & Henderson, J. H. Dynamic cell behavior on shape memory polymer substrates. *Biomaterials* **32**, 2285–2293 (2011).
94. Davis, K. A., Luo, X., Mather, P. T. & Henderson, J. H. Shape Memory Polymers for Active Cell Culture. *J. Vis. Exp.* e2903–e2903 (2011). doi:10.3791/2903
95. Le, D. M., Kulangara, K., Adler, A. F., Leong, K. W. & Ashby, V. S. Dynamic Topographical Control of Mesenchymal Stem Cells by Culture on Responsive Poly( $\epsilon$ -caprolactone) Surfaces. *Adv. Mater.* **23**, 3278–3283 (2011).
96. Tseng, L.-F., Mather, P. T. & Henderson, J. H. Shape-memory-actuated change in scaffold fiber alignment directs stem cell morphology. *Acta Biomater.* **9**, 8790–8801 (2013).
97. Ebara, M., Uto, K., Idota, N., Hoffman, J. M. & Aoyagi, T. Shape-Memory Surface with Dynamically Tunable Nano-Geometry Activated by Body Heat. *Adv. Mater.* **24**, 273–278 (2012).
98. Mengsteab, P. Y. *et al.* Spatiotemporal control of cardiac anisotropy using dynamic nanotopographic cues. *Biomaterials* **86**, 1–10 (2016).
99. Yang, P. *et al.* In vitro wrinkle formation via shape memory dynamically aligns adherent cells. *Soft Matter* **9**, 4705 (2013).
100. Ebara, M. *et al.* Focus on the interlude between topographic transition and cell response on shape-memory surfaces. *Polymer (Guildf)*. **55**, 5961–5968 (2014).
101. Xu, X. *et al.* Shape Memory RGD-Containing Networks: Synthesis, Characterization, and

- Application in Cell Culture. *Macromol. Symp.* **309–310**, 162–172 (2011).
102. Gong, T. *et al.* The Control of Mesenchymal Stem Cell Differentiation Using Dynamically Tunable Surface Microgrooves. *Adv. Healthc. Mater.* **3**, 1608–1619 (2014).
103. Lee, E. M., Smith, K., Gall, K., Boyan, B. D. & Schwartz, Z. Change in surface roughness by dynamic shape-memory acrylate networks enhances osteoblast differentiation. *Biomaterials* **110**, 34–44 (2016).
104. Tseng, L.-F. *et al.* Osteogenic Capacity of Human Adipose-Derived Stem Cells is Preserved Following Triggering of Shape Memory Scaffolds. *Tissue Eng. Part A* **22**, 1026–1035 (2016).
105. Kai, D. *et al.* Elastic poly( $\epsilon$ -caprolactone)-polydimethylsiloxane copolymer fibers with shape memory effect for bone tissue engineering. *Biomed. Mater.* **11**, 15007 (2016).
106. Wang, J., Quach, A., Brasch, M. E., Turner, C. E. & Henderson, J. H. On-command on/off switching of progenitor cell and cancer cell polarized motility and aligned morphology via a cytocompatible shape memory polymer scaffold. *Biomaterials* **140**, 150–161 (2017).
107. Baker, R. M., Brasch, M. E., Manning, M. L. & Henderson, J. H. Automated, contour-based tracking and analysis of cell behaviour over long time scales in environments of varying complexity and cell density. *J. R. Soc. Interface* **11**, 20140386 (2014).
108. Wang, J. *et al.* Shape memory activation can affect cell seeding of shape memory polymer scaffolds designed for tissue engineering and regenerative medicine. *J. Mater. Sci. Mater. Med.* **28**, 151 (2017).
109. Gu, H., Lee, S. W., Buffington, S. L., Henderson, J. H. & Ren, D. On-Demand Removal

- of Bacterial Biofilms via Shape Memory Activation. *ACS Appl. Mater. Interfaces* **8**, 21140–21144 (2016).
110. Maška, M. *et al.* A benchmark for comparison of cell tracking algorithms. *Bioinformatics* (2014). doi:10.1093/bioinformatics/btu080
111. Chenouard, N. *et al.* Objective comparison of particle tracking methods. *Nat. Methods* (2014). doi:10.1038/nmeth.2808
112. Song, F. *et al.* How Bacteria Respond to Material Stiffness during Attachment: A Role of *Escherichia coli* Flagellar Motility. *ACS Appl. Mater. Interfaces* (2017). doi:10.1021/acsami.7b04757
113. Brasch, M. E. *et al.* Nuclear position relative to the Golgi body and nuclear orientation are differentially responsive indicators of cell polarized motility. *PLoS One* (2019). doi:10.1371/journal.pone.0211408
114. Passucci, G., Brasch, M. E., Henderson, J. H., Zaburdaev, V. & Manning, M. L. Identifying the mechanism for superdiffusivity in mouse fibroblast motility. *PLoS Comput. Biol.* (2019). doi:10.1371/journal.pcbi.1006732
115. Luo, X. & Mather, P. T. Triple-Shape Polymeric Composites (TSPCs). *Adv. Funct. Mater.* **20**, 2649–2656 (2010).

## Chapter 2: Enzymatically Triggered Shape Memory

### Polymers<sup>‡</sup>

#### 2.1 Synopsis

This chapter discusses the design and development of a novel shape memory polymer that changes shape in response to enzymatic activity. To accomplish this, an enzymatically stable polymer (Pellethane™) and an enzymatically vulnerable polymer (poly( $\epsilon$ -caprolactone)) were dual electrospun together to create a blended fiber mat. In this system, the enzymatically vulnerable fiber holds the temporary shape and as it is degraded away the enzymatically stable fiber drives the material recovery back to the original shape. We successfully demonstrated both enzymatic shape recovery and the cytocompatibility of the shape change. We expect this isothermally triggered shape memory polymer will be a powerful material platform for future active cell culture experiments.

#### 2.2 Introduction

Development of shape memory polymers possessing cytocompatible shape memory triggering mechanisms has led to increased application of these “smart” materials in both basic and translational research. SMPs memorize a permanent shape through chemical or physical cross-linking. Following manipulation and fixing in a temporary shape by an immobilizing

<sup>‡</sup>Adapted with permission from S.L. Buffington, J.E. Paul, M.M. Ali, M.M. Macios, P.T. Mather, and J. H. Henderson, *Acta Biomaterialia*, 2019, 84, © 2019 Acta Biomaterialia Inc. Published by Elsevier Ltd.



transition, such as vitrification or crystallization, an SMP can subsequently recover to the permanent shape by a triggering event,<sup>1-4</sup> such as thermal, electrical, or solvent activation.<sup>5-7</sup> Although biocompatible SMPs initially featured recovery temperatures too high for cells to maintain viability during the thermal trigger,<sup>8,9</sup> in 2011 we<sup>10-12</sup> and then Ashby and colleagues<sup>13</sup> successfully applied SMPs as two-dimensional cell culture substrates with triggering of shape recovery at or near normal body temperature (37 °C). Subsequently, photothermally-triggered cytocompatible SMPs, activated by near-infrared wavelengths, were developed.<sup>14</sup> Two-dimensional SMP substrates and three-dimensional SMP scaffolds employing these cytocompatible triggering mechanisms have since been used in the study of mechanobiological aspects of cell morphology,<sup>15-19</sup> cell differentiation,<sup>20-22</sup> and cell motility,<sup>23,24</sup> in the development of strategies for bone,<sup>25-33</sup> cartilage<sup>34</sup> and nerve tissue engineering,<sup>35</sup> and in the design of approaches for control of bacterial biofilms.<sup>36</sup>

Enzymatically triggered, cytocompatible SMPs could open new fields of study and substantially broaden the range of existing basic and translational applications but have not previously been reported. If successfully achieved, enzymatic triggering of shape memory could enable, for example: drug delivery vehicles that affect the target cells/organs through controlled release that is modulated by the physiological status of the cells/organs; scaffolds that guide tissue regeneration through alterations in material and mechanical properties modulated by properties and behavior of the regenerating tissue; platforms for stem cell culture that present a tailored microenvironment to maintain stem cell phenotype or, alternatively, to differentiate cells down a specific lineage in response to the phenotypic state of the cells; and decision-making biosensors that use feedback systems to control patient treatment. Moreover, the achievement of enzymatic triggering of shape memory would add to the growing field of enzyme-responsive

materials, which currently includes materials based on material assembly or disassembly,<sup>37</sup> coil–globule transitions,<sup>38</sup> or degradation<sup>39</sup>.

The goal of this study was to develop an SMP that responds directly to enzymatic activity and can do so under isothermal cell culture conditions. To achieve this goal, we designed an SMP with a shape fixing component that is vulnerable to enzymatic degradation and a shape memory component that is enzymatically stable—as the shape fixing component undergoes enzymatically-catalyzed degradation, the SMP returns to its original, programmed shape (Scheme 2-1). We quantitatively and qualitatively analyzed material properties, shape-memory performance, and cytocompatibility of the enzymatically-catalyzed shape memory response.

## 2.3 Experimental Methods

### 2.3.1 Materials

Pellethane (5380-80A) (afterward referred to as Pellethane) was kindly provided by Lubrizol Corporation. Poly ( $\epsilon$ -caprolactone) (Mn = 80,000) pellets, Chloroform (CHCl<sub>3</sub>), N,N-Dimethylformamide (DMF) and lipase derived from the *pseudomonas cepacian* were purchased from Sigma Aldrich and Tetrahydrofuran (THF) was purchased from VWR International. All materials were used as received. C3H10T1/2 cells were obtained from the American Type Culture Collection (ATCC) and expanded to passage 12-15 for experiments. Basal medium eagle (BME), fetal bovine serum (FBS), GlutaMAX, penicillin/streptomycin, LIVE/DEAD stain, Formaldehyde, Triton X-100, BSA, DAPI stain and Phalloidin 568 were all purchased from Invitrogen and used as received.

## 2.3.2 Fabrication

### 2.3.2.1 *Preparing Electrospinning Solutions*

An 11 wt% electrospinning solution of Pellethane was prepared by dissolving 11 g of Pellethane in a 1:1.5 by volume solution of DMF:THF, as previously described.<sup>40</sup> A 10 wt% electrospinning solution of PCL was prepared by dissolving 10 g of PCL in a 1:4 by volume solution of DMF:CHCl<sub>3</sub>. Solutions were stirred continuously for at least 24 h, at which time the complete dissolution of the polymer was confirmed visually.

### 2.3.2.2 *Electrospinning Bulk Enzyme Recovery Experiments*

All samples were fabricated by dual electrospinning, in which two materials can be spun simultaneously to create a blended fiber mat. Samples were electrospun at Bucknell by Matthew Ali using a custom electrospinning apparatus composed of a rotating cylindrical drum collector (95.6 mm diameter, 300 mm width), Spraybase® electrospinning syringe pumps, and Spraybase voltage sources with a multi-head emitter (Schm. 2-2). Two solution emitters, one for the Pellethane solution and one for the PCL solution, were used for this work, although the set up would allow for the addition of more emitters to allow more materials to be electrospun at a time. To vary the compositional ratio of the PCL to Pellethane in fiber composites, the flow rate of PCL was set between 2.02 and 8.07 mL/h, while the Pellethane flow rate was held constant at 11 mL/h, resulting in composites ranging from 20% to 50% PCL by mass. The time of electrospinning was adjusted based on the flow rate of PCL to ensure the fiber mats were of similar mass and thickness. 22 G needles were attached to emitters and a voltage applied to the needle tip: 9-10.5 kV for the PCL, depending on the flow rate; and 12.5 kV for the Pellethane. The needle tip to mandrel distance was held constant at 148 mm for both emitters. A negative voltage of -1000 V was applied to the mandrel to improve fiber deposition. A rotational speed of

2000 rpm was used to align the fibers during electrospinning. To ensure uniform fiber deposition, the emitter needle tips were translated across the width of the mandrel following a square wave velocity profile with a peak velocity of 100 mm/s. Non-composite PCL and Pellethane fiber mat controls were fabricated similarly, but using only one emitter. A flow rate of 8.07 mL/h with 10.5 kV was used for PCL and a flow rate of 11 mL/h with 12.5 kV was used for Pellethane. All other spin conditions were held constant.

### 2.3.2.3 Heat Processing of Fiber Mats

For enzymatic recovery experiments, because the PCL fiber mats (containing no Pellethane) were difficult to mechanically program, PCL controls were pressed in a hot press between two Teflon spacers at 70 °C to create a PCL film. In addition, the PCL present in fiber composites melts during heat treatment (Fig. 2-1, and described later in this section) and during programming; the resultant PCL film morphology present in fiber composites is similar to the PCL films prepared for the enzymatic recovery experiments. For assessment of the cytocompatibility of material *prior* to enzymatic recovery (Section 2.3.6.2), non-composite PCL fiber mats were washed in hexane and then cut in half. A portion of each fiber mat was compression-molded (as above), and cell culture samples were cut from both the fiber mat and the film. We studied the cytocompatibility of both the PCL fiber and film morphologies in the event that the mixed PCL fiber and film morphologies present in fiber composites differentially affected cells. For assessment of cytocompatibility of material *during* enzymatic shape recovery (Section 2.3.6.3), of the PCL fiber and film samples, only the PCL film samples were studied, due to the difficulty in mechanically programming PCL fiber mats.

Thermal analysis (Section 2.3.3) was performed to measure the thermal degradation of the materials and to ensure that only fiber composites that had calculated composition values

close to the prescribed values were used in subsequent experiments. Following thermal analysis, samples were heat-treated, by heating the samples to 70 °C, to allow any residual strain programmed during the electrospinning process to recover.<sup>41</sup> Heat treatment was performed before dynamic mechanical analysis, shape-memory testing, and enzymatic degradation experiments. For all cell experiments, samples were washed with hexane, to remove any residual toxic solvents that may have remained from electrospinning of the samples, dried and then heat-treated at 70 °C.

### 2.3.3 Thermal Analysis

Thermal gravimetric analysis (TGA) (TA Instruments Q500) was performed on all-fiber samples to measure the thermal degradation of the materials. To allow high-resolution analysis of thermal degradation events, the analysis employed a protocol in which samples are run at a variable heating rate that decreases as detected mass loss rate increases (TA Instruments Dynamic Rate Hi-Res™ Ramp). Briefly, and following methods we have previously reported,<sup>42</sup> samples were heated at a maximum rate of 50 °C/min to 600 °C with a resolution of 4 °C and a sensitivity (instrument-specific) of 1. When the instrument detected a thermal degradation, the heating rate automatically decreased (below 50 °C/min) to capture fully the degradation event, before continuing with the test.

Differential scanning calorimetry (DSC) (TA Instruments Q200) was performed on all samples using a DSC equipped with a refrigerated cooling system to record thermal transitions. For each test, samples weighing 3-5 mg were loaded into a T-zero aluminum pan and equilibrated by cooling to -60 °C. Samples were then heated at 10 °C/min to 170 °C and then immediately cooled at 5 °C/min to -50 °C. This initial heating and cooling cycle erased any thermal history present in the fiber composites. Samples were then heated at 10 °C/min to 170 °C

to measure the glass transition ( $T_g$ ) and melting transition ( $T_m$ ) of the fiber mats. The theoretical composition of each sample was calculated using the heat of crystallization of the PCL via Eqn. 1.[47,48] This equation assumes that the degree of crystallinity of the PCL phase is the same in all samples, which is reasonable because PCL readily crystallizes at room temperature.

Calculated values were compared to predicted values prescribed by the flow rate of the PCL during electrospinning. Only fiber composites that had calculated composition values close to the prescribed values were used in subsequent experiments.

$$W_{PCL}(\%) = \frac{\Delta H_{PCL-COMP}}{\Delta H_{PCL-pure}} * 100 \quad (2-1)$$

Dynamic mechanical analysis (DMA) was used to measure the temperature dependences of the tensile storage modulus for all materials, as the temperature dependence of the storage modulus is a strong predictor of shape memory ability. Dog bones (ASTM D638 type IV, scaled down by a factor of 4) with a gauge length of 6.25 mm and width of 1.5 mm, were cut from fiber mats. Samples were then loaded into a DMA TA Q800, cooled to -70 °C, and then heated to 200 °C at a 2 °C/min while applying a small tensile deformation at a frequency of 1 Hz.

#### 2.3.4 Shape Memory Characterization

Thermal (not enzymatic) shape memory cycles were performed on a DMA (TA Instruments Q800) operated in controlled-force mode to quantify the shape memory ability of the fiber composites.<sup>43</sup> Briefly, each sample was first heated to 60 °C (above the  $T_m$  of PCL) and loaded at 0.03 N/min until 100% strain was reached. Samples were then cooled at 2 °C/min to 0 °C and the load released at 0.1 N/min. To complete the cycle, samples were then heated at 2 °C/min and the shape recovery recorded. This full cycle was repeated three times. The fixing ( $R_f$ ) and recovery ( $R_r$ ) ratios for each recovery event were then calculated using Eqns. 2-2 and 2-3,

where shape “ $x$ ” refers to the shape or deformation being programmed into the sample in the current cycle and shape “ $y$ ” is the shape or deformation after the previous cycle.<sup>43</sup>

$$R_f(x) = \frac{\varepsilon_x}{\varepsilon_{x, load}} \quad (2-2)$$

$$R_r(x \rightarrow y) = \frac{\varepsilon_x - \varepsilon_{y, rec}}{\varepsilon_x - \varepsilon_y} \quad (2-3)$$

In Eqn. (2-2),  $\varepsilon_x$  and  $\varepsilon_{x, load}$  are, respectively, the strains measured after cooling and unloading (thus, the strain fixed) and before unloading (or the attempted programmed strain).  $\varepsilon_{y, rec}$  is the strain achieved after recovery for shape  $y$ , and  $\varepsilon_y$  is the strain before programming shape  $y$ .

### 2.3.5. Bulk Enzymatic Shape Recovery

Enzymatic shape recovery was assessed using bulk enzymatic degradation studies under simulated cell culture conditions. Samples were cut using a dog bone punch (the same punch used for DMA shape memory cycling), then heated and stretched to 100% strain using a custom screw-driven manual stretcher, six samples at a time.<sup>44</sup> With samples so stretched but still in the stretching device, the stretcher and samples were transferred to a freezer at -20 °C to quickly fix the temporary shape (note: such fixing was stable at room temperature). Samples were photographed before and after mechanical programming (stretching and fixing) for subsequent use in image-based calculation of both the programmed strain and strain during enzymatic shape recovery. Samples were then weighed and incubated in PBS solutions containing 0, 0.05, 0.1, or 0.5 mg/mL of lipase. The enzyme concentration range of 0.5 – 0.05 mg/mL was selected based on a previous experimental and kinetic modeling evaluation of lipase activity with respect to concentration for degradation experiments<sup>45</sup> and was chosen such that the highest enzyme concentration would ensure degradation of the PCL in a relatively short time frame (i.e., days)

while the lower concentrations would reflect more physiological enzyme concentrations, though it is difficult to correlate *in vitro* concentration to activity *in vivo*. Experiments were conducted over 7 d, with one sample collected for analysis every 24 h. Experiments were repeated 3 times using fiber mats independently prepared (electrospun) on different days. Upon collection, the samples were washed using deionized water, dried in a desiccator for 24 h, and then transferred to a vacuum oven at 40 °C for 48 h to ensure full drying of the samples. Samples were then photographed and weighed. Mass loss was calculated using Eqn. 2-4:

$$M_r (\%) = \frac{M(t)}{M_o} * 100 \quad (2-4)$$

Where  $M_r$  is the % mass remaining,  $M(t)$  is the measured mass after degradation, and  $M_o$  is the original mass of the sample.

To calculate programmed strain and strain during enzymatic shape recovery, images of samples before programming, after programming, and after sample collection were analyzed in ImageJ 1.51j8 (National Institutes of Health, Bethesda, MD, USA). In each image, a linear measurement of the gauge length was made along both sides of the dog bone samples. The two measurements were averaged, and the measurements were performed independently by three separate users and averaged across all users. The change in strain ( $\epsilon$ ) over the course of enzymatic strain recovery for each sample was calculated using Eqn. 2-5:

$$\Delta \epsilon (\%) = \frac{(l_o - l_s)}{l_o} * 100 \quad (2-5)$$

Where  $l_o$  is the measured gauge length for the original, pre-strained sample and  $l_s$  is either the measured gauge length for the strained sample immediately after programming or after collection. DSC experiments were used to assess the PCL crystallinity before and after



degradation. Samples were run hydrated immediately post degradation to better capture the crystallinity of PCL at the point of sample recovery.

Fiber mats were imaged using SEM (JEOL 5600) to assess changes in fiber morphology during enzymatic shape recovery experiments and, additionally, to ensure that fiber morphologies were similar between fiber composite batches. Samples of fiber mats were collected for SEM immediately after electrospinning, immediately after the heat treatment used to recover residual strain programmed during the electrospinning process, and after days 0 through 7 of the enzymatic shape recovery experiments. All samples were mounted on a metal plate and sputter coated for 45 s (Denton Vacuum-Desk II). Samples were imaged with an accelerating voltage of 10 kV and a spot size of 36.

### 2.3.6 Cell Culture Experiments

#### *2.3.6.1 Cell Selection and Expansion Culture*

All cell experiments were performed with the C3H/10T1/2 mouse embryonic fibroblast line, a cell line we have frequently used in the development and application of cytocompatible SMPs.<sup>10,11,23</sup> Cells were obtained from the ATCC at passage 8 and expanded to passage number 12-15 to use for experiments, following the recommendations of the ATCC. Cells were cultured in basal medium Eagle with 10% fetal bovine serum, 1% GlutaMAX, and 1% penicillin/streptomycin and passaged once 70-80% confluence was reached. Cells were passaged by first rinsing the flask with PBS and incubating in a solution 0.25% Trypsin-EDTA for 10 m. The cell solution was then collected and diluted with an equal amount of complete BME. Cells were then spun for 10 m at 200 g to centrifuge out the cells. Cells were then resuspended in BME and either seeded on materials or re-plated in a tissue culture flask. For storage, cells were frozen in a solution of complete BME with 5% Dimethyl sulfoxide.

#### *2.3.6.2 Assessing Cell Cytocompatibility to Material Chemistry*

Cells were directly cultured on samples to assess material cytocompatibility. Fiber and film PCL samples were sterilized using UV light for 10 h, flipped over, and sterilized using UV for an additional 10 h. All materials were soaked in complete medium overnight to allow proteins to adsorb throughout the samples and then C3H/10T1/2 cells were solution seeded onto the materials at 10,000 cells/cm<sup>2</sup>. Cell-seeded materials were then washed with PBS and stained with LIVE/DEAD at 24, 48, and 72 h time points with tissue culture polystyrene (TCPS) well plates acting as live controls for counting and analysis. Cell viability was calculated by dividing the total number of cells by the total number of live cells.

#### *2.3.6.3 Assessing Cell Cytocompatibility to Enzymatic Shape Recovery*

The cytocompatibility of enzymatic shape triggering was assessed by culturing cells on samples as the samples were incubated in lipase-containing medium over a one-week period. Samples were washed and sterilized as described in Section 7.3.6.2. Cells were seeded onto the samples at 5,000 cells/cm<sup>2</sup> and allowed to attach for 3 h. The culture medium was then replaced with medium containing 0.5 mg/mL lipase, the highest lipase concentration used for shape recovery experiments. The lipase-containing medium was sterilized via filtration with a 0.45 μm filter prior to use. The non-toxic control was a lipase-free medium. Media were changed every 2 days to mimic conditions used in the bulk degradation experiments. Samples were collected and cells stained with LIVE/DEAD stain at 1, 3, and 7-day time-points to assess cell viability. Cell viability was calculated as above (Section 2.3.6.2).

## 2.4 Results

### 2.4.1 Fabrication

Fiber composites of varying compositions were successfully electrospun using the methods described. All fiber composites were imaged using SEM both before and after heat treatment to assess changes in fiber morphology (Fig. 2-1). As shown, Pellethane controls showed no change in fiber alignment, while the PCL samples transitioned from a fiber morphology to a film morphology. The fiber composites transitioned to a mixed morphology composed of both Pellethane fibers and PCL films.

### 2.4.2 Thermal Analysis

As anticipated, thermal transitions quantified by TGA (Fig. 2-2), DSC (Fig. 2-3, Table 2-1), and DMA (Fig. 2-4) showed that both PCL and Pellethane were present in fiber composites and existed as separate phases, as evidenced by the separate transitions recorded in thermal analysis. TGA analysis (Fig. 2-2) showed that all fiber mats were dry before processing. PCL showed a single sharp degradation event, while Pellethane showed a two-step degradation event. Fiber composites likewise showed a two-step degradation; however, the degradation of the PCL was occluded by the degradation of the Pellethane, making TGA analysis of the two weight %s difficult. As a result, DSC was used to analyze the % content of the fiber mats. For the analyzed temperature range, Pellethane controls demonstrated only a  $T_g$ , at approximately  $-20\text{ }^{\circ}\text{C}$ , while PCL controls showed only a  $T_m$ , at approximately  $56\text{ }^{\circ}\text{C}$  (Table 2-1). To ensure consistency across experimental runs, only fiber composites that came within a  $\pm 5\%$  predicted PCL content were used for subsequent experiments. Gradient fiber composites were likewise thermally characterized but showed the same thermal properties as the 20:80 PCL:Pellethane fiber composites as these thermal characterization techniques are not sensitive to material distribution,

only percent composition. Analysis of post-heat treatment samples confirmed that the thermal transitions quantified by TGA and DSC were unaffected by the heat treatment used to recover residual strain programmed during the electrospinning process.

#### 2.4.3 Shape Memory Characterization

Thermal shape memory cycles demonstrated that strong shape fixing and recovery were achieved for fiber composite samples (Fig. 2-5). The PCL control yielded during the first stretch of the first cycle and was not included in the analysis. The Pellethane control (Fig. 2-5A) showed a poor fixing ratio of 53%, indicating a low ability to fix a shape, and demonstrated a recovery ratio of 89%. We note, for comparison, that an ideal rubber features no (0%) fixing and complete (100%) recovery. The high recovery ratio for the Pellethane control is attributed to the elasticity of the Pellethane fibers, which is the driving force for shape recovery. This recovery ratio indicates that some strain is lost during mechanical cycling, which we attribute to minor plastic deformation that occurs during the first thermo-mechanical cycle. The fixing ratio of fiber composites was 89% and 96% for the 20:80 (Fig. 2-5B) and 50:50 (Fig. 2-5C) PCL:Pellethane, respectively (summarized in Table 2-2), indicating that increasing the PCL content increased the fixing ability of the fibers. The recovery ratio showed weak dependence on composition, with values of 89% and 84% for the 20:80 (Fig. 2-5B) and 50:50 (Fig. 2-5C) PCL:Pellethane, respectively (summarized in Table 2-3). The 30:70 and 40:60 PCL:Pellethane compositions showed similar results, with an increase in PCL content increasing the fixing ability of the fibers and the recovery ratio showing weak dependence on composition (Figure 2-5). All samples showed a diminished recovery ratio for the first cycle, which we attribute to minor plastic deformation of the Pellethane fibers, as indicated by the strain in the samples not returning fully to zero. After a single mechanical conditioning step, the recovery of the materials increased. In

light of the modest differences in shape memory ability observed across the four fiber composite compositions tested, only the two most extreme compositions, 20:80 and 50:50 PCL:Pellethane, were studied in the ensuing enzymatic shape recovery and cytocompatibility experiments.

#### 2.4.4 Bulk Enzymatic Shape Recovery

Enzyme-triggered shape recovery was observed in fiber composites (50:50 and 20:80 PCL:Pellethane, Fig. 2-6, 2-7), as evidenced by decreasing strain over the 7-day experiment. However, shape recovery was only evident for the highest enzyme concentration studied (0.5 mg/mL). Pellethane showed no measurable changes in strain for all conditions, as expected, while the fiber composites decreased in length over time (Fig. 2-6A). Lower concentrations of lipase degraded the PCL film control samples but did not trigger shape recovery in the fiber composites (Fig. 2-6B, 2-6C). For fiber composites, sample lengths (and associated strains) in 0.5 mg/mL lipase solutions (Fig. 2-6A) remained significantly greater ( $P < 0.05$ ) than the Pellethane controls until day 5, after which no statistical difference in length was observed, consistent with samples having recovered to the preferred length of the Pellethane. In contrast, when incubated in 0.1 (Fig. 2-6B) and 0.05 mg/mL (Fig. 2-6C) lipase, fiber composite sample lengths remained significantly greater than that of the Pellethane controls at all time-points ( $P < 0.05$ ), consistent with fiber composite samples having not recovered. Further, PBS controls showed no measurable recovery for all groups, as anticipated (Fig. 2-6D). In particular, those samples incubated in only PBS exhibited no measurable change in strain with time, remaining strained at the magnitude programmed, which was significantly greater than that of Pellethane control (incapable of strain-fixing), for all time points ( $P < 0.05$ ). PCL control samples were not included in statistical comparisons, as samples degraded significantly for all enzyme concentrations, including day 1. Images of the samples incubated in 0.5 mg/mL lipase visually

show the samples returning to their original shape over the course of the 7 d experiments (Fig 2-7).

Mass change measurements revealed significant mass loss for the PCL film, and the rate of degradation increased with increasing lipase concentration, while all other samples exhibited no measurable mass loss (Fig. 2-8). Control samples immersed in PBS showed no measurable mass change for any of the samples (Fig. 2-8D), indicating that mass loss was driven by enzymatic degradation instead of much slower hydrolytic degradation, as expected. The lack of observed mass change in fiber composites (Fig. 2-8) suggests that the observed strain recovery (Fig. 2-6) occurs primarily through the reduction of PCL molecular weight, or disruption of the percolation of the PCL phase, not through loss of PCL mass. This finding is supported by the observed decrease in PCL crystallinity as samples are degraded (Fig 2-9). Upon exposure to lipase, the PCL crystalline peak diminishes supporting the degradation disrupting the PCL crystallinity and thereby allowing the Pellethane to recover.

Morphological analysis by SEM of samples undergoing degradation during exposure to enzyme revealed changes in sample morphology indicative of PCL degradation. Surface analysis of morphological changes in the 50:50 PCL:Pellethane fiber composite incubated in 0.5 mg/mL lipase (Fig. 2-10) showed an initial (pre-degradation) morphology of fibers with a film or binder at the surface (Fig. 2-10A). Over the course of the degradation experiment, the morphology of the fiber composite transitioned from a mixed film-fiber morphology (Fig. 2-10A-C) to a predominantly fiber morphology (Fig. 2-10D) as PCL degraded, leaving behind primarily Pellethane fibers. Analysis of cross-sections of 50:50 PCL:Pellethane samples (Fig. 2-10E) showed an initial semi-continuous network of Pellethane fibers interpenetrated incompletely by PCL binder, with significant porosity evident. As enzymatic degradation progressed over 7 days,

the PCL binder increasingly degraded until, at day 7 (Fig. 2-10H), the fraction of PCL had diminished substantially. The 20:80 PCL:Pellethane samples showed similar morphological changes when incubated in 0.5 mg/mL lipase (Fig. 2-11), and both fiber composites (20:80 and 50:50) also showed similar morphological changes when incubated in the lower, 0.1 mg/mL, lipase concentration (Fig. 2-12B, C). In contrast, fiber composites incubated in 0.05 mg/mL lipase retained a mixed film-fiber morphology (Fig. 2-13B, C). The Pellethane control showed no morphological changes, regardless of enzyme concentration (Figs. 2-11A, 2-12A, 2-13A, 2-14A). All fiber composites and controls showed no morphological changes when incubated in PBS (Fig. 2-14).

## 2.4.5 Cell Culture Experiments

### *2.3.5.1 Assessing Cell Cytocompatibility to Material Chemistry*

When mouse fibroblasts were cultured directly on fiber composites and non-composite controls in the absence of lipase, no statistically significant differences in viability were found (Fig. 2-15). Moreover, all groups had a viability of 75% or greater at all time-points. The Pellethane control, PCL control, and fiber composites showed an average viability not statistically different from the TCPS control, indicative of cytocompatibility (representative cell images for all groups are shown in Fig. 2-16). Qualitatively, cells cultured on the 50:50 PCL:Pellethane fibrous composite showed a random orientation that contrasted with that of cells cultured on the Pellethane control, which showed an oriented morphology (Fig. 2-16). This difference is likely due to the morphology of the PCL, which acts as a film (binder) in the fiber composites (Figs. 2-1), a morphological feature that does not exist between the aligned fibers of the Pellethane control. Image analysis revealed a significantly higher number of cells on TCPS

compared to all material groups (Fig. 2-17,  $P < 0.05$ ), likely due to cells attaching to the bottom of the well (rather than the sample) during the seeding of material groups.

#### *2.3.6.2 Assessing Cell Cytocompatibility to Enzymatic Shape Recovery*

When mouse fibroblasts were cultured on fiber composites and non-composite controls incubated with 0.5 mg/mL of lipase or a lipase-free control medium (Fig. 2-18), no statistical differences in viability were found. Moreover, all groups had a viability of 75% or greater at all time-points. As had been observed in the study of cytocompatibility prior to enzymatic shape recovery (Fig. 2-15), in the presence of lipase the Pellethane control, PCL control, and fiber composites showed an average viability not statistically different from the TCPS control, indicative of the enzymatic degradation of PCL and, therefore, the phenomenon of enzymatic shape recovery being cytocompatible (Fig. 2-18, and representative cell images for all groups are shown in Figs. 2-19 and 2-20). Image analysis again revealed a significantly higher number of cells on TCPS compared to all material groups (Fig. 2-21,  $P < 0.05$ ), which is again likely due to cells attaching to the bottom of the well (rather than the sample) during the seeding of material groups.

## 2.5 Discussion

Here we have introduced and studied a new SMP design that responds directly to enzymatic activity to allow isothermal shape change, demonstrated as contraction of tensile specimens, under cell culture conditions. Electrospun fiber composites prepared using this design showed good thermal shape memory ability, with a PCL component acting as a shape fixer and a Pellethane component acting as the memory component. When cultured in a 0.5 mg/mL lipase solution, programmed fiber composites showed enzymatic shape recovery within a 7-day test period. Cells cultured on enzymatic SMPs with or without 0.5 mg/mL lipase showed viability



comparable to non-toxic controls, indicating that both the enzymatically-responsive SMP materials and the process of enzymatic shape recovery are cytocompatible.

The enzymatic shape recovery achieved in the present work is dependent on enzyme concentration. Only samples incubated in the highest enzyme concentration, 0.5 mg/mL lipase, showed complete shape recovery, while samples incubated in lower enzyme concentrations and in a lipase-free control showed no measurable recovery. This enzyme concentration sensitivity is consistent with the strategy used to achieve enzymatic recovery (Schm. 2-1), wherein shape recovery is enabled by the degradation of an enzymatically labile fixing component and is only achieved when that component has degraded sufficiently. It is expected that, if degradation experiments were lengthened, all fiber composites would eventually show full strain recovery for all enzyme conditions studied.

The enzymatic SMPs did not demonstrate mass loss during recovery. This finding suggests that the mechanism of enzyme shape recovery is either a decrease in PCL molecular weight or de-percolation of the fixing phase. As either of these processes continue, the force exerted by the Pellethane is able to overcome the force exerted by the PCL, leading to recovery back to the sample's original shape. Analysis of SEM micrographs suggests that the PCL phase is, in fact, degrading, lending support to the hypothesized de-percolation of PCL. This theory is supported by the observed decrease in the heat of crystallization of PCL over time, a decrease from 9.031 to 0 W/g over 7 days for the 50:50 PCL:Pellethane fiber composite (Fig 2-9). In addition, the PCL control samples degrade within 2 days, compared to the 5 days required to observe sample recovery in the programmed fiber composites. These findings suggest that the presence of Pellethane in the composite samples inhibits the ability of the lipase to diffuse into the fiber composites and degrade the PCL shape fixing component and, further, that the

mechanism of degradation is not mass loss but loss of crystallinity and concomitant softening of the PCL-based fixing phase.

A potential limitation of this first instantiation of the new SMP design is the relatively long time and high enzyme concentration required for enzymatic shape recovery. Few cell types may release enzymes at concentrations necessary for enzymatic shape recovery to occur in time-spans less than weeks or months. Because we speculate that the present material composition would recover in low enzyme concentrations, but over long time periods, the present composition may be best suited for applications in which slow response is beneficial or for applications in which cells, such as macrophages or hepatic cells,<sup>46,47</sup> secrete high concentrations of enzyme. It is anticipated that the new SMP design could be adapted for more rapid recovery and/or low enzyme concentration triggering by increasing the enzymatic sensitivity of the labile fixing component. Conversely, even more, gradual recovery than that demonstrated here could be achieved by decreasing enzymatic sensitivity of the labile fixing component. More generally, enzymatically responsive SMPs could, in theory, be designed to be triggered by any arbitrary enzyme by engineering the enzyme's target sequence into the polymer, though risk of cytotoxicity would likely be a constraint for many candidate enzymes.

In addition to contributing to SMP science, the new design reported here adds SMPs to the field of enzyme responsive materials (ERMs)—materials that undergo a material action, such as self-assembly/disassembly,<sup>48</sup> transformation of surface properties, or swelling/deswelling,<sup>38</sup> in response to enzymatic activity. ERMs have gained increasing attention due to the extreme specificity with which they can be designed to respond to the biological environment. For example, Zelzer and colleagues<sup>49</sup> developed an ERM that changes surface properties in response to dephosphorylation, with sensitivity sufficient for cells to provide the trigger. Liu and

colleagues<sup>50</sup> designed enzymatically stiffening hydrogels to study how cancer cells modify their behavior in response to stiffening gels. Despite advances, such as these, in ERM science, prior to the present work, there was not an ERM capable of applying a programmed shape change or direct mechanical force.

In addition to bringing shape-changing functionality to the field of ERMs, the SMP design reported here represents the first SMP that could respond directly to biological activity. The majority of cell culture compatible SMPs have been thermally or photothermally triggered. Dependence on these triggers prevents application as stimuli-responsive materials designed to respond directly to biological activity.<sup>51</sup> With the advent of enzymatically triggered SMPs, SMPs can now be designed for such an application.

## 2.6 Conclusions and Future Work

We have developed an enzymatically triggered SMP that changes its shape isothermally in response to enzymatic activity under cell culture conditions. We successfully demonstrated enzymatic recovery using bulk enzymatic degradation experiments. The results show that shape recovery is achieved by degradation of the PCL shape-fixing phase, which enables one-way and one-time shape recovery, leaving the material in a final state that, while useful in itself, does not allow for reprogramming. We further showed that both the materials and the process of enzymatic shape recovery are cytocompatible. This new SMP design can be anticipated to enable new applications in basic and applied materials science as a stimulus-responsive material.

## 2.7 Acknowledgements

Funding from the NSF IGERT Program, DGE-1068780, and the NSF BMAT program, DMR-1609523 and REU Supplement DMR-1743080, is gratefully acknowledged, as is use of

the facilities of the Syracuse Biomaterial Institute at Syracuse University. In addition, the student contributions of Justine Paul, Mark Macios and Jose Waimin are all gratefully acknowledged.

**Table 2-1.** Measured thermal transitions. For the analyzed temperature range, Pellethane controls demonstrated only a  $T_g$ , at approximately  $-20\text{ }^\circ\text{C}$ , while PCL controls showed only a  $T_m$ , at approximately  $56\text{ }^\circ\text{C}$ . Fiber composites demonstrated both thermal transitions, and the heat of melting of the PCL melt transition was used to quantify the %PCL content in the fiber composites.

Material	$T_g$ <sup>[a]</sup>	$T_m$ <sup>[a]</sup>	dH <sup>[b]</sup>	% PCL <sup>[c]</sup>
Pellethane	-20.1	-	-	0
20:80 PCL:Pellethane	-20.6	57.0	6.85	17.9
30:70 PCL:Pellethane	-18.9	56.2	11.9	31.3
40:60 PCL:Pellethane	-19.7	56.6	14.9	39.0
50:50 PCL:Pellethane	-19.9	57.0	19.2	50.3
PCL	-	56.1	38.2	100

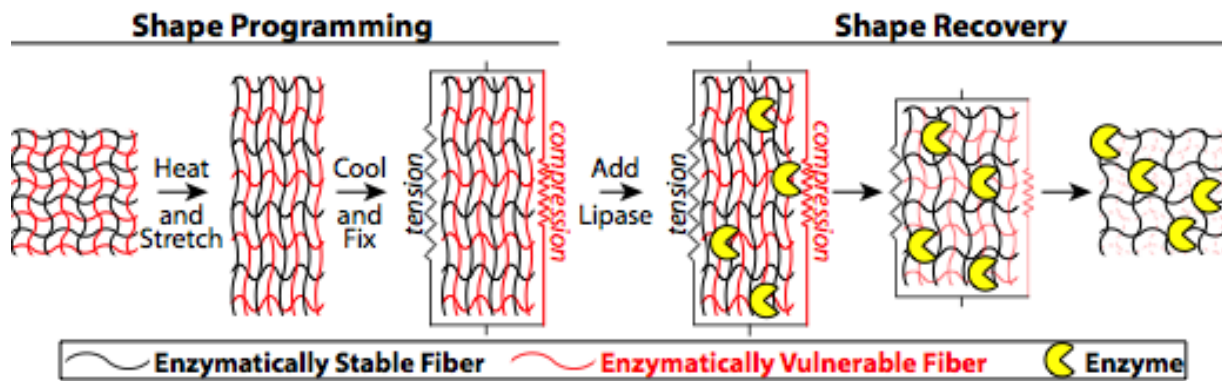
[a] Units of  $^\circ\text{C}$ . [b] Heat of the melt transition of PCL in units of W/g. [c] The % content of PCL in the fiber mat.

**Table 2-2.** Calculated fixing ratios for all materials by cycle. PCL is not shown, because the material yields during shape memory testing. All units are %.

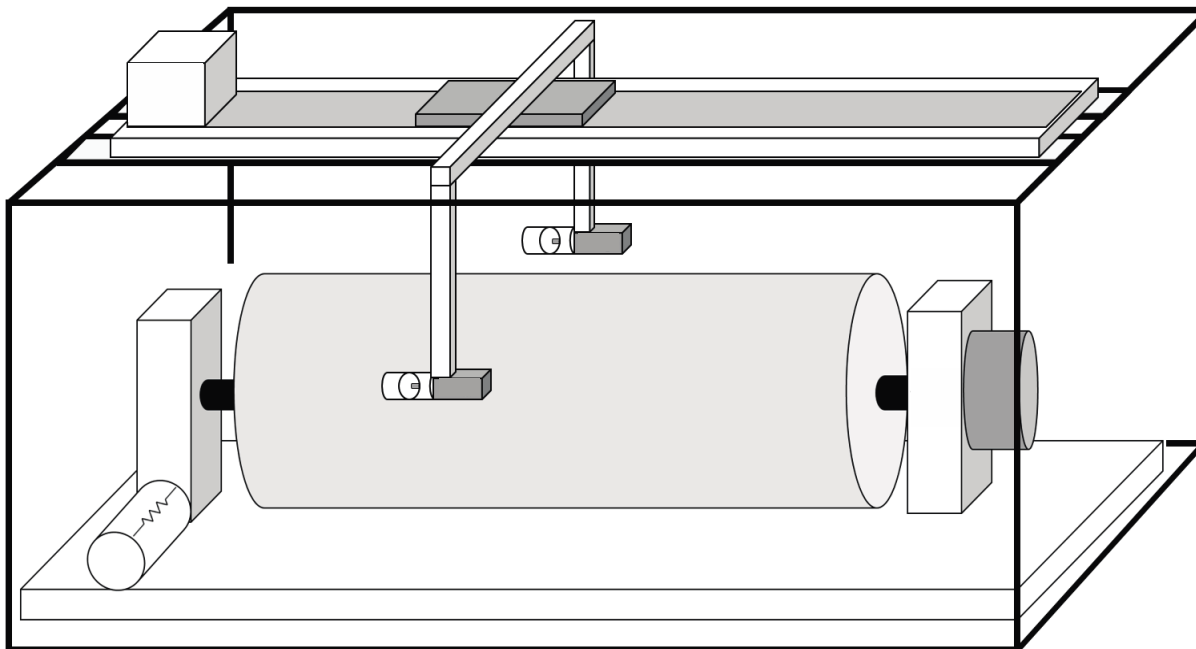
Material	Cycle 1	Cycle 2	Cycle 3	Average	Standard Deviation
Pellethane	52.6	53.8	53.9	53.4	0.7
20:80 PCL:Pellethane	87.5	89.3	89.3	88.7	1.03
30:70 PCL:Pellethane	92.6	94.1	105.7	97.5	7.17
40:60 PCL:Pellethane	94.6	96.3	96.5	95.8	1.07
50:50 PCL:Pellethane	95.5	96.3	96.4	96.1	0.47

**Table 2-3.** Calculated recovery ratios for all materials by cycle. PCL is not shown, because the material yields during shape memory testing. All units are %.

Material	Cycle 1	Cycle 2	Cycle 3	Average	Standard Deviation
Pellethane	76.4	93.7	96.3	88.8	10.9
20:80 PCL:Pellethane	74.8	97.4	95.5	89.2	12.5
30:70 PCL:Pellethane	65.9	95.5	97.6	86.4	17.7
40:60 PCL:Pellethane	53.6	94.0	96.6	81.4	24.1
50:50 PCL:Pellethane	63.3	92.7	95.8	83.9	17.9



**Scheme 2-1.** The strategy used to achieve enzymatic shape memory fiber composites. Fiber composites composed of poly( $\epsilon$ -caprolactone) (PCL) (red) and Pellethane (black) are heated and stretched above the  $T_m$  of PCL to program the samples. The composites are then cooled to fix the temporary shape, putting the Pellethane in an entropically unfavorable state. In this state, the Pellethane applies a compressive force to the PCL, as the Pellethane tries to recover back to its original shape but is resisted by the PCL crystallites that hold the temporary shape. Exposure to the enzyme lipase degrades the PCL portion of the fiber composite. As the PCL degrades, the force resisting the Pellethane is gradually removed and the Pellethane acts as an entropic spring to return back to its original conformation, recovering the permanent shape of the composite.



**Scheme 2-2.** The custom electrospinning apparatus used in the present study. A metallic mandrel with variable rotational speed is suspended above an electrically insulating platform. A separate metallic frame is placed over the platform to suspend a translator as well as protective Plexiglas to isolate the interior environment. Attached at the bottom of both translator arms are electrical connection points for the needle tips, which dispense the polymer solution. Syringe pumps (not shown) dispense the polymer solution through the tubing, which connects the syringes to the electrical connections on the translator arms.



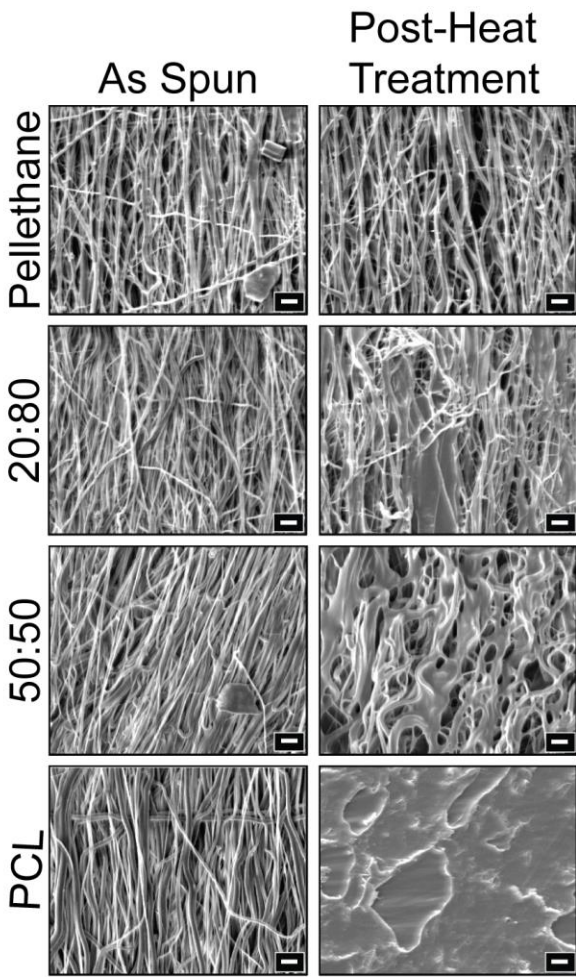


**Figure 2-1.** A comparison of the fiber morphologies of fiber composites and material controls (left) immediately after electrospinning and (right) immediately after the heat treatment used to recover residual strain programmed during the electrospinning process. The Pellethane fibers showed no noticeable morphological changes due to heat treatment and no noticeable shrinking. The 20:80 PCL:Pellethane showed fiber morphologies both before and after heat treatment. The 50:50 PCL:Pellethane showed a fiber morphology after electrospinning but showed a film morphology after heat treatment due to the melting of the PCL. The PCL control also transitioned from a fiber morphology before heat treatment to a film morphology after heat treatment. Scale bar is 10  $\mu\text{m}$ .

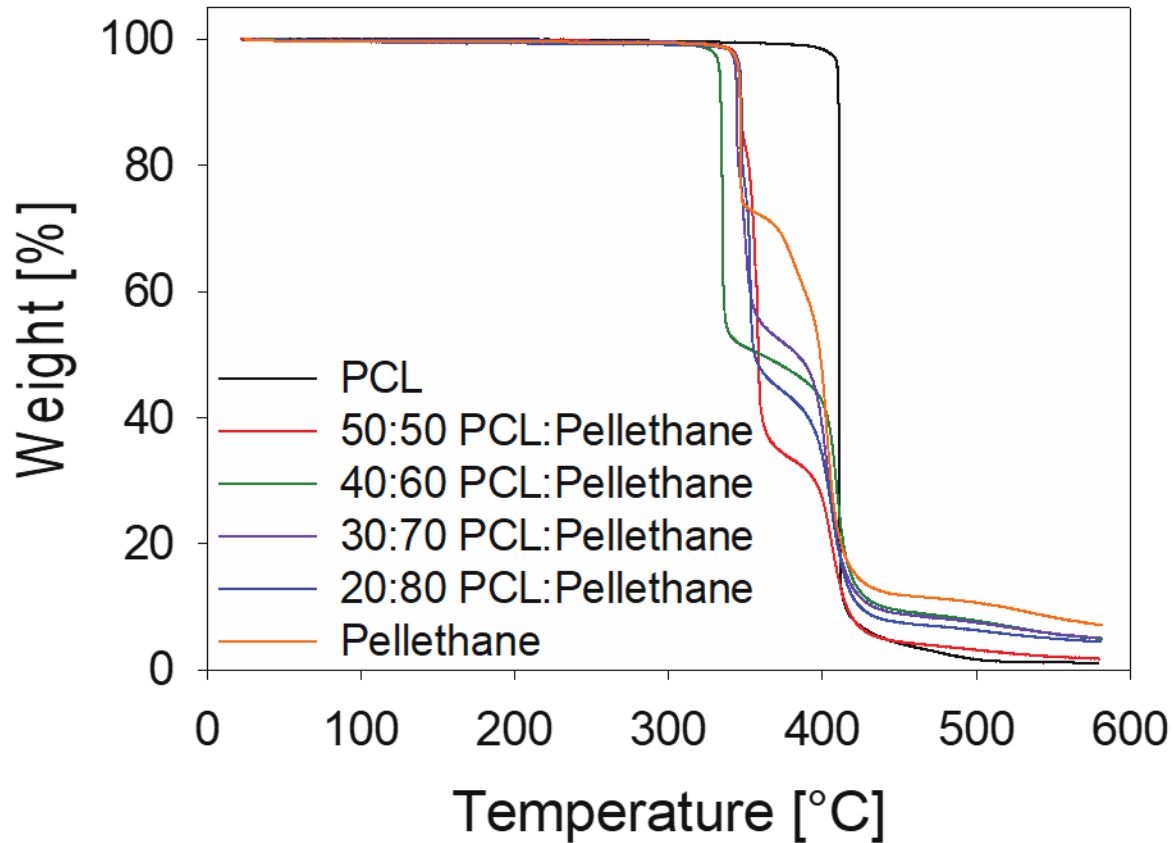


**Figure 2-2.** Thermal gravimetric analysis (TGA) analysis of fiber composites and controls. The poly( $\epsilon$ -caprolactone) (PCL) control (brown) showed a single-step degradation, while the Pellethane control (black) showed a two-step degradation. The fiber composites all showed a two-step degradation, similar to the Pellethane, although it should be noted that the second step of the Pellethane occludes the single PCL step. Due to this occlusion, dynamic scanning calorimetry, not TGA, was used to assess sample compositions.

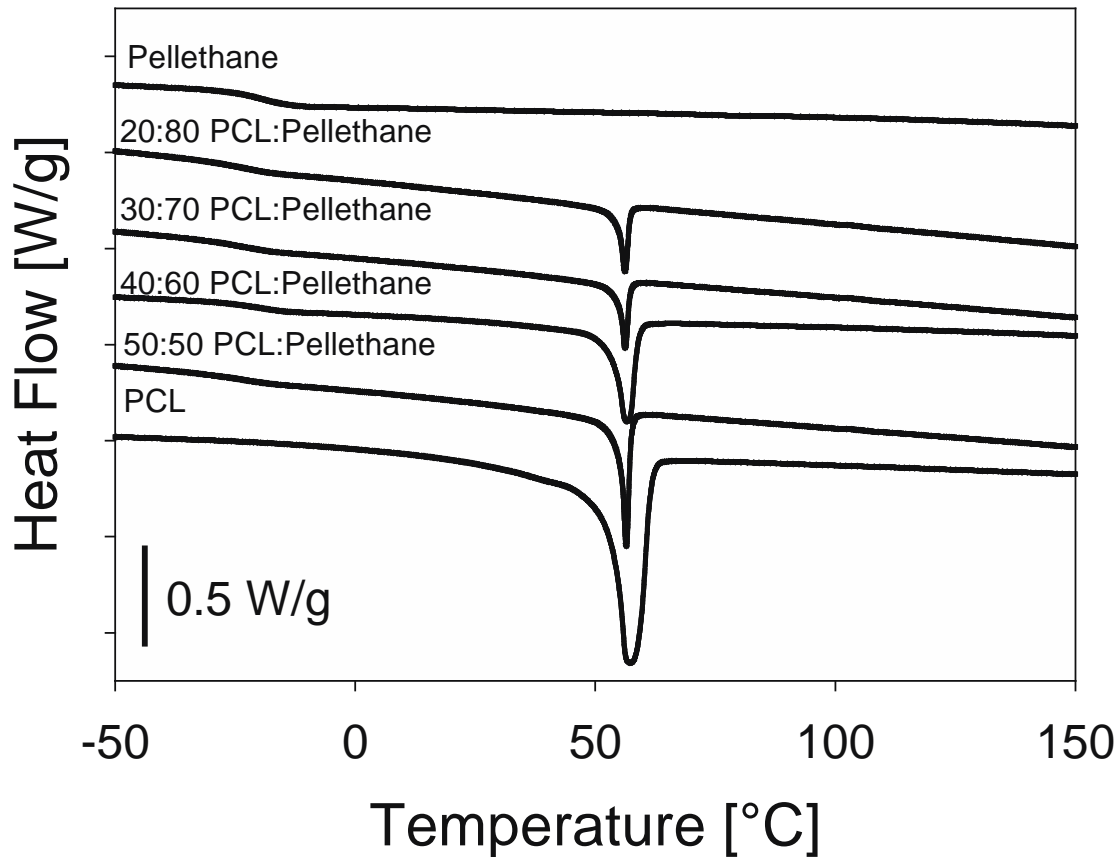


**Figure 2-3.** Differential scanning calorimetry (DSC) thermograms of all dual spun materials ordered in order of increasing poly( $\epsilon$ -caprolactone) (PCL) content. Increasing PCL content resulted in a large exotherm for the PCL melt transition but did not result in the shifting of the  $T_m$  of PCL. This exotherm at approximately 56 °C was used to calculate the predicted incorporation of PCL during the electrospinning process, and only fiber mats within 5% of the predicted PCL content were used in subsequent experiments. DSC traces are in order of increasing PCL content, from top to bottom: Pellethane, 20:80 PCL:Pellethane, 30:70 PCL:Pellethane, 40:60 PCL:Pellethane, 50:50 PCL:Pellethane, and PCL.

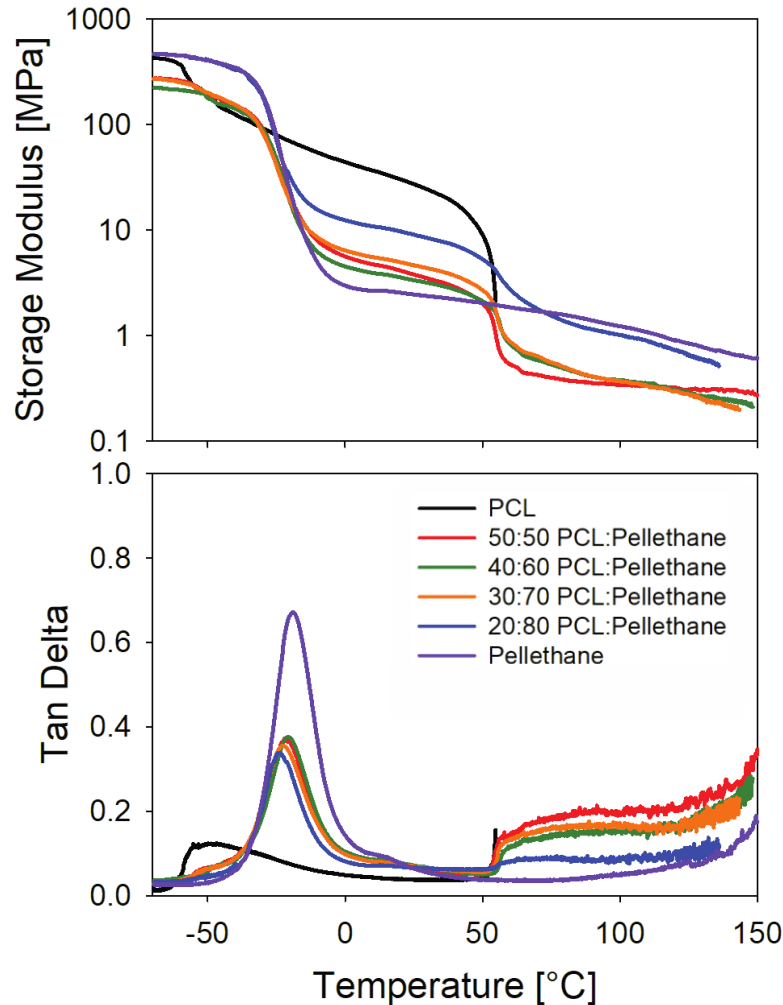


**Figure 2-4.** Dynamic mechanical analysis (DMA) curves of fiber composites and control showing (top) storage modulus and (bottom) tan delta traces. Peaks in tan delta traces correspond to changes in the storage modulus. There is a  $T_g$  for Pellethane at approximately  $-20\text{ }^\circ\text{C}$ , a  $T_m$  for poly( $\epsilon$ -caprolactone) (PCL) at  $56\text{ }^\circ\text{C}$ , and a  $T_m$  for Pellethane at approximately  $160\text{ }^\circ\text{C}$ . The ideal range for shape memory behavior would be above the  $T_g$  of Pellethane, so the material is in its elastic region, but below the  $T_m$  of Pellethane, to hold the permanent shape. The  $T_m$  of PCL then acts as the triggering transition that holds the temporary shape.

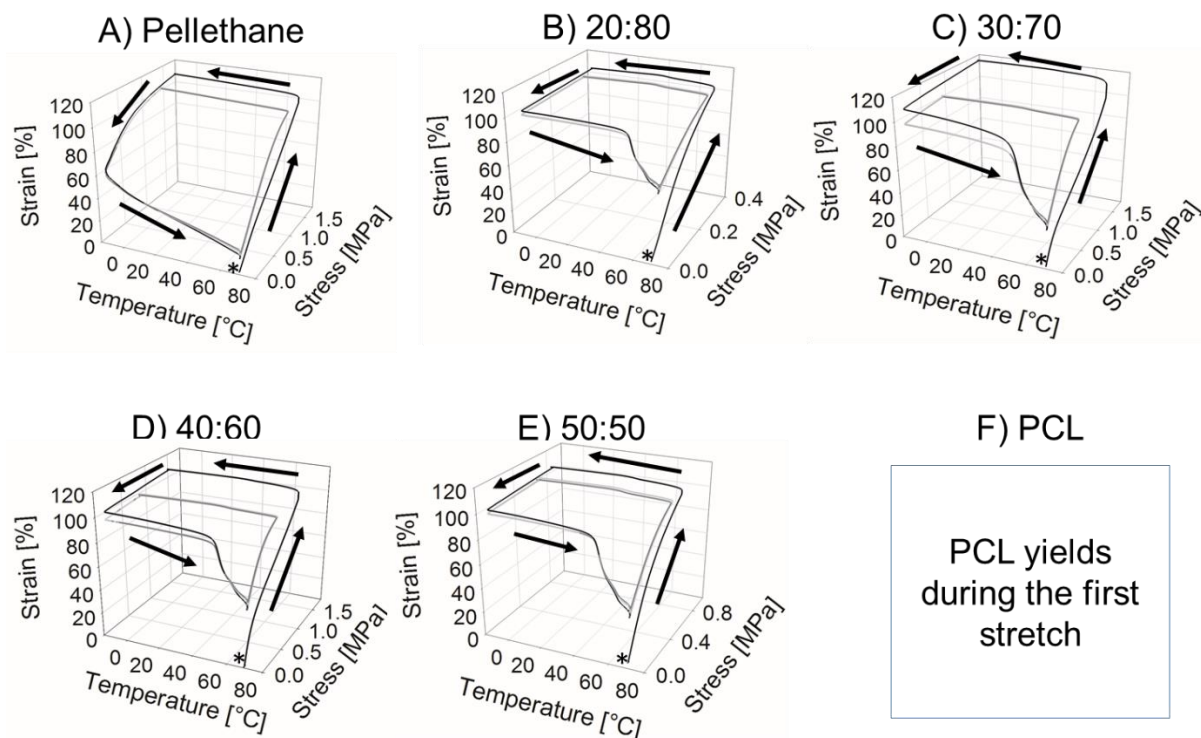


**Figure 2-5.** Thermal shape memory cycles. A) Pure Pellethane showed a fixing ratio ( $R_f$ ) of 54% and a recovery ratio ( $R_r$ ) of 87%. B) The 20:80 PCL:Pellethane fiber composite showed an  $R_f$  of 93.5% and an  $R_r$  of 85.1%. C) The 30:70 PCL:Pellethane fiber composite showed an  $R_f$  of 94.45% and an  $R_r$  of 86.3%. D) The 40:60 PCL:Pellethane fiber composite showed an  $R_f$  of 95.2% and an  $R_r$  of 89.8%. E) The 50:50 PCL:Pellethane fiber composite showed an  $R_f$  of 97.5% and an  $R_r$  of 83.2%. F) Pure PCL yielded during the first stretch of the first cycle and is not reported. One shape memory cycle comprises the following steps: starting at the asterisk, the sample is heated to 60 °C, and then the force is ramped to stretch the sample; the sample is then cooled to 0 °C and unloaded; the sample is then heated back to 60 °C to measure recovery. This cycle was completed three times with cycles 1, 2, and 3 shown in black, light gray, and dark gray, respectively.

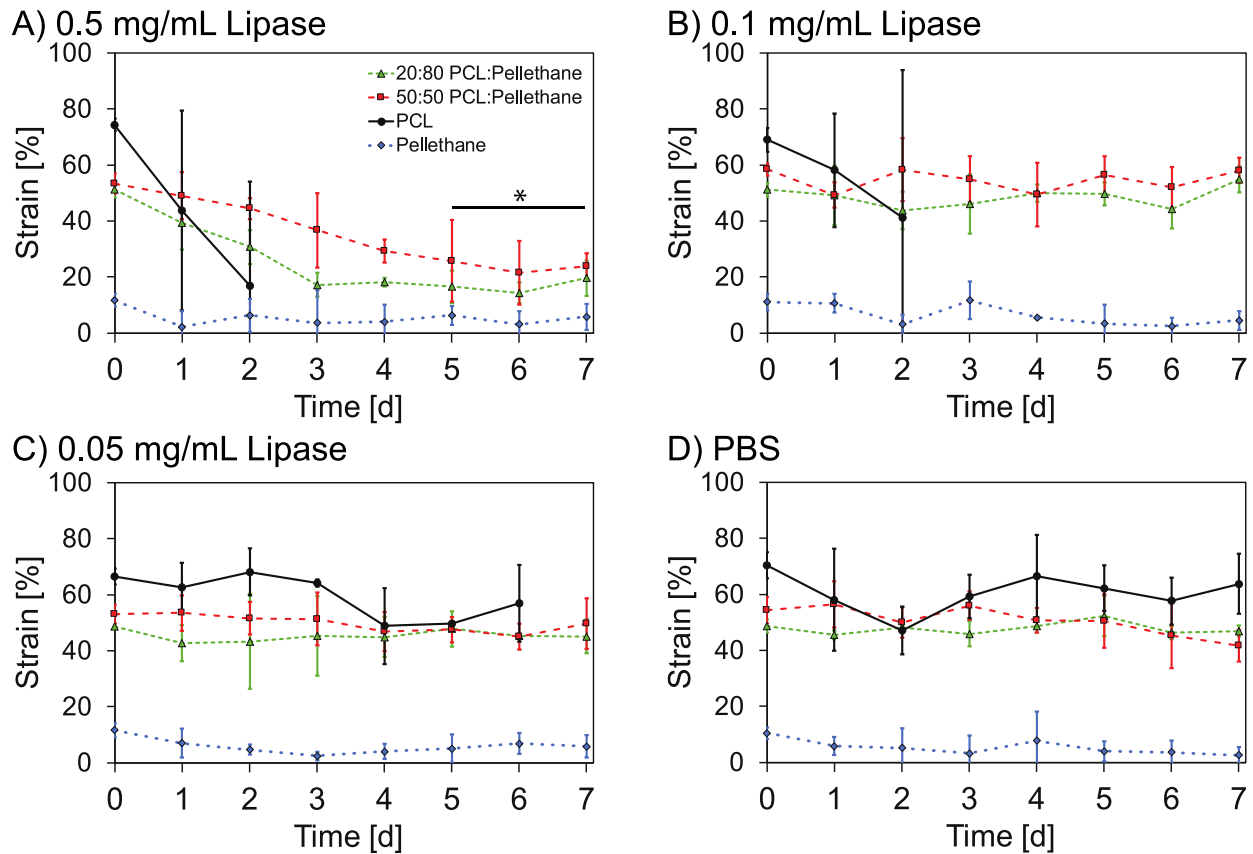


**Figure 2-6.** Enzyme-triggered shape recovery over 7 days. The 0.5 mg/mL condition (A) is the only condition for which fiber composites showed measurable, significant sample recovery. The 0.1 mg/mL (B) and 0.05 mg/mL (C) conditions showed no measurable sample recovery. The PBS control (D) showed no strain changes for any groups, including the PCL control, over the course of the 7-day experiment. For all conditions, the fiber composites (20:80 and 50:50 PCL:Pellethane) showed a significantly different length compared to Pellethane controls, except for days 5-7 in the 0.5 mg/mL condition. \* and bar indicate the three-time points for which the strain of fiber composites was no longer statistically different from that of the Pellethane controls ( $P>0.05$ ), indicating sample recovery. For all groups, the value at day 0 is the mean programmed strain of all 21 samples (3 replicates  $\times$  7-time points), and the value at each subsequent time point is the mean of the 3 samples collected at that time point.

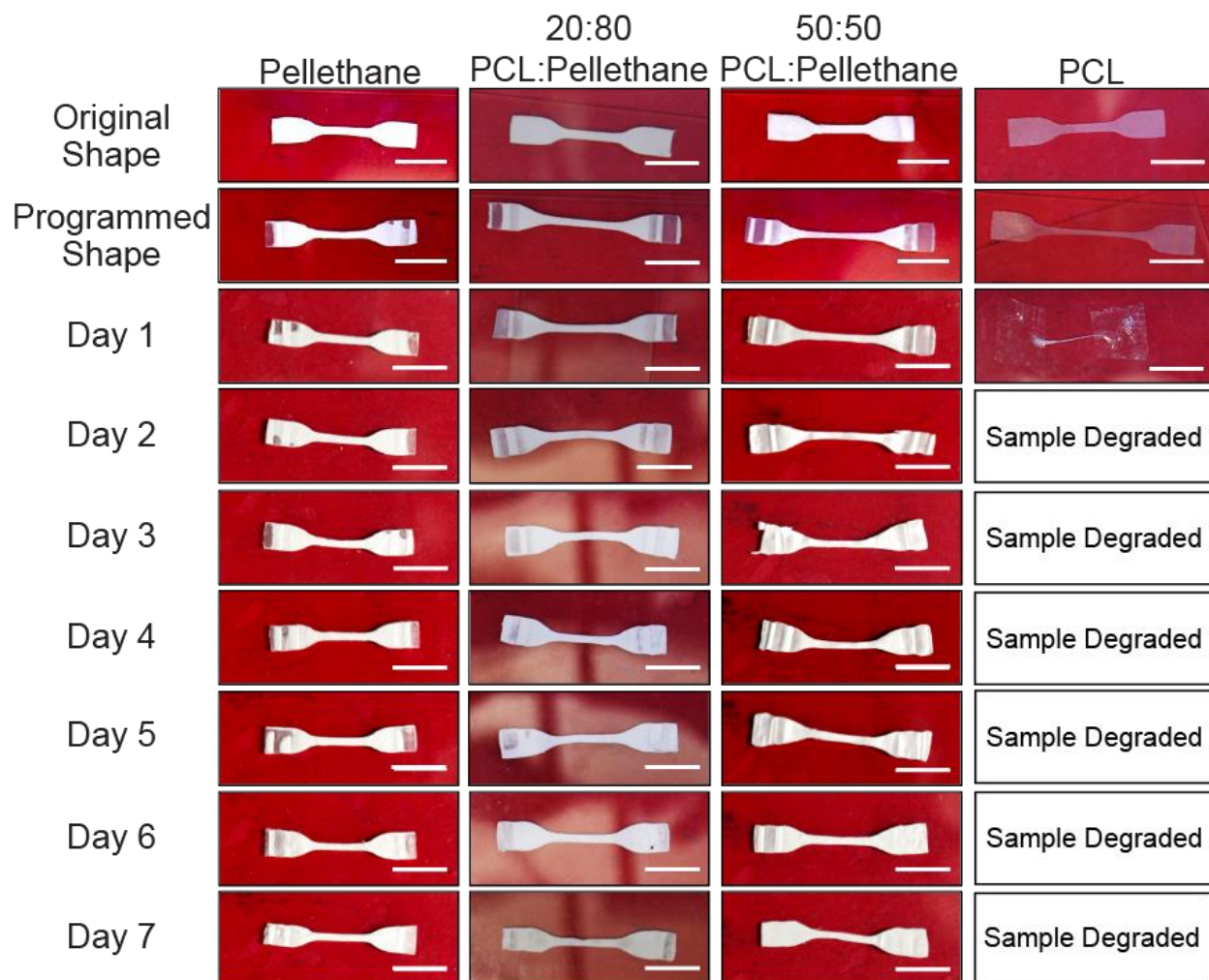


**Figure 2-7.** Macroscopic view of enzymatic recovery. Pictures of samples were taken before and after programming and after being exposed to 0.5 mg/mL lipase solution over the course of 7 days. The Pellethane, 20:80 PCL:Pellethane, 50:50 PCL:Pellethane and PCL are shown in order from left to right. After programming, the Pellethane showed no shape fixing and no measured change in length over the 7-day incubation. In contrast, both fiber composites fixed a temporary shape and then contracted over the course of 7 days. The PCL control fixed a temporary shape and then degraded fully instead of changing shape. The glare in 20:80 samples from days 1 through 7 is due to covering glass used to position the samples during imaging. The scale bar is 10 mm.



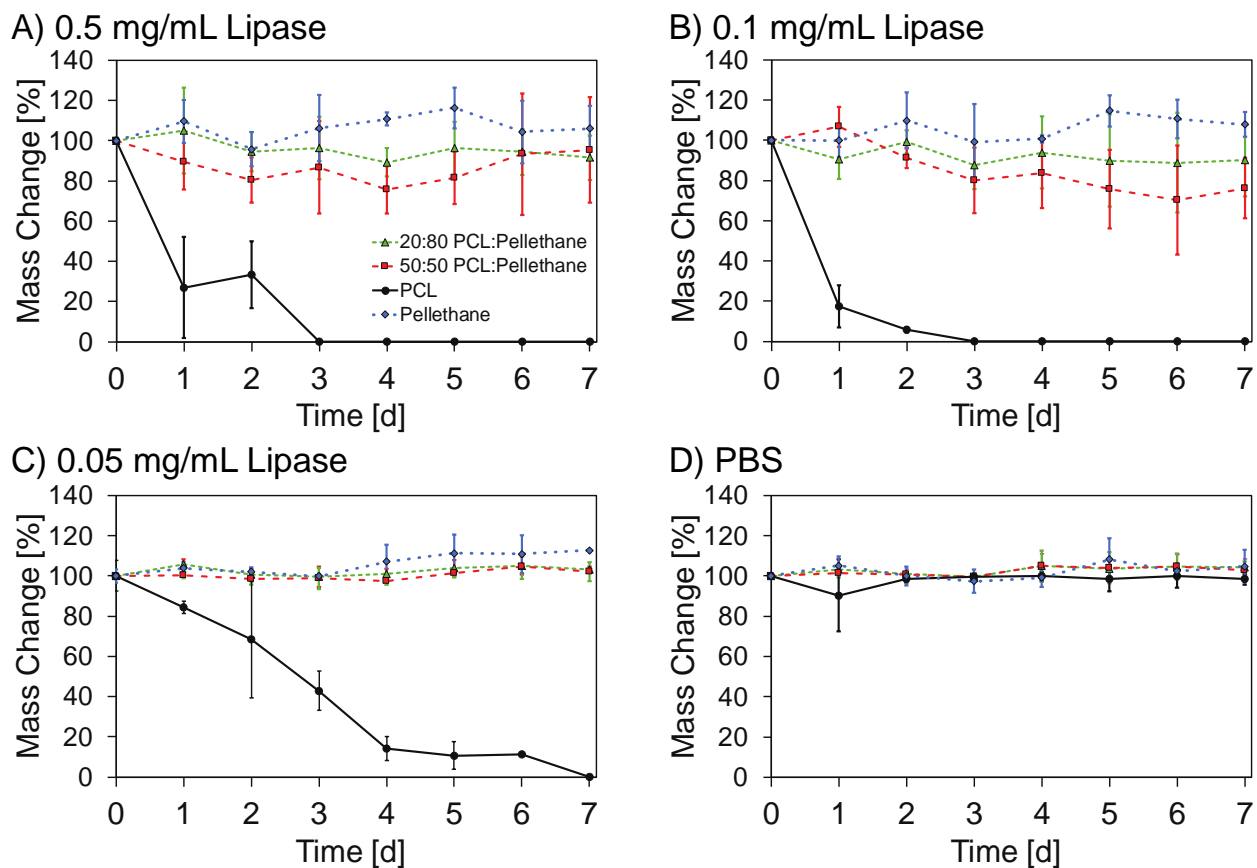


**Figure 2-8.** Mass change during degradation. Significant mass loss was observed for the PCL film in all conditions: (A) 0.5 mg/mL lipase; (B) 0.1 mg/mL lipase; (C) 0.05 mg/mL lipase; and (D) PBS (0 mg/mL lipase)). All other samples exhibited no measurable mass loss.



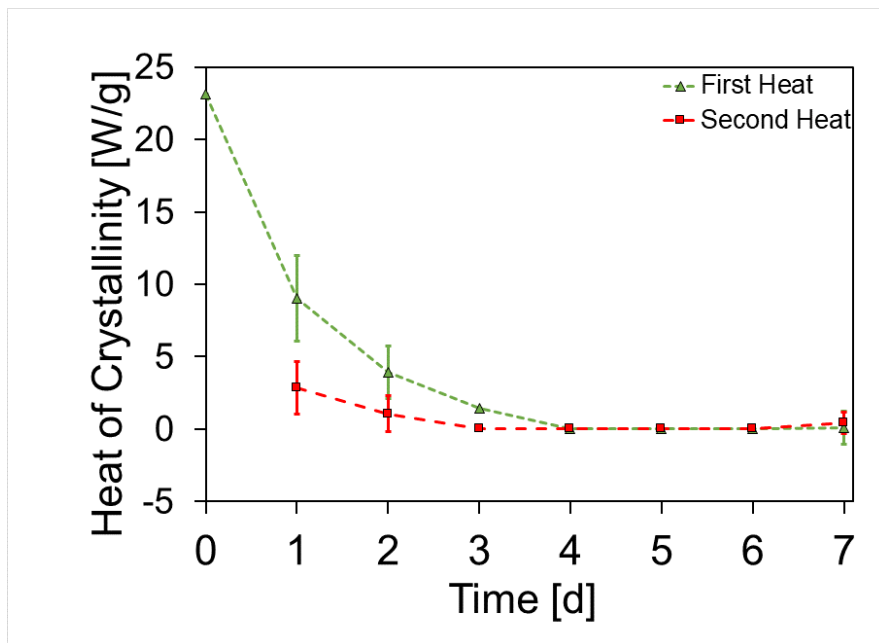


**Figure 2-9.** Heat of crystallinity of hydrated 50:50 PCL:Pellethane fiber composites immediately following exposure to lipase. The heat of crystallinity of the PCL, as measured by differential scanning calorimetry (DSC), decreases over the course of degradation experiments, indicating that the PCL crystal structure is being broken up. The data also suggest that the water present in the sample interferes with the re-crystallization of PCL, resulting in the crystallization being lower for the second heat compared to the first heat.

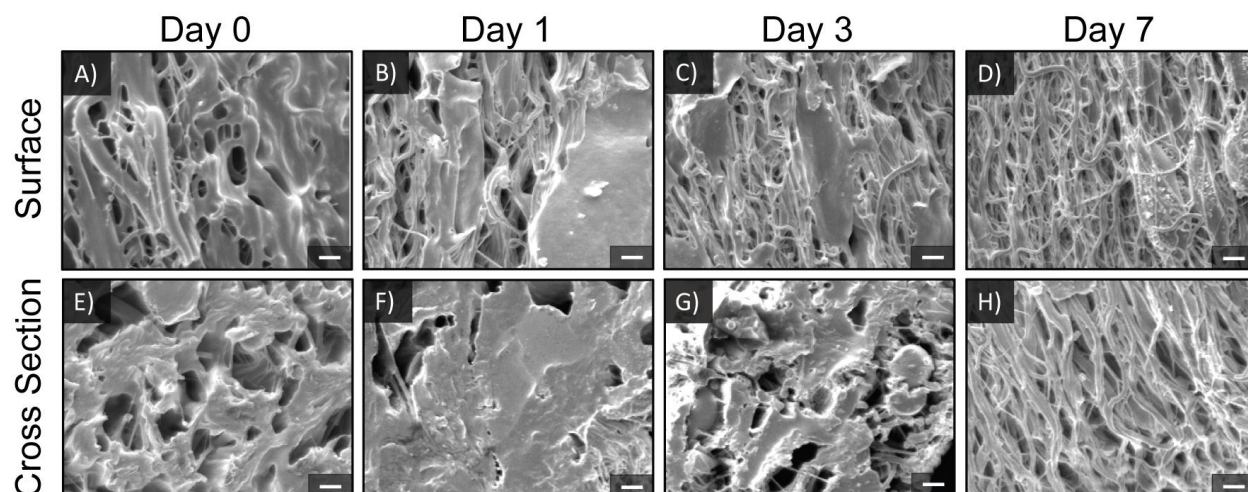


**Figure 2-10.** SEM micrographs of 50:50 PCL:Pellethane incubated in 0.5 mg/mL of lipase.

Morphological analysis shows changes in sample morphology indicative of PCL degradation (A-D) at the surface and (E-H) in cross-section of 50:50 PCL:Pellethane fiber composites for day 0, 1, 3, 7, respectively. Day 0 shows the 50:50 fiber composite after heat treatment but before any strain programming or enzymatic recovery. Scale bar is 10  $\mu\text{m}$ . Results for both fiber composites (20:80 and 50:50 PCL:Pellethane) and for the PCL controls under all incubation conditions (0.5 mg/mL, 0.1 mg/mL, and 0.05 mg/mL lipase and PBS) are available in Figs. S6 through S9).

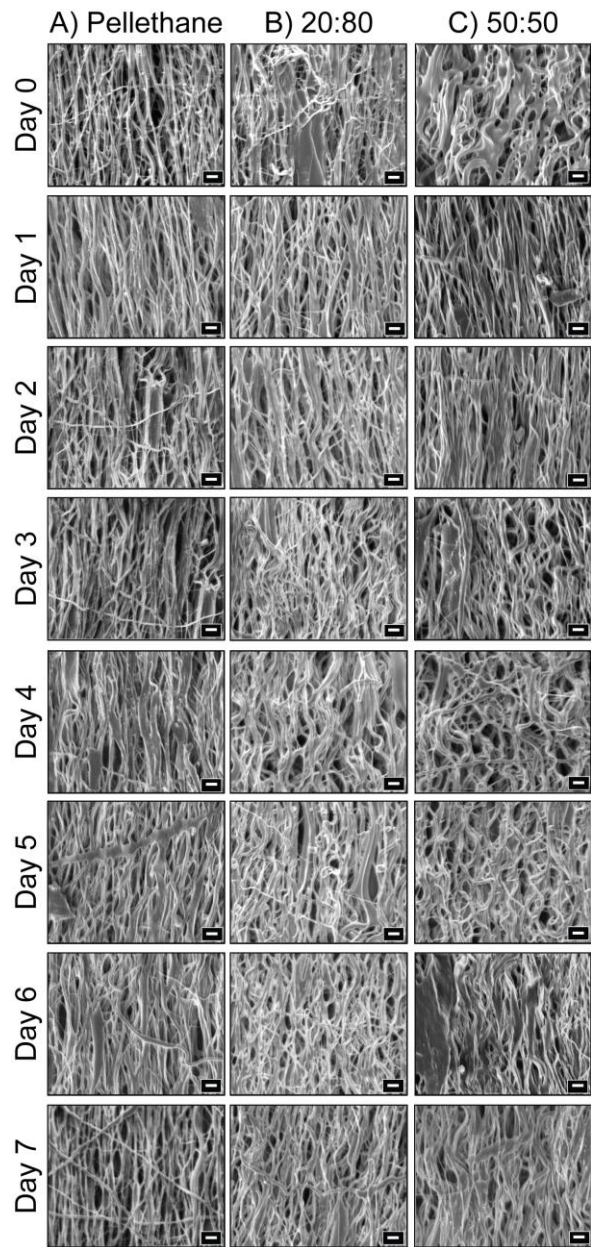


**Figure 2-11.** SEM images of Pellethane and fiber composites as samples are incubated in a solution with 0.5 mg/mL of Lipase. Fiber composites go from a fiber-film morphology to a pure fiber morphology over the course of experiments. Pellethane, 20:80 PCL:Pellethane, 50:50 PCL:Pellethane are shown in row A, B, and C, respectively. Scale bar is 10  $\mu$ m.

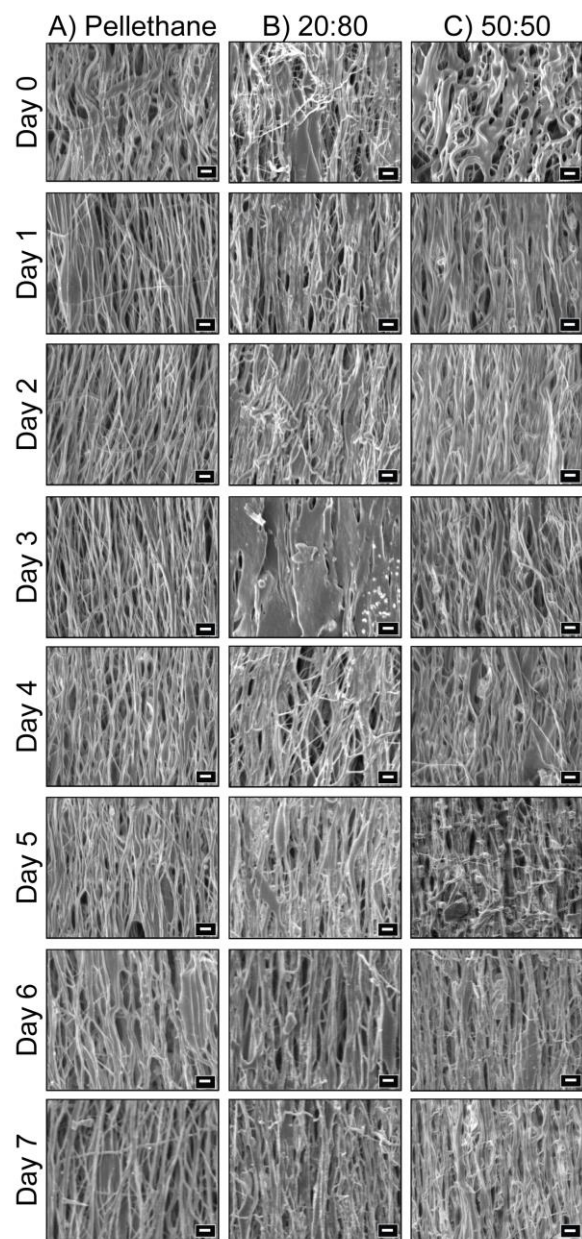


**Figure 2-12.** SEM images of Pellethane and fiber composites as samples are incubated in a solution with 0.1 mg/mL of Lipase. Fiber composites go from a fiber-film morphology to a pure fiber morphology over the course of experiments. Pellethane, 20:80 PCL:Pellethane, 50:50 PCL:Pellethane are shown in row A, B, and C, respectively. Scale bar is 10  $\mu$ m.



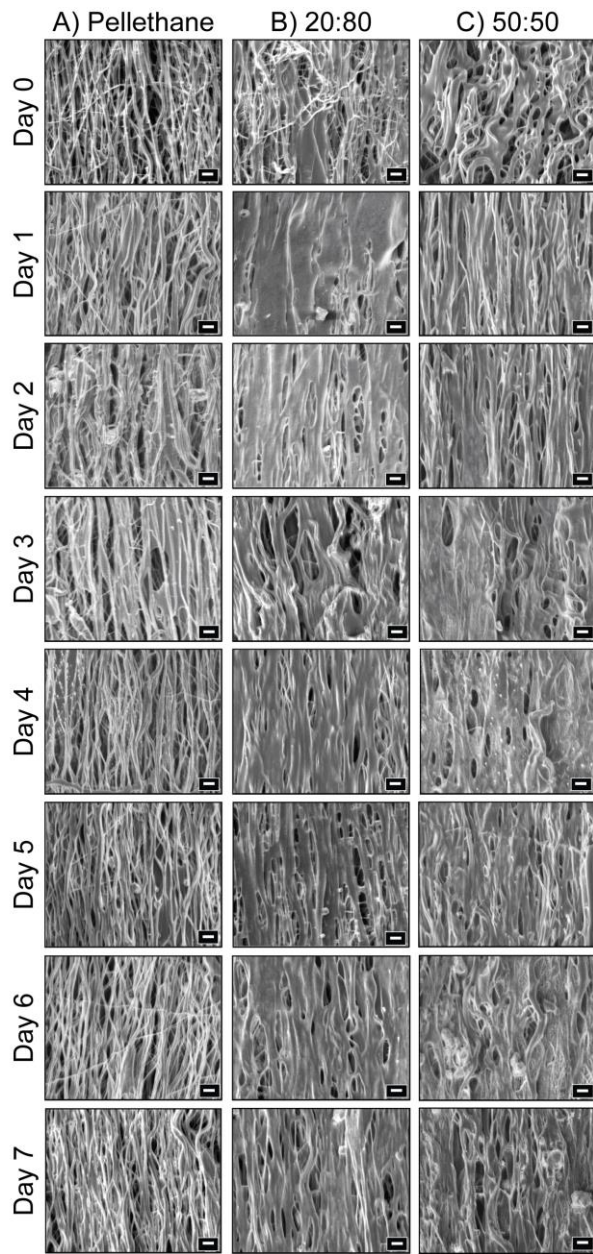


**Figure 2-13.** SEM images of Pellethane and fiber composites as samples are incubated in a solution with 0.05 mg/mL of Lipase. Fiber composites go from a fiber-film morphology to a pure fiber morphology over the course of experiments. Pellethane, 20:80 PCL:Pellethane, 50:50 PCL:Pellethane are shown in row A, B, and C, respectively. Scale bar is 10  $\mu$ m.

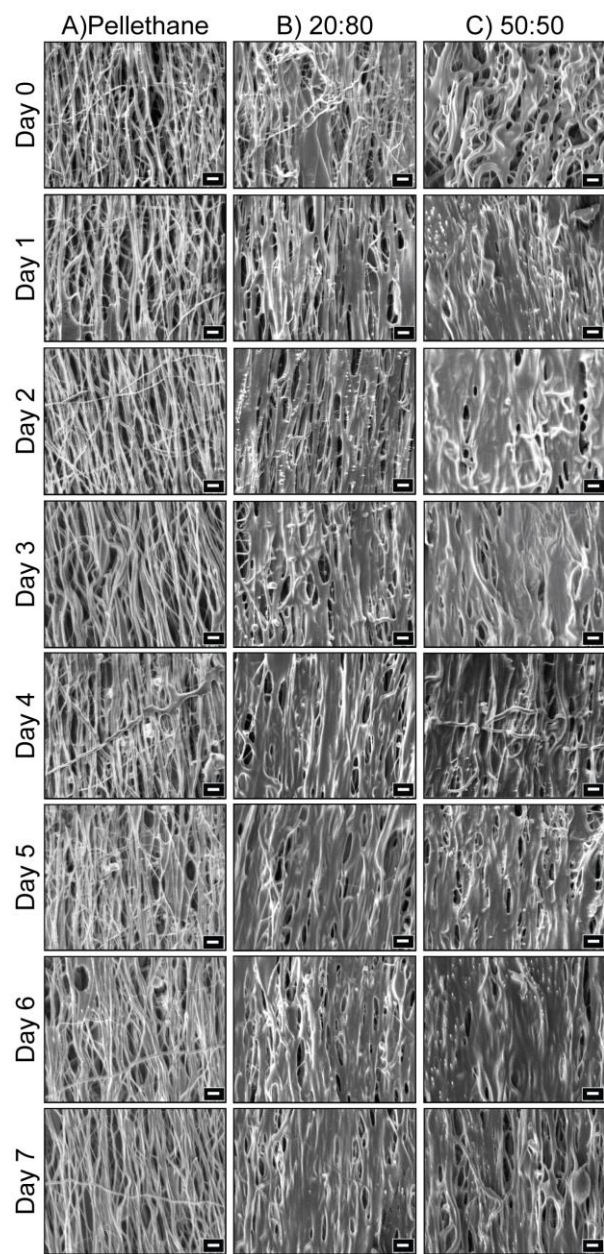


**Figure 2-14.** SEM images of Pellethane and fiber composites as exposed to PBS over a course of 7 days. Samples showed no changes in sample morphology. Pellethane, 20:80 PCL:Pellethane, 50:50 PCL:Pellethane are shown in row A, B, and C, respectively. Scale bar is 10  $\mu\text{m}$ .

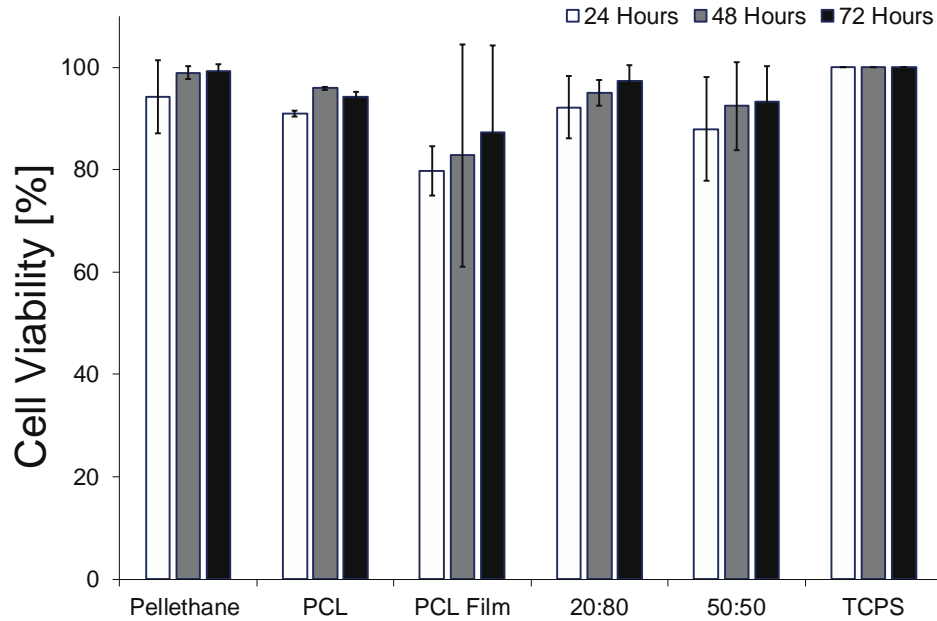


**Figure 2-15.** Cell viability of C3H/10T1/2 cells cultured directly on fiber composite and non-composite control samples in the absence of lipase. No significant differences were found between any groups ( $P>0.05$ ), and viability was  $>75\%$  for all groups. Groups are Pellethane control, PCL control, compressed PCL Film control, 20:80 PCL:Pellethane fiber composite, 50:50 PCL:Pellethane fiber composite, and tissue culture polystyrene control.

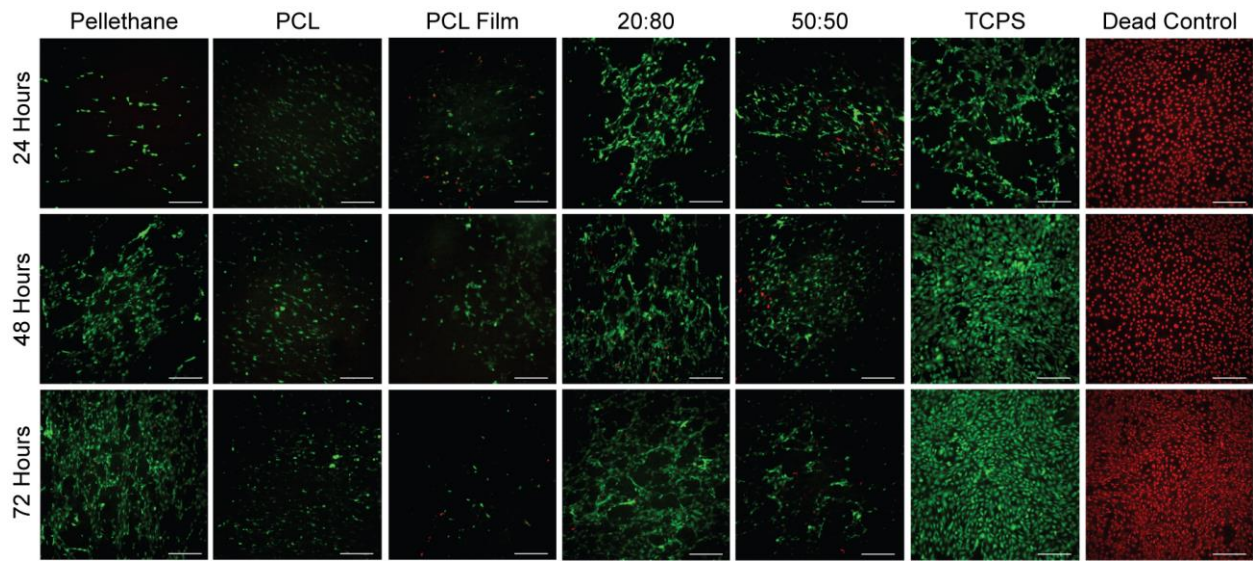


**Figure 2-16.** Representative micrographs of C3H/10T1/2 cells cultured directly on fiber composite and non-composite control samples in the absence of lipase. Live cells are shown in green and dead cells are shown in red. Groups are Pellethane control, PCL control, compressed PCL Film control, 20:80 PCL:Pellethane fiber composite, 50:50 PCL:Pellethane fiber composite, and tissue culture polystyrene control. The scale bar is 100  $\mu\text{m}$ .



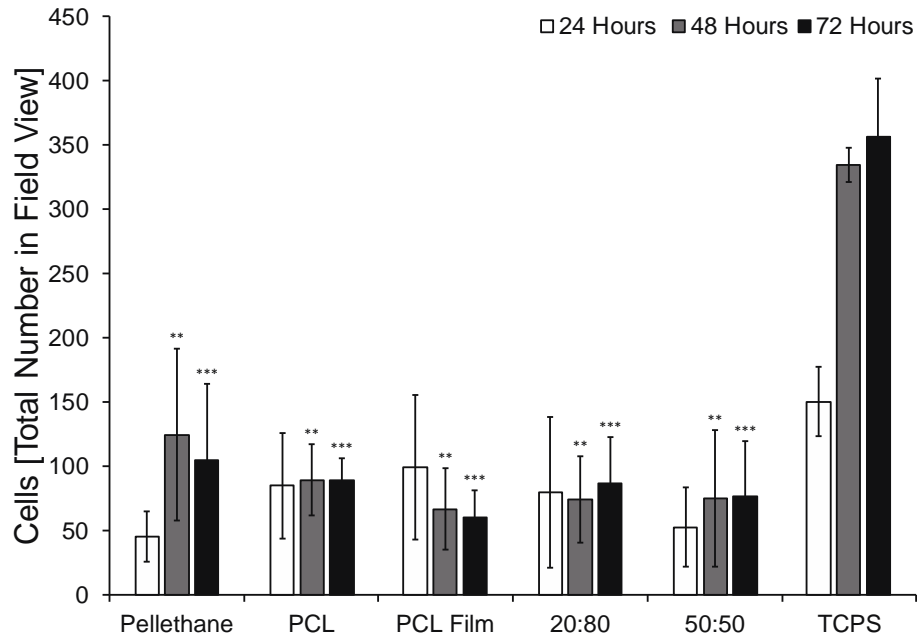


**Figure 2-17.** Cell numbers of C3H/10T1/2 cells cultured directly on fiber composite and non-composite control samples in the absence of lipase. Groups are Pellethane control, PCL control, compressed PCL Film control, 20:80 PCL:Pellethane fiber composite, 50:50 PCL:Pellethane fiber composite, and tissue culture polystyrene control. \*\* and \*\*\* indicate material groups that are significantly different than TCPS control at 48 and 72 h, respectively.

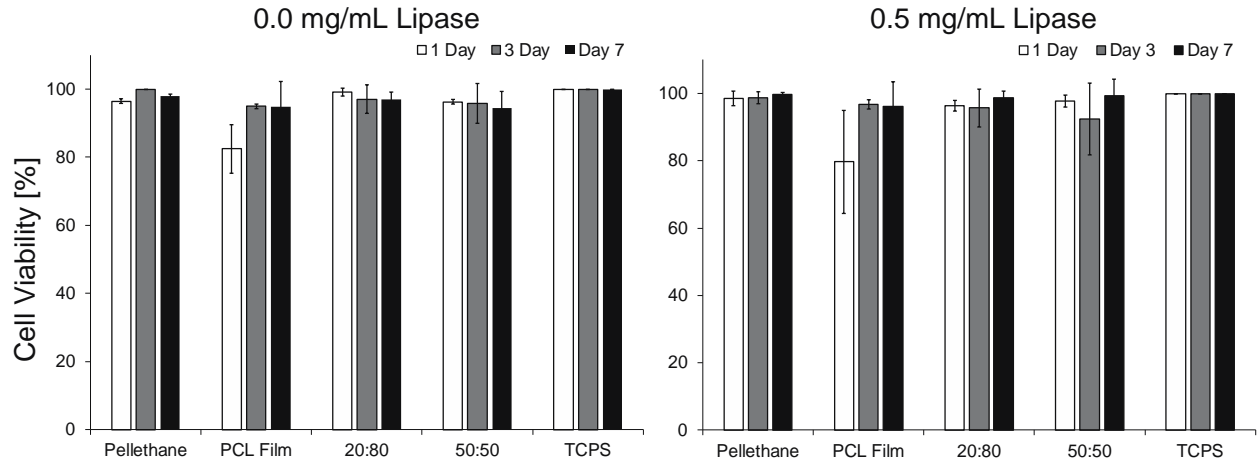


**Figure 2-18.** Cell viability of C3H/10T1/2 cells cultured directly on fiber composite and non-composite control samples in (left) a lipase-free control medium or (right) the presence of 0.5 mg/mL lipase. No significant differences were found between any groups ( $P>0.05$ ), and viability was  $>75\%$  for all groups. Groups are Pellethane control, compressed PCL Film control, 20:80 PCL:Pellethane fiber composite, 50:50 PCL:Pellethane fiber composite, and tissue culture polystyrene control.

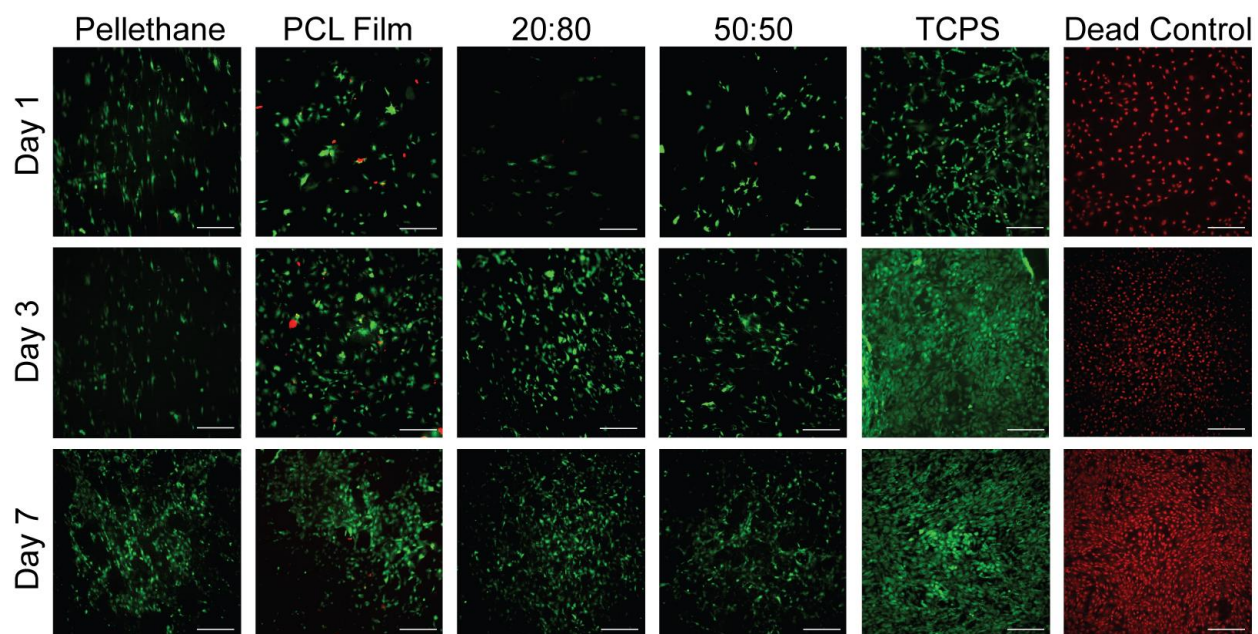


**Figure 2-19.** Representative micrographs of C3HT101/2 cells cultured directly on fiber composite and non-composite control samples in the absence of lipase (control for cells studied in Fig. S13). Live cells are shown in green and dead cells are shown in red. Groups are Pellethane control, PCL control, compressed PCL Film control, 20:80 PCL:Pellethane fiber composite, 50:50 PCL:Pellethane fiber composite, and tissue culture polystyrene control. The scale bar is 100  $\mu\text{m}$ .

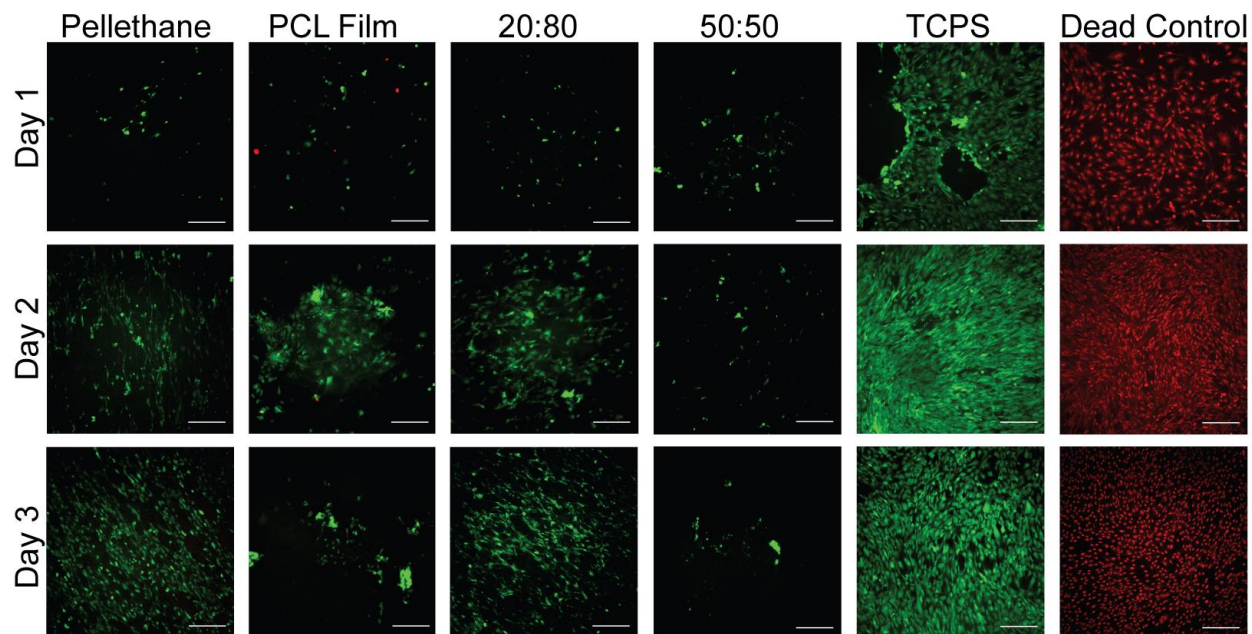


**Figure 2-20.** Representative micrographs of C3H/10T1/2 cells cultured directly on fiber composite and non-composite control samples in the presence of 0.5 mg/mL lipase. Live cells are shown in green and dead cells are shown in red. Groups are Pellethane control, PCL control, compressed PCL Film control, 20:80 PCL:Pellethane fiber composite, 50:50 PCL:Pellethane fiber composite, and tissue culture polystyrene control. The scale bar is 100  $\mu\text{m}$ .

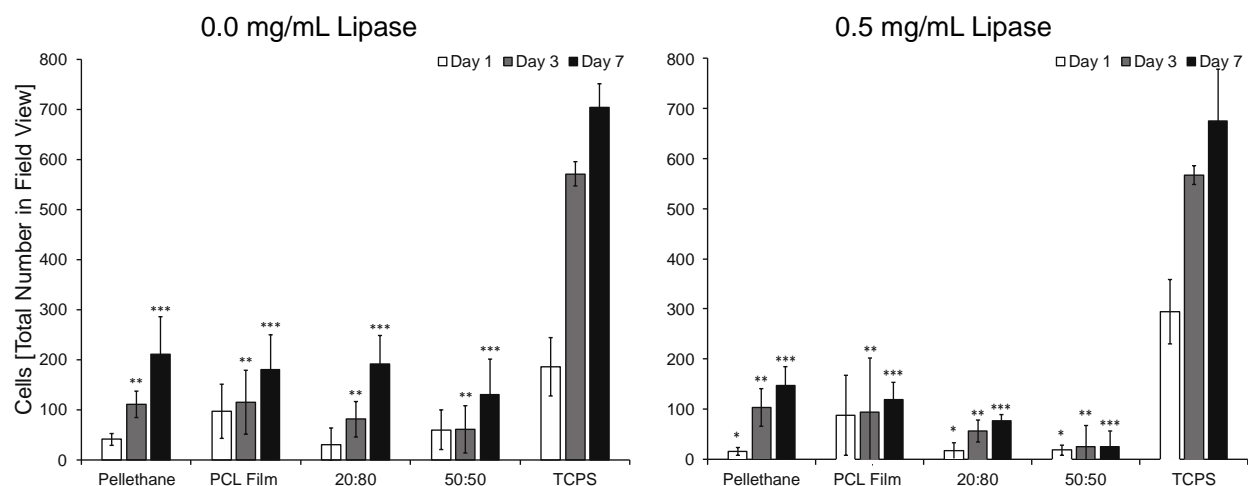


**Figure 2-21.** Cell numbers of C3H/10T1/2 cells cultured directly on fiber composite and non-composite control samples in the (left) absence or (right) presence of lipase. Groups are Pellethane control, compressed PCL Film control, 20:80 PCL:Pellethane fiber composite, 50:50 PCL:Pellethane fiber composite, and tissue culture polystyrene control. \*, \*\*, and \*\*\* indicate material groups that are significantly different than TCPS control at 24, 48, and 72 h, respectively.

## 2.8 References

1. Hager, M. D., Bode, S., Weber, C. & Schubert, U. S. Shape memory polymers: Past, present and future developments. *Prog. Polym. Sci.* **49–50**, 3–33 (2015).
2. Liu, C., Qin, H. & Mather, P. T. Review of progress in shape-memory polymers. *J. Mater. Chem.* **17**, 1543 (2007).
3. Meng, H. & Li, G. A review of stimuli-responsive shape memory polymer composites. *Polym. (United Kingdom)* **54**, 2199–2221 (2013).
4. Lendlein, A. & Kelch, S. Shape-Memory Polymers. *Angew. Chemie Int. Ed.* **41**, 2034 (2002).
5. Luo, X. & Mather, P. T. Conductive shape memory nanocomposites for high speed electrical actuation. doi:10.1039/c001295e
6. Gu, X. & Mather, P. T. Water-triggered shape memory of multiblock thermoplastic polyurethanes (TPUs)<sup>3</sup>. **3**, (2013).
7. Mendez, J. *et al.* Bioinspired mechanically adaptive polymer nanocomposites with water-activated shape-memory effect. *Macromolecules* **44**, 6827–6835 (2011).
8. Lendlein, A., Behl, M., Hiebl, B. & Wischke, C. Shape-memory polymers as a technology platform for biomedical applications. *Expert Rev. Med. Devices* **7**, 357–379 (2010).
9. Neuss, S. *et al.* The use of a shape-memory poly( $\epsilon$ -caprolactone)dimethacrylate network as a tissue engineering scaffold. *Biomaterials* **30**, 1697–1705 (2009).
10. Davis, K. A., Burke, K. A., Mather, P. T. & Henderson, J. H. Dynamic cell behavior on shape memory polymer substrates. *Biomaterials* **32**, 2285–2293 (2011).
11. Davis, K. A., Luo, X., Mather, P. T. & Henderson, J. H. Shape Memory Polymers for Active Cell Culture. *J. Vis. Exp.* e2903–e2903 (2011). doi:10.3791/2903
12. Xu, X. *et al.* Shape Memory RGD-Containing Networks: Synthesis, Characterization, and Application in Cell Culture. *Macromol. Symp.* **309–310**, 162–172 (2011).
13. Le, D. M., Kulangara, K., Adler, A. F., Leong, K. W. & Ashby, V. S. Dynamic Topographical Control of Mesenchymal Stem Cells by Culture on Responsive Poly( $\epsilon$ -caprolactone) Surfaces. *Adv. Mater.* **23**, 3278–3283 (2011).
14. Shou, Q., Uto, K., Lin, W. C., Aoyagi, T. & Ebara, M. Near-infrared-irradiation-induced remote activation of surface shape-memory to direct cell orientations. *Macromol. Chem. Phys.* **215**, 2473–2481 (2014).
15. Yang, P. *et al.* In vitro wrinkle formation via shape memory dynamically aligns adherent cells. *Soft Matter* **9**, 4705 (2013).
16. Tseng, L.-F., Mather, P. T. & Henderson, J. H. Shape-memory-actuated change in scaffold fiber alignment directs stem cell morphology. *Acta Biomater.* **9**, 8790–8801 (2013).
17. Ebara, M. *et al.* Focus on the interlude between topographic transition and cell response

- on shape-memory surfaces. *Polymer (Guildf)*. **55**, 5961–5968 (2014).
18. Mengsteab, P. Y. *et al.* Spatiotemporal control of cardiac anisotropy using dynamic nanotopographic cues. *Biomaterials* **86**, 1–10 (2016).
  19. Ebara, M., Uto, K., Idota, N., Hoffman, J. M. & Aoyagi, T. Shape-Memory Surface with Dynamically Tunable Nano-Geometry Activated by Body Heat. *Adv. Mater.* **24**, 273–278 (2012).
  20. Lee, E. M., Smith, K., Gall, K., Boyan, B. D. & Schwartz, Z. Change in surface roughness by dynamic shape-memory acrylate networks enhances osteoblast differentiation. *Biomaterials* **110**, 34–44 (2016).
  21. Gong, T. *et al.* The Control of Mesenchymal Stem Cell Differentiation Using Dynamically Tunable Surface Microgrooves. *Adv. Healthc. Mater.* **3**, 1608–1619 (2014).
  22. Tseng, L.-F. *et al.* Osteogenic Capacity of Human Adipose-Derived Stem Cells is Preserved Following Triggering of Shape Memory Scaffolds. *Tissue Eng. Part A* **22**, 1026–1035 (2016).
  23. Baker, R. M., Brasch, M. E., Manning, M. L. & Henderson, J. H. Automated, contour-based tracking and analysis of cell behaviour over long time scales in environments of varying complexity and cell density. *J. R. Soc. Interface* **11**, 20140386 (2014).
  24. Wang, J., Quach, A., Brasch, M. E., Turner, C. E. & Henderson, J. H. On-command on/off switching of progenitor cell and cancer cell polarized motility and aligned morphology via a cytocompatible shape memory polymer scaffold. *Biomaterials* **140**, 150–161 (2017).
  25. Wang, J. *et al.* Shape memory activation can affect cell seeding of shape memory polymer scaffolds designed for tissue engineering and regenerative medicine. *J. Mater. Sci. Mater. Med.* **28**, 151 (2017).
  26. Baker, R. M., Tseng, L.-F., Iannolo, M. T., Oest, M. E. & Henderson, J. H. Self-deploying shape memory polymer scaffolds for grafting and stabilizing complex bone defects: A mouse femoral segmental defect study. *Biomaterials* **76**, 388–398 (2016).
  27. Baker, R. M., Henderson, J. H. & Mather, P. T. Shape memory poly( $\epsilon$ -caprolactone)-copoly(ethylene glycol) foams with body temperature triggering and two-way actuation. *J. Mater. Chem. B* **1**, 4916 (2013).
  28. Zhang, B., Filion, T. M., Kutikov, A. B. & Song, J. Facile Stem Cell Delivery to Bone Grafts Enabled by Smart Shape Recovery and Stiffening of Degradable Synthetic Periosteal Membranes. *Adv. Funct. Mater.* **27**, 1604784 (2017).
  29. Rychter, P. *et al.* Scaffolds with shape memory behavior for the treatment of large bone defects. *J. Biomed. Mater. Res. Part A* **103**, 3503–3515 (2015).
  30. Kai, D. *et al.* Elastic poly( $\epsilon$ -caprolactone)-polydimethylsiloxane copolymer fibers with shape memory effect for bone tissue engineering. *Biomed. Mater.* **11**, 15007 (2016).
  31. Zhang, D. *et al.* A bioactive ‘self-fitting’ shape memory polymer scaffold with potential to treat cranio-maxillo facial bone defects. *Acta Biomater.* **10**, 4597–4605 (2014).

32. Xie, R., Hu, J., Guo, X., Ng, F. & Qin, T. Topographical Control of Preosteoblast Culture by Shape Memory Foams. *Adv. Eng. Mater.* **19**, 1–10 (2017).
33. Liu, X. *et al.* Delivery of Growth Factors Using a Smart Porous Nanocomposite Scaffold to Repair a Mandibular Bone Defect. *Biomacromolecules* **15**, 1019–1030 (2014).
34. Almeida, H. V. *et al.* Anisotropic Shape-Memory Alginate Scaffolds Functionalized with Either Type I or Type II Collagen for Cartilage Tissue Engineering. *Tissue Eng. Part A* **23**, 55–68 (2017).
35. Kai, D. *et al.* Biocompatible electrically conductive nanofibers from inorganic-organic shape memory polymers. *Colloids Surfaces B Biointerfaces* **148**, 557–565 (2016).
36. Gu, H., Lee, S. W., Buffington, S. L., Henderson, J. H. & Ren, D. On-Demand Removal of Bacterial Biofilms via Shape Memory Activation. *ACS Appl. Mater. Interfaces* **8**, 21140–21144 (2016).
37. Mart, R. J., Osborne, R. D., Stevens, M. M. & Ulijn, R. V. Peptide-based stimuli-responsive biomaterials. *Soft Matter* **2**, 822 (2006).
38. Phillips, D. J., Wilde, M., Greco, F. & Gibson, M. I. Enzymatically Triggered, Isothermally Responsive Polymers: Reprogramming Poly(oligoethylene glycols) To Respond to Phosphatase. *Biomacromolecules* **16**, 3256–3264 (2015).
39. Wang, Y., Byrne, J. D., Napier, M. E. & DeSimone, J. M. Engineering nanomedicines using stimuli-responsive biomaterials. *Adv. Drug Deliv. Rev.* **64**, 1021–1030 (2012).
40. Robertson, J. M., Birjandi Nejad, H. & Mather, P. T. Dual-Spun Shape Memory Elastomeric Composites. *ACS Macro Lett.* **4**, 436–440 (2015).
41. Tseng, L.-F., Mather, P. T. & Henderson, J. H. Shape-memory-actuated change in scaffold fiber alignment directs stem cell morphology. *Acta Biomater.* **9**, 8790–8801 (2013).
42. Birjandi Nejad, H., Robertson, J. M. & Mather, P. T. Interwoven polymer composites via dual-electrospinning with shape memory and self-healing properties. *MRS Commun.* **5**, 211–221 (2015).
43. Luo, X. & Mather, P. T. Design strategies for shape memory polymers. *Curr. Opin. Chem. Eng.* **2**, 102–110 (2013).
44. Burke, K. A. & Mather, P. T. Evolution of microstructure during shape memory cycling of a main-chain liquid crystalline elastomer. *Polymer (Guildf).* **54**, 2808–2820 (2013).
45. Mark A. Rice, †, Johannah Sanchez-Adams, † and Kristi S. Anseth\*, †,‡. Exogenously Triggered, Enzymatic Degradation of Photopolymerized Hydrogels with Polycaprolactone Subunits: Experimental Observation and Modeling of Mass Loss Behavior. (2006). doi:10.1021/BM060086+
46. Busch, S. J., Martin, G. A., Barnhart, R. L. & Jackson, R. L. THE JOURNAL OF BIOLOGICAL CHEMISTRY Heparin Induces the Expression of Hepatic Triglyceride Lipase in a Human Hepatoma (HepG2) Cell Line\*. **264**, 9527–9532 (1989).
47. Busch, S. J., Barnhart, R. L., Martin, G. A., Flanagan, M. A. & Jackson, R. L. Differential



- regulation of hepatic triglyceride lipase and 3-hydroxy-3-methylglutaryl-CoA reductase gene expression in a human hepatoma cell line, HepG2. *J Biol Chem* **265**, 22474–22479 (1990).
48. Mart, R. J., Osborne, R. D., Stevens, M. M. & Ulijn, R. V. Peptide-based stimuli-responsive biomaterials. *Soft Matter* **2**, 822–835 (2006).
  49. Zelzer, M. *et al.* Phosphatase responsive peptide surfaces. *J. Mater. Chem.* **22**, 12229 (2012).
  50. Liu, H. Y., Korc, M. & Lin, C. C. Biomimetic and enzyme-responsive dynamic hydrogels for studying cell-matrix interactions in pancreatic ductal adenocarcinoma. *Biomaterials* **160**, 24–36 (2018).
  51. Roy, D., Cambre, J. N. & Sumerlin, B. S. Future perspectives and recent advances in stimuli-responsive materials. *Prog. Polym. Sci.* **35**, 278–301 (2010).

# Chapter 3: Light-Triggered Shape Memory Polymers

## 3.1 Synopsis

Herein, we discuss the design of visible-light triggered shape memory polymers (SMPs), or polymers that trigger a shape change upon exposure to visible light. To accomplish this, we modified our previously developed *tert*-butyl acrylate system by increasing the cross-linker concentration. This modification increased the glass transition of the SMP, making it stable (no longer triggered to recover) at 37 °C. Instead, methacrylated graphene oxide was incorporated into the SMP films, allowing the materials to recover in response to visible light exposure. Additionally, we were able to show that visible-light triggered SMPs are capable of localized recovery, an ability not previously demonstrated in our thermally triggered SMPs.

## 3.2 Introduction

Development of shape memory polymers possessing cytocompatible shape memory triggering mechanisms has led to increased application of these “smart” materials in both basic and translational research. However, these SMP platforms have all been thermally triggered, which requires culture at 30 °C and then increasing the temperature to 37 °C. This limits the applications of these material platforms in both biomaterial applications and as *in vitro* experimental models to probe cell behavior. As such, work has been done to design SMPs that respond to other stimuli, such as exposure to light. For instance, Maitland *et. al.* designed an SMP foam that expands in response to a high powered near-infrared laser for aneurysm treatment.<sup>1</sup> Since then, many SMP platforms that are light-sensitive have been developed. Lendlein *et. al.* made a light-triggered SMP using cinnamic groups that could be deformed and fixed into a temporary shape using UV light.<sup>2</sup> Upon later exposure to light, the material

recovered. A popular method for imparting light sensitivity to a material is by incorporating metal particles<sup>3</sup> or dyes<sup>4</sup> that show a photoexcitation. This photoexcitation results in the production of thermal energy<sup>5</sup> that can then be transferred to the SMP, heating the material and thus inducing shape recovery. Photo-thermal triggered SMPs have been designed using silver nanoparticles, gold nanoparticles<sup>6,7</sup> and graphene oxide.<sup>8-10</sup> Recently, Ebara and colleagues were able to design an SMP that responds to near-infrared light (NIR) light using gold nanoparticles and successfully demonstrated SMP triggering in the presence of cells.<sup>11</sup> Due to the ease of controlling the area of light exposure, they were also able to show localized recovery of the SMP and demonstrate that cells changed their alignment along the border of that recovery.

While NIR light has the advantage of being able to penetrate biological tissue, it also has a high capacity to transmit heat to the surrounding tissue. While this may not be a concern in some biomedical applications, as a cell mechanobiological platform, however, heat transfer to culture cells is a potential problem. As such, the goal of this work was to design an SMP platform that triggers its shape recovery in response to visible or white light. Herein we describe modifying our previously used SMP bilayer system<sup>12</sup> by adjusting the monomer composition to increase the SMP glass transition ( $T_g$ ), ensuring shape stability while culturing cells at 37 °C. We next methacrylated graphene oxide and sonicated it with the unreacted monomers, thus allowing the graphene oxide to be chemically cross-linked into the backbone. We then assessed the light shape recovery of the SMP as well as characterized local wrinkle formation.

### 3.3 Experimental Section

#### 3.3.1 Materials

*Tert*-butyl acrylate and benzyl acrylate were both purchased from Sigma Aldrich and passed through an SDHR-4 purification column to remove the inhibitor. The initiator Irgacure

184 was provided by BASF Formulation Additives. Graphene oxide was purchased from Sigma Aldrich as an unexfoliated paste and then exfoliated following the manufacturer's procedure. Triethylene glycol dimethacrylate (TEGDMA) was purchased from Sigma Aldrich and used as received. C3H10T1/2 cells were obtained from the American Type Culture Collection (ATCC) and expanded to passage 10-15 for experiments. Basal medium eagle (BME), fetal bovine serum (FBS), GlutaMAX, penicillin/streptomycin, LIVE/DEAD stain, Formaldehyde, Triton X-100, heat-inactivated bovine serum albumin (BSA), DAPI stain and Phalloidin 568 were all purchased from Invitrogen and used as received.

### 3.3.2 Light Triggered Shape Memory Polymer Fabrication

#### 3.3.2.1 Graphene Oxide Methacrylation

Graphene oxide was first exfoliated in water to create a homogenous dispersion following the manufacturer's protocol. Briefly, 25 mL of water was added to 1g of graphene oxide paste and stirred for 16 hr. The mixture was sonicated for 30 min and then centrifuged at 3500 rpm for 10 min to remove any large, unexfoliated particles. The supernatant was subsequently decanted to yield a 2mg/mL solution of graphene oxide in water. The graphene oxide solution was dried and resuspended in ethanol at a concentration of 1 mg/mL graphene oxide. Following methods established by Cha *et al.*, we slowly added 50  $\mu$ L of 3-(trimethyloxysilyl)propyl methacrylate per mg of graphene oxide to the suspension under continuous stirring and sonicated the solution for 60 min.<sup>13</sup> The mixture was continuously stirred for 12 h at 50 °C. The resulting methacrylated graphene was then dialyzed against aqueous ethanol to remove any unreacted product and vacuum dried to obtain the methacrylated graphene.

### 3.3.2.2 SMP Film Fabrication

A copolymerization technique was employed to synthesize substrates with a tunable glass transition temperature ( $T_g$ ). Two monomers, *tert*-butyl acrylate (tBA) and benzyl acrylate (BenA) were mixed with a cross-linker (TEGDMA) and a photoinitiator Irgacure 184 and injected between two glass slides with a 1 mm Teflon™ spacer. Glass slides were treated with Rain-X™ to prevent adhesion with the cured SMP films. After injection, the mold was then placed in a UV box (Black Ray, 365 nm, 2.0 mW/cm<sup>2</sup>) featuring symmetric illumination from both sides of each specimen and allowed to cure for 1 h. To determine the effect of monomer and graphene oxide composition on the  $T_g$  of the SMP film, the composition was varied. Briefly, monomer compositions tested were 100tBA-0BenA (100 wt% tBA, 0wt% BenA), 50tBA-50BenA, 20tBA-80BenA, 0tBA-100BenA and the cross-linking weight percent tested were 1, 5, 10 wt% TEGDMA. The m-GO concentrations tested were 0.5, 1 and 2.5 wt%. A constant initiator concentration of 0.1 wt% Irgacure-184 was used. By varying the  $T_g$  of the SMP film, we aimed to ensure the temporary shape was held during cell culture experiments as we have had trouble with the tBA platform pre-recovering during active cell culture experiments.

### 3.3.3 Thermal Characterization

Differential scanning calorimetry (DSC; TA Instruments Q200) was performed on all samples using a DSC equipped with a refrigerated cooling system to record thermal transitions. For each test, samples weighing 3-5 mg were loaded into a DSC consumables pan and equilibrated by heating to 100 °C. Samples were cooled at 10 °C/min to -20 °C and held isothermally for 1 min to remove any thermal history. Samples were then heated at 10 °C/min to 100 °C to measure the glass transition ( $T_g$ ). The  $T_g$  of each sample was measured using

Universal Analysis Software (TA Instruments) to calculate the inflection point of the step transition in heat flow from the heat tracing.

### 3.3.4 Shape Memory Analysis

#### 3.3.4.1 Thermal Shape Memory Analysis

Thermal (not light) shape memory cycles were performed on a dynamic mechanical analysis (DMA) (TA Instruments Q800) operated in controlled-force mode to quantify the shape memory ability of the SMP films. Briefly, each sample was first heated to 100 °C and loaded at 0.05 N/min until 20% strain was reached. Samples were next cooled at 2 °C/min to 0 °C and the load released at 0.1 N/min. To complete the cycle, samples were then heated at 2 °C/min and the shape recovery recorded. This full cycle was repeated three times. The fixing ( $R_f$ ) and recovery ( $R_r$ ) ratios for each recovery event were calculated using Eqns. 3-1 and 3-2, where shape “ $x$ ” refers to the shape or deformation being programmed into the sample in the current cycle and shape “ $y$ ” is the shape or deformation after the previous cycle.<sup>14</sup>

$$R_f(x) = \frac{\varepsilon_x}{\varepsilon_{x, load}} \quad (3-1)$$

$$R_r(x \rightarrow y) = \frac{\varepsilon_x - \varepsilon_{y, rec}}{\varepsilon_x - \varepsilon_y}. \quad (3-2)$$

In Eqn. (3-1),  $\varepsilon_x$  and  $\varepsilon_{x, load}$  are, respectively, the strains measured after cooling and unloading (thus, the strain fixed) and before unloading (or the attempted programmed strain).  $\varepsilon_{y, rec}$  is the strain achieved after recovery for shape  $y$ , and  $\varepsilon_y$  is the strain before programming shape  $y$ .

#### 3.3.4.2 Light Triggered Shape Memory Analysis

Light-triggered shape memory behavior was also characterized using the DMA Q800. First, the sample was loaded into the DMA and heated to 100 °C, above the  $T_g$  of the polymer. The sample was stretched at a rate of 0.08 N/min until a strain of 20% was reached. The sample was then cooled to 0 °C at a rate of 3 °C/min, held isothermally for 5 minutes and the force unloaded at a rate of 0.1 N/min. At this point, the furnace was opened and the DMA was programmed to isothermally hold the temperature for 30 min. Since the oven was open, this would prevent the temperature controller from activating and allow the DMA to record data as it normally does while the sample was exposed to light. The sample was exposed to 0.3 W/cm<sup>2</sup> by a light source (Fiber-Lite® DC-950) directed by a light tube (kindly provided by the Hosein Lab at Syracuse University). The light tube prevented any of the heat caused by the light generation from reaching the sample, thus ensuring that any sample recovery was due to light exposure. The sample strain was recorded over a period of 30 min to measure light-triggered recovery. The  $R_f$  and  $R_r$  were calculated using Eqn 3-1 and 3-2, respectively.

#### 3.3.5 Localized Light-Based Triggering of Shape Recovery

Localized light-based recovery was characterized using the same bilayer approach developed by Yang *et al.* that caused wrinkles to form along the surface of SMPs as materials recovered.<sup>12</sup> Briefly, samples were programmed to 10% strain and sputter-coated with gold 10x for 10 s. This strain level has previously been used to induce wrinkle formation along the surface of SMPs and was hence used again for this study. Sample strips were then sectioned into 5 mm x 5 mm pieces. Three samples were thermally recovered to show the wrinkle formation due to temperature, and three samples were then triggered to recover by light. The wrinkle patterns were imaged using the Hirox microscope and the atomic force microscope (AFM). Next, sample

strips were sectioned into 5 mm x 10 mm pieces. One side of the material was then exposed to the white light source and the sides and the interface were imaged using the Hirox microscope.

### 3.3.6 Cell Culture

#### 3.3.6.1 Cell Culture Methods

All cell experiments were performed with the C3H/10T1/2 mouse embryonic fibroblast line, a cell line we have frequently used in the development and application of cytocompatible SMPs.<sup>15-17</sup> Cells were obtained from the ATCC at passage 8 and expanded to passage number 12-15 to use for experiments, following the recommendations of the ATCC. Cells were cultured in basal medium Eagle with 10% fetal bovine serum, 1% GlutaMAX, and 1% penicillin/streptomycin and passaged once 70-80% confluence was reached. Cells were passaged by first rinsing the flask with PBS and incubating in a solution of 0.25% Trypsin-EDTA for 10 min. The cell solution was collected and diluted with an equal amount of complete BME. Cells were then spun for 10 min at 200 g to centrifuge out the cells. Cells were resuspended in BME and either seeded on materials or re-plated in a tissue culture flask. For storage, cells were frozen in a solution of complete BME with 5% Dimethyl sulfoxide.

#### 3.3.6.2 Material Cytocompatibility

To assess the material cytocompatibility, cells were directly cultured on programmed, gold-coated samples. Gold-coated tBA-mGO samples were sterilized for 10 h on each side using a UV light. All materials were then soaked in complete medium overnight to allow proteins to adsorb to the surface. C3H10T1/2 cells were seeded onto the materials at 10,000 cells/cm<sup>2</sup>. Cell-seeded materials were washed with PBS and stained with LIVE/DEAD at 24 and 48 h time points with tissue culture polystyrene (TCPS) well plates acting as live controls for counting and analysis. Cell viability was calculated by dividing the total number of cells by the total number



of live cells. Samples were visually checked for signs that wrinkles formed, to ensure that samples did not recover during cell experiments and thus the temporary shape was stable for long cell culture experiments.

### *3.3.6.3 Cell Cytocompatibility to Light-Triggering*

To assess the cytocompatibility of the visible light-triggered recovery we first seeded C3H10T1/2 cells on programmed material substrates. The cells were allowed to attach for 24 hrs. At this point, the white light source was shined on the sample for either 30 s, 1 min, or 2 min to trigger material recovery and then incubated for another 24 h. The samples were washed with PBS and stained with LIVE/DEAD to assess cell viability and morphology. Cells seeded on TCPS and exposed to the same amount of white light were used as controls.

## 3.4 Results

### 3.4.1 Light Triggered Shape Memory Polymer Fabrication

The SMP films with m-GO incorporated were visually dark (close to brown) in color. In addition, one side of the m-GO SMP films was rough while a second side was smooth. We believe this is caused by the settling of the m-GO during polymerization, leading to a higher content of m-GO on the bottom side of the film. We believe this may be advantageous in cell experiments as the portion of the SMP with m-GO will likely get hotter than the rest of the sample. Thus, this dispersion may provide an additional level of protection to the adhered cells, which would be cultured on the smoother side away from the m-GO.

### 3.4.2 Thermal Characterization

The  $T_g$  of the SMP films was characterized using DSC. First, DSC was used to compare the  $T_g$  of SMP films composed of different monomer ratios and cross-linker concentrations. This

was done to identify the material components that resulted in a high  $T_g$ . The  $T_g$  could then be optimized for both light recovery and active cell culture experiments. In general, the  $T_g$  of SMP films increased with increasing BenA and TEGDMA content (Fig 3-1, Table 3-1) with the 100tBA 1wt% TEGDMA film showing the lowest  $T_g$  at 49.7 °C and the 100BenA 10% TEGDMA showing the highest at 61 °C. However, as the BenA content increased so did the broadness of the  $T_g$ , likely due to the tacticity of the benzyl group in the polymer backbone. As such, only 100tBA, 50tBA-50BenA, and 20tBA-80BenA compositions were selected to test the impacts of graphene oxide content. Due to the higher  $T_g$ , the cross-linker concentration was set to 10 wt% for the remainder of the study. Next, the  $T_g$  dependence on m-GO content was assessed for the selected compositions (Fig 3-2, Table 3-2). No trend in  $T_g$  was observed with increasing m-GO content, however, the  $T_g$  of the tested SMPs was higher than the  $T_g$  of the base materials.

### 3.4.3 Shape Memory Analysis

The shape memory behavior of the SMP films was assessed in a DMA using the methods described above. Both thermal and photo-thermal shape memory behavior was measured and compared.

#### 3.4.3.1 Thermal Shape Memory Analysis

Thermal shape memory cycles demonstrated that the m-GO tBA substrates had a strong shape fixing and recovery (Fig. 3-3). All material compositions tested showed an  $R_f$  of over 98 % and an  $R_r$  of over 96% with small decreases in the recovery ratio with an increase in m-GO content (Table 3-3).

### 3.4.3.2 Light Triggered Shape Memory Analysis

Light-triggered shape memory behavior was also characterized using the DMA. First, the SMP was thermally programmed and the  $R_f$  was calculated. Next, the furnace was opened, and the light source was shined on the SMP for 30 min to capture any recovery event (Fig 3-4). The 0.5 wt% m-GO SMP showed no measurable recovery in response to visible-light exposure. However, the 1 wt% m-GO and 2.5 wt% m-GO both showed good shape recovery with an  $R_r$  of 82.2 and 78.1%, respectively (Table 3-3). These values were smaller compared to the  $R_r$  of the thermal shape memory behavior. A visual demonstration of visible-light triggered shape recovery was performed by first heating a dog bone sample up to 80 °C and then deforming the sample into a temporary “C” shape (Fig 3-5). The SMP was then exposed to white light and the material was photothermally triggered to return back to its original flat shape.

### 3.4.4 Localized Light-Based Triggering of Shape Recovery

Localized light-triggered recovery of SMP films was visually demonstrated using a wrinkling system where programmed SMPs are sputter-coated with gold (Fig 3-6). Wrinkling and localized wrinkling experiments were carried out using 50:50 tBA:BenA and 20:80 tBA:BenA samples containing 2.5wt% m-GO. First, programmed samples were thermally recovered to visually confirm the samples formed the expected wrinkle pattern (Fig 3-7). This was repeated by exposing the samples to light and the resulting AFM images were visually compared. No visual differences in wrinkle pattern formation were noted, however, these patterns do need to be more quantifiable compared in the future. Next, a rectangular strip m-GO SMP film was cut and one half of the material was exposed to light. As expected, we observed a wrinkled side and a flat side with a very tight interface between the two topographies (Fig 3-8).

This successfully demonstrated that the m-GO SMPs were capable of visible-light triggered recovery.

#### 3.4.5 Cell Cytocompatibility to Material Chemistry and to Light-Triggered Shape Recovery

SMP material composition was standardized to 100-tBA 10wt% TEGDMA for all cell culture experiments. Mouse fibroblasts cultured on the surface of m-GO SMP samples showed strong viability to material chemistry for 24 h and 48 h time points except for the 2.5 wt% m-GO sample at 24 h. However, two of these samples floated up during experiments, potentially negatively impacting the viability results. In general, all SMP platforms showed a high cell number (Fig. 3-10).

To assess the cytocompatibility of light-triggered recovery, we first cultured C3H10T1/2 cells directly on programmed and coated SMP films for 24 h. We then exposed the SMP films to either 30 s, 1 min, or 2 min of visible white light to trigger material recovery. Cells were then cultured for an additional 24 h before staining and imaging to allow for any potential changes in cell morphology to occur, although no morphological changes were observed, even for samples that showed shape recovery. The only samples that showed wrinkle formation (and thus shape recovery) were the SMP films containing 1wt% m-GO or 2.5 wt% m-GO and had been exposed to light for either 1 min or 2 min. Shape recovery was not observed for all samples exposed to 30 s of white light and for samples containing only 0.5 wt% m-GO. However, samples exposed to 2 min of white light exposure showed a decreased cell number and viability compared to other experimental groups. This is likely due to the SMP heating up in response to light exposure and exposing the cells to a hyperthermic environment. SMP films exposed to 1 min of light exposure still showed a high viability but demonstrated a decreased cell number compared to samples exposed for 30 s.

### 3.5 Discussion

Here we have introduced and studied a new SMP that responds to visible light to allow for an isothermal shape change during active cell culture experiments. We found that SMPs composed of 100tBA and 10 wt% TEGDMA showed a high  $T_g$  that should offer stable shape fixing during cell culture experiments. In addition, the designed SMPs showed excellent thermally triggered shape memory behavior and showed good photo-thermal shape memory behavior. It is worth noting that the decreased shape recovery of the samples triggered by visible light may be a weakness of the experimental test. The DMA clamps do occlude part of the sample that is stretched making it difficult to expose the entire sample to the same dose of white light.

The SMPs also showed localized recovery in response to visible-light exposure which was assessed and demonstrated using a bilayer wrinkling system. We visually compared wrinkle patterns made using heat and light as a trigger and saw no discernible differences in the formed wrinkle patterns. However, future studies will need to quantify the wrinkle patterns to enable a more quantitative comparison. In addition, localized recovery was observed for samples using the Hirox microscope. However, these samples could not be imaged using the AFM due to the high level of curvature caused by localized wrinkling. This effect will have to be optimized in the future, both to allow for more direct quantitative comparison but also for future cell experiments. Particularly during active cell culture experiments, sample curvature can complicate imaging, potentially causing samples to fall out of focus.

Cultured C3H10T1/2 cells showed strong viability on the SMP films. However, cells cultured on SMPs exposed to 2 min of white light showed a low viability for samples that showed wrinkle formation. This is likely due to the SMP getting too hot for the attached cells

leading to cell death. In addition, even the samples that showed wrinkle formation and good cell viability did not seem to show any cell morphology changes in response to the formation of topography. However, it should be noted that cell morphology is difficult to assess using a LIVE/DEAD stain. It is also possible that even for the samples that showed wrinkle formation, there could have been some damage inflicted on the cells, preventing them from changing morphology as expected. The balance between SMP,  $T_g$ , light exposure, and cell viability will need to be further explored before using this SMP for active cell culture experiments.

### 3.6 Conclusions and Future Work

We have successfully demonstrated a visible-light triggered SMP platform that changes its shape in response to white light. In addition, we successfully demonstrated localized wrinkle formation in response to photo-thermal shape recovery. Both the material and process of light-triggered recovery are cytocompatible at specified concentrations of m-GO and light exposure. We believe SMP cytotoxicity is due to the m-GO efficient absorption of the white light heating the material to a temperature that is no longer cytocompatible, and these parameters will have to be carefully controlled in the future. This new design of visible light-triggered SMPs can be anticipated to enable new isothermal active cell culture experiments to probe cell mechanobiological responses. In particular, localized material recovery will enable experiments focused on how cell behavior transitions as it crosses topographical interfaces and how this behavior compares to cells that are far away from the transition.

### 3.7 Acknowledgements

Funding from the NSF IGERT Program, DGE-1068780, and the NSF BMAT program, DMR-1609523 and REU Supplement DMR-1743080, is gratefully acknowledged, as is use of

the facilities of the Syracuse Biomaterial Institute at Syracuse University. In addition, the student contributions of Jose Waimin and Johnson Agyapong are all gratefully acknowledged.

**Table 3-1.** Measured thermal transitions with varying monomer and cross-linking concentrations. In general, there was an increase in the measured  $T_g$  with increasing BenA and TEGDMA concentration.

Material	1 wt% TEGDMA <sup>[a]</sup>	5 wt% TEGDMA <sup>[a]</sup>	10 wt% TEGDMA <sup>[a]</sup>
tBA	49.7	49.9	50.9
50:50 tBA:BenA	52.6	52.5	58.1
20:80 tBA:BenA	46.2	51.8	51.8
BenA	-	59.4	61.2

[a] Units of °C.



**Table 3-2.** Measured thermal transitions at different monomer and m-GO concentrations at a fixed cross-linking concentration of 10% TEGDMA. Little change in the  $T_g$  of the SMP films was observed with different m-GO content however all compositions tested showed a higher  $T_g$  than the pure SMP materials.

Material	0.5 wt% m-GO <sup>[a]</sup>	1 wt% m-GO <sup>[a]</sup>	2.5 wt% m-GO <sup>[a]</sup>
tBA	57.3	55.5	57.3
50:50 tBA:BenA	57.8	61.5	61.4
20:80 tBA:BenA	56.3	56.6	57.4

[a] Units of °C.

**Table 3-3.** Calculated fixing and recovery ratios for both thermal and light shape memory cycles. Both thermal and light shape memory showed excellent fixing capabilities. However, the light recovery ratio was lower. We believe this is due to some of the light being blocked by the metal clamps of the DMA.

	<b>Thermal Shape Memory</b>		<b>Light Shape Memory</b>	
	R <sub>f</sub>	R <sub>r</sub>	R <sub>f</sub>	R <sub>r</sub>
0.5 wt% m-GO	98.5	99.3	99.3	-1.672
1 wt% m-GO	98.3	97.1	99.1	82.2
2.5 wt% m-GO	98.1	96.0	99.1	78.1

All listed values are in units of percent.

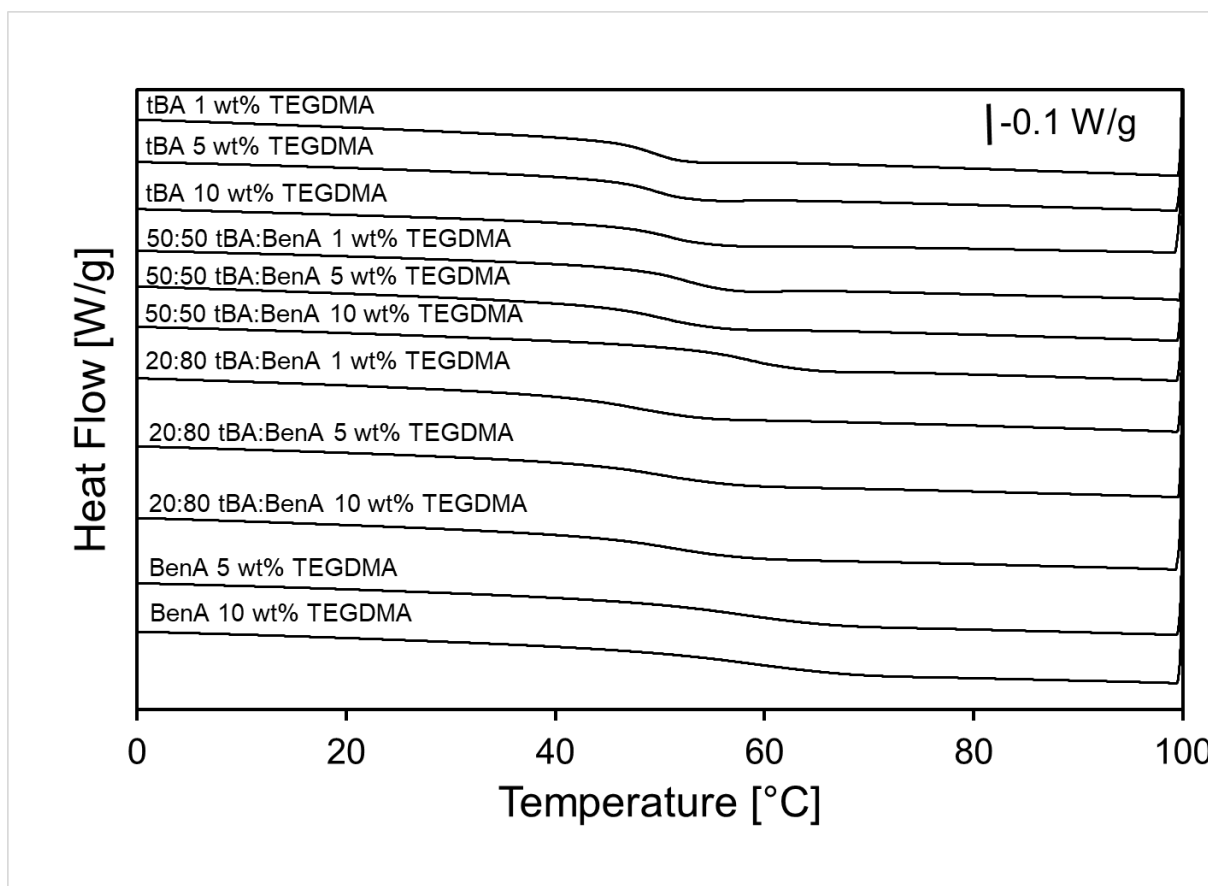


**Figure 3-1.** DSC scans of SMP films of different monomer and cross-linker compositions. In general,  $T_g$  increased from 49.7 °C (100tBA 1wt% TEGDMA) to a maximum of 61 °C (100BenA 10 wt% TEGDMA) with increasing BenA and TEGDMA content. However, the broadness of the  $T_g$  also increased with BenA content which would broaden the recovery event of SMP films.

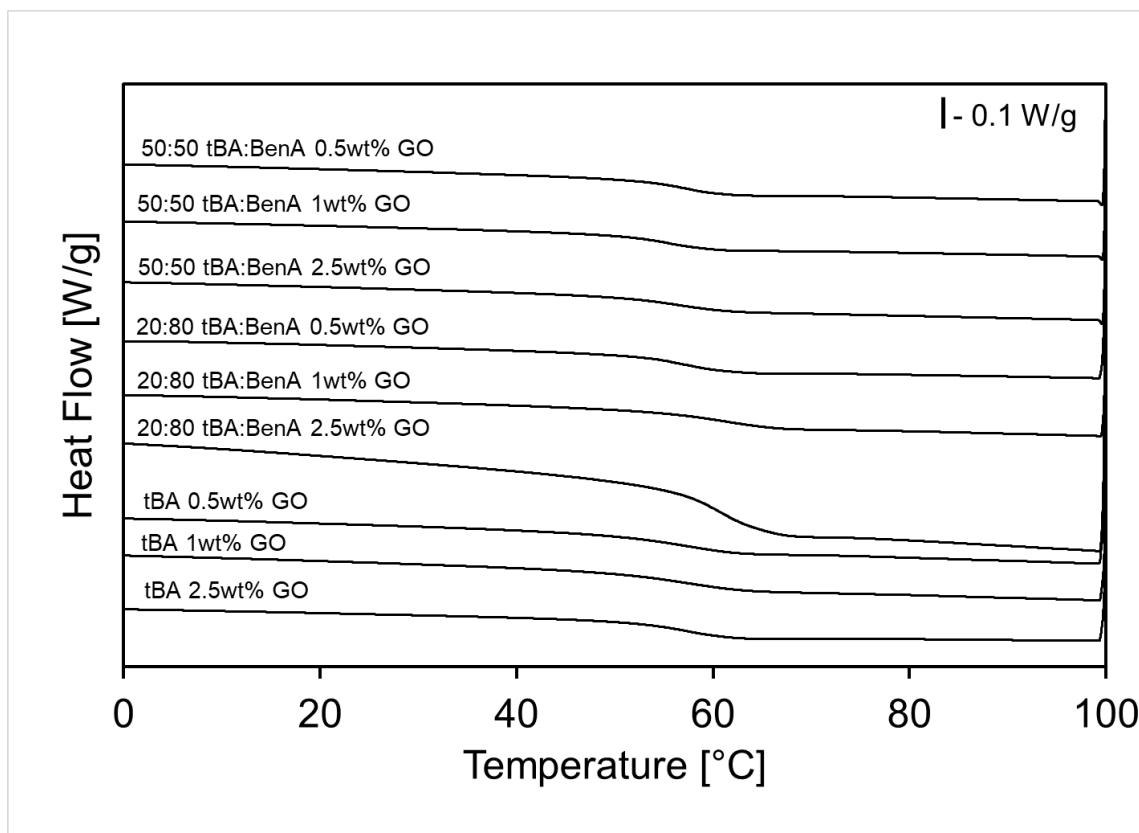


**Figure 3-2.** DSC scans of the SMP films with different levels of graphene oxide embedded in the material using 10 wt% TEGDMA as the cross-linker. The amount m-GO content appears to have no effect on the overall  $T_g$  of the SMP system, however, all SMP films showed a higher  $T_g$  compared to base films. This is compared to the pure tBA systems which showed the lowest  $T_g$  but the sharpest.

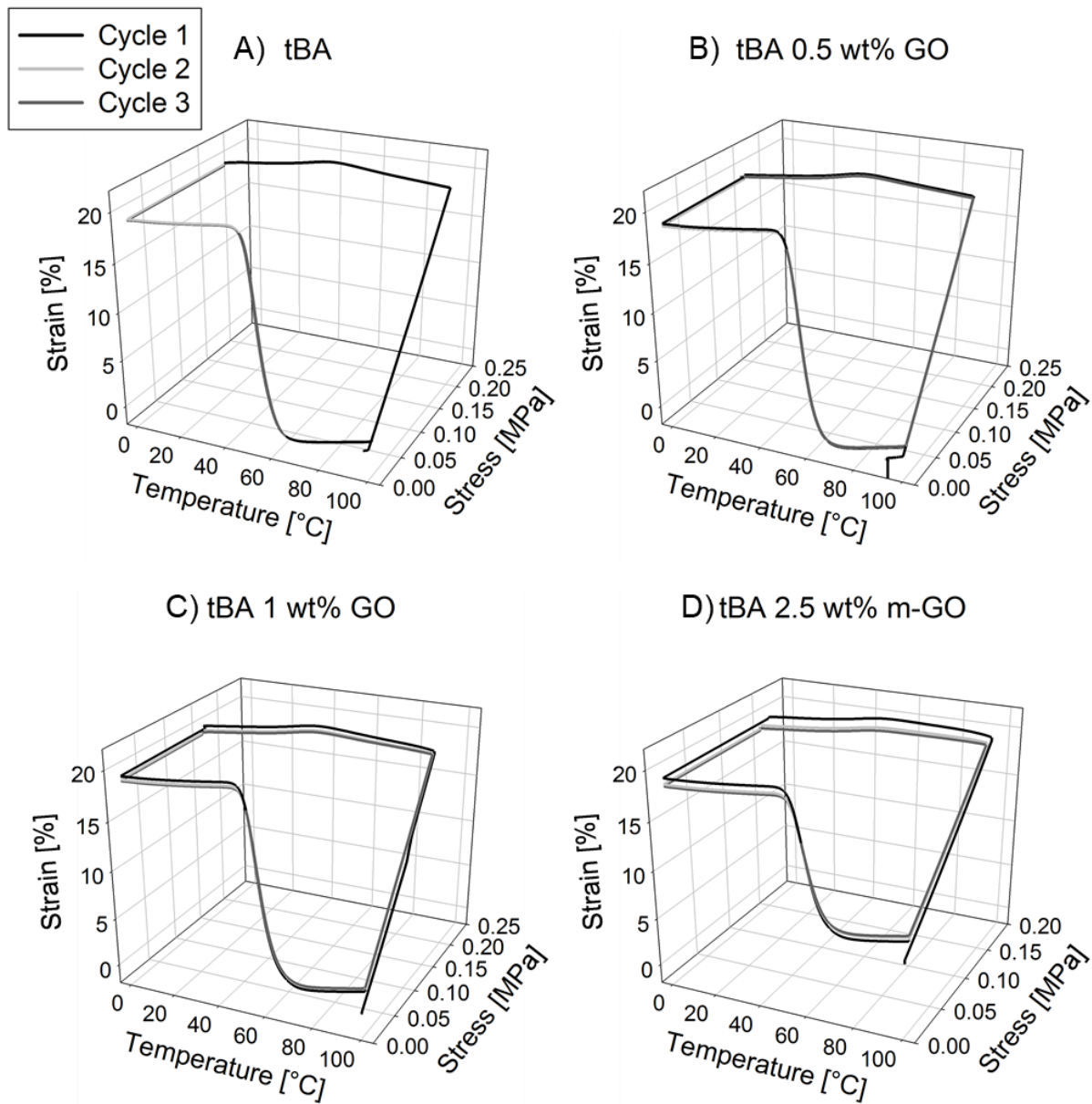


**Figure 3-3.** Thermal shape memory cycles of A) 100tBA 10% TEGDMA 0 wt% m-GO, B) 100tBA 10% TEGDMA 0.5wt% m-GO, C) 100tBA 10% TEGDMA 1wt% m-GO and D) 100tBA 10% TEGDMA 2.5wt% m-GO. All compositions showed excellent shape fixing and recovery ability as well as a sharp recovery event.

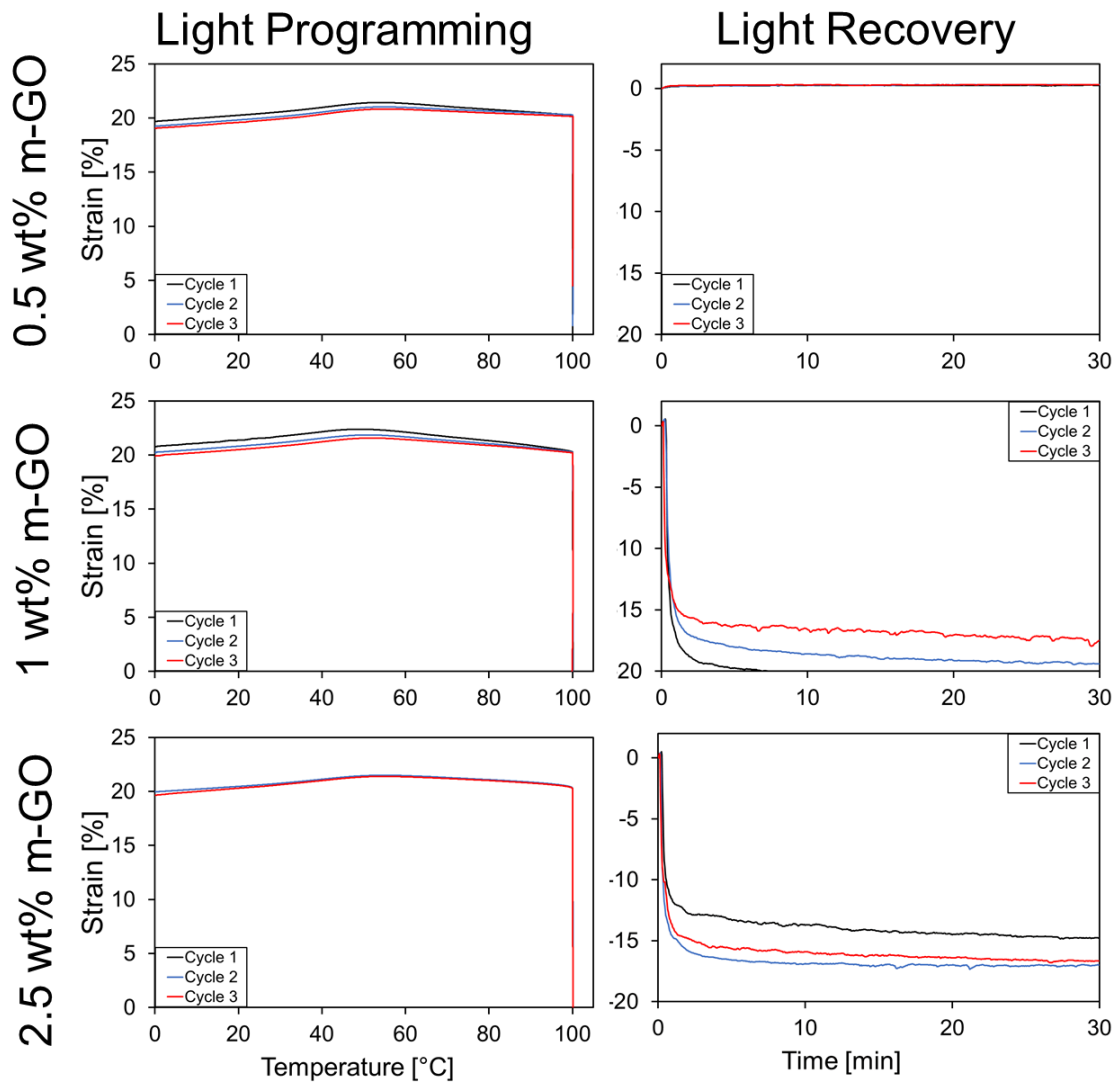


**Figure 3-4.** Light shape memory graphs. On the left is the thermal programming of the sample before light exposure and on the right is the visible light-triggered recovery. Where the 0.5wt m-GO samples showed strong shape fixing ability it showed no measurable visible light-triggered recovery, likely due to the wt% of the m-GO being too low. Both the 1 wt% and 2.5 wt% m-GO samples showed excellent shape fixing and recovery abilities with the 1 wt% m-GO sample demonstrating the highest shape recovery ability.

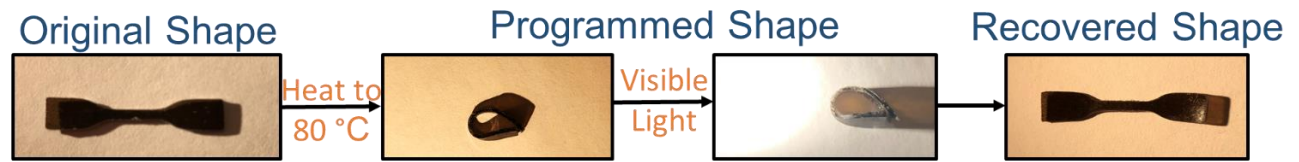


**Figure 3-5.** Demonstration of visible-light triggering of SMPs. The materials are first thermally programmed by heating to 80 °C and then deformed into the temporary shape of a “C”. The SMP is then exposed to white light and recovers back to its original shape.

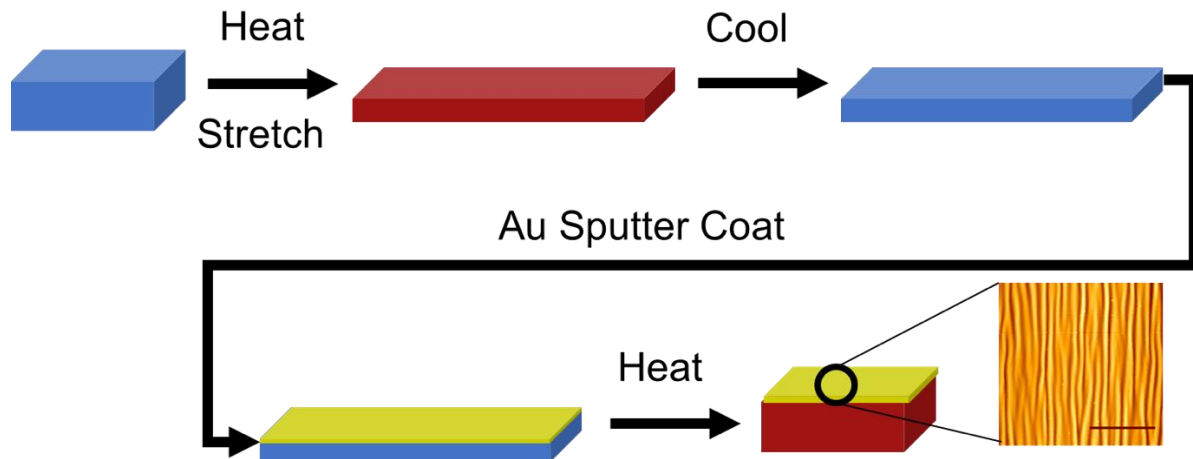


**Figure 3-6.** To create nano-wrinkles along the surface of SMPs, materials are first thermally programmed to 10% strain. The samples were then sputter-coated with gold and triggered to recover. Upon recovery, the SMP places a compressive strain along the surface of the material causing the gold coating to buckle and form nano-wrinkle patterns. Scale bar is 10  $\mu\text{m}$ .



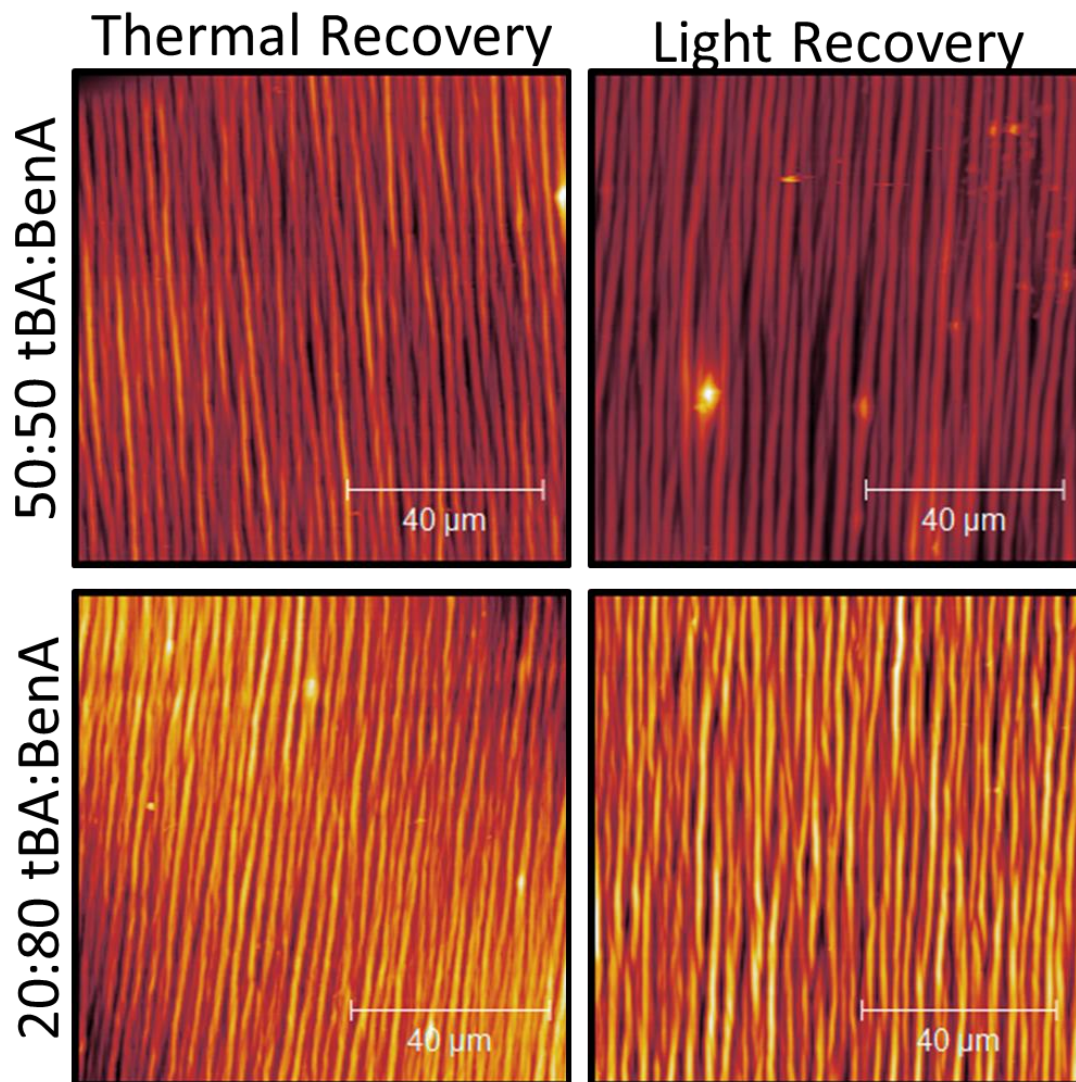


**Figure 3-7.** Wrinkle patterns formed along the surface of light-triggered SMPs that are both thermally and visible-light triggered. No noticeable difference in the wrinkle pattern can be observed.

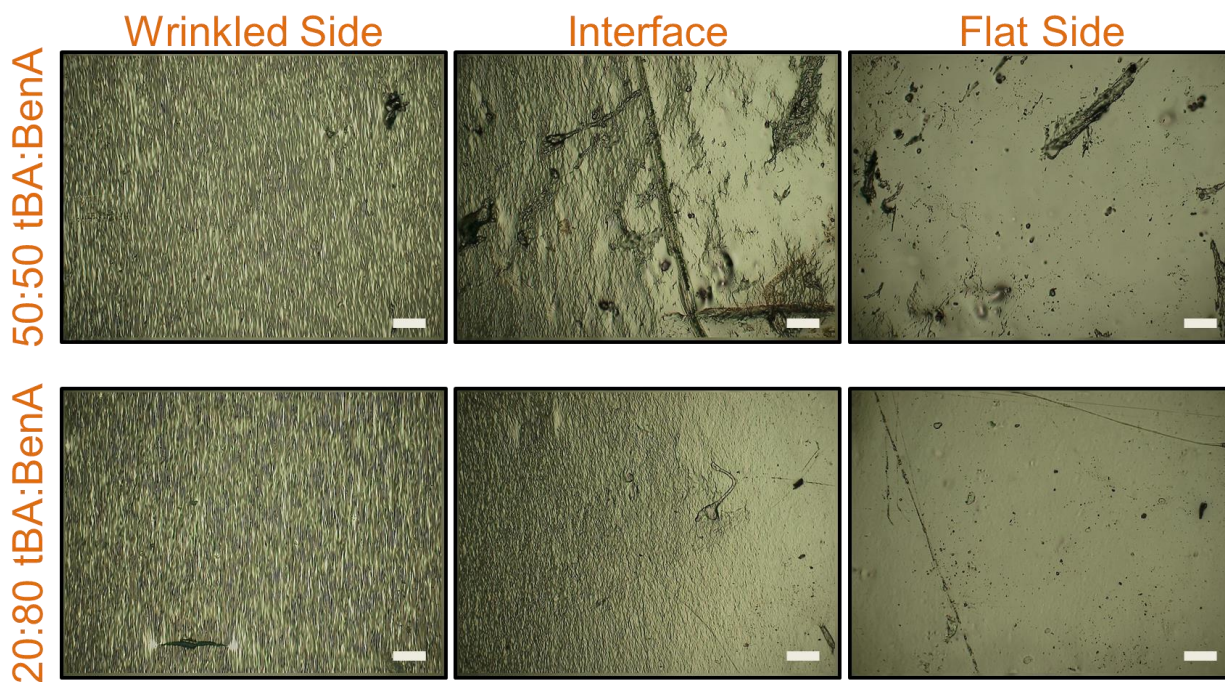


**Figure 3-8.** Since the light exposure can be spatially controlled, the SMPs can be locally recovered creating areas with a wrinkled topography (Left) and areas with a flat topography (Right). As can be seen in the figure the boundary between the wrinkled and non-wrinkled areas of the sample is very sharp. Scale bar is 20  $\mu\text{m}$ .

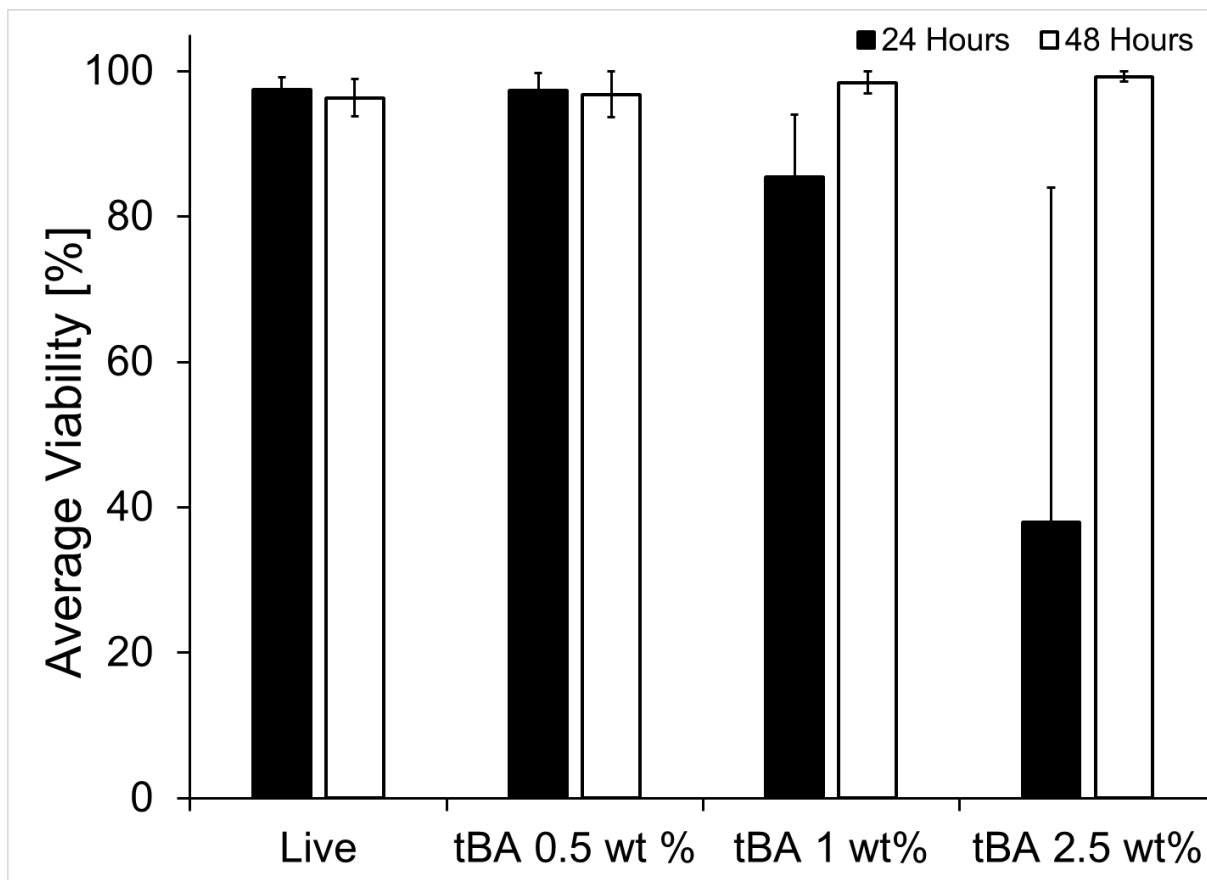


**Figure 3-9.** The average viability of C3H10T1/2 cells cultured on the surface of programmed and coated SMPs. The viability for the 24 h time points was lower than the 48 h time points but this is potentially due to the sample floating during experiments versus material cytotoxicity.

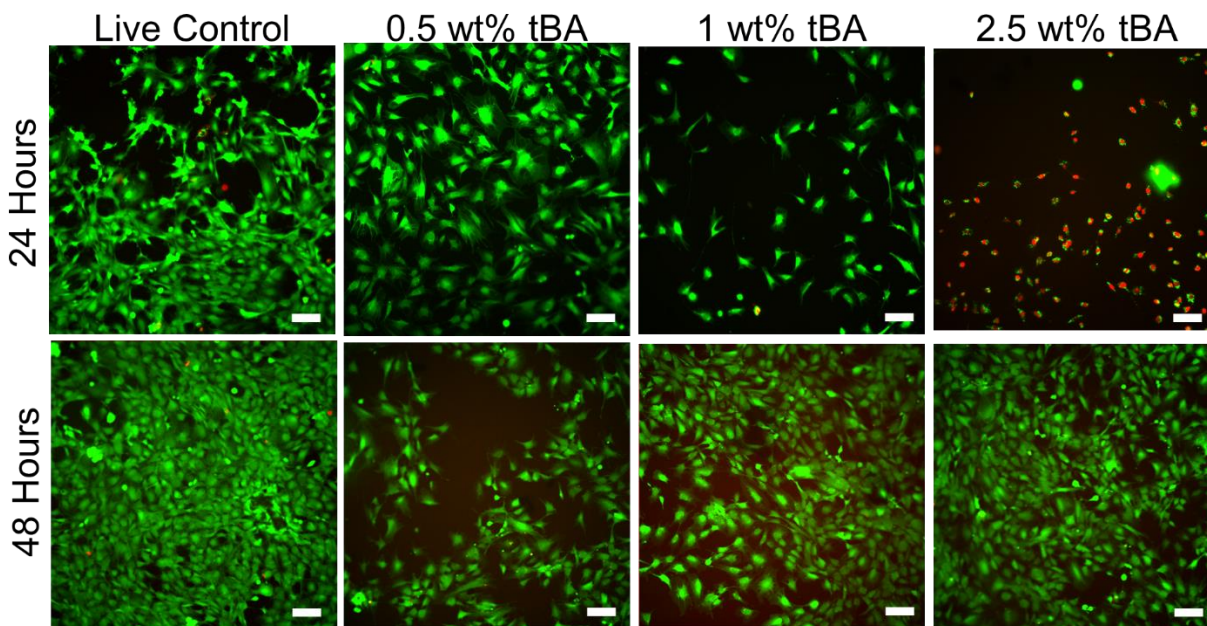


**Figure 3-10.** Representative cell micrographs of C3H10T1/2 cells cultured on the surface of gold-coated SMPs. Live cells are shown in green and dead cells are shown in red. The scale bar is 100  $\mu\text{m}$ . Groups are the TCPS live control, 0.5wt% m-GO, 1 wt% m-GO and 2.5 wt% m-GO. The SMP composition was set to 100tBA 10wt% TEGDMA for this study.

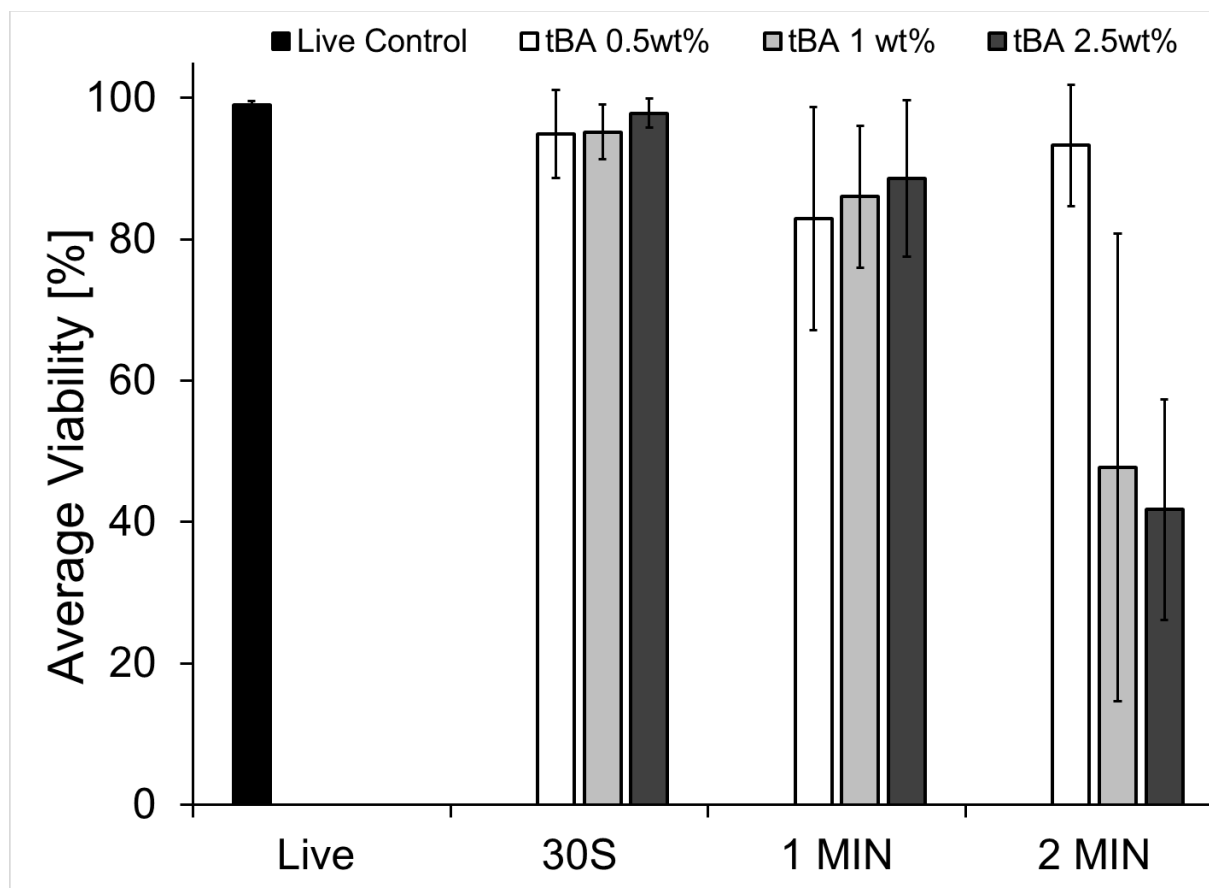


**Figure 3-11.** Cell viability of C3H10T1/2 cells cultured directly on programmed and coated SMP films exposed to white light for either 30 s, 1 min, or 2 min. The live control was cells grown on a TCPS well plate. The highest viability was observed for the 30 s of exposure, but material recovery was not observed until at least 1 min of exposure in the sample containing 1 wt% or 2.5 wt% m-GO. However, the samples exposed to 2 mins of white light exposure showed poor viability potentially due to hyperthermic cytotoxicity.



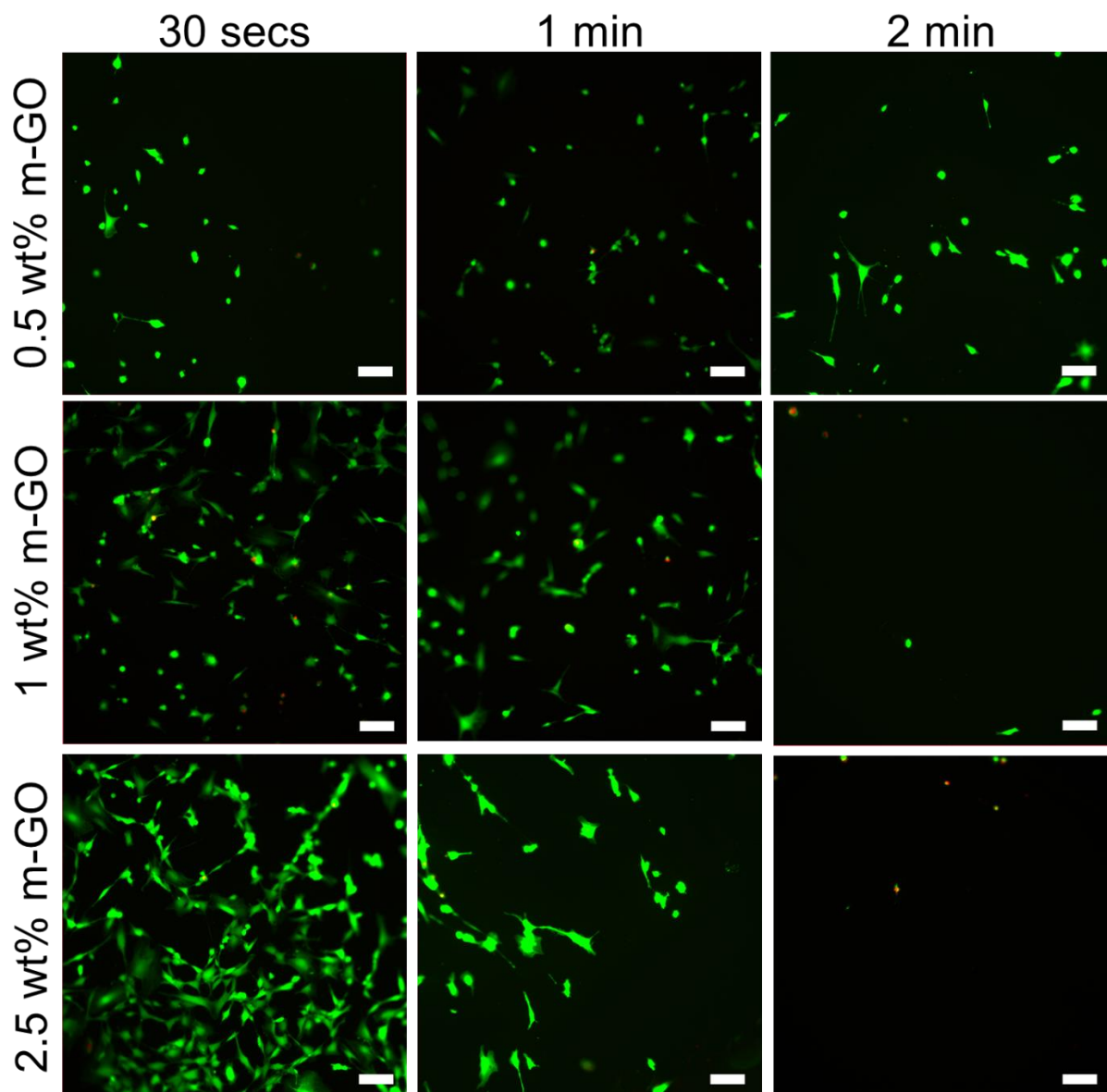


**Figure 3-12.** Representative micrographs of C3H10T1/2 cells cultured directly on programmed and coated SMP films exposed to either 30 s, 1 min or 2 min of white light. Cell number decreased with increased exposure with very few cells present on the samples exposed to 2 min of white light. The samples showing the highest viability were those cultured on 0.5 wt% m-GO which did not show any material recovery. In addition, samples exposed to 30 s of white light

exposure showed a high viability but also did not show any material recovery. The scale bar is 100  $\mu\text{m}$ .

### 3.8 References

1. Maitland, D. J. *et al.* Prototype laser-activated shape memory polymer foam device for embolic treatment of aneurysms. *J. Biomed. Opt.* **12**, 030504 (2007).
2. Lendlein, A., Jiang, H., Jünger, O. & Langer, R. Light-induced shape-memory polymers. *Nature* **434**, 879–882 (2005).
3. Maity, S., Bochinski, J. R. & Clarke, L. I. Metal Nanoparticles Acting as Light-Activated Heating Elements within Composite Materials. *Adv. Funct. Mater.* **22**, 5259–5270 (2012).
4. Duchowicz, R. *et al.* Photothermal analysis of polymeric dye laser materials excited at different pump rates. *Appl. Opt.* **42**, 1029 (2003).
5. Loarer, T., Greffet, J.-J. & Huetz-Aubert, M. Noncontact surface temperature measurement by means of a modulated photothermal effect. *Appl. Opt.* **29**, 979 (1990).
6. Hribar, K. C., Metter, R. B., Ifkovits, J. L., Troxler, T. & Burdick, J. A. Light-Induced Temperature Transitions in Biodegradable Polymer and Nanorod Composites. *Small* **5**, 1830–1834 (2009).
7. Le, D. M., Tycon, M. A., Fecko, C. J. & Ashby, V. S. Near-infrared activation of semi-crystalline shape memory polymer nanocomposites. *J. Appl. Polym. Sci.* **130**, n/a-n/a (2013).
8. Cheng, Z., Wang, T., Li, X., Zhang, Y. & Yu, H. NIR – Vis – UV Light-Responsive Actuator Films of Polymer-Dispersed Liquid Crystal / Graphene Oxide Nanocomposites. (2015). doi:10.1021/acsami.5b09676
9. Liang, J. *et al.* Infrared-Triggered Actuators from Graphene-Based Nanocomposites.



- 9921–9927 (2009).
10. Materials, S. Infrared light actuated shape memory effects in crystalline polyurethane / graphene chemical hybrids. doi:10.1088/0964-1726/23/2/025038
  11. Shou, Q., Uto, K., Lin, W. C., Aoyagi, T. & Ebara, M. Near-infrared-irradiation-induced remote activation of surface shape-memory to direct cell orientations. *Macromol. Chem. Phys.* **215**, 2473–2481 (2014).
  12. Yang, P. *et al.* In vitro wrinkle formation via shape memory dynamically aligns adherent cells. *Soft Matter* **9**, 4705 (2013).
  13. Shin, S. R. *et al.* Reduced Graphene Oxide-GelMA Hybrid Hydrogels as Scaffolds for Cardiac Tissue Engineering. 3677–3689 (2016). doi:10.1002/sml.201600178
  14. Luo, X. & Mather, P. T. Design strategies for shape memory polymers. *Curr. Opin. Chem. Eng.* **2**, 102–110 (2013).
  15. Davis, K. A., Luo, X., Mather, P. T. & Henderson, J. H. Shape Memory Polymers for Active Cell Culture. *J. Vis. Exp.* e2903–e2903 (2011). doi:10.3791/2903
  16. Davis, K. A., Burke, K. A., Mather, P. T. & Henderson, J. H. Dynamic cell behavior on shape memory polymer substrates. *Biomaterials* **32**, 2285–2293 (2011).
  17. Baker, R. M., Brasch, M. E., Manning, M. L. & Henderson, J. H. Automated, contour-based tracking and analysis of cell behavior over long time scales in environments of varying complexity and cell density. *J. R. Soc. Interface* **11**, 20140386 (2014).

# Chapter 4: Development of a Real-Time Cell Tracking

## Algorithm

### 4.1 Synopsis

Herein we discuss the development and implementation of a real-time cell tracking algorithm. To accomplish real-time cell tracking, we modified a previously developed cell tracking algorithm, automated contour-based cell tracking of *in vitro* environments (ACTIVE), to control a microscope directly during live-cell imaging and to segment and link cell tracks as each new frame is acquired. These advances enable ACTIVE to acquire real-time cell images, segment, and link stained nuclei to generate long-timescale cell tracks, and analyze cell tracking behavior, all in real-time.

### 4.2 Introduction

Synthetic biomaterials are actively being employed as *in vitro* models to assess cell behaviors critical to understanding biological functions and treat disease. To date, these platforms have been an attractive means to study how cells respond to changes in stiffness,<sup>1-3</sup> patterned surface chemistries,<sup>4,5</sup> or ordered topographies.<sup>6-10</sup> In addition, recent biomaterial advances have enabled the development of dynamic, *in vitro* systems that can be used to study how cells respond to alterations in their environment. These material platforms are sensitive to a variety of triggering mechanisms, such as temperature change,<sup>11,12</sup> light<sup>13-16</sup>, or enzymatic activity,<sup>17</sup> and these broadly applicable models are being applied to study cancer cell biology,<sup>18,19</sup> cell mechanobiology,<sup>20,21</sup> and developmental biology.<sup>22,23</sup>

Cell migration is a cellular behavior of interest in many research areas and, therefore, in many studies that employ synthetic biomaterials. To date, the standard for cell tracking remains manual cell tracking, where a user manually identifies cells frame-by-frame to generate cell tracks.<sup>24,25</sup> However, these methods are time-consuming and prone to human error. As such, a number of efforts have focused on the implementation of accurate, semi-autonomous, and fully autonomous tracking methods with popular segmentation approaches that include pixel thresholding to isolate cells<sup>26,27</sup> and active contours to trace boundaries.<sup>28,29</sup> A recent comparison of cell tracking algorithms found that tracking by detection methods such as pixel thresholding outperformed tracking by contour methods unless the cell tracking data sets have a high degree of cell overlap.<sup>30</sup> In these situations, contour methods are better adapted to tracking cells over longer time frames, indicating that contour-based methods may be more relevant in analyzing biological samples.

Previously, we have developed an automated, contour-based tracking algorithm that tracks nuclear-stained images and has successfully deployed the approach in the study of cell motility on anisotropic surfaces and in the study of mechanisms of cell migration. The algorithm, automated contour-based tracking for *in vitro* environments (ACTIVE), identifies stained cell nuclei in low contrast images, segments and links the nuclei over long time periods (or through large image stacks), and processes multi-cell interactions that have traditionally limited the accuracy of automated systems. In conjunction with our active cell culture platforms, we have also studied how cell behavior changes in response to the formation of mechanical topography. For instance, Wang *et. al.* was able to demonstrate on-demand on/off switching of polarized motility in an HT-1080 cancer cell line.<sup>31</sup> Brasch *et. al.* utilized our active SMP platforms in conjunction with ACTIVE to quantify the relationship between nuclei orientation and the

orientation of the Golgi body relative to the nucleus before, during, and after exposure to a change in substrate topography.<sup>32</sup> This change in topography caused a shift towards polarized motility and indicated that the vector between the nucleus and the Golgi body may be a more sensitive indicator of substrate features than nuclear orientation.

However, in both of these experimental platforms, decisions on when to use the formation of substrate topography to perturb the cell migration behavior were made based on pre-determined time points rather than real-time cell migration behavior. Particularly if used in conjunction with active cell platforms, the development of a real-time cell tracking algorithm would enable researchers to design topography formation events around quantitative cell behavior, which could enable the formation and study of semi-autonomous feedback loops. Such an experimental system would be achieved by combining previously developed active cell culture platforms with a real-time cell tracking algorithm. To reach this goal, this chapter discusses the modification of *ACTIVE* from a post-processing platform to a real-time cell tracking platform. We assess this real-time tracking algorithm based on its accuracy (similarity of the cell tracks compared to post-processing techniques) and processing time using different imaging modes and analysis functions.

## 4.3 Development and Methodology of the Real-Time *ACTIVE* Tracking Algorithm

### 4.3.1 Post-Processing *ACTIVE* Platform

The original *ACTIVE* code was written in MATLAB and requires a valid commercial license to operate. *ACTIVE* was designed to analyze cell populations that had been nuclear-stained, as cell segmentation was achieved by fitting a contour to the nuclei. Following contour fitting, *ACTIVE* then used linking system a previously established by Kilfoil and colleagues to relate cell information between consecutive frames.<sup>33</sup> Briefly, the total number of cells is first

identified in each frame. Then, each image pair is systematically compared using positional analysis, separating cell-cell identification matches into trivial (one potential match is identified) or non-trivial (multiple potential matches are identified) classifications. Non-trivial cases are sorted by minimizing the overall distance between the center of mass values. Afterward, each particle is assigned an identification tag, which is sequentially used by ACTIVE to sort inaccuracies associated with division and cell collision events. After corrections, the cell track information is tabulated and run through a separate suite of analysis functions. One such analysis function of substantial importance is the gyration tensor, used to calculate asphericity and the mean squared displacement (MSD), which were used in the current work (Summarized in Sch. 4-1).

#### 4.3.2 Real-Time Modification

First, the real-time ACTIVE modification (RT-ACTIVE) was written in MATLAB 2018 and includes a graphic user interface (GUI) that requires MATLAB 2017a or newer to properly operate. Similar to the original version of ACTIVE, RT-ACTIVE also requires the Image Processing Toolbox. The current version of RT-ACTIVE is programmed to interface with  $\mu$ Manager 1.4, and compatibility with other versions is not known.

To begin, we first ported the available scope commands into MATLAB following methods established by Edelstein *et al.*<sup>34</sup> and additional support from the creators of  $\mu$ Manager. Using these resources, we were able to load the full library of  $\mu$ Manager commands available for the scope. Next, the main wrapper function was modified following the code map outlined in Sch. 4-2. Briefly, the experimental parameters from the input GUIs (including the MMC Java functions for  $\mu$ Manager) are loaded and the variables for tracking are initialized. The code then goes into two large loops and iterates the core functions of ACTIVE through every experimental

time point and position (a maximum of three tracking locations may be specified). Briefly, the code will go through and sequentially capture and process images (only if scope controls are enabled), conduct segmentation, manage linking, run post-processing corrections, choose or continue to follow a cell (only if single-cell tracking is enabled), move the microscope so the cell is centered (only if single-cell tracking is enabled), perform real-time calculation of tracking metrics, and plot and display real-time cell tracks and tracking metrics. The code then iterates through the number of specified positions (from one to three) and then iterates over the number of specified time points.

RT-ACTIVE may be run in a combination of eight different modes depending on the experimental needs of the user. When the user initializes RT-ACTIVE, a GUI is prompted and guides the user through setting up their cell tracking experiment. All of the parameters that could be specified in the original ACTIVE are still available for user modification on the left side of the GUI (Fig 4-1). The GUI then asks the user to specify the imaging, tracking and position mode. If the imaging mode is set to microscope, RT-ACTIVE will initialize  $\mu$ Manager in preparation for running a cell tracking experiment using live experimental data. If the imaging mode is set to test stack, RT-ACTIVE will instead allow the user to load in an image stack of previously acquired and processed images. In this regard, RT-ACTIVE could still be used as a post-processing platform but will instead generate videos of how the analysis metrics change as new images are added to the analysis. Next, if tracking mode is set to “Single-cell”, RT-ACTIVE will choose a single cell per position and will attempt to track it over the course of an experiment. Currently, RT-ACTIVE is programmed to pick a new cell if the cell is lost due to imaging problems or undergoes a division or multi-body event. This was designed to improve the stability of the code, as RT-ACTIVE can fail when a cell undergoes a complex interaction event. If the tracking mode

is set to “Multi-Cell”, RT-ACTIVE will pull up to three positions from the position list in the multi-D acquisition function in  $\mu$ Manager. If the scope controls are enabled, RT-ACTIVE will then load the positions and will translate the scope between those two positions to acquire cells at those locations. If the image mode is set to “Test Stack”, RT-ACTIVE will allow the user to upload up to three image stacks for analysis. Finally, if Position mode is set to “Single-Position” the scope will track cells only at a single position. If position mode is set to “Multi-Position” RT-ACTIVE will track up to three positions at once. Three positions are the computational limit to ensure that the processing time between frames does not become too lengthy during experiments but to still allow for the inclusion of experimental controls during cell tracking experiments. During our previous active cell culture experiments, three samples were typically used to make up a single group. Two samples were static with either a flat or a wrinkled topography, while the third was an active sample that would transition topographies at a set time-point.

## 4.4 Demonstrating the Accuracy of RT-ACTIVE

### 4.4.1 Multi-Position RT-ACTIVE Time-Lapse Microscopy

For cell-tracking tests, C3H10T1/2 cells were seeded on a 35 mm<sup>2</sup> petri dish at 5,000 cells/cm<sup>2</sup>. Cells were stained using Hoechst 33342 and then incubated in a stage incubator during imaging. The RT-ACTIVE code was then initialized in MATLAB and the initial experimental parameters were set (Imaging Mode = Microscope, Tracking Mode = Multi-Cell, Position Mode = Multi-Position). At this point, the experiment commenced and  $\mu$ Manager was initialized. The user was next prompted to set the imaging conditions of the microscope to ensure good nuclear images were acquired (exposure, gain). The user was subsequently asked to load three positions into the position list under Multi-D Acquisition and then the run began. RT-ACTIVE collected the first 10 frames of data before starting the cell tracking plots and gyration tensor analysis. This

multi-position acquisition was demonstrated for three separate experimental plates and a representative run is shown in Fig 4-2.

#### 4.4.2 Processing Time and Accuracy Validation

To ensure there was enough time between acquiring images during an experiment, we recorded the processing time for every frame as the *RT-ACTIVE* moved through a 288-frame test stack (Fig 4-3). The processing time increased as the number of frames processed increased, as expected. In addition, all analysis functions increased the processing time, but only by a small increment. Even for the last frame were all frames had to be processed, the overall processing time for the entire image stack was under 35 s, which is well below the 3-5 min interval typically used between image acquisition for live cell experiments.

To ensure the accuracy of cell analysis, we compared the cell tracking data generated by *RT-ACTIVE* to the previously developed version of *ACTIVE*. To do this, we visually compared the cell tracks generated by the two tracking codes by overlaying them in ImageJ (Fig. 4-4). We believe this difference stems from the post-processing functions meant to correct for cell-interaction events. In the post-processing platform, *ACTIVE* can correct these cell tracks with all the tracking information available. However, *RT-ACTIVE* only has a limited amount of the frame information. Currently, *RT-ACTIVE* does reanalyze the cell tracks in every frame to allow for corrections to be made to these events so the source of this discrepancy is currently unknown and under investigation. We also compared the accuracy between the multi-position function of the code (Fig 4-5) and found no difference between cell tracks generated using the same test stack but run at different positions.



## 4.5 Discussion

Here, we developed a real-time cell tracking code that can run in eight separate modes, depending on the experimental needs of the user. The test stack function allows the user to easily make videos showing the analysis of cell behavior changing as more frames of data are added. The multi-position versus single-position feature allows users to prioritize experimental controls to run fewer experiments overall or computational speed to run more complicated analysis. Finally, the multi-cell versus single cell allows for two different experiments; either to track all cells at a single location or translate the scope to follow a single cell while tracking all cells around it. Although these options have been implemented, further experimentation is still needed to fully assess their accuracy. For example, to assess the accuracy of single-cell tracking, a synthetic data set that replicates the translation of the microscope is needed. In addition, work still needs to be done on improving the overall accuracy of the RT-ACTIVE code compared to the original code.

This work demonstrates the development of a real-time cell tracking algorithm and, to date, the algorithm still needs to be implemented for active cell culture experiments. We hope this real-time tracking will enable researchers to set the experimental conditions on when to trigger material recovery based on actual cell behavior versus pre-set experimental time-points. In addition, we hope to combine this real-time analysis with our visible-light triggered SMP to create a semi-autonomous feedback loop system to enable us to study cell mechanobiological experiments in the presence of a feedback loop.

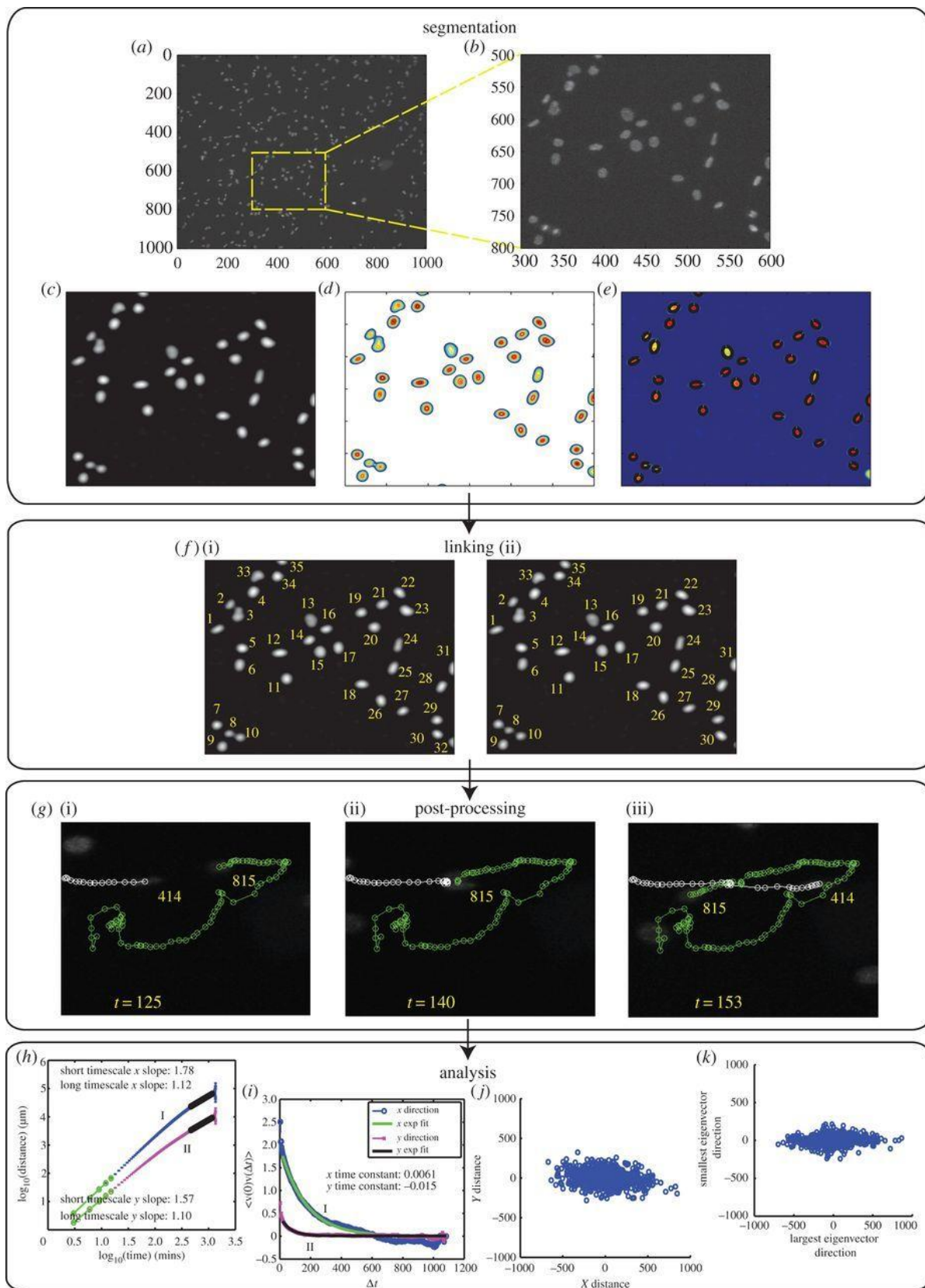
## 4.6 Conclusions and Future Work

We have successfully developed a real-time cell tracking algorithm capable of running in two separate modes: a multi-position acquisition in which the code tracks cells entering and

exiting three separate locations and a single-cell acquisition where the code follows three separate cells as they migrate and tracks all the cells within the translating frame. We have shown that the resulting cell tracks differ slightly when compared to a post-processing method. We suspect this is due to errors in the correction algorithms meant to increase the accuracy of *ACTIVE*. We have successfully demonstrated the real-time *ACTIVE* using cells migrating along a sample of TCPS. In the future, this real-time *ACTIVE* will be combined with active cell culture platforms to enable real-time analysis of cell behaviors that will then be used to “decide” when to apply mechanical perturbations.

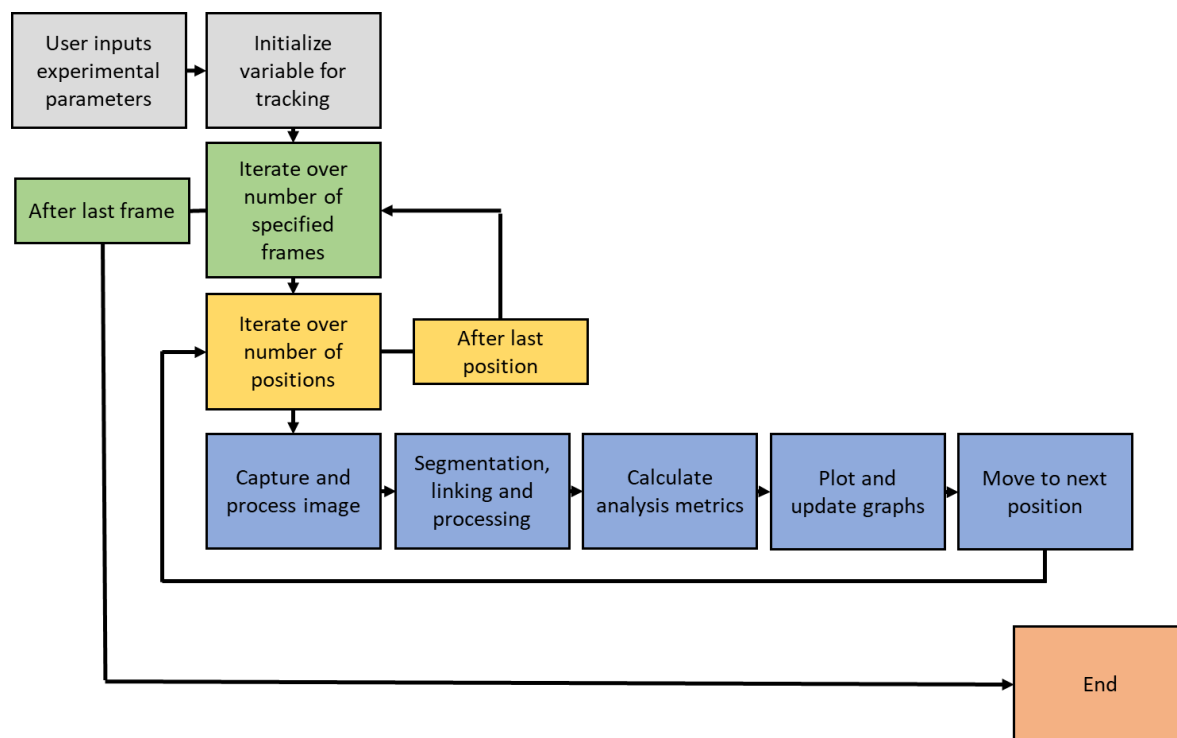
#### 4.7 Acknowledgments

Funding from the NSF IGERT Program, DGE-1068780, and the NSF BMAT program, DMR-1609523 and REU Supplement DMR-1743080, is gratefully acknowledged, as is use of the facilities of the Syracuse Biomaterial Institute at Syracuse University. In addition, the student contributions of Benjamin Posnick and Phil Mohun are all gratefully acknowledged who wrote most of the cell tracking code. The efforts of Bence Kotis and Jakub Kochanowski are also acknowledged.



**Scheme 4-1.** ACTIVE executes four major tasks: (A-E) nuclear segmentation, (F) nuclear

linking, (G) cell division and merging event post-processing, and (H-K) individual and collective cell motility analysis. (A) Cells were stained with Hoechst 33342 and imaged for 24 h; (B) image subsections exhibited variable intensity in nuclear staining. (C) Individual frames were first processed using a bandpass filter and (D) contour profiles were established based on fluctuations in nuclear intensity. (E) Single peak contours were fit with an ellipse at half-height, denoting cell identification. Multi-peak intensity profiles were tagged as either a division or merging event and reevaluated for accuracy during post-processing. (F-i) Once segmentation was complete, cell identification tags were established and (F-ii) cell track information was linked between consecutive frames. (G-i) Post tracking, cell-cell interaction events were identified, (G-ii) processed using a custom cost function, and (G-iii) track information was updated. Motility behavior was then characterized using different analysis metrics such as (H) decomposed mean-squared displacement, (I) velocity-autocorrelation, (J) diffusion plots and (K) final cell locations rotated by the principal axis of the gyration tensor. Adapted with permission from R.M. Baker, M.E.Brasch, M.L. Manning and J.H. Henderson, *Journal of The Royal Society Interface*, **2014**, 11, 20140386. **Copyright © The Royal Society 2014.**



**Scheme 4-2.** A map showing the program structure of the real-time ACTIVE modification. First, the experimental parameters from the input GUIs are loaded and the variables for tracking are initialized. The code then goes into two large loops that loop the core functions of ACTIVE through every experimental time point and position (a maximum of three). Briefly, the code will go through and sequentially: capture and process images (only if scope controls are enabled), conduct segmentation, conduct linking, conduct post-processing corrections, choose or continue to follow a cell (only if single-cell tracking is enabled), move microscope so the cell is centered (only if single-cell tracking is enabled), conduct real-time calculation of tracking metrics, and plot and display real-time cell tracks and tracking metrics. The code then iterates through the number of specified positions (from one to three) and then iterates over the number of specified time points.

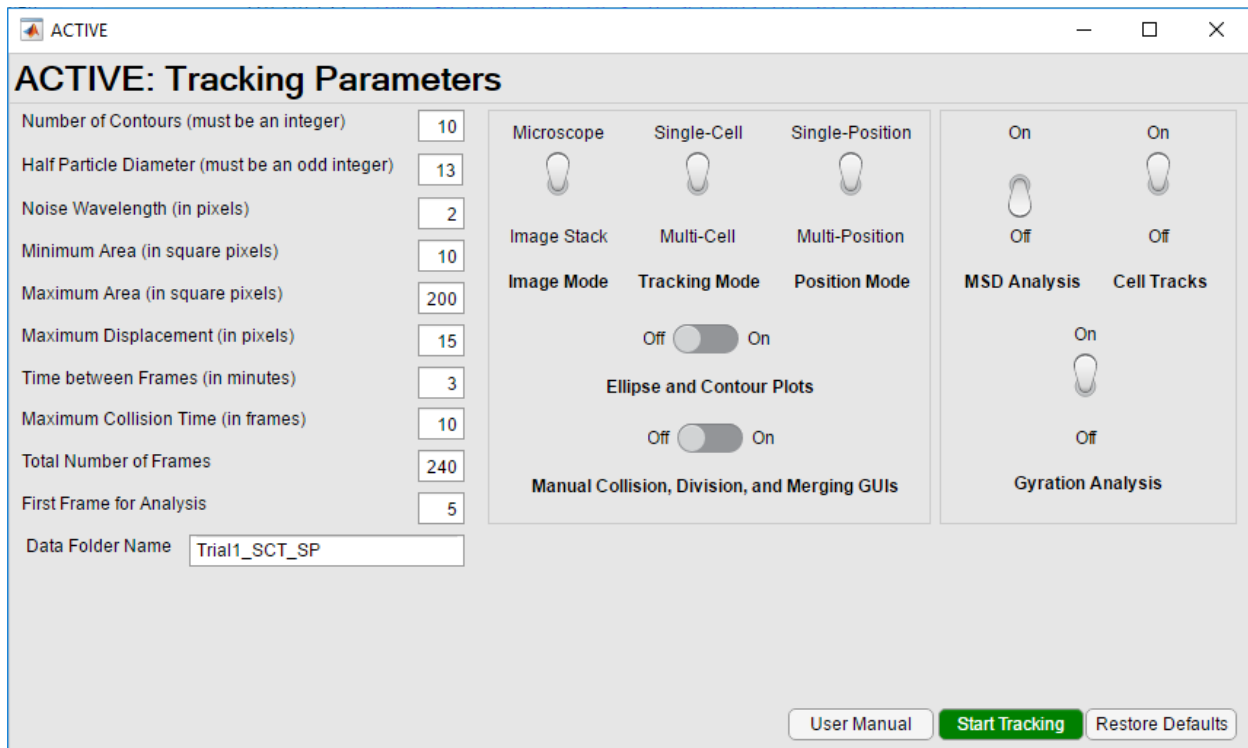


**Figure 4-1.** The GUI for the real-time ACTIVE tracking code. Users are given the same input parameters from the original version of ACTIVE. Users then specify a data file name and choose which tracking options they want to have turned on. The code can be run in 8 different combinations depending on the structure of the experiments. First, the code can be run in “Microscope” or “Image Stack”. Image stack disables the microscope control functions and the code will instead feed images in from an image stack one frame at a time. Second, the user will specify between “single-cell” and “multi-cell”. Single-cell will trigger RT-ACTIVE to pick a single cell and follow it over the course of an experiment. Multi-cell will have RT-ACTIVE stay in a single location and track the cells entering and exiting the frame. Finally, the user needs to specify between “Single-Position” and “Multi-Position”. Single-position means RT-ACTIVE will only track a single spot or cell while multi-position will allow the user to specify up to three

locations. It should be noted that if the scope mode is enabled RT-ACTIVE will read these locations from the position list loaded into  $\mu$ Manager.

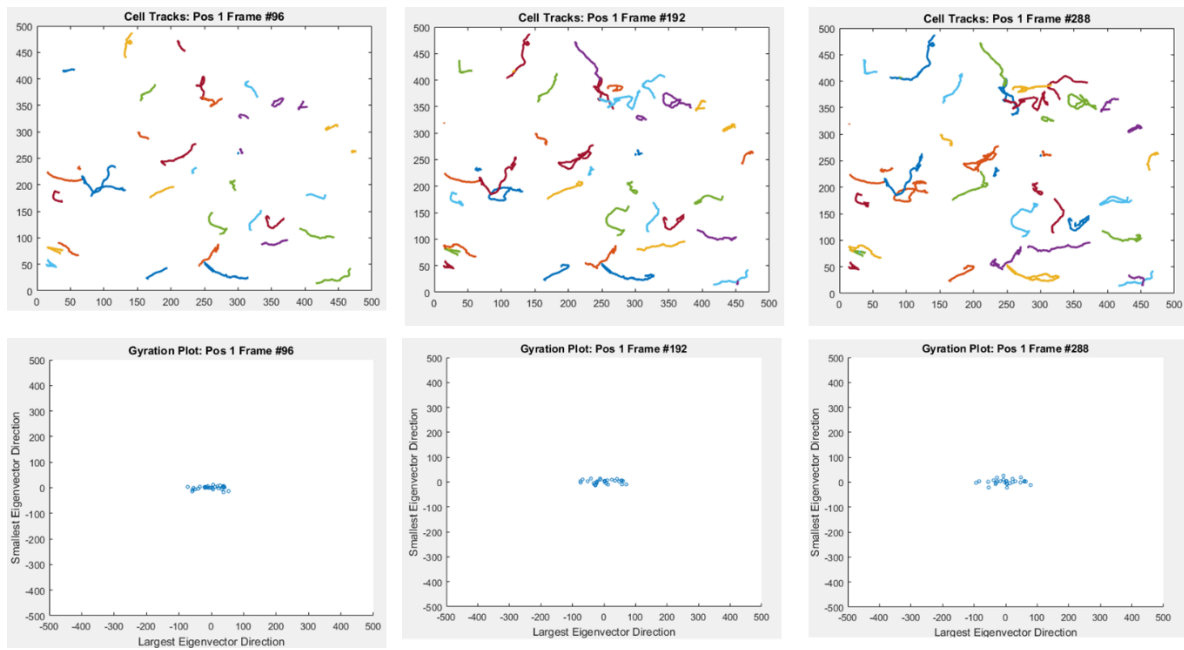
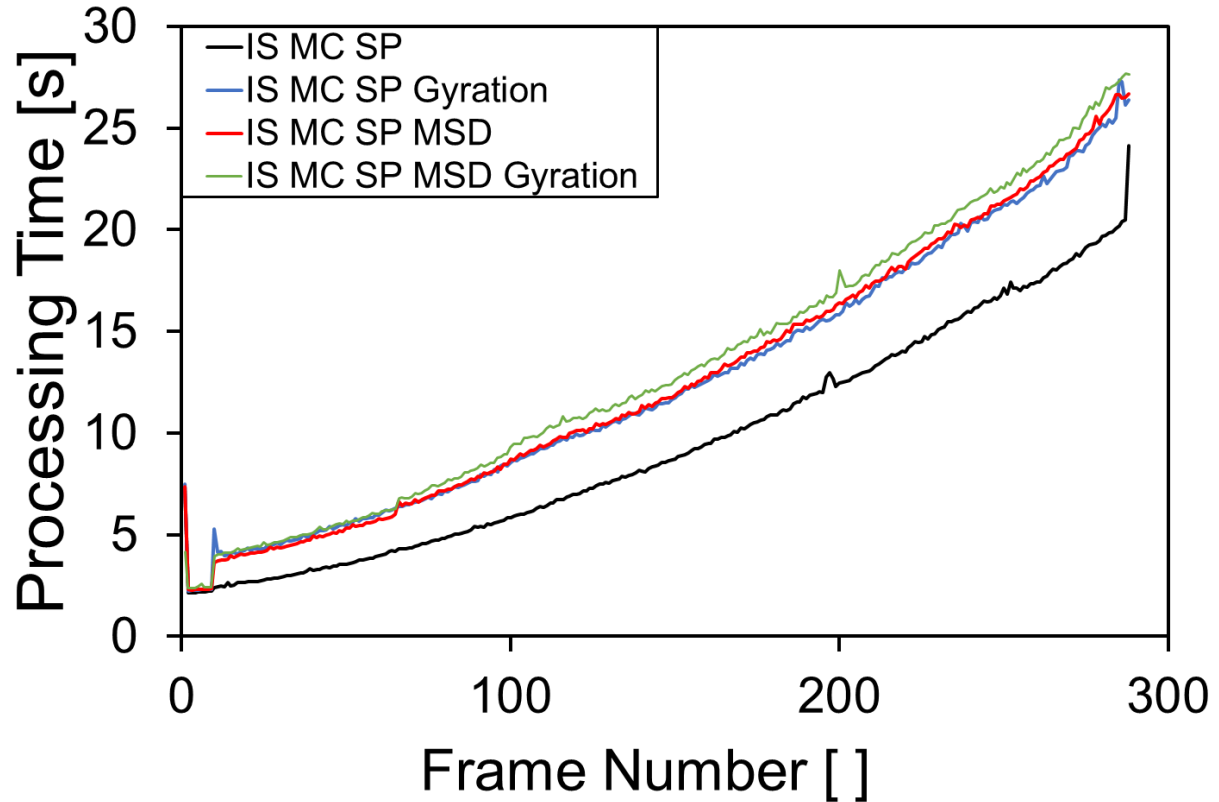


**Figure 4-2.** The cell tracks (top) and gyration tensor (bottom) for position 1 of the first Multi-Position experiment.





**Frame 4-3.** The measured processing time for the full tracking and analysis of a 288-frame test stack. The conditions tested were: Image stack (IS), multi-cell mode (MC), single position (SP) while running no analysis, the radius of gyration analysis, the mean-squared displacement analysis or both the mean squared displacement and the radius of gyration. As expected, the processing time increased as the frame number increased. In addition, the analysis functions increased the processing time as well.

## Overlay of Cell Tracks Generated by ACTIVE and RT-ACTIVE

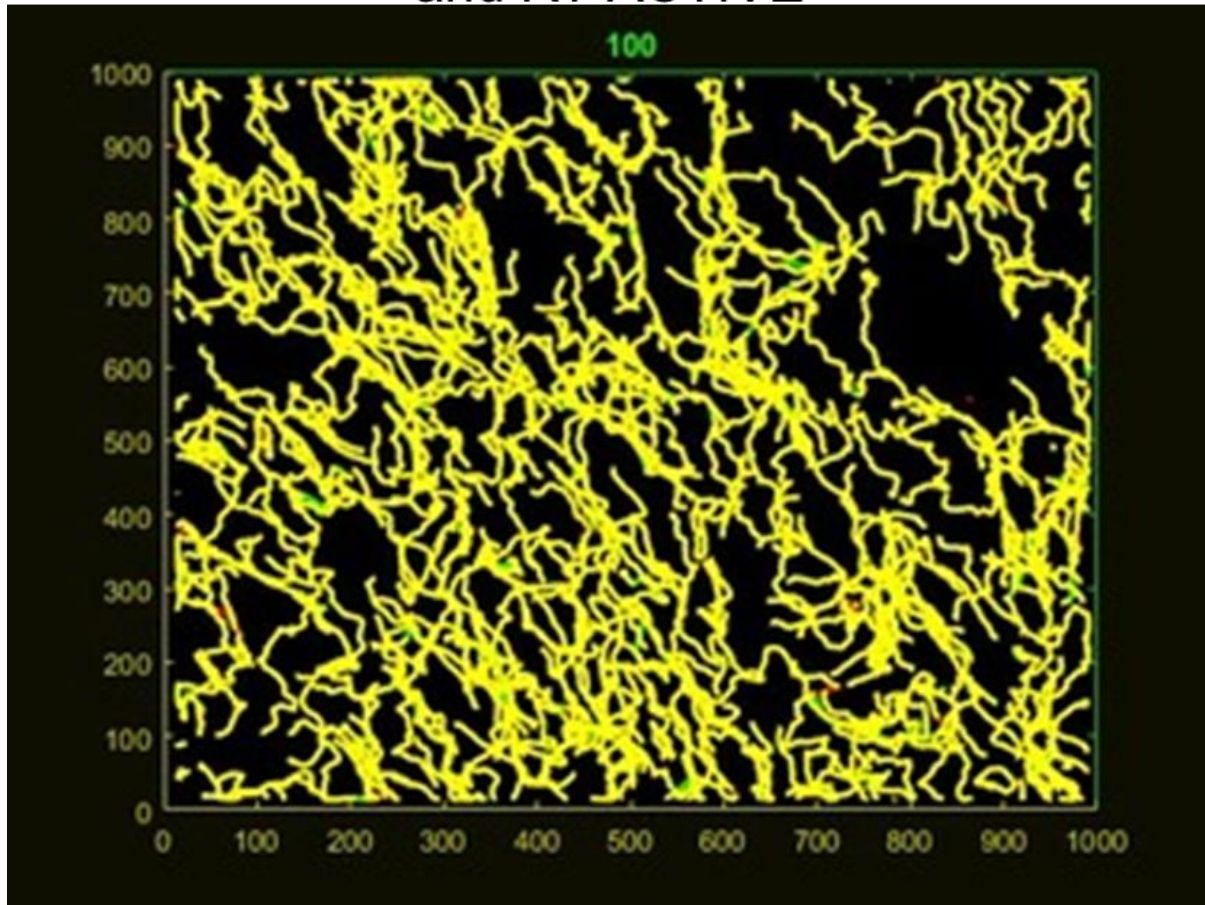


**Figure 4-4.** An overlay of the generated cell tracks created using ImageJ. The cell tracks generated by the RT-ACTIVE are shown in green and the tracks generated by the original version of ACTIVE are shown in red. Where the tracks overlap, the image is yellow. Upon close inspection, one can see the overlap between the two cell tracking images is not perfect.

## Overlay of Cell Tracks Generated by Single Position Versus Multi Position

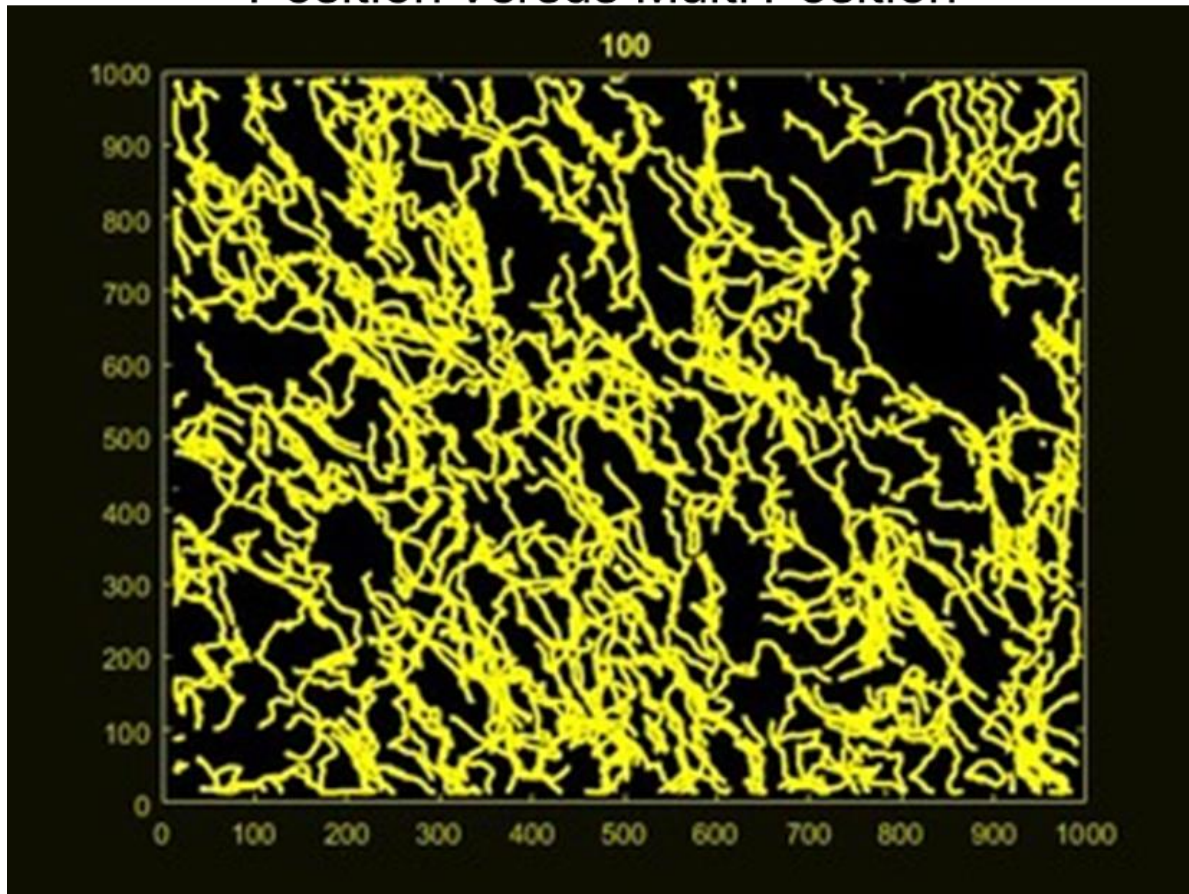


**Figure 4-5.** An overlay of the generated cell tracks created using ImageJ. The cell tracks generated by the RT-*ACTIVE* position 1 are shown in green and the tracks generated by the RT-*ACTIVE* position 2 are shown in red. No differences in cell tracks were observed.

## 4.8 References

1. Gray, D. S., Tien, J. & Chen, C. S. Repositioning of cells by mechanotaxis on surfaces with micropatterned Young's modulus. *J. Biomed. Mater. Res. - Part A* (2003). doi:10.1002/jbm.a.10585
2. Discher, D. E., Janmey, P. & Wang, Y. L. Tissue cells feel and respond to the stiffness of their substrate. *Science* (2005). doi:10.1126/science.1116995
3. Engler, A. J., Sen, S., Sweeney, H. L. & Discher, D. E. Matrix elasticity directs stem cell lineage specification. *Cell* (2006). doi:10.1016/j.cell.2006.06.044
4. Missirlis, D. & Spatz, J. P. Combined effects of PEG hydrogel elasticity and cell-adhesive coating on fibroblast adhesion and persistent migration. *Biomacromolecules* (2014). doi:10.1021/bm4014827
5. Magnani, A., Priamo, A., Pasqui, D. & Barbucci, R. Cell behavior on chemically microstructured surfaces. *Mater. Sci. Eng. C* (2003). doi:10.1016/S0928-4931(02)00284-9
6. Ann Dalton, B. *et al.* Modulation of epithelial tissue and cell migration by microgrooves. *J. Biomed. Mater. Res.* (2001). doi:10.1002/1097-4636(200108)56:2<195::AID-JBM1084>3.0.CO;2-7
7. Yim, E. K. F. *et al.* Nanopattern-induced changes in morphology and motility of smooth muscle cells. *Biomaterials* (2005). doi:10.1016/j.biomaterials.2005.01.058
8. Kim, D. H. *et al.* Mechanosensitivity of fibroblast cell shape and movement to anisotropic substratum topography gradients. *Biomaterials* (2009). doi:10.1016/j.biomaterials.2009.06.042

9. Kim, D. H., Provenzano, P. P., Smith, C. L. & Levchenko, A. Matrix nanotopography as a regulator of cell function. *Journal of Cell Biology* (2012). doi:10.1083/jcb.201108062
10. Guvendiren, M. & Burdick, J. A. Stem Cell Response to Spatially and Temporally Displayed and Reversible Surface Topography. *Adv. Healthc. Mater.* **2**, 155–164 (2013).
11. Lendlein, A. & Langer, R. Biodegradable, elastic shape-memory polymers for potential biomedical applications. *Science* **296**, 1673–6 (2002).
12. Gall, K. *et al.* Thermomechanics of the shape memory effect in polymers for biomedical applications. *J. Biomed. Mater. Res. - Part A* (2005). doi:10.1002/jbm.a.30296
13. Maitland, D. J., Metzger, M. F., Schumann, D., Lee, A. & Wilson, T. S. Photothermal properties of shape memory polymer micro-actuators for treating stroke. *Lasers Surg. Med.* (2002). doi:10.1002/lsm.10007
14. Baer, G. M. *et al.* Fabrication and in vitro deployment of a laser-activated shape memory polymer vascular stent. *Biomed. Eng. Online* (2007). doi:10.1186/1475-925x-6-43
15. Lendlein, A., Jiang, H., Jünger, O. & Langer, R. Light-induced shape-memory polymers. *Nature* **434**, 879–882 (2005).
16. Zheng, Y., Li, J., Lee, E. & Yang, S. Light-induced shape recovery of deformed shape memory polymer micropillar arrays with gold nanorods. *RSC Adv.* (2015). doi:10.1039/c5ra01469g
17. Buffington, S. L. *et al.* Enzymatically triggered shape memory polymers. *Acta Biomater.* (2019). doi:10.1016/j.actbio.2018.11.031
18. Lu, P., Weaver, V. M. & Werb, Z. The extracellular matrix: A dynamic niche in cancer

- progression. *Journal of Cell Biology* (2012). doi:10.1083/jcb.201102147
19. Bissell, M. J. & Radisky, D. Putting tumours in context. *Nat. Rev. Cancer* (2001). doi:10.1038/35094059
  20. Plotnikov, S. V., Pasapera, A. M., Sabass, B. & Waterman, C. M. Force fluctuations within focal adhesions mediate ECM-rigidity sensing to guide directed cell migration. *Cell* (2012). doi:10.1016/j.cell.2012.11.034
  21. Tan, J. L. *et al.* Cells lying on a bed of microneedles: an approach to isolate mechanical force. *Proc. Natl. Acad. Sci. U. S. A.* (2003). doi:10.1073/pnas.0235407100
  22. Nelson, C. M., VanDuijn, M. M., Inman, J. L., Fletcher, D. A. & Bissell, M. J. Tissue geometry determines sites of mammary branching morphogenesis in organotypic cultures. *Science* (80-. ). (2006). doi:10.1126/science.1131000
  23. Aman, A. & Piotrowski, T. Cell migration during morphogenesis. *Developmental Biology* (2010). doi:10.1016/j.ydbio.2009.11.014
  24. Strachan, L. R. & Condic, M. L. Neural crest motility and integrin regulation are distinct in cranial and trunk populations. *Dev. Biol.* (2003). doi:10.1016/S0012-1606(03)00187-8
  25. Eilken, H. M., Nishikawa, S. I. & Schroeder, T. Continuous single-cell imaging of blood generation from haemogenic endothelium. *Nature* (2009). doi:10.1038/nature07760
  26. Tonkin, J. A. *et al.* Automated cell identification and tracking using nanoparticle moving-light-displays. *PLoS One* (2012). doi:10.1371/journal.pone.0040835
  27. Becker, T. & Madany, A. Morphology-based Features for Adaptive Mitosis Detection of In Vitro Stem Cell Tracking Data. *Methods Inf. Med.* (2012). doi:10.3414/me11-02-0038

28. Deng, Y., Coen, P., Sun, M. & Shaevitz, J. W. Efficient Multiple Object Tracking Using Mutually Repulsive Active Membranes. *PLoS One* (2013).  
doi:10.1371/journal.pone.0065769
29. Xu, T., Vavylonis, D. & Huang, X. 3D actin network centerline extraction with multiple active contours. *Med. Image Anal.* (2014). doi:10.1016/j.media.2013.10.015
30. Ulman, V. *et al.* An objective comparison of cell-tracking algorithms. *Nat. Methods* (2017). doi:10.1038/nmeth.4473
31. Wang, J., Quach, A., Brasch, M. E., Turner, C. E. & Henderson, J. H. On-command on/off switching of progenitor cell and cancer cell polarized motility and aligned morphology via a cytocompatible shape memory polymer scaffold. *Biomaterials* **140**, 150–161 (2017).
32. Brasch, M. E. *et al.* Nuclear position relative to the Golgi body and nuclear orientation are differentially responsive indicators of cell polarized motility. *PLoS One* (2019).  
doi:10.1371/journal.pone.0211408
33. Gao, Y. & Kilfoil, M. L. Accurate detection and complete tracking of large populations of features in three dimensions. *Opt. Express* (2009). doi:10.1364/oe.17.004685
34. Edelstein, A. D. *et al.* Advanced methods of microscope control using  $\mu$ Manager software. *J. Biol. methods* **1**,



# Chapter 5: Generating Complex Wrinkle Patterns Using Triple Shape Memory Polymers

## 5.1 Synopsis

Herein, we describe the utilization of multi-shape memory composites to generate complex wrinkle patterns. Briefly, we programmed triple shape polymeric composites to have two separate strains programmed into two separate material phases. The materials were then coated with gold and the strains were either recovered simultaneously or sequentially to induce the formation of double or complex wrinkle patterns. It was noted that in order for the second wrinkle pattern to form the second programmed strain needed to be higher than the first programmed strain, likely due to a corrugation stiffening effect.

## 5.2 Introduction

The formation of controlled surface patterns has become an important topic in the field of material science because nano/micro-scale topographies can give rise to a variety of material properties.<sup>1</sup> In nature, surface topography leads to a variety of surface properties such as the adhesive properties of the gecko foot,<sup>2</sup> the antibacterial properties of shark skin,<sup>3</sup> or the superhydrophobicity of the rose petal,<sup>4</sup> to give a few examples, and much research has been devoted to mimicking these properties. As such, a variety of nano and micro-scale patterning techniques have been developed, including laser writing and photolithography.

Surface wrinkling is an alternative method for producing nano and micro-scale patterns and has the advantage of allowing the formation of highly structured surface patterns over a large area. A common wrinkling method involves a bilayer system where a material is deformed and then



coated in a thin stiff film.<sup>5</sup> Once the force is released, the material then applies a compressive force to the thin film causing the film to buckle, creating highly ordered sinusoidal wrinkles perpendicular to the direction of the applied force. Surface wrinkles have been generated using thermal contraction,<sup>5-7</sup> externally applied forces,<sup>7-9</sup> ion beam bombardment,<sup>10</sup> or differential swelling or shrinking<sup>11-13</sup> to apply buckling forces to thin films. For small strains, the formation of wrinkles is predicted well by minimizing the total elastic energy in a uniaxial bilayer system whose wavelength ( $\lambda$ ) and amplitude (A) are given by the following:<sup>14,15</sup>

$$\lambda = 2\pi h_f \left( \frac{\bar{E}_f}{3E_s} \right)^{\frac{1}{3}} \quad (\text{Eqn. 5-1})$$

$$A = h_f \left( \frac{\varepsilon}{\varepsilon_c} - 1 \right)^{\frac{1}{2}} \quad (\text{Eqn. 5-2})$$

$$\varepsilon_c = \frac{1}{4} \left( \frac{3E_s}{\bar{E}_f} \right)^{\frac{2}{3}} \quad (\text{Eqn. 5-3})$$

Where,

$$\bar{E} = E / (1 - \nu^2) \quad (\text{Eqn. 5-4})$$

And  $\varepsilon_c$  is the critical minimum strain required for buckling,  $h_f$  is the film thickness,  $\nu$  is the Poisson ratio, and  $E_f$  and  $E_s$  are the plane-strain moduli of the film and substrate, respectively.

A large variety of wrinkling platforms that generate many different types of wrinkles have all been developed. Poly(dimethylsiloxane) is a widely used wrinkling substrate and has

been used to generate wrinkles by coating with metals<sup>16,17</sup> or the surface has been hardened using plasma oxidation,<sup>18</sup> UV exposure<sup>6,19–22</sup> or ion beam bombardment<sup>10</sup> to generate a hard film. Using these materials and film platforms, wrinkle patterns ranging from homogenous<sup>23</sup> to hierarchical,<sup>12,24–26</sup> one-dimensional ripple patterns<sup>27</sup> to two-dimensional herringbone,<sup>17</sup> and more complex patterns<sup>28</sup> have all been generated. There is a growing interest in such wrinkling platforms for application in stretchable electronics,<sup>21,23,29</sup> microfluidics devices,<sup>30</sup> controlled wettability,<sup>19,20</sup> micro-lens arrays,<sup>31</sup> optical gratings,<sup>32</sup> precision metrology,<sup>23</sup> smart adhesion,<sup>33</sup> and for controlling cell behavior.<sup>12,34,35</sup>

Recently, researchers have begun using shape memory polymers (SMPs) as material platforms to “actively” induce wrinkling in response to an external stimulus. The first reported use of an SMP as a wrinkling substrate was done by Fu and colleagues where they stretched a sheet of polystyrene, both uniaxially and biaxially and coated the surface with a 10 nm layer of gold to generate both uniaxial and biaxial wrinkle patterns.<sup>36</sup> Since then, several examples of SMP wrinkling platforms have been developed<sup>14,37–39</sup> and recently reviewed.<sup>29</sup> Our group has also generated two active wrinkling platforms to study cell behavior in response to the formation of topographies during cell experiments. Both platforms developed by Yang *et. al.*<sup>35</sup> and Ash-Shakoor *et. al.* could generate wrinkles while cells were adhered to, causing the cells to transition their morphology and migration behavior.<sup>34</sup> Ash-Shakoor also explored the potential for reversible wrinkling using this SMP platform.

Despite high interest in SMPs as wrinkling platforms, wrinkling using multi-shape materials have not to date been reported. Multi-shape memory materials are a subset of SMPs that can learn multiple temporary shapes, enabling the material to change shape multiple times. This could enable the formation of more complex surface wrinkles using a very controlled and

deliberate method. Other groups have developed more complex and hierarchical wrinkle patterns in the past using a PDMS platform strained into various complex shapes. Most notably Vandeparre *et al.* generated complex radial wrinkles along the surface of a titanium coated polystyrene film using solvent deformation.<sup>12</sup> Most notably when they cultured cells on such patterns they observed that the cells seemed to be pinned down by the wrinkle patterns. By utilizing multi-shape memory materials we hypothesize that we can form complex wrinkle patterns in a controlled way that could later be applied to cell mechanobiological studies.

To accomplish this, we used a triple shape polymeric composite (TSPC) previously designed in our group by Luo and colleagues<sup>40</sup> as a platform to generate complex or double wrinkle patterns. TSPCs made by encasing a PCL fiber mat in a matrix of epoxy were programmed either uniaxially or biaxially and then coated with a gold film. By exploiting an SMPs precise recovery ability we were able to study the formation of these patterns by using both a 1 step and 2 step recovery approach.

## 5.3 Materials and Methods

### 5.3.1 Materials

All chemicals including diglycidyl ether of bisphenol-A (DGEBA), neopentyl glycol diglycidyl ether (NGDE), O,O'-Bis(2-aminopropyl)polypropylene glycol (Jeffamine D230), dimethyl formadine and poly( $\epsilon$ -caprolactone) (PCL) (nominal Mw = 90 000 g/mol) were purchased from Sigma-Aldrich and used as received. Chloroform was purchased from Fisher Scientific and used as received.

### 5.3.2 Preparation of Triple Shape Polymeric Composites

Triple shape memory composites (TSPCs) were prepared using methods established by Luo *et. al.*<sup>40</sup> Briefly, a 20 wt% electrospinning solution of PCL was first prepared by dissolving 2g of PCL in 10 mL of a 4:1 by volume solution of chloroform to DMF. Electrospinning was conducted using a custom-built set up that is composed of a high voltage power supply (Agilent E3630A), a syringe pump (KDS100, KD Scientific), a low voltage negative power supply (PS 500XT, Hofer Scientific) and a 5 cm diameter rotating drum. Fiber mats were spun using a constant flow rate of 2 mL/h with an applied voltage of 12kV at needle-collector distance of 10 cm. The fibers were collected on a negatively charged mandrel (-500V) rotating at 800 rpm with a slow horizontal translation along the collecting drum axis (perpendicular to the electrospinning jet direction) to ensure that a uniform, randomly oriented fiber mat was produced. Then a molar solution of NGDE:DGEBA monomer solution was mixed together for 2 min. The molar solution was varied to precisely control the glass transition ( $T_g$ ) of the resulting epoxy matrix to ensure the programmed strain was stable during processing but far enough away from the melt transition of the PCL to be resolvable. A 50 molar ratio of Jeffamine-230 was added to the solution and stirred for an additional 2 min. The solution was then imbibed into an electrospun PCL fiber mat and vacuum-infiltrated for 20 min. The composite was finally cured at 40 °C for 48 h, to prevent melting of the PCL fiber phase before matrix vitrification, and then 60 °C for 24h to ensure complete cure.

### 5.3.3 Thermal Characterization

TSPCs were thermally characterized using Dynamic scanning calorimetry (DSC) and dynamic mechanical analysis (DMA). DSC was performed on all composites to ensure the glass transition ( $T_g$ ) and melt transitions ( $T_m$ ) were suitably apart, using a Q200 (TA instrument)

equipped with a refrigerated cooling system. For each test, samples weighing 3-5 mg were loaded into a T-zero aluminum pan and first equilibrated by cooling to -10 °C. Samples were then heated at a rate of 10 °C/min to 100 °C and cooled at a rate of 5 °C/min to -10 °C, this initial heating being used to erase any thermal history. Samples were then heated by 10 °C/min to 100 °C to measure the  $T_g$  and  $T_m$  of the composite materials. Dynamic Mechanical Analysis was used to measure the temperature dependences of the tensile storage modulus for all materials using a Q800 (TA Instruments). Samples featured variable dimensions with typical values of length, width and thickness of 6.25, 1.5, and 0.2 mm, respectively. The samples were first heated to 80 °C and then cooled at a rate of 2 °C/min to 0 °C to erase the thermal history of the sample. Samples were then heated at a rate of 2 °C/min to 180 °C while applying a small tensile deformation of 20  $\mu\text{m}$  (0.4 %) at an oscillation frequency of 1 Hz. Only composites that showed separation between the  $T_g$  of the epoxy and  $T_m$  of the PCL were used in subsequent studies to ensure both material recoveries could be triggered independently.

#### 5.3.4 Triple Shape Memory Behavior

The triple shape memory behavior of the composites was measured in the DMA. First dog bone samples were cut from the composites using a dog bone punch. The sample was then loaded into the DMA and heated to 80 °C. At this point, the instrument was stopped and restarted to zero out any thermal strain and the run restarted. The sample was heated to 80 °C and stretched to 10% strain. The sample was then cooled to 0 °C to crystallize the PCL and fix the first temporary shape. The sample was then heated to 50 °C, just below the  $T_m$  of the PCL. The sample was then stretched another 10% to program into the epoxy phase of the composite and again cooled to 0 °C to fix the second temporary shape. The force was then unloaded and the

sample was heated at 2 °C/min to capture the recovery of the material. The shape fixing of the epoxy and PCL phases was assessed using eqns. (5) and (6):

$$R_f(x) = \frac{\varepsilon_x}{\varepsilon_{x, \text{load}}} \quad (\text{Eqn. 5-5})$$

$$R_r(x \rightarrow y) = \frac{\varepsilon_x - \varepsilon_{y, \text{rec}}}{\varepsilon_x - \varepsilon_y}. \quad (\text{Eqn. 5-6})$$

In Eqn. (5),  $\varepsilon_x$ ,  $\varepsilon_{x, \text{load}}$  are the strains measured after cooling and after unloading (thus, the strain fixed) and before unloading (thus attempted strain fixing). In Eqn. (6), additional terms include  $\varepsilon_{y, \text{rec}}$ , the strain achieved after recovery for shape y and  $\varepsilon_y$ , the strain before programming shape y (x can be a strain at 80 °C or 50 °C, or 0 °C, the same holds for y). For strains programmed at 80 °C (strain programmed for PCL-based fixing),  $\varepsilon_x$  was measured after the sample had been heated to 50 °C to ensure that only the strain programmed into the PCL was used for the final calculation.

### 5.3.5 Programming Triple Shape Polymeric Composites to Make Complex Wrinkle Patterns

To program TSPCs to generate complex wrinkle patterns, TSPCs were first cut into 25 x 125 mm strips and mounted into a custom manual stretcher. The location of the clamps was marked using a sharpie and the length of the sample between the stretcher was recorded. The stretcher was then placed in an isothermal oven at 70 °C, above the  $T_m$  of PCL for 10 m. The distance between the clamps was then adjusted so the samples were flat and straight in between the clamps and the length measured again to zero out any thermal strain. The samples were then strained to either 10, 15 or 20% strain and then left to sit in the isothermal oven for an additional 2 m. The stretcher was placed in a freezer to cool the sample to -20 °C and fix the first strain. The sample strip was then removed from the stretcher and the distance between the sharpie

marks was measured again since the sample had a tendency to thermally expand as the PCL crystallized. The sample strip was then placed in an isothermal oven at 49 °C, just above the  $T_g$  of the epoxy but below the  $T_m$  of the PCL. This allowed the strain programmed into the epoxy to recover, leaving only the strain programmed into the PCL. The length between the sharpie marks was then measured again and the final fixed strain was calculated.

At this point, the samples were cut into 4 x 25 mm strips to maintain the 1:5 width to length ratio required for uniaxial stretching conditions. Eight strips were cut parallel to the original strain direction and eight strips were cut perpendicular to the original strain direction. Upon strain recovery, this would either create two wrinkling events in the same direction (uniaxial wrinkles) or wrinkle patterns with a 90° angle between them (biaxial wrinkling). The smaller sample strips were then mounted into a Q800 Dynamic mechanical analyzer (DMA). The DMA then equilibrated the temperature to 49 °C, re-measured the length of the sample and then strained the composite to either 5, 10, or 15% epoxy strain, cooled the sample to 0 °C, and the force was unloaded. Once programmed the samples were stored in the freezer to prevent any pre-recovery from occurring until the samples were ready to be coated. The TSPC strips were then washed with soap and water to clean the surface and then placed in a sputter coater with the surface cured against the glass face up (or the smoothest side). The samples were then sputter-coated in 10s increments for a total of 100s to create a 36 nm thick layer of gold over the surface.<sup>35</sup> Samples were carefully monitored during sputter coating to ensure the samples did not recover before being completely coated which is indicated by the sample strips curling during coating.

### 5.3.6 Sample Recovery and Imaging Protocol

Once coated, the samples were imaged using an atomic force microscope (AFM) before any recovery could take place. Briefly, the samples were cut into small squares and mounted onto an imaging plate. The samples were then loaded into the AFM and a 100 x 100  $\mu\text{m}$  square section was scanned using contact mode at a frequency of 2 Hz. The samples were then divided in half and put through two separate recovery protocols. The first recovery protocol was a two-step method where the two strains were triggered to recover sequentially. After taking the first image scan, the samples were then heated to 50  $^{\circ}\text{C}$ , above the  $T_g$  of the epoxy but below the  $T_m$  of the PCL, which allowed the strain programmed into the epoxy to recover and for the first wrinkle pattern to form. The samples were then imaged again to assess the characteristics of the first wrinkle pattern. Afterward, the samples were placed in an oven at 60  $^{\circ}\text{C}$ , above the  $T_m$  of the PCL, to recover the second strain and allow the second wrinkle pattern to form. The samples were then imaged one final time to characterize the features of the double or complex wrinkle patterns. The second recovery protocol was a one-step method, where the samples were heated directly to 60  $^{\circ}\text{C}$  allowing both the epoxy and PCL strains to recover as close to the same time as possible. It should be noted however that there will always be a small lag between the triggered recovery of the epoxy phase and the recovery of the PCL phase due to the difference in temperature used. The resulting double wrinkle patterns were then imaged.

### 5.3.7 Characterizing Wrinkled Surfaces

AFM images were analyzed with the software platform Gwyddion 2.52. Multiple image correction commands were implemented. First, the image was leveled by mean squared subtraction and then horizontal scars were removed using the “leveling” and “remove horizontal scars” command, respectively. The “align rows using various methods” were then used to



remove any remaining horizontal line artifacts in the images. The minimum data was then shifted to zero and the color balance was set to warm. The average roughness ( $R_a$ ) (Eqn. 5-7) and the means square roughness ( $R_{ms}$ ) (Eqn. 5-8) were then pulled from the statistical quantities chart.

$$R_a = \frac{1}{N} \sum_{j=1}^N |x_j - \hat{x}| \quad \text{Eqn. 5-7}$$

$$R_{ms} = \sqrt{\frac{1}{N} \sum_{j=1}^N |x_j - \hat{x}|^2} \quad \text{Eqn. 5-8}$$

Where  $x_j$  is the peak and valleys height value and  $\hat{x}$  is the average height across the image.

A two-dimensional fast-Fourier transform (2D FFT) was then taken of the image and saved. A 2D power spectrum density was then taken from the 2D FFT to evaluate any characteristic spatial frequencies occurring on the surface indicative of wrinkle formation. The peaks in the PSDF function correspond to the principle sinusoidal waveforms characteristic of the wrinkle patterns formed along the surface. The main three peaks of the PSDF are then fit with a Lorentzian curve (Eqn. 5-9) and the  $x_0$  and  $a$  terms were recorded.

$$f(x) = y_0 + \frac{a}{[b^2 + (x - x_0)^2]} \quad \text{Eqn. 5-9}$$

$x_0$  is the inverse of the principle wavelength of the sinusoidal curve and the  $a$  term is related to the amplitude. For evaluation, the  $x_0$  values were inverted and averaged to report an average wavelength for the image. The  $a$  terms were summed for each image, converted from units of pm to m, and then square rooted. The calculated value was then reported as a relative amplitude since we believe that there is a numerical conversion that we have yet to address. As such the amplitude can only be judged based on its relative trends and no further statistical trends can be reported.

For the scope of this study, all wrinkle images came from a single experimental run from two separate composites that were compositionally similar using both DSC and mass measurements. This was done to minimize the potential variable impacts of composition on wrinkle pattern formation which would have made it difficult to see any noticeable trends. However, due to the difficulty with making composites that were compositionally similar the number of experimental replicates was limited. This means that all samples stretched at the three different PCL strains all came from one large strip that was correspondingly cut into the 24 sample strips used to then program the epoxy strain. In addition, the 15% PCL, 10% epoxy biaxially strained samples were recovered prematurely which prevented them from being used in subsequent analysis.

## 5.4 Results

### 5.4.1 Preparation of Triple Shape Memory Composites

TSPCs were prepared by embedding an electrospun mat of PCL in an epoxy matrix of with a 51:49 molar ratio of DGEBA to NGDE according to methods established by Luo and colleagues.<sup>40</sup> Briefly, the PCL fiber mat was soaked in the epoxy monomer solution and then laid on a clean piece of glass. The glass ensured that one side of the material was perfectly smooth for the formation of wrinkle patterns. The composite was then rolled against the glass to remove any excess epoxy monomers. The composite was then cured at 40 °C for 48 hours to allow the matrix to vitrify. This preserved the morphology of the PCL fibers even after cure. The temperature was then increased to 60 °C for 24 hours to ensure complete cure of the epoxy matrix (Scheme 5-1). The resulting composite was opaque, indicating the composite components existed in two separate phases.

### 5.4.2 Thermal Characterization

DSC (Fig. 5-1) was used to ensure the  $T_g$  of the epoxy was within the target range before any further experiments were run. If the epoxy  $T_g$  deviated from the target  $T_g$  of 45-48 °C, the material was discarded and a new one was made to prevent the pre-recovery of the SMP during coating. DMA was used to measure the temperature dependence of the storage modulus and to ensure that there were two separate mechanical transitions, a requirement for multi-shape memory. DMA revealed (Fig. 5-2) that there were two separate mechanical transitions, one large from the  $T_g$  of the epoxy and one small from the  $T_m$  of the PCL.

### 5.4.3 Triple Shape Memory Behavior

The triple shape memory behavior was assessed (Fig. 5-3) by first loading a dog bone sample into a DMA. The sample was first heated to 80 °C (above the  $T_g$  and  $T_m$  of the composite) and strained to 10%. The sample was then cooled to 0 °C to fix the temporary shape in the PCL phase of the material. The sample was then heated to 51 °C, just above the  $T_g$  of the epoxy but below the  $T_m$  of the PCL and strained another 10%. The sample was then cooled to 0 °C and the strain unloaded. The sample was then heated at a rate of 2 °C/min to capture the recovery event. The cycle was repeated three times and the fixing (Eqn. 5-5) and recovery ratios (Eqn. 5-6) were calculated from each cycle. Upon recovery, the composite showed two clearly defined recovery events first for the epoxy and then the PCL. The epoxy and PCL showed high fixing ratios of 91.4% and 93.3% respectively. The recovery ratios of the epoxy and PCL were 84.2% and 88.7%, respectively demonstrating the strong recovery ability of the composites. It should be noted that the strain was not unloaded between the programming of PCL and epoxy however, making an accurate measure of the strain fixed in the PCL phase difficult.

#### 5.4.4 Generating Complex Wrinkle Patterns

All samples were programmed in a two-step fashion using the method described above. Samples programmed with 5, 10, 15% strain in the PCL phase and 5, 10, 15% strain in the epoxy phase in either the same direction (uniaxial) or orthogonal to each other (biaxial) (Scheme 5-2). Each sample was then sputter-coated with gold and then imaged in the AFM prior to recovery (Fig 5-4, 5-5). All samples prior to recovery showed a flat, smooth surface with minor surface imperfections from processing. The 2DFFT showed only a circle in the center of the pattern indicating that no sinusoidal patterning existed in the material. The samples were then put through either a two-step or one-step recovery process to allow for the strains to either recover sequentially or at the same time.

The samples with either 5, 10, or 15% strain programmed into the samples all showed the formation of a sinusoidal wrinkles after heating to 50 °C (above the  $T_g$  of the epoxy), while the sample programmed with 0% epoxy strain remained flat (Fig 5-6, 5-8). The 2DFFT for images with wrinkles transitioned from a round circle to a barbell shape, indicating the presence of a sinusoidal pattern along the surface. The 15% PCL, 15% Epoxy biaxially samples were damaged during processing and as such are not shown with the current analysis. The  $R_a$ ,  $R_{ms}$ , average wavelength and average relative amplitude were measured (Fig 5-7, 5-9) for both the biaxially and uniaxially programmed samples. For both the biaxially (Fig 5-7A, 5-7B) and uniaxially (Fig 5-9A, 5-9B) programmed samples, no trend was observed in the  $R_a$  or the  $R_{ms}$  for either the epoxy or PCL strain. The average wavelength (Fig 5-7C) of the biaxially programmed wrinkles increased with increasing PCL strain but remained constant with increasing epoxy strain. The relative amplitude (Fig 5-7D) showed no trend with either the PCL or epoxy strain. Similarly, the average wavelength for the uniaxially programmed samples (Fig 5-9C) showed a slight

increasing trend with increasing epoxy strain, but the trend was much weaker than what was observed in the biaxially programmed samples. There was no discernible trend in the relative amplitude for the uniaxially programmed samples (Fig 5-9D).

Samples were then recovered at 60 °C, and complex double wrinkle patterns were observed in the case where the strain was programmed biaxially and the programmed epoxy strain was low. For the case where no epoxy strain was programmed, the samples showed a wrinkle pattern in the direction of the PCL strain, either 90° for the biaxially programmed samples (Fig. 5-10) or 0° for the uniaxially programmed samples (Fig. 5-12). For the biaxially programmed strain, only the 5% epoxy strained samples showed a discernable double wrinkle pattern, indicated by the presence of two barbell patterns in the 2DFFT scans of the images (Fig 5-10). As the programmed epoxy strain increased the double wrinkle pattern did not form. Interestingly the 15% PCL strain-0% epoxy samples showed some double wrinkle patterns which may be due to a Poisson effect (Fig 5-12). The  $R_a$ ,  $R_{ms}$ , average wavelength and average relative amplitude were assessed for both the parallel and perpendicular (when applicable) wrinkles separately (Fig 5-11, 5-13). Again for both the biaxially (Fig 5-11A, B) and uniaxially (Fig 5-13A, B) no trend was observed in the average roughness or mean square roughness with either epoxy or PCL strain. For the biaxially programmed samples (Fig 5-11C), the wavelength of the wrinkle patterns formed by the PCL strain was higher than the wavelength of the wrinkles formed by the PCL. The wavelength of the epoxy wrinkles increased with increasing PCL strain as observed for the 50 °C recovery. The relative amplitude of the PCL wrinkles decreased with increasing epoxy strain (Fig. 5-11D) and no trend was observed in the epoxy wrinkles. Similarly, the wrinkles formed with PCL strain had a higher wavelength compared to the epoxy wrinkles but were only observable for the case where no strain had been programmed into the epoxy (Fig. 5-

13C). The wavelength of the uniaxial wrinkles showed no trend with increasing epoxy strain and did not noticeably change in value from the 50 °C recovery. There was no observable change in the relative amplitude for the uniaxially programmed samples (Fig 5-13D).

Samples recovered with a one-step recovery profile showed double wrinkle patterns under more programming conditions compared to those recovered using a two-step recovery profile. Similar to the two-step recovery, some samples with no epoxy programmed strain showed the double wrinkle patterns, potentially due to a Poisson effect. For biaxially programmed samples the double wrinkle patterns were observable for samples programmed with more than 15% PCL strain (6% fixed) and less than 15% epoxy strain (Fig. 5-14). For the uniaxially programmed samples, programmed with a large amount of PCL strain and no epoxy strain also showed some double nature, most likely due to the Poisson effect (Fig. 5-16). For both uniaxially and biaxially programmed samples, no trend in the  $R_a$  or the  $R_{ms}$  was observed with programmed PCL or epoxy strain (Fig 5-15, 5-17). The wavelength of the PCL wrinkles increased with increasing epoxy strain while the wavelength of the epoxy wrinkles showed no change over time (Fig 5-15C). The relative amplitude of the PCL wrinkles decreased with increasing epoxy strain and no trend was observed for the relative amplitude of the epoxy wrinkles in the biaxially programmed samples (Fig. 5-15D). No trend was observable for either the average wavelength or relative amplitude for either the PCL or epoxy wrinkles in the uniaxially programmed samples (Fig. 5-17).

## 5.5 Discussion

Overall, the generation of complex wrinkle topographies along the surface of TSPCs was successful when the programmed strains were perpendicular and the final fixed strains were close in value. To the best of our knowledge, this is the first example of applying a wrinkling

platform to a multi-shape memory material to generate complex, double wrinkle patterns utilizing two independent and well-controlled step transitions. We did observe that the complex wrinkle patterns did not form in samples where the epoxy strain was high compared to the PCL strain. For the cases where double wrinkle patterns were observed the wavelength of the 2<sup>nd</sup> pattern was larger compared to the wavelength of the first wrinkle pattern. We believe this increase is due to the corrugation stiffening of the gold film after the formation of the first wrinkle pattern. Another potential reason for the difference is during the formation of the first wrinkle pattern, the SMP matrix is undergoing a T<sub>g</sub> which changes the stiffness of the matrix. This means that during the formation of the first wrinkle pattern, the matrix stiffness is transitioning from stiff to soft which would impact the formation of the wrinkle patterns. In contrast, when the 2<sup>nd</sup> pattern forms the matrix is fully soft which according to Eqn. 5-1 would decrease the predicted wavelength of the wrinkle patterns.

However, there are many limitations to the current work. The first is the shape memory ability of multi-shape memory composites is highly dependent on the composition of the composite, a factor that can be difficult to control using the current manufacturing method. For the current system, the main problem was in the cases where the PCL composition was high (thus giving the PCL transition a stronger shape memory fixing ability) the PCL fibers would pull out to the surface of the composite. This added a separate roughness pattern that disrupted the formation of wrinkles which forced us to use a lower composition of PCL. This could be potentially addressed by using a polymerization induced phase separation technique, similar to the one developed by Torbati and colleagues.<sup>41</sup> Due to these limitations all the samples analyzed are taken from just two composites and cut from just four larger strips. This means that the PCL stretch was only done once for each PCL strain condition, while the epoxy stretch was done three

times. Ideally, this would be repeated at least 3 times however the difficulty with controlling the %PCL content made doing so difficult. Being able to better control these factors would allow us to both repeat this study but also further change the angle between the programmed strains to potentially observe different patterns.

The second limitation is in the analysis technique. These double wrinkle patterns were difficult to analyze since it was difficult to separate the two patterns even using multiple filtering methods. This limited the conclusions that could be drawn from the experimental data. Ideally, future work for this will include a mathematical model to better understand what factors are important in this type of double wrinkle formation.

Finally, the current TSPC is not ready for cell culture due to two factors. The first is to the best of our knowledge and ability it appears that the epoxy matrix used in the fabrication of TSPCs is cytotoxic. This conclusion was drawn after several attempts made by several researchers to grow cells on the surface of the epoxy materials. This could be addressed by changing this matrix out for another SMP material like Yang and colleagues<sup>35</sup> used in their work. The second is the PCL recovery requires heating the polymer above 55 °C, which is too high for cultured cells to survive. We could switch this out for a material with a lower transition temperature, but that would make it impossible to program two separate strains into the two material phases. An alternative would be designing a multi-shape memory composite that is both temperature and light-triggered, allowing the first wrinkle pattern to be triggered by temperature and the second wrinkle pattern to be triggered by light. Light triggered wrinkle formation is already being explored by other research groups because of the advantage of being able to precisely control the formation of wrinkles along the surface of a material. For instance, Haan and colleagues developed wrinkle platform by coating liquid crystal elastomers with gold and



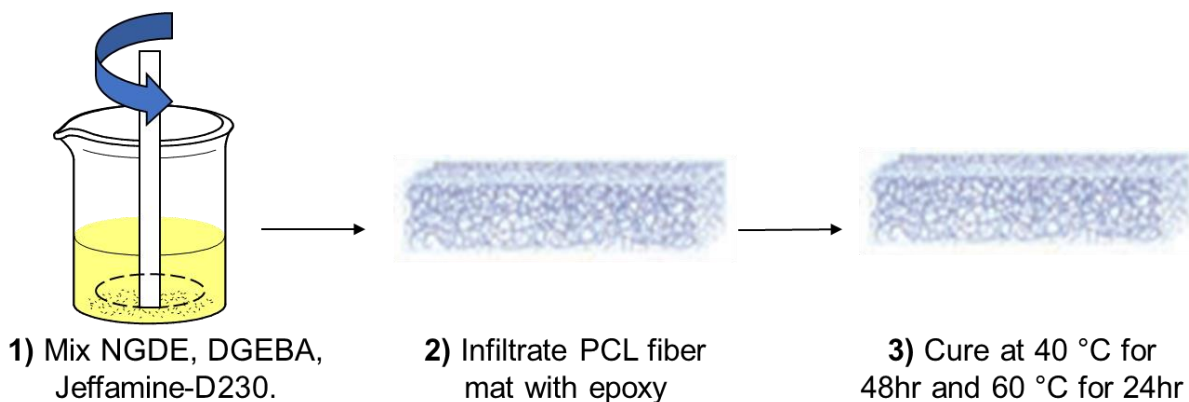
showed contactless wrinkle pattern formation that could be spatially controlled well enough to draw the face of a person.<sup>1</sup> In addition, this could be a potentially powerful platform to study cell behavior as one could create very precise boundary conditions and assess cell behavior as cells move across these boundaries.

## 5.6 Conclusions and Future Work

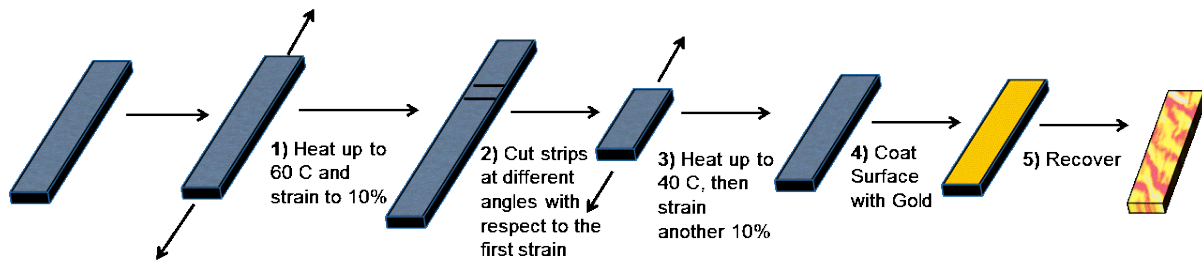
In conclusion, we have successfully demonstrated using TSPCs to generate complex or double wrinkle patterns. There were no observable trends in the roughness of the surfaces or amplitude of the wrinkles formed. The wavelength, however, did show a dependence on what shape recovery generated the wrinkle pattern either due to a corrugation stiffening effect or due to a decrease in the substrate modulus. However, there are several challenges that need to be addressed before using this platform for cell mechanobiological studies. These challenges would involve changing the material composition, fabrication method and using different shape memory triggering mechanisms.

## 5.7 Acknowledgements

Funding from the NSF IGERT Program (DGE-1068780), the NSF DMREF award (DGE-1334658) and REU Supplement (DMR-1743080), is gratefully acknowledged, as is use of the facilities of the Syracuse Biomaterial Institute at Syracuse University. In addition, the student contributions of Leila Hart and Derek Loh are acknowledged



**Scheme 5-1.** Fabrication schematic for making TSPCs. The epoxy components were first mixed in a beaker until well mixed. The mixture was then poured over an electrospun fiber mat of PCL and placed against a piece of clean and smooth glass. The material was rolled to get some excess epoxy out of the fibers and ensure good contact with the glass. This ensured that one side of the material was atomically smooth like the glass. The epoxy was then cured against the glass at 40 °C for 48 hours to partially cure the epoxy to hold the fiber morphology of the PCL in the composite material. The temperature was then increased to 60 °C to ensure complete cure of the epoxy.



**Scheme 5-2.** Schematic of how to program the TSPCs to generate complex or double wrinkle patterns. First, a large strip of the material is heated to 70 C, above the  $T_m$  of the PCL component and strained to either 10, 15 or 20% strain. The strip is then cooled and cut into smaller sections either parallel to the original stretch direction, or perpendicular (depicted here). The smaller strips are then heated to 49 C and strained a second time to program in the second strain. The samples are then coated with a thin layer of gold and triggered to recover, forming wrinkle patterns.

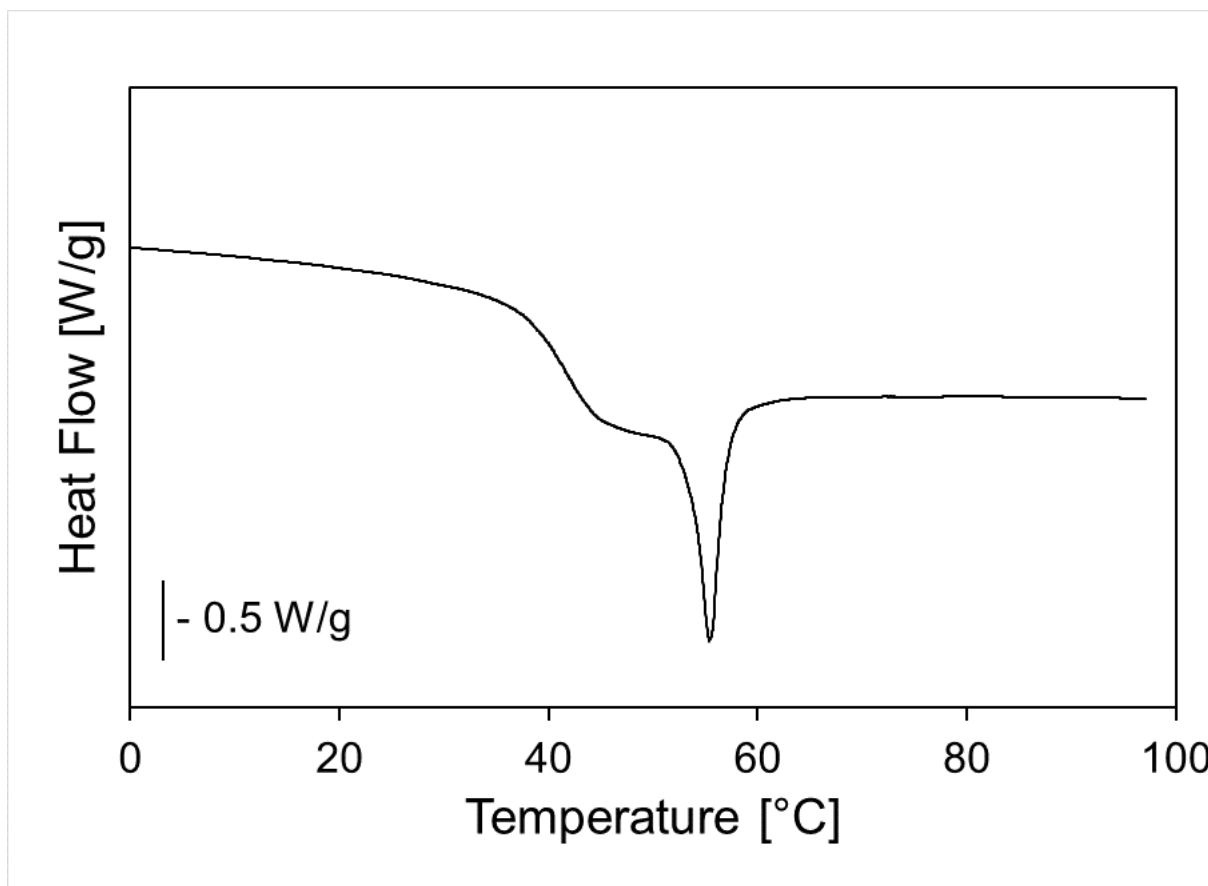


**Figure 5-1.** An example DSC trace of a TSMC showing two distinct thermal transitions per composite. The  $T_g$  of the epoxy was carefully controlled by controlling the composition of the epoxy monomers and selected so that the  $T_g$  was high enough to prevent recovery during gold coating but low enough to ensure good separation between the  $T_g$  of the epoxy and the  $T_m$  of the PCL. Specifically, a  $T_g$  of 45-48 °C was target for the epoxy monomers.

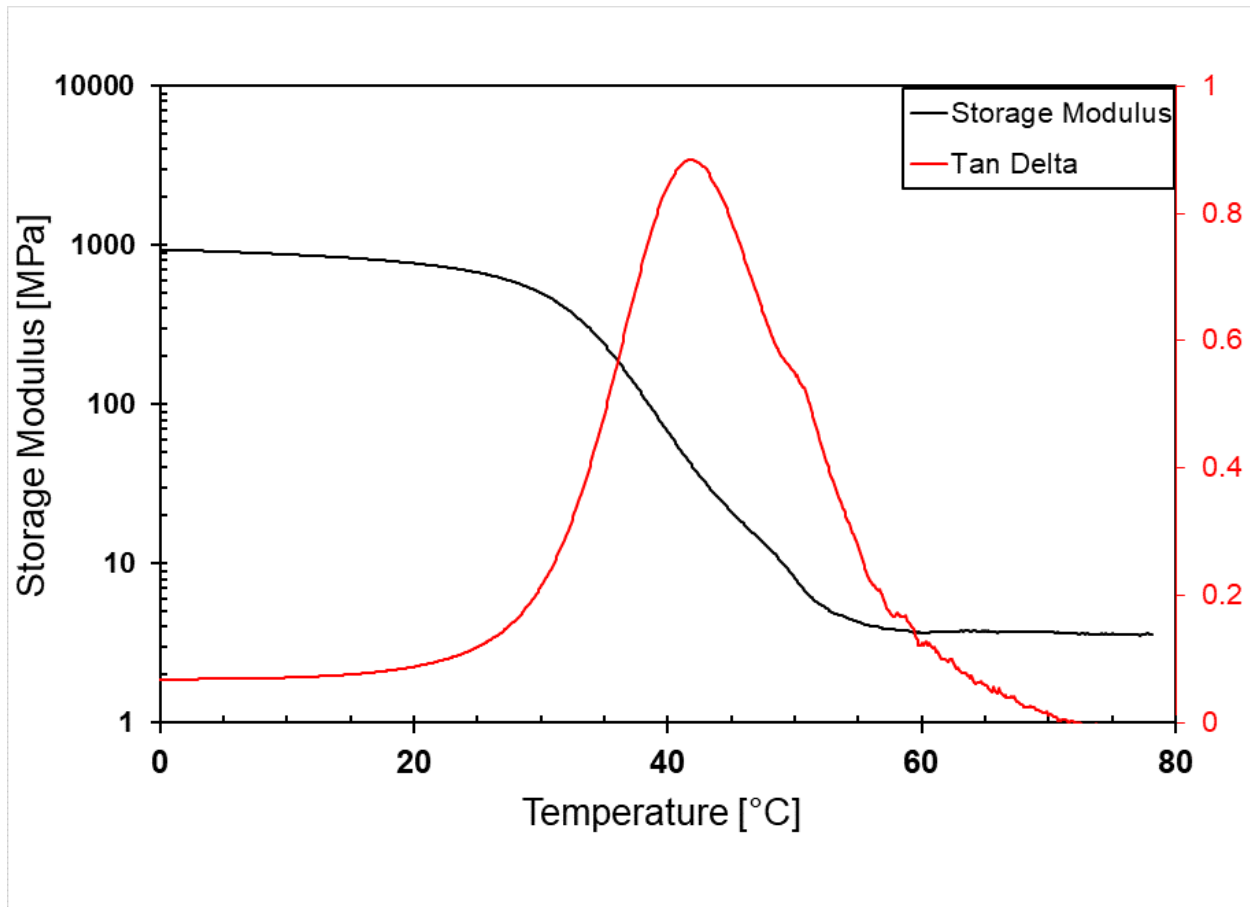


**Figure 5-2.** A DMA sweep showing the temperature dependence of the modulus of the TSPCs. The storage modulus trace shows a small separation between the two transitions, while the tan delta shows a secondary hump, indicating two separate mechanical transitions.

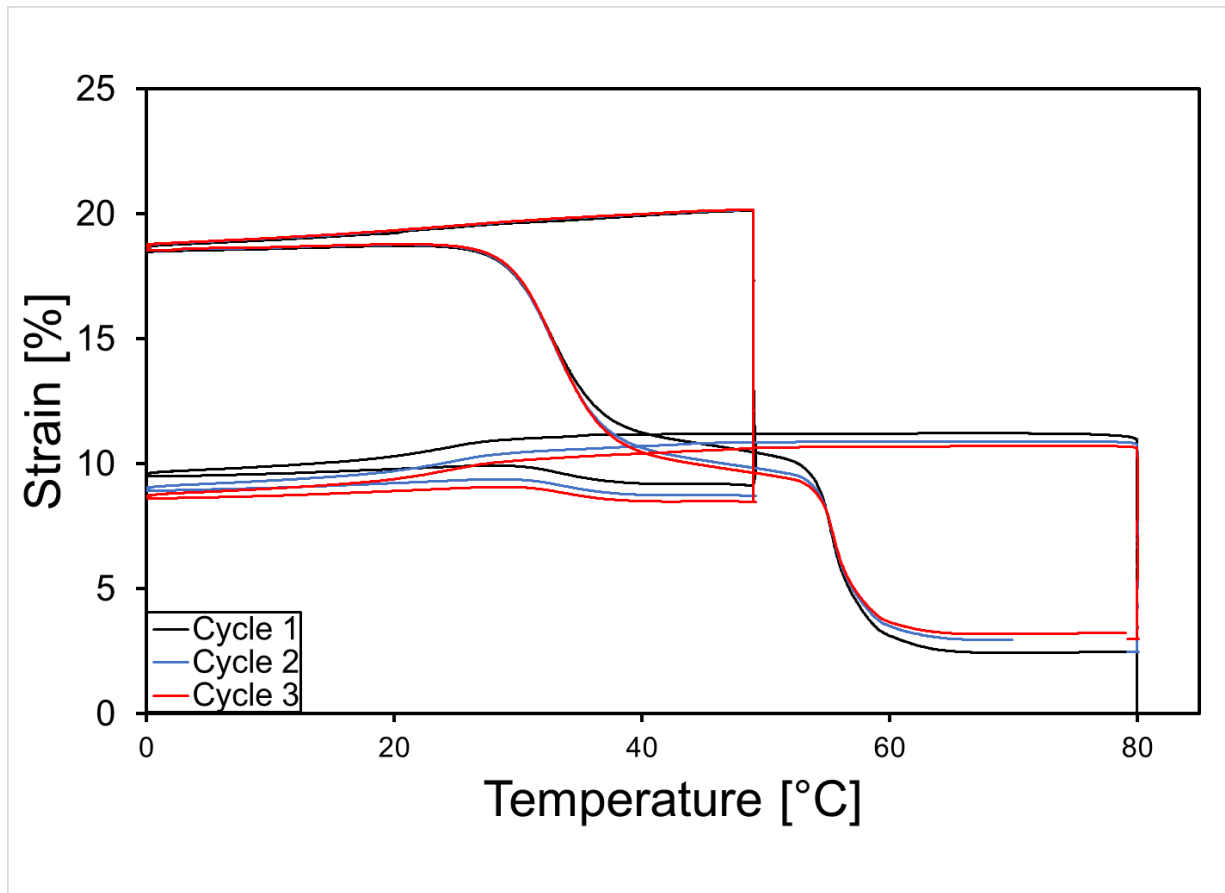


**Figure 5-3.** An example triple shape memory cycle (TSMC). The dog bone sample is first heated to 80 °C and stretched to program a strain into the PCL phase of the sample. The temperature is then cooled to 0 °C to crystallize the PCL and fix the first temporary shape. The temperature is then increased to 50 °C and strained again to program a temporary shape into the epoxy phase of the material. The material is then cooled to 0 °C to fix the second temporary shape and the force removed. The sample is then heated at a continuous rate to capture the recovery event. The epoxy and PCL showed a fixing ratio of 91.4% and 93.3%, respectively and a recovery ratio of 84.2% and 88.7%, respectively.

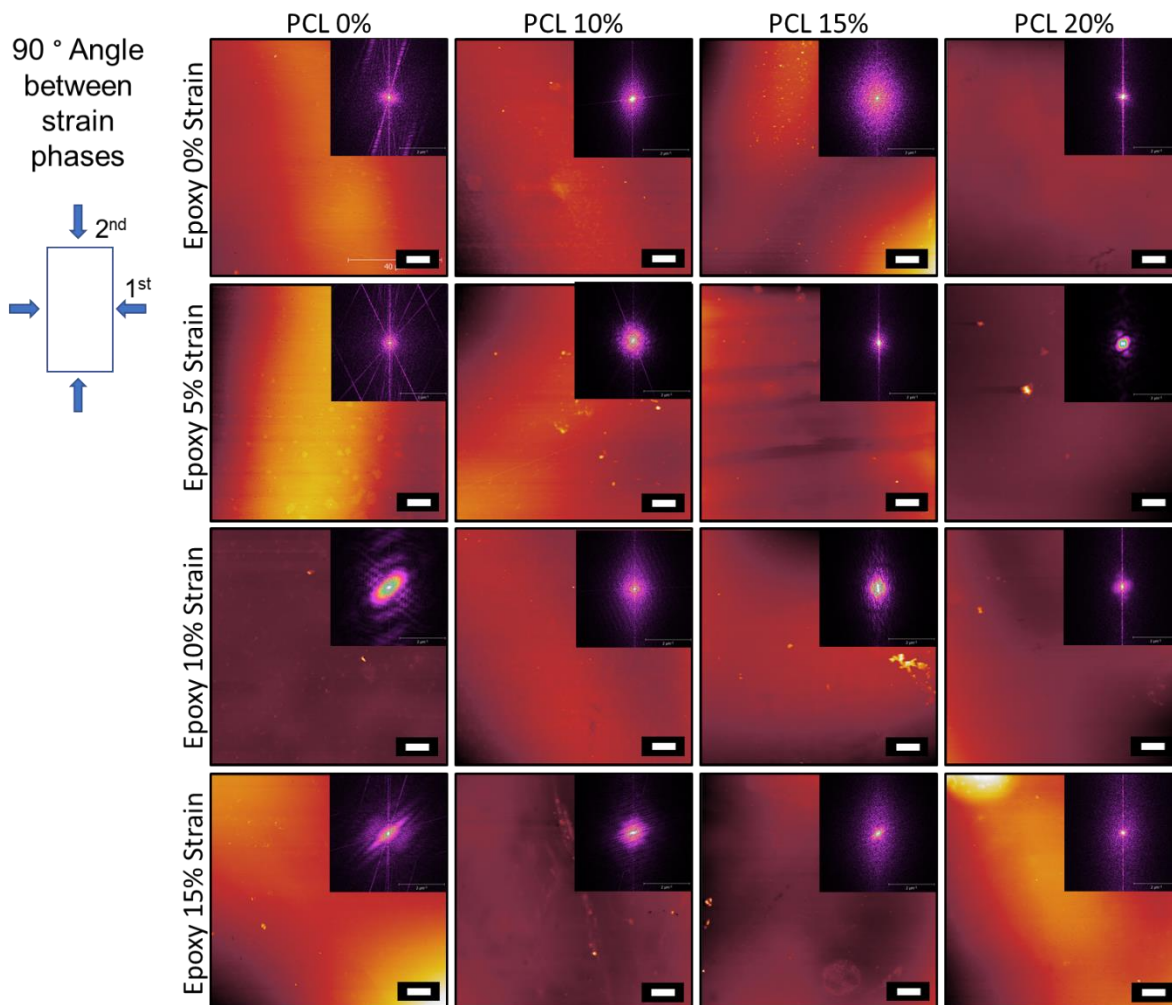


**Figure 5-4.** AFM micrographs of the TSPC surfaces after coating the samples with gold but prior to any recovery steps for the biaxially programmed samples. The surfaces all showed no sinusoidal wrinkle patterns and were all very flat. Scale bar is 10  $\mu\text{m}$ .

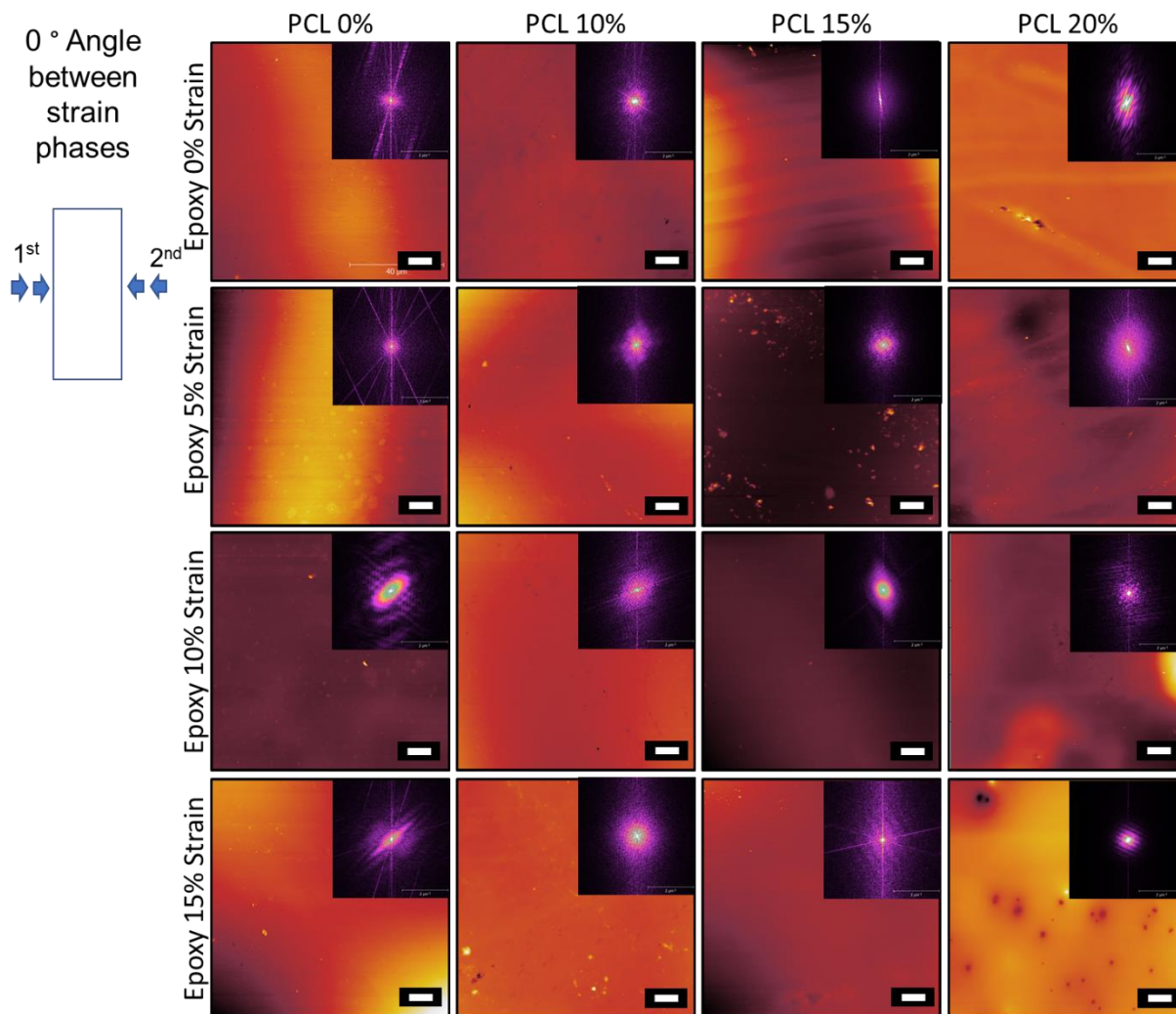


**Figure 5-5.** AFM micrographs of the TSPC surfaces after coating the samples with gold but prior to any recovery steps for the uniaxially programmed samples. The surfaces all showed no sinusoidal wrinkle patterns and were all very flat. Scale bar is 10  $\mu\text{m}$ .



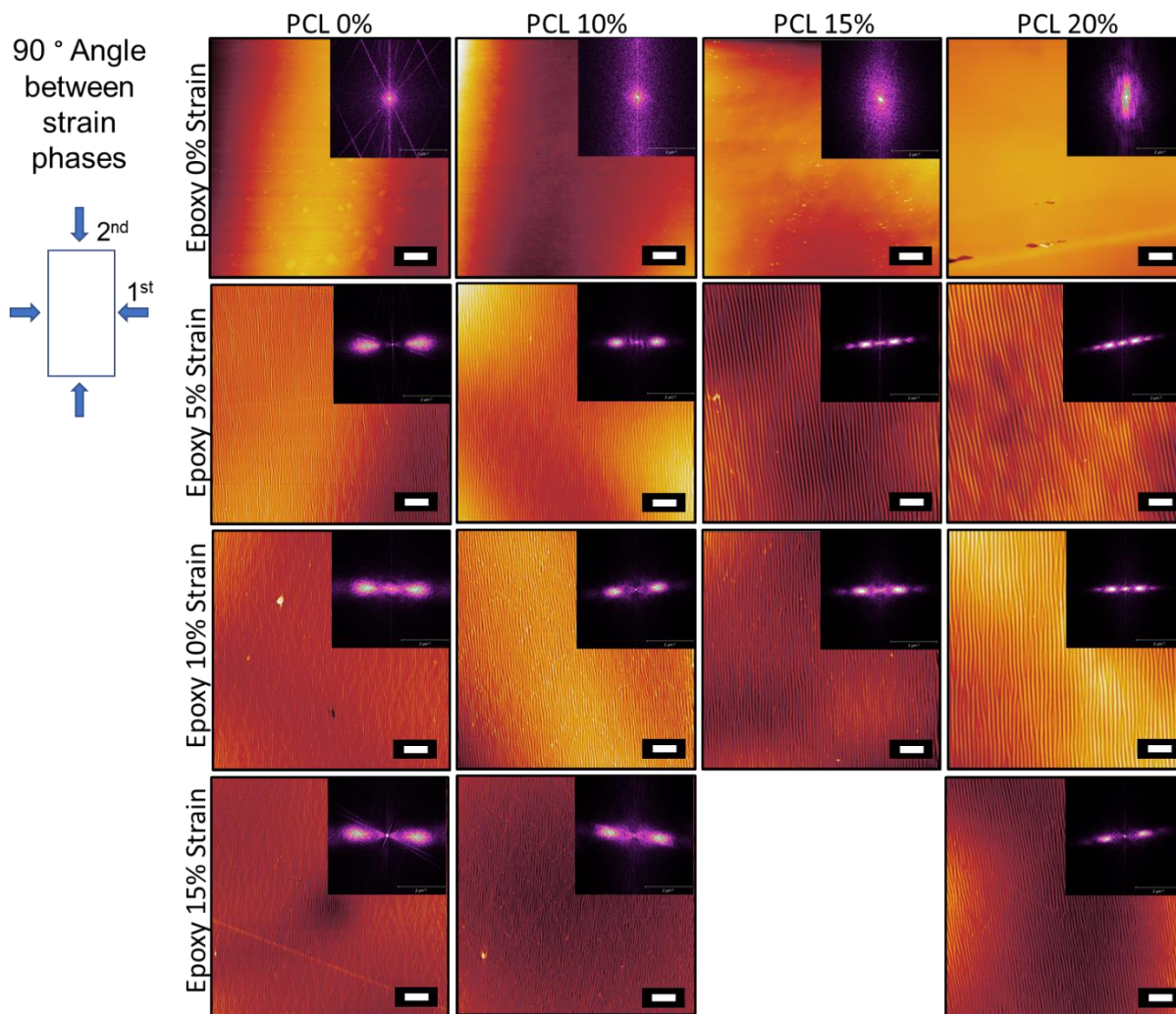


**Figure 5-6.** AFM micrographs of the TSPC surfaces after the first recovery step at 50 °C for the biaxially programmed samples with the 2D-FFT shown in the upper right-hand corner. As the epoxy recovered its strain the gold surface buckled forming wrinkle patterns along the surface of the materials. As this occurred the 2DFFT scans developed are barbell shapes indicating the presence of a sinusoidal pattern on the surface. The samples with no epoxy strain programmed in did not show any wrinkle pattern formations as expected. The wavelength of the epoxy wrinkles actually increased with increasing PCL strain, indicating the presence of some cross-talk between the programmed strains. The 15% epoxy strain for the 15% PCL samples is not present as it recovered prematurely. Scale bar is 10  $\mu\text{m}$

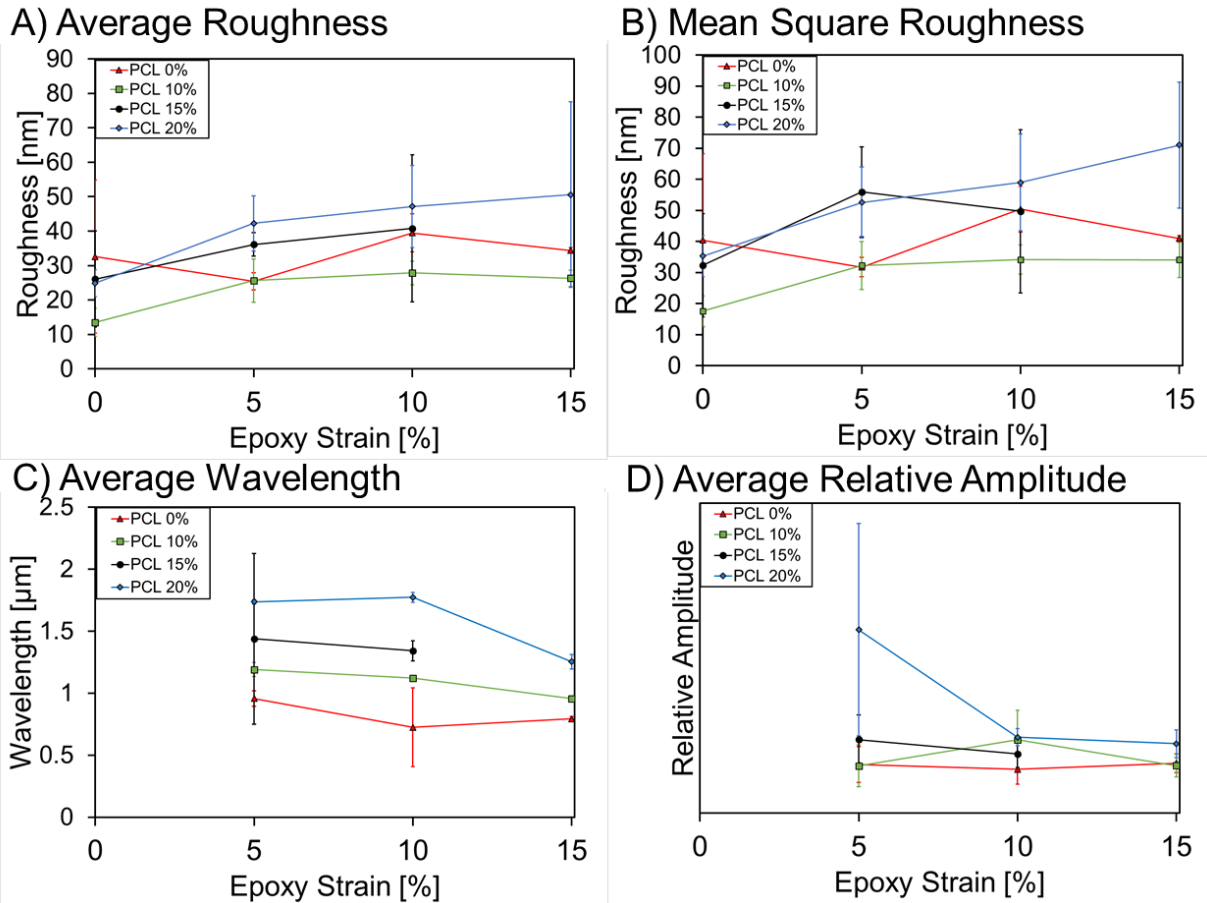


**Figure 5-7.** Graphs showing the average roughness, wavelength and relative amplitude of the wrinkle patterns formed after the first 50 °C recovery of the biaxially programmed samples. The 20% PCL samples showed a small increasing trend in the average roughness while the other samples showed little change as the strain increased overtime. The average wavelength of the wrinkle patterns increased with increasing PCL strain stain and showed no trend in increasing epoxy strain. The amplitude of the developed wrinkles showed no noticeable trend.

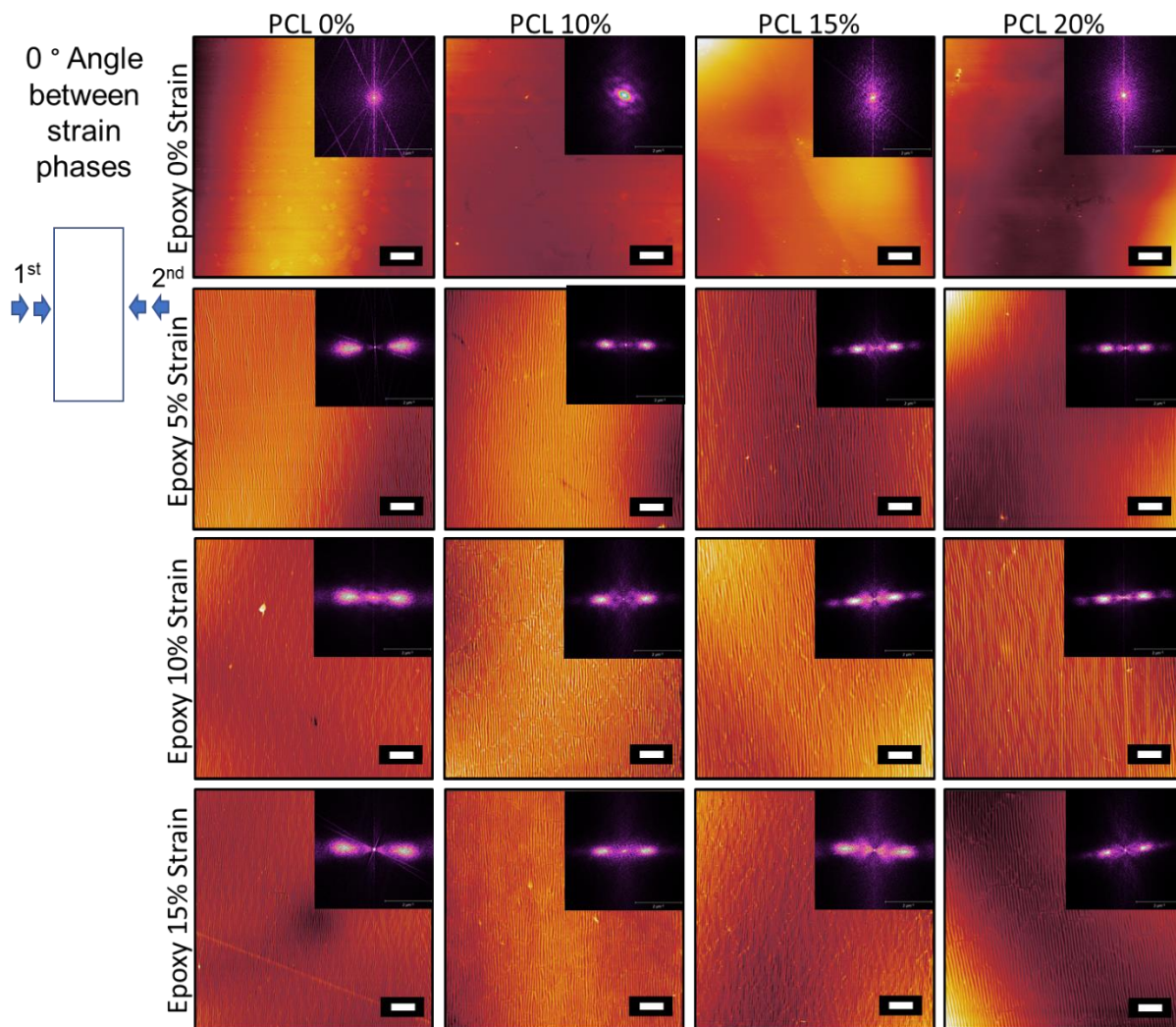


**Figure 5-8.** AFM micrographs of the TSPC surfaces after the first recovery step at 50 °C for the biaxially programmed samples with the 2D-FFT shown in the upper right-hand corner. As the epoxy recovered its strain the gold surface buckled forming wrinkle patterns along the surface of the materials. As this occurred the 2DFFT scans developed are barbell shapes indicating the presence of a sinusoidal pattern on the surface. The samples with no epoxy strain programmed in did not show any wrinkle pattern formations as expected. The wavelength of the epoxy wrinkles actually increased with increasing PCL strain, indicating the presence of some cross-talk

between the programmed strains. The 15% epoxy strain for the 15% PCL samples is not present as it recovered prematurely. Scale bar is 10  $\mu\text{m}$

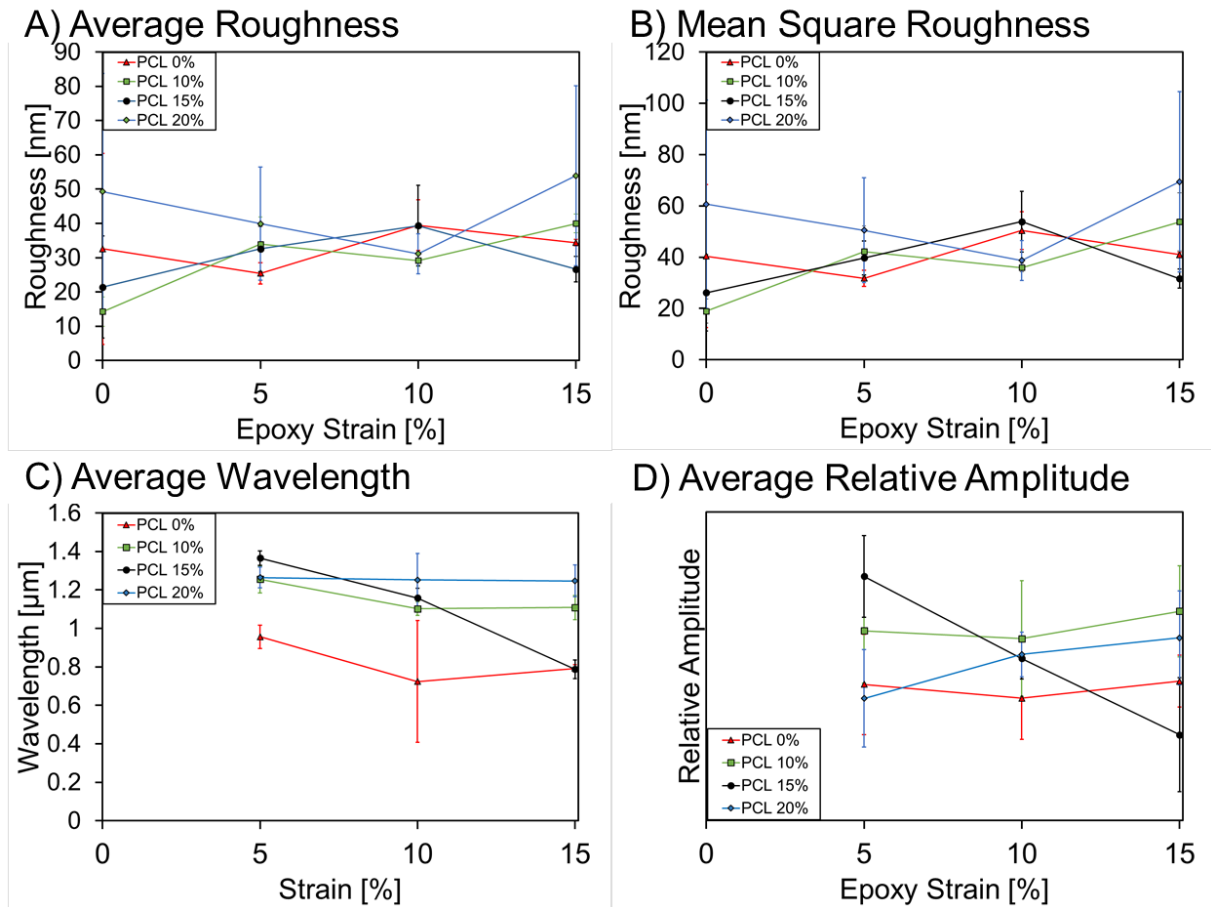


**Figure 5-9.** Graphs showing the average roughness, wavelength and relative amplitude of the wrinkle patterns formed after the first 50 °C recovery of the uniaxially programmed samples. No noticeable trend in the surface roughness was observed with the strain of the materials. The average wavelength of the wrinkle patterns remained the same as the epoxy strain increased, except for the samples programmed with 15% PCL strain, which showed a general decreasing trend. The relative amplitude of all the samples showed no general trend except for the samples programmed with 20% PCL strain which showed a decreasing trend in the amplitude.



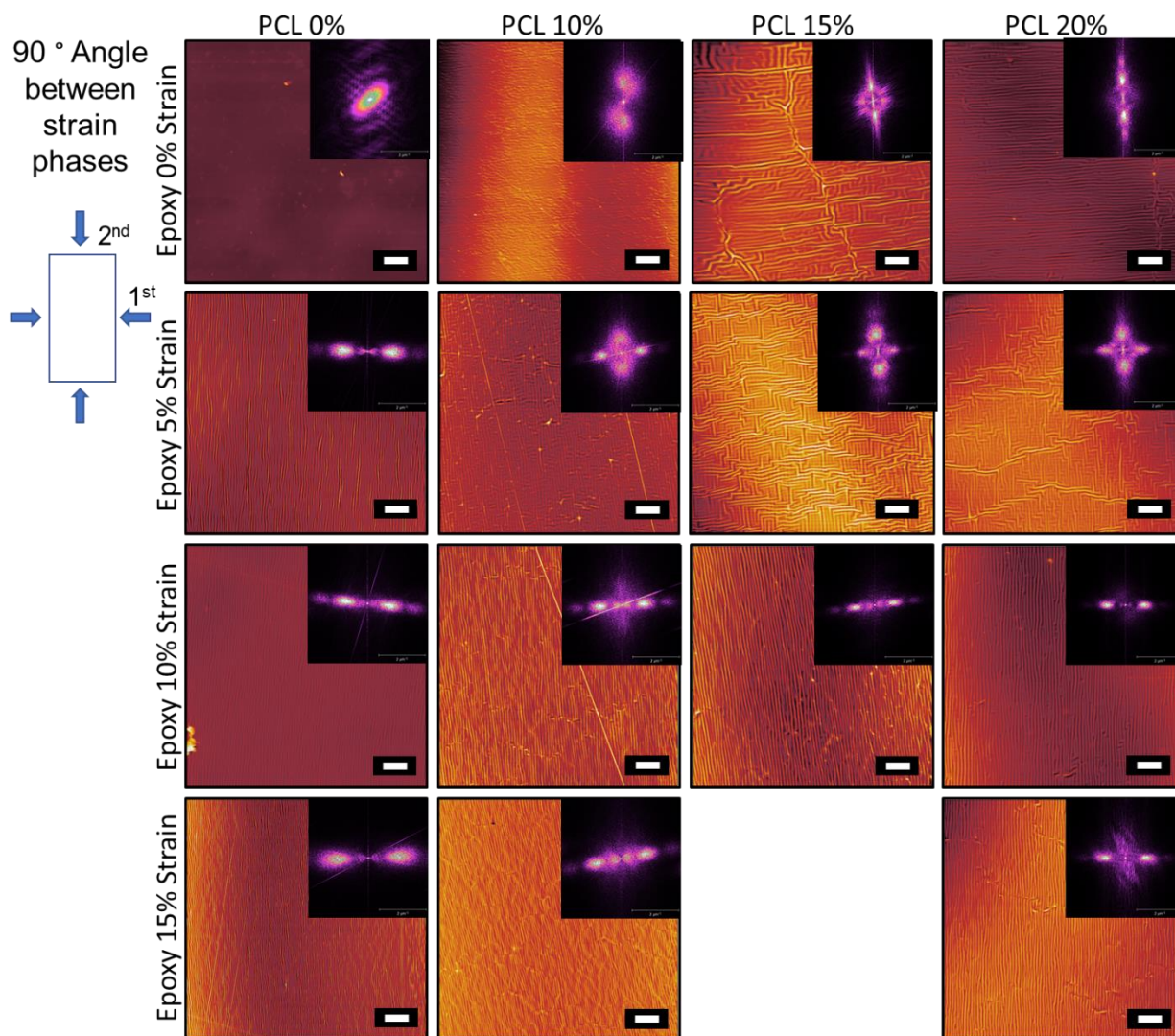


**Figure 5-10.** AFM micrographs of the TSPC surfaces after the second recovery step at 60 °C for the biaxially programmed samples with the 2D-FFT shown in the upper right-hand corner. For the samples with no epoxy strain, a perpendicular wrinkle pattern formed along the surface as the PCL recovered its strain. As this occurred the 2DFFT scans developed are barbell shapes in an up-down direction indicating the presence of a sinusoidal pattern on the surface. For the samples where the epoxy wrinkles had already formed, the PCL recovery caused an additional wrinkle pattern to form along the surface, but only for those samples with a small amount of epoxy strain. The double wrinkle patterns showed a double bar-bell shape in their 2DFFT scans,

indicating that two sinusoidal patterns existed. The 15% epoxy strain for the 15% PCL samples is not present as it recovered prematurely. Scale bar is 10  $\mu\text{m}$

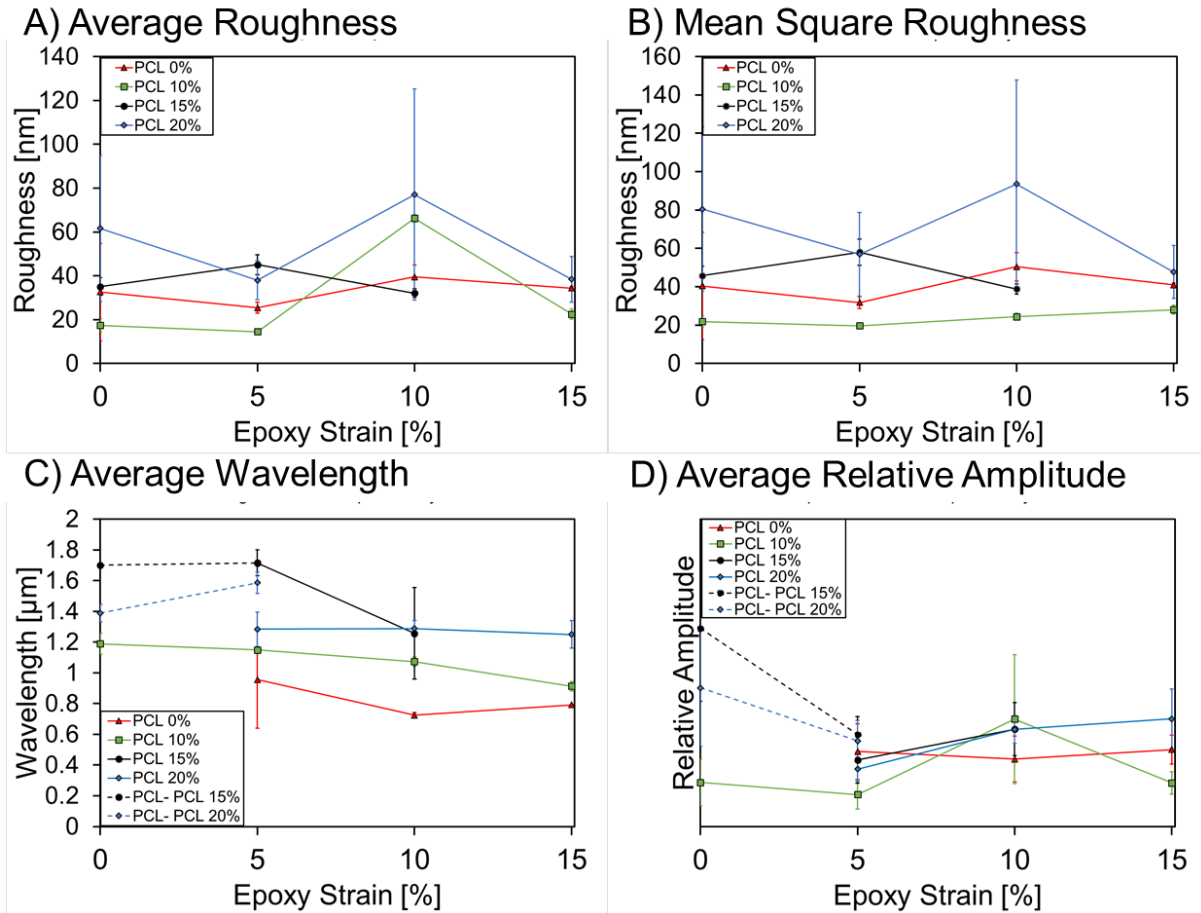


**Figure 5-11.** Graphs showing the average roughness, wavelength and relative amplitude of the wrinkle patterns formed after the second 60 °C recovery of the biaxially programmed samples. No noticeable trend in the surface roughness was observed with the strain of the materials. The average wavelength of the samples increased with programmed PCL strain but remained constant with increasing epoxy strain. The wavelength of the wrinkles formed by the PCL was on average higher than the wavelength of the wrinkles formed by the epoxy recovery. The amplitude of the wrinkles remained similar for all epoxy strain groups, however, the amplitude of the PCL wrinkles showed a decreasing trend with increasing epoxy strain.



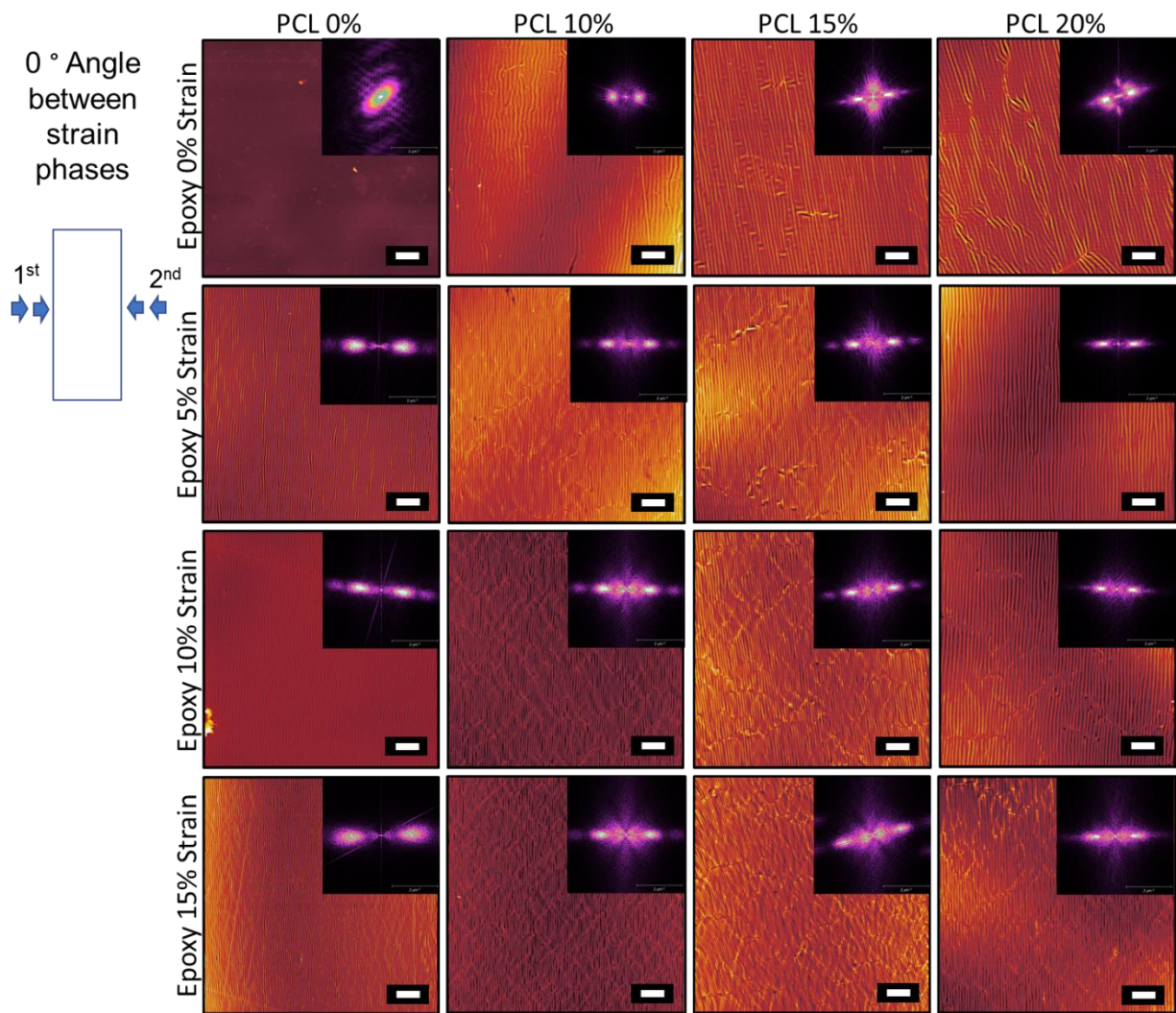


**Figure 5-12.** AFM micrographs of the TSPC surfaces after the second recovery step at 60 °C for the uniaxially programmed samples with the 2D-FFT shown in the upper right-hand corner. For the samples with no epoxy strain, a wrinkle pattern with the recovery of the PCL, and in some cases showed a double nature, despite there being no biaxially programmed strain. The samples with epoxy wrinkles pre-formed showed a decrease in the wavelength of the wrinkle patterns compared to the patterns formed at 50 °C. Scale bar is 10  $\mu\text{m}$

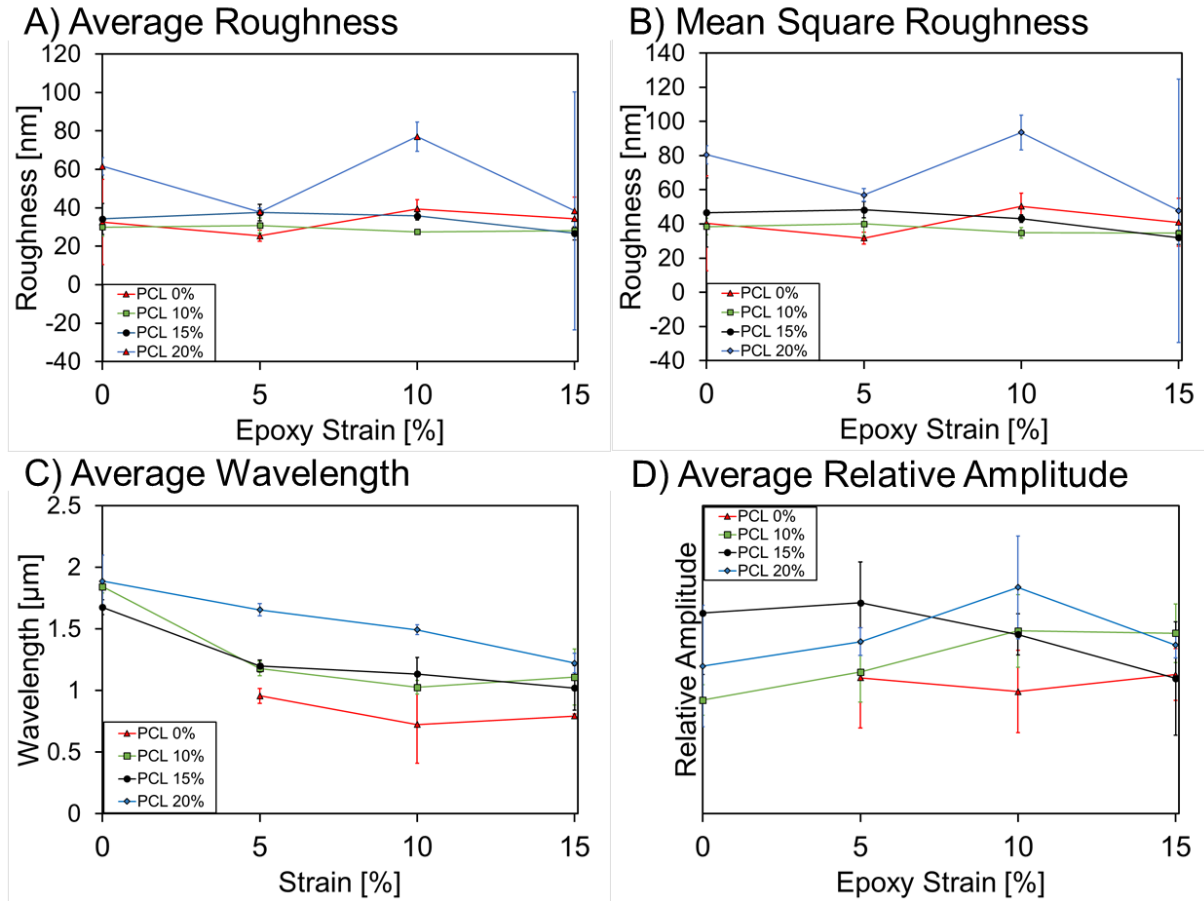


**Figure 5-13.** Graphs showing the average roughness, wavelength and relative amplitude of the wrinkle patterns formed after the second 60 °C recovery of the uniaxially programmed samples. No noticeable trend in the surface roughness was observed with the strain of the materials. The average wavelength of the samples increased with programmed PCL strain but remained constant with increasing epoxy strain. The wavelength of the wrinkles formed by the PCL was on average higher than the wavelength of the wrinkles formed by the epoxy recovery. The amplitude of the wrinkles remained similar for all epoxy strain groups, however, the amplitude of the PCL wrinkles showed a decreasing trend with increasing epoxy strain.

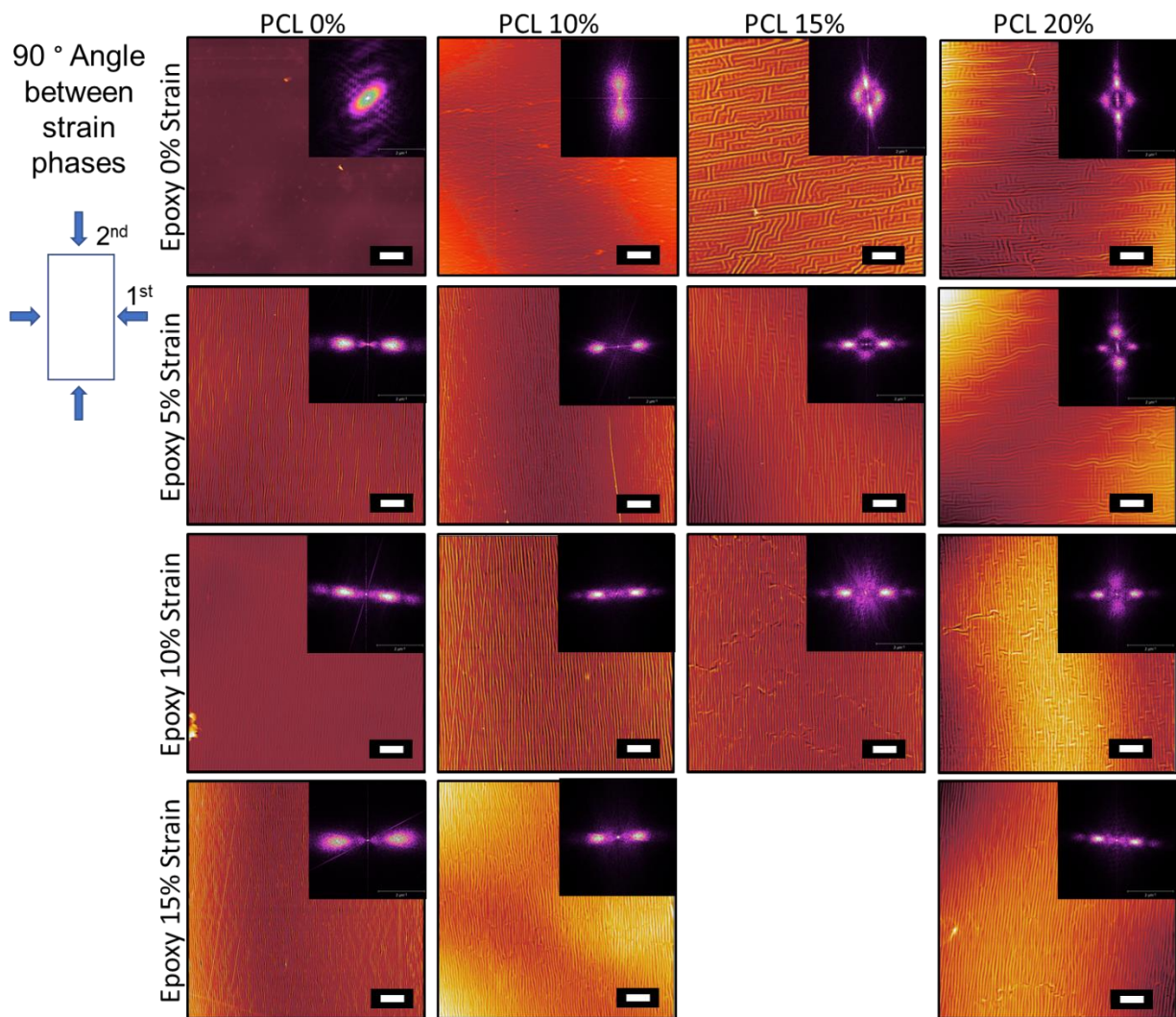


**Figure 5-14.** AFM micrographs of the TSPC surfaces after the 1 step recovery 60 °C for the biaxially programmed samples with the 2D-FFT shown in the upper right-hand corner. This allowed for both strains to recover at approximately the same time, although there would still be a lag between the recovery for the PCL compared to the epoxy due to the temperature difference). For the samples with no epoxy strain, a perpendicular wrinkle pattern formed along the surface as the PCL recovered its strain. As this occurred the 2DFFT scans developed are barbell shapes in an up-down direction indicating the presence of a sinusoidal pattern on the surface. Similar to above the samples with a large amount of the PCL strain did show some

double wrinkle patterns forming, likely due to a Poisson effect. For samples with both epoxy and PCL strain programmed in you saw the formation of various wrinkle patterns. In the case where the epoxy strain is high compared to the PCL strain, only the orthogonal wrinkle patterns are observable, however as the PCL strain increases the formation of double wrinkle patterns is evident. In the case of 15% epoxy strain, only the orthogonal wrinkle pattern was observed. The double wrinkle patterns showed a double bar-bell shape in their 2DFFT scans, indicating that two sinusoidal patterns existed. The 15% epoxy strain for the 15% PCL samples is not present as it recovered prematurely. Scale bar is 10  $\mu\text{m}$

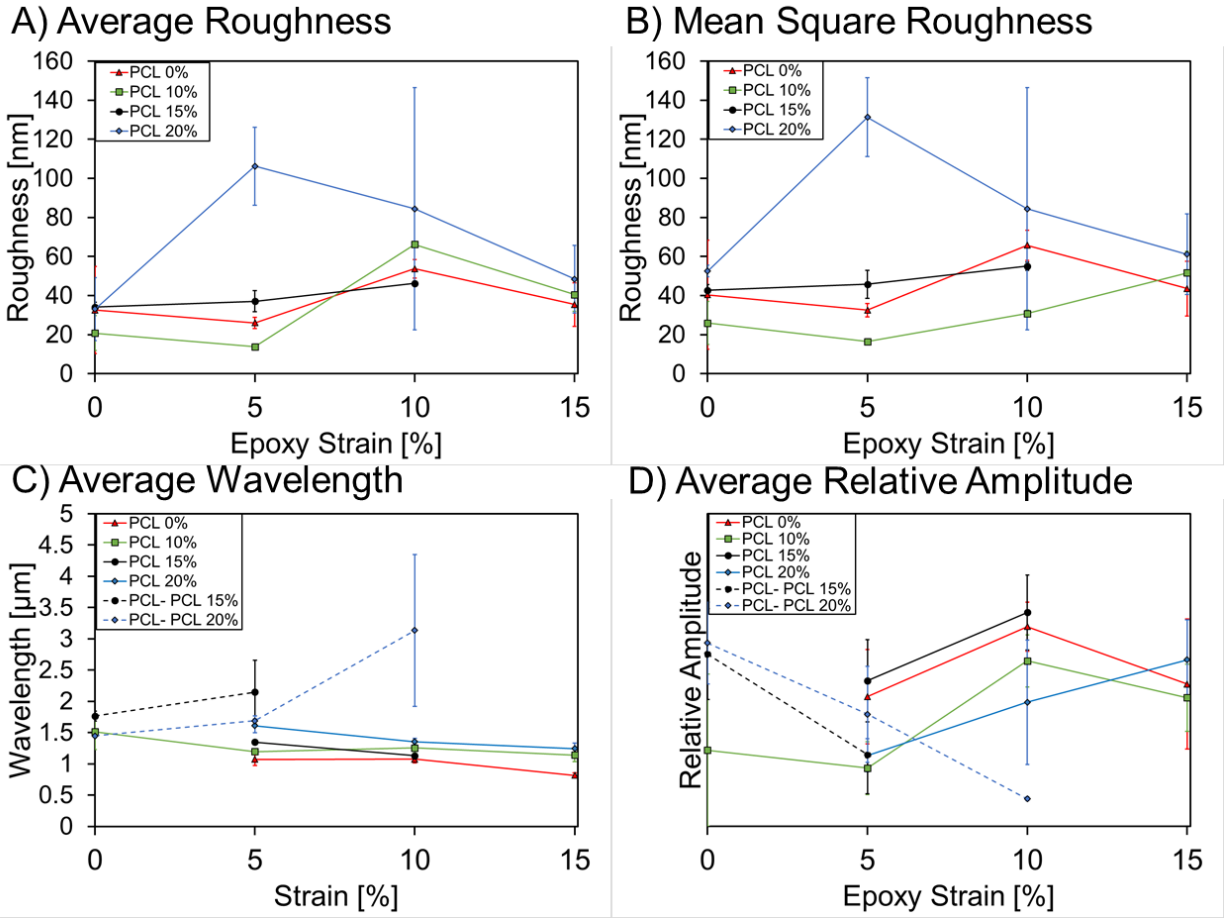


**Figure 5-15.** Graphs showing the average roughness, wavelength and relative amplitude of the wrinkle patterns formed for the 1-step recovery at 60 °C for the biaxially programmed samples. No noticeable trend in the surface roughness was observed with the strain of the materials. The average wavelength of the samples increased with programmed PCL strain but remained constant with increasing epoxy strain. The wavelength of the wrinkles formed by the PCL was on average higher than the wavelength of the wrinkles formed by the epoxy recovery and increased with increasing epoxy strain. The amplitude of the wrinkles remained similar for all epoxy strain groups, however, the amplitude of the PCL wrinkles showed a decreasing trend with increasing epoxy strain.



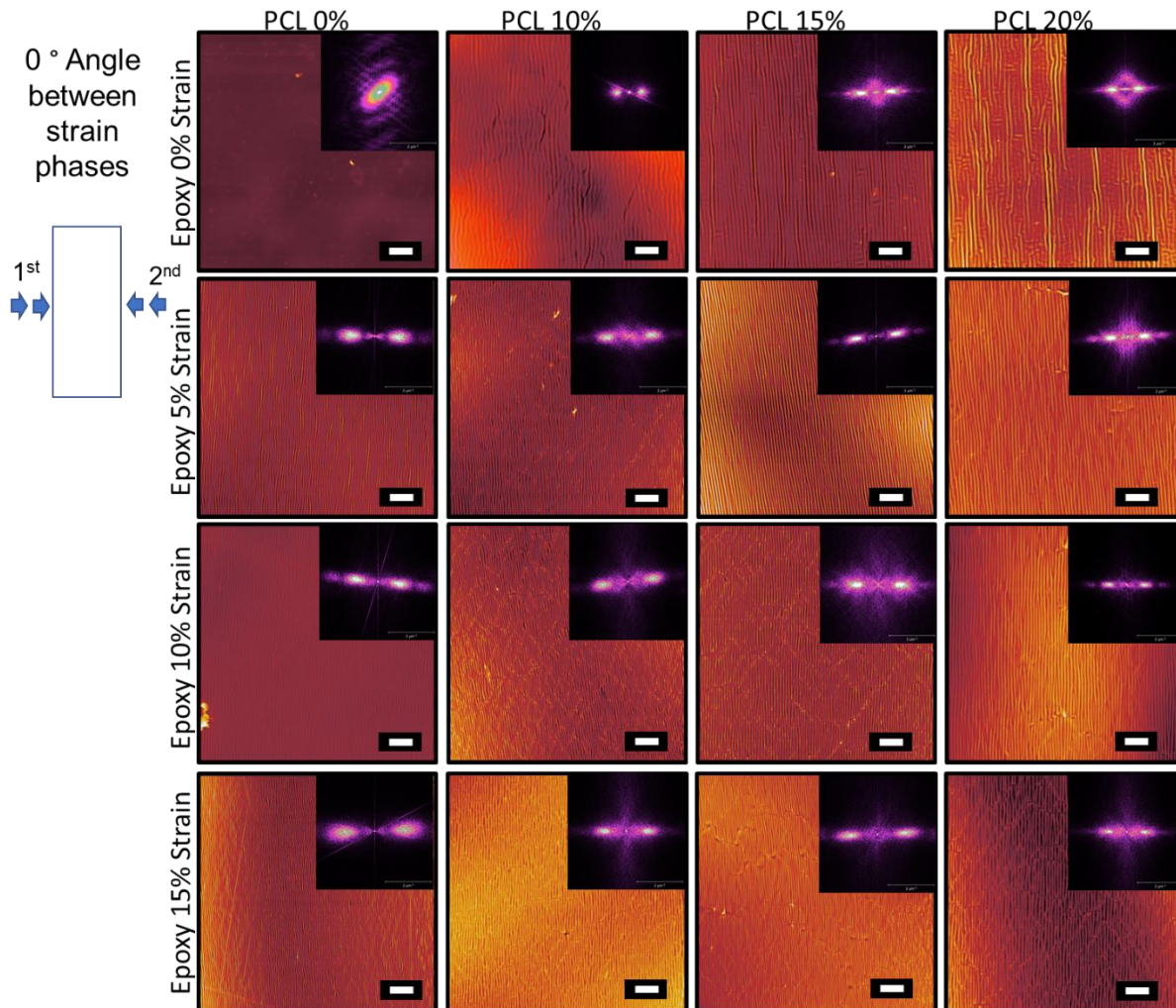


**Figure 5-16.** AFM micrographs of the TSPC surfaces after the 1 step recovery at 60 °C for the uniaxially programmed samples with the 2D-FFT shown in the upper right-hand corner. For the samples with no epoxy strain, a wrinkle pattern with the recovery of the PCL, and in some cases showed a double nature, despite there being no biaxially programmed strain; likely due to a Poisson effect since the modulus of the composite would be lower for the PCL recovery since the epoxy is already rubbery. Scale bar is 10  $\mu\text{m}$

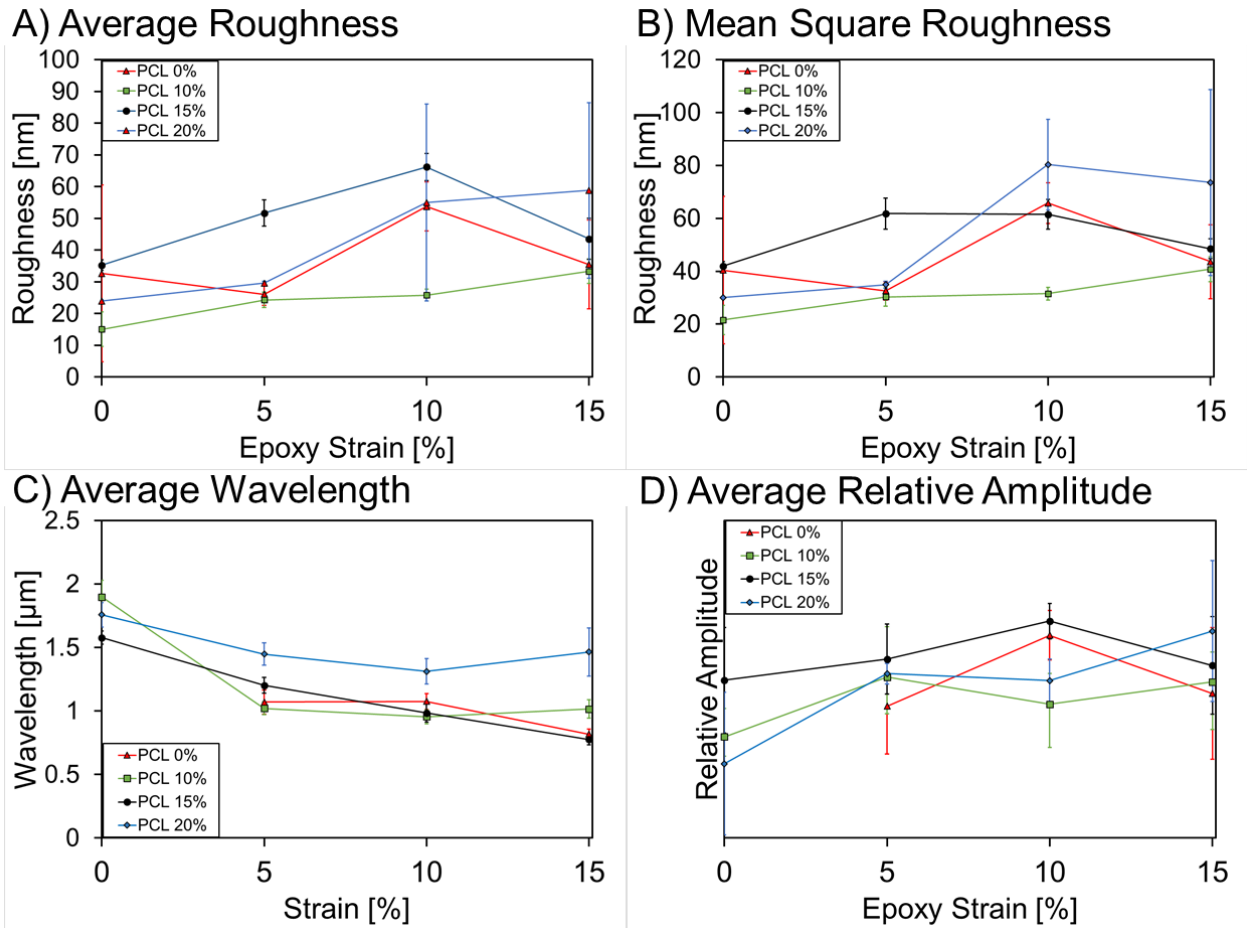


**Figure 5-17.** Graphs showing the average roughness, wavelength and relative amplitude of the wrinkle patterns formed after the second 60 °C recovery of the uniaxially programmed samples. No noticeable trend in the surface roughness was observed with the strain of the materials. The average wavelength of the samples increased with programmed PCL strain but remained constant with increasing epoxy strain. The wavelength of the wrinkles formed by the PCL was on average higher than the wavelength of the wrinkles formed by the epoxy recovery. The amplitude of the wrinkles remained similar for all epoxy strain groups, however, the amplitude of the PCL wrinkles showed a decreasing trend with increasing epoxy strain.

## 5.8 References

1. Haan, L. T. De *et al.* Contactless Control of Local Surface Buckling in Photoaligned Gold/Liquid Crystal Polymer Bilayers. *Langmuir* **34**, 10543–10549 (2018).
2. Watson, G. S. *et al.* A gecko skin micro/nano structure – A low adhesion, superhydrophobic, anti-wetting, self-cleaning, biocompatible, antibacterial surface. *Acta Biomater.* **21**, 109–122 (2015).
3. Sakamoto, A. *et al.* Antibacterial effects of protruding and recessed shark skin micropatterned surfaces of polyacrylate plate with a shallow groove. *FEMS Microbiol. Lett.* **361**, 10–16 (2014).
4. Bhushan, B. & Her, E. K. Fabrication of Superhydrophobic Surfaces with High and Low Adhesion Inspired from Rose Petal. *Langmuir* **26**, 8207–8217 (2010).
5. Bowden, N., Brittain, S., Evans, A. G., Hutchinson, J. W. & Whitesides, G. M. Spontaneous formation of ordered structures in thin films of metals supported on an elastomeric polymer. *Nature* **393**, 146–149 (1998).
6. Huck, W. T. S. *et al.* Ordering of Spontaneously Formed Buckles on Planar Surfaces. *Langmuir* 3497–3501 (2000). doi:10.1021/la991302l
7. Wilhelm T. S. Huck, † *et al.* Ordering of Spontaneously Formed Buckles on Planar Surfaces. (2000). doi:10.1021/LA991302L
8. Tanaka, T. *et al.* Mechanical instability of gels at the phase transition. *Nature* **325**, 796–798 (1987).
9. A. L. VOLYNSKII, S. BAZHENOV O. V. LEBEDEVA, N. F. B. Mechanical buckling



- instability of thin coatings deposited on soft polymer substrates. *J. Mater. Sci.* **35**, (2000).
10. Jeong, H., Park, H., Lee, J. H. & Seo, D. Localized Ion-Beam Irradiation-Induced Wrinkle Patterns. (2015). doi:10.1021/acsami.5b07147
  11. Guvendiren, M., Burdick, A. & Yang, S. Solvent induced transition from wrinkles to creases in thin-film gels with depth-wise crosslinking gradients †‡. *Soft Matter* 5795–5801 (2010). doi:10.1039/c0sm00317d
  12. Vandeparre, H. *et al.* Hierarchical wrinkling patterns †. **1**, 5751–5756 (2010).
  13. DuPont Jr., S. J., Cates, R. S., Stroot, P. G. & Toomey, R. Swelling-induced instabilities in microscale, surface-confined poly(N-isopropylacryamide) hydrogels. *Soft Matter* **6**, 3876 (2010).
  14. Chung, J. Y., Chastek, T. Q., Fasolka, M. J., Ro, H. W. & Stafford, C. M. Quantifying Residual Stress in Nanoscale Thin Polymer Films via Surface. *ACS Nano* **3**, (2009).
  15. Chung, J. Y., Nolte, A. J. & Stafford, C. M. Surface Wrinkling: A Versatile Platform for Measuring Thin-Film Properties. *Adv. Mater.* **23**, 349–368 (2011).
  16. Pampuch, C. *et al.* A Stretchable Form of Single-Crystal. **311**, 208–213 (2006).
  17. Chen, X. & Hutchinson, J. W. Herringbone Buckling Patterns of Compressed Thin Films on Compliant Substrates. *J. Appl. Mech.* **71**, 597–603 (2004).
  18. Yang, B. S., Khare, K. & Lin, P. Harnessing Surface Wrinkle Patterns in Soft Matter. **10617**, 2550–2564 (2010).
  19. Bukowsky, C., Torres, J. M. & Vogt, B. D. Slip-stick wetting and large contact angle hysteresis on wrinkled surfaces. *J. Colloid Interface Sci.* **354**, 825–831 (2011).

20. Chung, J. Y., Youngblood, P. & Stafford, C. M. Anisotropic wetting on tunable micro-wrinkled surfaces. 1163–1169 (2007). doi:10.1039/b705112c
21. Sun, Y., Choi, W. O. N. M., Jiang, H., Huang, Y. Y. & Rogers, J. A. Controlled buckling of semiconductor nanoribbons for stretchable electronics. 201–207 (2006). doi:10.1038/nnano.2006.131
22. Chiche, A., Stafford, C. M. & Cabral, J. Complex micropatterning of periodic structures on elastomeric surfaces. *Soft Matter* **4**, (2008).
23. Khang, D.-Y., Rogers, J. A. & Lee, H. H. Mechanical Buckling: Mechanics, Metrology, and Stretchable Electronics. *Adv. Funct. Mater.* **19**, 1526–1536 (2009).
24. Efimenko, K. *et al.* Nested self-similar wrinkling patterns in skins. **4**, 0–4 (2005).
25. Moon, M.-W. & Vaziri, A. Surface modification of polymers using a multi-step plasma treatment. *Scr. Mater.* **60**, 44–47 (2009).
26. Wang, B. M. *et al.* Formation of Hierarchically Structured Thin Films. 2236–2243 (2009). doi:10.1002/adfm.200801867
27. Hyun, D. C. & Jeong, U. Substrate thickness: An effective control parameter for polymer thin film buckling on PDMS substrates. *J. Appl. Polym. Sci.* **112**, 2683–2690 (2009).
28. Jiang, C., Singamaneni, S., Merrick, E. & Tsukruk, V. V. Complex Buckling Instability Patterns of Nanomembranes with Encapsulated Gold Nanoparticle Arrays. *Nano Lett.* **6**, 2254–2259 (2006).
29. Sun, L. *et al.* Wrinkling atop Shape Memory Materials Thin Film Solar Cells. doi:10.1142/S0218625X12500102

30. Thorsen, T., Roberts, R. W., Arnold, F. H. & Quake, S. R. Dynamic Pattern Formation in a Vesicle-Generating Microfluidic Device. *Phys. Rev. Lett.* **86**, 4163–4166 (2001).
31. Xiong, G.-R. *et al.* Liquid microlens with tunable focal length and light transmission. *Appl. Phys. Lett.* **92**, 241119 (2008).
32. Kim, Y. H., Lee, Y. M., Lee, J. Y., Ko, M. J. & Yoo, P. J. Hierarchical Nanoflake Surface Driven by Spontaneous Wrinkling of Polyelectrolyte/Metal Complexed Films. *ACS Nano* **6**, 1082–1093 (2012).
33. Pholpabu, P., Kustra, S., Wu, H., Balasubramanian, A. & Bettinger, C. J. Lithography-free fabrication of reconfigurable substrate topography for contact guidance. *Biomaterials* **39**, 164–172 (2015).
34. Ash-Shakoor, A. The Dynamic Effects of Surface Topography and Chemistry on Cell Attachment, Alignment, and Motility on Smart, Polyelectrolyte Materials. (Syracuse University, 2017).
35. Yang, P. *et al.* In vitro wrinkle formation via shape memory dynamically aligns adherent cells. *Soft Matter* **9**, 4705 (2013).
36. Fu, C.-C. *et al.* Tunable Nanowrinkles on Shape Memory Polymer Sheets. *Adv. Mater.* **21**, 4472–4476 (2009).
37. Jackson, A. S., Sheiko, S. S. & Ashby, V. S. Grafting Poly(OEGMA) Brushes from a Shape Memory Elastomer and Subsequent Wrinkling Behavior. 29–34 (2015).  
doi:10.1021/la504826w
38. SUN, L., ZHAO, Y., HUANG, W. M. & TONG, T. H. FORMATION OF COMBINED

SURFACE FEATURES OF PROTRUSION ARRAY AND WRINKLES ATOP SHAPE-MEMORY POLYMER. *Surf. Rev. Lett.* **16**, 929–933 (2009).

39. Xie, B. T., Xiao, X., Li, J. & Wang, R. Encoding Localized Strain History Through Wrinkle Based Structural Colors. 4390–4394 (2010). doi:10.1002/adma.201002825
40. Luo, X. & Mather, P. T. Triple-Shape Polymeric Composites (TSPCs). *Adv. Funct. Mater.* **20**, 2649–2656 (2010).
41. Torbati, A. H., Nejad, H. B., Ponce, M., Sutton, J. P. & Mather, P. T. Properties of triple shape memory composites prepared via polymerization-induced phase separation. *Soft Matter* **10**, 3112–3121 (2014).

# Chapter 6: Development of Quadruple Shape Memory

## Composites<sup>‡</sup>

### 6.1 Synopsis

This chapter discusses the design of a quadruple shape memory composite using a similar composite approach used in chapter 5. Here we combined two composite making methods used by Luo *et. al.*<sup>1</sup> and Torbati *et. al.*<sup>2</sup> to design a triphasic quadruple shape memory composite capable of learning three temporary shapes and one permanent shape. In addition, we demonstrate that these composites are capable of multi-surface shape memory. This effect could be used to design materials that can transition between several topographical patterns.

### 6.2 Introduction

Shape memory polymers (SMPs) are a special class of materials that can store one or more temporary shapes and macroscopically transition from a stored shape to a permanent, “remembered” shape in response to an external stimulus.<sup>3</sup> Such behavior requires two components: a memory component (phase or macromolecular constituent) that can be in the form of physical or chemical cross-links, crystalline domains, or interpenetrating networks; and a shape-fixing component (phase or macromolecular constituent) that can come from either crystallization, vitrification, liquid crystal transitions, reversible molecular cross-linking and supramolecular associations.<sup>4,5</sup> In a typical shape memory cycle (SMC), the SMP is heated above a characteristic transition temperature to a compliant, rubbery state. An external stress is then applied to the material, resulting in deformation to a new, temporary shape with mechanical

<sup>‡</sup>Adapted with permission from S.L. Buffington, B.M. Posnick, J.E. Paul, and P.T. Mather, *ChemPhysChem*, 2018, 19, © 2018 ChemPhysChem Inc. Published by Wiley Online Library.

resistance from the memory component of the material. This deformation – often termed “mechanical programming” – decreases the polymer network’s configurational entropy to an unfavorable state which is locked in when the material is cooled below its transition temperature and the constituent network chains of the memory phase are immobilized. Once heated above this transition temperature, however, the network chains are remobilized so that rubber (entropy) elasticity acts to return the object toward its permanent shape.<sup>4–6</sup>

SMPs with a wide range of material properties have been designed and are reviewed briefly here for the interested reader.<sup>3–8</sup> Due to inherent versatility, SMPs have been proposed for applications spanning biomedical devices<sup>9</sup>, space applications, microsensors and actuators, drug delivery systems and intelligent textiles, among others.<sup>3,4</sup> The most common trigger for an SMP is heat; however, SMPs triggered by light<sup>10,11</sup> ultrasound<sup>12</sup>, electricity<sup>13</sup>, water<sup>14,15</sup> solvents<sup>16</sup> and magnetism<sup>17,18</sup> have been reported as well. SMPs exhibiting unique properties like anisotropy<sup>19</sup>, soft actuation<sup>20</sup>, light emission<sup>21</sup>, self-healing<sup>22</sup> and other special properties reviewed here<sup>23</sup> have also been developed. In addition, SMPs with reconfigurable permanent shapes have been introduced, allowing the possibility that the SMP could be mass-produced but with the permanent shape being amenable to reprogramming as desired for specific applications.<sup>24,25</sup> SMPs that can reversibly actuate between their permanent and temporary shape, called reversible SMPs, have also been proposed for applications involving switches and actuators,<sup>25,26</sup> for instance, soft muscle actuators.<sup>27</sup>

An important limitation of the described SMP systems is that most are only able to fix one shape, yielding limited actuation between just two shapes: one fixed (or “programmed”) and one permanent. Multi-shape memory polymers (multi-SMPs) are capable of being programmed into at least two temporary shapes while possessing one permanent shape which allows the

materials to undergo more complex shape changes.<sup>8</sup> The first example of a triple shape memory (TSM) material was designed by Bellin and co-workers who combined two crystalline switching segments, poly( $\epsilon$ -caprolactone) (PCL) and poly(ethylene glycol) (PEG) within the context of a polymer network.<sup>28</sup> Since this development, two primary methods for producing multi-shape memory materials have been employed. The first is combining materials with separate thermal transitions in either a macromolecular chemistry or by blending two or more polymers in a composite approach. For example, our group designed a triple shape polymeric composite by embedding a PCL fiber mat into an epoxy-based SMP matrix.<sup>1</sup> This created a composite with two interpenetrating phases – with separate thermal transitions – capable of fixing two temporary shapes. In addition, our group developed a triple shape composite using polymerization induced phase separation (PIPS).<sup>2</sup> In this method, epoxy monomers and low molecular weight PCL were mixed into a single phase melt that, upon polymerization, underwent phase separation to create an SMP matrix with pockets of PCL distributed throughout the material. Using a similar method we also designed the first example of triple shape composite foams,<sup>29</sup> while other groups have expanded the abilities of multi-shape materials by designing systems that respond to different triggers, such as pH<sup>30</sup>, light<sup>30</sup>, and magnetism.<sup>31</sup>

Another approach to make multi-SMPs involves materials with distinctly broad glass transitions that allow one glass transition event (albeit broad) to mechanically program multiple shapes at different temperatures within the transition and to recover them at temperatures close to the programming temperature as the material moves through its recovery. This is sometimes referred to as the “temperature memory effect”. Using this method, researchers have been able to achieve a quadruple and even quintuple SMP effect. For instance, researchers composed a semi-interpenetrating network composed of cross-linked poly(methyl methacrylate) (PMMA) and

linear PEG. After polymerization, the PMMA displayed a broad glass transition and the PEG had a sharp melt transition.<sup>32</sup> With these two separate phases they were able to program three shapes into the PMMA matrix and had one shape programmed into the PEG phase, creating the first example of quintuple shape memory. A second example from Luo and colleagues used a living radical copolymerization with changing monomer feed ratios to create a compositional gradient along the polymer backbone.<sup>33</sup> This gradient resulted in a broad glass transition that yielded a multi-SMP capable of both quadruple and quintuple shape memory effects. We are aware of one previous example of a quadruple shape memory composite using three distinct thermal transitions, in contrast to broad thermal transitions as described above. Podgórski and colleagues used a combination of Michael-thiol and Michael/thiol-isocyanate layers in bi-layer and tri-layer structures that demonstrated triple and quadruple shape properties, respectively.<sup>34</sup> Using this method they obtained fixing and recovery ratios above 70% for all shape transitions. Intrinsically, this multilayer approach presents a limitation of multi-shape phenomena to the bulk, a limitation we sought to address in the present work.

Herein, we introduce the design of a multi-phase quadruple shape memory composite that displayed both bulk and surface quadruple shape memory behavior. We accomplished this by combining two fabrication methods that we previously contributed to yield triple shape composites.<sup>1,2</sup> Briefly, we imbibed an electrospun PCL fiber mat with a PIPS precursor solution of PMMA dissolved in uncured epoxy liquid. Further processing led to a ternary composite with one permanent shape and capacity to program three temporary shapes locally or macroscopically. In what follows, we will explain the preparation, thermo-mechanical and quadruple shape memory properties of these composites.



## 6.3 Experimental Methods

### 6.3.1 Materials

All chemicals including diglycidyl ether of bisphenol-A (DGEBA), neopentyl glycol diglycidyl ether (NGDE), O,O'-Bis(2-aminopropyl)polypropylene glycol (Jeffamine D230) and poly( $\epsilon$ -caprolactone) (PCL) (nominal Mw = 90 000 g/mol) were purchased from Sigma-Aldrich and used as received. PMMA (nominal Mw = 75 000 g/mol) was purchased from Scientific Polymer Products, Inc.

### 6.3.2. Fabrication of Composite Materials

#### 6.3.2.1 *Electrospinning*

The electrospinning solution was prepared by dissolving 2 g of PCL in 10 mL of chloroform:DMF (Vchloroform:VDMF 8:2) solution and set to stir for 24 h, yielding a clear and colorless viscous solution. Electrospinning was conducted using a custom-built set up that is composed of a high voltage power supply (Agilent E3630A), a syringe pump (KDS100, KD Scientific), a low voltage negative power supply (PS 500XT, Hoefer Scientific) and a 5 cm diameter rotating drum. Fiber mats were spun using a constant flow rate of 2 mL/h with an applied voltage of 12kV at needle-collector distance of 10 cm. The fibers were collected on a negatively charged mandrel (-500V) rotating at 800 rpm with a slow horizontal translation along the collecting drum axis (perpendicular to the electrospinning jet direction) to ensure that a uniform, randomly oriented fiber mat was produced.

#### 6.3.2.2 *Fabricating Triple Shape Polymeric Composites*

TSMCs were fabricated using previously described methods.<sup>1</sup> Briefly, a 60:40 molar ratio of NGDE:DGEBA monomer solution was mixed together for 2 min. A 50 molar ratio of

Jeffamine-230 was added to the solution and stirred for an additional 2 min. The solution was then imbibed into an electrospun PCL fiber mat and vacuum-infiltrated for 20 min. The composite was finally cured at 40 °C for 48 h, to prevent melting of the PCL fiber phase before matrix vitrification, and then 60 °C for 24h to ensure complete cure.

#### *6.3.2.2 Fabricating Triple Shape Composites Using Polymerization Induced Phase Separation*

PIPS composites were fabricated using previously reported methods.<sup>2</sup> Briefly, 20 g of 60:40 molar ratio of NGDE:DGEBA was added to a flask and 2 g of PMMA pellets subsequently added to yield a 10 wt-% solution of PMMA in the liquid epoxy monomer. The flask was heated at 80 °C for at least 3 h under vacuum (to degas the solution) and magnetic stirring, resulting in a single-phase viscous liquid. The cross-linker, Jeffamine-230, was then added to the solution, the temperature reduced to 70 °C and stirring continued for 15 min under continued application of vacuum. Next, the PIPS solution was poured into a Teflon™ casting mold with square rectangular bar-shaped cavities (80 x 80 x1 mm) and transferred to a convection oven to cure the materials at 40 °C for 24 h and then 60 °C for 48 h, conditions previously found to yield complete cure as evidenced by post-cure calorimetric analysis.

#### *6.3.2.3 Fabricating Quadruple Shape Memory Composites*

A PMMA-based PIPS solution was first prepared as described above. When a homogeneous solution was obtained, a portion was poured first onto a glass slide, following which a PCL fiber mat was laid on top of it, partially absorbing the epoxy liquid. This approach was taken to minimize fiber melting, noting that the PIPS solution was prepared at a temperature exceeding the melt transition of the fiber mat. Imbibing of the PIPS solution was further advanced by hand manipulation until uniform translucency was achieved. Next, the composite was vacuum-infiltrated under an excess PIPS solution for 20 min to assure complete imbibing.

Finally, the fiber mat was clamped between two glass slides, squeezing out a minor excess of PIPS solution, and cured at 40 °C for 24 h followed by 60 °C for 48 h. All materials, including 4SMC, PIPS Composite and TSMC, were prepared and cured using the same matrix solutions to minimize the potential for batch-to-batch variability.

### 6.3.3 Thermal Characterization

Thermogravimetric Analysis (TGA) was performed on all composite and control samples to characterize the thermal degradation of the materials. Such analyses were performed in high-resolution mode to better capture the specific thermal degradation points. Samples were heated at a maximum rate of 50 °C/min with a resolution of 4 °C and a sensitivity of 1 to 600 °C. In this mode, the TGA ramped the temperature at a rate of 50 °C/min until temperature where the instrument detected mass loss, at which point the heating rate was decreased to capture fully the degradation event before continuing with the test.

Differential Scanning Calorimetry (DSC) was performed on all composite and control samples using a Q200 (TA instrument) equipped with a refrigerated cooling system. For each test, samples weighing 3-5 mg were loaded into a T-zero aluminum pan and first equilibrated by cooling to -50 °C. Samples were then heated at a rate of 10 °C/min to 120 °C and cooled at a rate of 5 °C/min to -50 °C, this initial heating being used to erase any thermal history. Samples were then heated by 10 °C/min to 120 °C to measure the glass transition ( $T_g$ ) and melting transition ( $T_m$ ) of the composite materials. The composition of all composite materials was measured using the heat of crystallization of the PCL and the stepwise change in heat capacity at  $T_g$  for the epoxy matrix. The material composition was estimated using Eqns. 1-3, and calculated values were compared to gravimetric values recorded during sample fabrication. Since the glass transition

signal for PMMA was small, the PMMA composition was calculated by summing the % composition of the other material phases and then subtracted from 100% (Eqn. 6-3).

$$W_{PCL}(\%) = \frac{\Delta H_{PCL-COMP}}{\Delta H_{PCL-pure}} * 100 \quad (6-1)$$

$$W_{epoxy}(\%) = \frac{\Delta C_{P_{epoxy-COMP}}}{\Delta C_{P_{epoxy-pure}}} * 100 \quad (6-2)$$

$$W_{PMMA}(\%) = 100 - W_{PCL} - W_{epoxy} \quad (6-3)$$

Dynamic Mechanical Analysis was used to measure the temperature dependences for all materials of the tensile storage modulus and the different thermal transitions via tensile loss modulus using a Q800 (TA Instruments). Samples featured variable dimensions with typical values of length, width and thickness of 6.25, 1.5, and 0.2 mm, respectively. The samples were first heated to 120 °C and then cooled at a rate of 2 °C/min to 0 °C to erase the thermal history of the sample. Samples were then heated at a rate of 2 °C/min to 120 °C while applying a small tensile deformation of 20 µm (0.4 %) at an oscillation frequency of 1 Hz.

#### 6.3.4 Wide Angle X-ray Scattering

Wide-Angle x-ray (WAXS) was used to ascertain the molecular and nanoscale ordering of all materials. A Rigaku S-MAX3000 pinhole camera system with a MacroMax-200 generator operating with a Cu K $\alpha$  emission ( $\lambda = 1.5406 \text{ \AA}$ ) was employed for all x-ray experiments. WAXS patterns were collected using a generator voltage of 45 kV, current of 0.88 mA and a sample-detector distance of 122.7 cm. This resulted in a scattering angle range of  $3^\circ < 2\theta < 40^\circ$  using Fujifilm image plates (CR HR-V) with a FujiFilm FLA7000 reader. Samples were exposed to achieve an adequate x-ray count for analysis, which was done using SAXSgui software v2.03.04.

### 6.3.5 Scanning Electron Microscopy

All samples were examined for their microstructural features using a Scanning Electron Microscope JOEL 5600. To obtain surface images, small sample portions were cut from the base material and mounted onto SEM stubs. Cross-sections were obtained by cryo-fracturing the material in liquid nitrogen and mounting the broken section onto a microscopy stub. Both surface and cross-sections were sputter-coated with gold for 45 s before imaging. Samples were imaged using an accelerating voltage of 8 kV and a spot size of 31.

### 6.3.5 Shape Memory Analysis

Shape memory cycles were performed on a Dynamic Mechanical Analyzer (TA Q800) operated in controlled-force mode. Briefly, each sample was first heated above the prescribed transition temperature and stretched at a rate of 0.05 N/min until the desired strain had been reached. Samples were then cooled at a rate of 2 °C/min to 0 °C and the force released at a rate of 0.1N/min. Samples were then heated at a rate of 2 °C/min to record the shape recovery. For materials that held more than one shape, the programming step was repeated above each transition temperature (for 4SMCs, samples were stretched at 120 °C, 70 °C and 45 °C) until the desired number of independent shapes had been programmed in. The fixing ( $R_f$ ) and recovery ( $R_r$ ) ratios for each recovery event were then calculated using Eqns. 4 and 5.

$$R_f(x) = \frac{\varepsilon_x}{\varepsilon_{x, \text{load}}} \quad (6-4)$$

$$R_r(x \rightarrow y) = \frac{\varepsilon_x - \varepsilon_{y, \text{rec}}}{\varepsilon_x - \varepsilon_y} \quad (6-5)$$

In Eqn. (6-4),  $\varepsilon_x$ ,  $\varepsilon_{x, \text{load}}$  are the strains measured after cooling and after unloading (thus, the strain fixed) and before unloading (thus attempted strain fixing). In Eqn. (6-5), additional terms include  $\varepsilon_{y, \text{rec}}$ , the strain achieved after recovery for shape y and  $\varepsilon_y$ , the strain before

programming shape  $y$  ( $x$  can be a strain at 115 °C, 70 °C, 45 °C or 0 °C, the same holds for  $y$ ). For strains programmed at 120 °C (strain programmed for PMMA-based fixing),  $\epsilon_x$  was measured after the force had been removed from the sample and any strain allowed to recover at 70 °C. This ensured that the strain used in the calculations only accounts for the strain fixed by the PMMA phase. This was done for all programming steps.

### 6.3.6 Macro Quadruple Shape Memory Demonstration

Bulk quadruple shape memory behavior was further characterized using a visual demonstration. Samples were manually bent in an isothermal oven above their highest (PMMA-based) glass transition by folding the sample and clamping it down using a binder clip. For this step, a glass slide was used as a spacer during bending steps to ensure the sample was not damaged. For the first programmed shape, the sample was heated above the transition of PMMA, 120 °C, and bent in the middle to program in a “U”. Once bent, the sample was held for 20 min at 120 °C to allow the PMMA to flow into the desired shape and then cooled to -20 °C by placing it in a freezer for 20 min. (Note: this low temperature was chosen out of convenience; any temperature below that of PMMA’s  $T_g$  should have been sufficient.) The sample was photographed once taken out of the freezer and then heated to 70 °C (above all transitions except for the PMMA  $T_g$ ) and photographed again. This allowed us to qualitatively compare the amount of strain attempted for programming into the material versus the amount actually programmed by vitrification of the PMMA phase. These steps were then repeated at 70 °C to program an “S” into the PCL network and then at 45 °C to program a temporary flat shape into the epoxy network.

### 6.3.7 Quadruple Shape Surface Shape Memory Demonstration

Surface multi-shape memory was visually analyzed using two common surfaces as embossing masters: the face of a one-cent US coin and the grooved pattern on a set of tweezers.

To mechanically program the surface shape, each master was pressed against a circular 4SMC disk and uniform pressure was applied via two glass slides configured as a “sandwich”. To apply pressure, the slides were clamped symmetrically with two binder clips and the sample held isothermally at 120 °C for 20 min in a convection oven. The full assembly was then moved to a freezer held at  $T = -20$  °C to fix the first temporary surface shape via PMMA phase vitrification. These steps were repeated using surface embossing at 70 °C and 45 °C to program parallel lines –oriented perpendicular to each other – fixed by the PCL phase and epoxy phases, respectively. Samples were imaged using a Hirox 3D microscope (Model KH-8700), and each embossed image compared to the embossing master.

## 6.4 Results

### 6.4.1. Fabrication of Composite Materials

Quadruple shape composites (4SMCs) were fabricated by combining two previously published methods; the first by combining an electrospun fiber mat in an SMP matrix, and the second by polymerization induced phase separation (PIPS). Both methods create biphasic materials that show two separate thermal transitions and triple shape memory behavior. By embedding a PCL fiber mat in a PIPS matrix we designed a triphasic composite composed of PCL, PMMA, and epoxy where an epoxy matrix with pockets of PMMA encase PCL fibers. At the beginning of the cure, the PIPS matrix was optically clear (Fig. 6-1) indicating the epoxy and PMMA materials were monophasic. As cure progressed the matrix turned opaque, indicating phase separation had occurred, while the pure epoxy matrix remained optically clear both before and after cure (Fig. 6-1). This transition was observed for both the epoxy/PMMA PIPS composition and the 4SMCs since the same matrix was used for both materials. In contrast, the

epoxy matrix and the matrix used for the epoxy/PCL composition remained clear both before and after the cure since the same matrix was used for both materials.

#### 6.4.2 Thermal Characterization

Calorimetric analysis using DSC revealed well-separated glass and melt transitions in the composite materials, supporting the assertion that the composites contained separate material phases (Fig. 6-2). The neat epoxy and PMMA samples (compositional controls) each showed a distinct glass transition ( $T_g$ ) at 31 °C and 110 °C, respectively. The PCL controlled showed a distinct melting transition ( $T_m$ ) at 55 °C. The epoxy/PCL triple shape composite showed both a step transition and a melting peak corresponding to the epoxy-rich phase with ( $T_g$  at 34 °C and the PCL rich phase with  $T_m$  at 55 °C respectively. The triple shape epoxy/PMMA PIPS composite showed two separate step transitions, the  $T_g$  of epoxy at 31 °C and the PMMA at 102 °C, respectively. The step transition of PMMA in DSC experiments was small compared to the epoxy, which has been previously reported for other PMMA composite systems.<sup>32</sup> The 4SMC displayed three separate thermal transitions, the  $T_g$  of the epoxy at 32 °C, the  $T_m$  of the PCL at 55 °C and the  $T_g$  of the PMMA at 106 °C. These results are summarized in Table 6-1.

The latent heat of melting of PCL was used to estimate the weight percentage of PCL in both 4SMCs (9% PCL) and the epoxy/PCL triple shape composition (9% PCL). The heat capacity of the epoxy  $T_g$  was used to calculate the percentage of epoxy in the blends by comparing the step change in the measured  $T_g$  to that of the pure epoxy control (0.074 J.g<sup>-1</sup> °C<sup>-1</sup>). For both the PIPS composite and the 4SMC materials, the total % composition for the PCL and epoxy phases were subtracted from 100% to estimate the incorporation percentage of PMMA (Table 6-1). It should be noted that the incorporation percentage of PMMA in the PIPS composite was 25%, which exceeds the value measured during fabrication.



The temperature-dependent dynamic mechanical transitions of all material composites were assessed using DMA traces (Fig 6-3). Similar to DSC, the epoxy/PCL triple shape composite displayed two thermomechanical relaxations, one for the epoxy  $T_g$  and one for the PCL  $T_m$  (Fig 6-3). The PIPS composite also displayed two thermal transitions, one for the epoxy  $T_g$  and one for the PMMA  $T_g$ . These transitions are evident most clearly in the loss modulus peaks at 29 and 98 °C, respectively. In contrast to the DSC traces, the PMMA signal was strong when measured with DMA. The 4SMC composition showed three distinct thermal transitions in the DMA data indicating three separate material phases and indicating the material should be able to fix three independent shapes.

#### 6.4.3 Wide Angle X-ray Scattering

WAXS experiments were carried out to gain an understanding of the molecular packing of the fabricated composites. The epoxy control material showed two amorphous halos, however, very little x-ray diffraction has been done with epoxy materials making interpreting the two distinct halos difficult. The PMMA showed one amorphous halo centered at  $2\theta = 14^\circ$  is attributed to a well-defined average spacing of the PMMA side chains along the polymer backbone.<sup>35,36</sup> This also overlaps in length-scale with the average intermolecular (backbone) spacing of the same chains. PCL showed sharp crystalline peaks at  $2\theta = 21^\circ$  and  $23.6^\circ$ , which correspond to d-spacings of 4.15 Å and 3.76 Å, respectively (Fig. 6-4).<sup>37-39</sup> In the PIPS composite and in the 4SMC the PMMA amorphous halo was not clearly evident. The 4SMC and epoxy/PCL triple shape composite both showed the double amorphous halo attributed to epoxy and the crystalline domains.

#### 6.4.4 Scanning Electron Microscopy

To examine the microstructure of the composite materials SEM inspections of the surfaces and freeze-fractured cross-sections of the composites were conducted (Fig. 6-5). When compared to the epoxy control, all composites showed evidence of rough fracture surfaces when viewed in cross-section. The PIPS composite and the 4SMC showed uneven “pocketing”, that may be attributed to the phase separation between the epoxy and PMMA phase.

#### 6.4.5 Shape Memory Analysis

All composites and controls were either assessed for one-way shape memory, triple shape memory or quadruple shape memory behavior, depending on the number of thermomechanical transitions the material demonstrated in DMA experiments (Fig 6-3). All samples were heated above the thermal transition needed to program a shape into a specific fixing phase. The programming temperatures used for the epoxy, PCL or PMMA were 40 °C, 70 °C and 120 °C, respectively and were selected to be just above the corresponding  $T_g$  or  $T_m$ . Once heated above the desired transition, each material was stretched and then cooled below the temperature transition to fix the temporary shape. This programming step was repeated once for triple shape composites and twice for 4SMCs. Once the programming was completed each material was heated at a continuous heating rate of 2 °C/min and the recovery events recorded. The individual steps are labeled in Fig. 6-6 according to the procedural activity of that step in the cycle, stretching, cooling or recovery, and the relevant material phase.

The epoxy control demonstrated one-way shape memory behavior (Fig. 6-6) and demonstrated a fixing and recovery ratio of 82% and 108% respectively. (Note: a recovery ratio greater than 100% is sometimes observed due to thermal expansion effects.) The triple shape memory composites for the epoxy/PCL showed a fixing ratio for the epoxy and PCL phases of

92% and 93% and a recovery ratio of 84% and 89% respectively (Fig. 6-6B). The triple shape memory composites for the epoxy/PMMA showed a fixing ratio for the epoxy and PMMA phases of 94% and 69%, and a recovery ratio of 110% and 102% respectively (Fig. 6-6C). The 4SMC shape memory ability was assessed for programming equal strains into all phases (Fig. 6-6D), programming more strain into the PCL phase (Fig. 6-6E) and programming more strain into the PMMA phase (Fig. 6-6F). The fixing and recovery ratios for the 4SMCs are summarized in Table 6-2. The epoxy phase showed the strongest shape memory ability with the fixing and recovery ratios over 95% for all tests. Both the PCL and PMMA phases showed a weaker fixing ability with fixing ratios ranging from 69-78%, however, all calculated recovery ratios were found to exceed 99%. A recovery ratio exceeding 100% indicates that the material recovered more strain than was fixed into that particular phase and is likely due to some cross-fixing between phases.

#### 6.4.6 Macro Quadruple Shape Memory Demonstration

A visual demonstration was performed to further show the quadruple shape memory behavior of the designed 4SMCs (Fig. 6-7). Three temporary shapes were programmed into 4SMCs by heating the composite above the three separate transition temperatures in the opposite order of recovery. Since the first shape programmed was the last to be recovered, the first shape programmed was a “U” in the PMMA phase, followed by an “S” in the PCL phase, and then a temporary flat shape in the epoxy phase. Upon recovery, the material transitioned from a temporary flat shape to an “S”, a “U” and finally returning back to the permanent flat shape. Briefly, a strip of the 4SMC was cut and heated to 115 °C, above the thermal transitions of all material phases. The sample was then folded into a temporary “U” shape and held in place using a binder clip. The sample was then cooled to -20 °C using a freezer to fix the temporary shape.

However, this would fix strain in both the epoxy and PCL phases as well. To erase this strain the sample was then heated to 70 °C, above the thermal transition of both the epoxy and PCL phases and the sample photographed. These steps were repeated exactly for programming strains into the PCL and epoxy phases at 70 °C (“S” shape) and 45 °C (temporary flat shape), respectively. The mechanical programming of shapes by the PMMA and PCL phase (Fig 6-7) was good although some strain was lost in the process. Upon heating, the material successfully transitioned from a temporary flat shape to an “S” shape to a “U” shape.

#### 6.4.7 Quadruple Shape Surface Shape Memory Demonstration

Surface shape memory or reversible embossing was also successfully demonstrated using a disk cut out of the 4SMC (Fig 6-8). Briefly, a series of surface patterns were successfully embossed on a disk cut out of the 4SMC material using a glass-sandwich mold and a series of embossing steps at progressively lower temperatures. To program a shape in the PMMA phase the “heads” side of a penny was stacked in contact with the 4SMC and placed between two glass slides. Pressure was applied using a set of large ACCO binder clips arranged with one along each edge of the glass slide, yielding an applied pressure of approximately 93 kPa distributed along the area of the glass slides. The assembly was then heated to 115 °C, allowing the penny head to be embossed in the PMMA phase. The assembly was then cooled to -20 °C to fix the temporary shape. The disk was then removed from the clamps and placed in the oven at 70 °C to allow any surface strain programmed into the PCL and epoxy phase to relax, but retaining the PMMA in its programmed state. These steps were repeated to program the horizontal lines into the PCL phase and the vertical lines into the epoxy phase at temperatures 70 °C and 45 °C respectively. The strains were then recovered by sequentially heating the disk to 45, 70 and 115 °C, and imaging the sample in-between each step (Fig 6-8). The disk transitioned from showing all three

temporary surface patterns (Fig 6-8A) to only showing the penny head and horizontal lines after heating to 45 °C (Fig 6-8B). After heating to 70 °C, the horizontal lines likewise recover (Fig 6-8C) and finally after heating to 115 °C the penny head recovers (Fig 6-8D). Some permanent strain remained on the surface of the material as evidenced by some pattern remaining on the surface of the 4SMC after full recovery.

## 6.5 Discussion

We successfully fabricated triphasic quadruple shape memory composites by embedding an electrospun PCL fiber mat in a matrix of PMMA and epoxy. Upon cure, the materials separated out into three separate phases, PCL, PMMA and epoxy which is supported by the three separate thermal transitions present in both DSC and DMA experiments. We do note that the depicted topology of the final 4SMC morphology has not been confirmed (Scheme 6-1). In particular, we show the PMMA phase existing as a discrete “Pockets”, through a co-continuous morphology is possible. In WAXS experiments the amorphous halo of PMMA was not clearly evident, but this may be due to the relatively low sensitivity of WAXS. The 4SMC and the TSMC both showed the double amorphous halo attributed to the epoxy and the crystalline domains for the PCL, indicating the persistence of microstructure for these two phases in the composites. While the unevening pocketing observed for the PIPS composite and the 4SMC in SEM experiments does support the hypothesis of the PMMA existing as discrete pockets their utility is limited due to the inherent limitations associated with analysis of fracture surfaces. Transmission electron microscopy with selective staining of particular phases would offer enhanced discernment potential and could be used to confirm the proposed topology.

It should be noted that the thermal transition (particularly the  $T_g$  of the epoxy and PMMA) was not consistent for all materials tested. The  $T_g$  of the epoxy was lower for the PIPS

composite and the 4SMC, and the same was true for the PMMA in both materials. This indicates that the phase separation between these two materials is incomplete resulting in some residual PMMA still present in the epoxy phase, plasticizing the  $T_g$ . Similarly, some epoxy resins would still be present in the PMMA phase resulting in a plasticized  $T_g$ . It is worth noting that this plasticization is less for the 4SMC than for the PIPS PMMA/epoxy triple shape, leading to speculation that the presence of the PCL helped drive the phase separation. This incomplete phase separation also skews the calculated incorporation of PMMA in the PMMA containing composites, resulting in the calculated composition being much higher than the value measured during fabrication. In addition, the step transition was small for the PMMA in the PMMA containing composites compared to that of the epoxy. This phenomenon has been observed in other PMMA composite systems. In contrast, the thermo-mechanical PMMA transition measured using the DMA was very strong indicating that where some incomplete phase separation does exist, the materials do likely still exist in two distinct phases.

Through both qualitative and quantitative analysis we successfully demonstrated the shape memory ability of our 4SMC composites. In addition, to the best of our knowledge, this is the first demonstrated example of quadruple surface shape memory. It is possible that the systems made by Luo<sup>33</sup> and Li<sup>32</sup> may have been capable of multi-shape memory behavior applied to surface embossing, given their broad transition behavior. However, such behavior was not reported. The laminated composite designed by Podgórski<sup>34</sup> would likely not be capable of QSSM, as not all material components are present on the surface. Our observed multi-shape memory embossing ability could prove to be highly relevant as topographical surface patterns have been proven to give material surfaces unique properties like adhesion,<sup>40</sup> antibacterial<sup>41</sup>, and hydrophobic<sup>42</sup> properties. We postulate that with QSSM one could design a material composite

that cycles through many different surface configurations with associated physical properties that could be tuned to a specific application.

In summary, this multiphase composite approach has proven to be a versatile and adaptable way to design new SMP systems that demonstrate both bulk and surface shape memory abilities. By combining an electrospun fiber mat with a triple shape PIPS solution we designed a 4SMC that demonstrated both quadruple bulk and surface shape memory behavior. However, one limitation is that the PIPS solution was very viscous and difficult to work into the fiber mats, indicating that this method may not work for incorporating additional material components, which would enable more material transitions.

## 6.6 Conclusions and Future Work

To conclude, we have developed a new ternary composite, 4SMC, exhibiting quadruple shape memory properties. The new material was prepared by imbining an electrospun web of PCL fibers with a single-phase blend of PMMA in epoxy liquid, which underwent polymerization induced phase separation (PIPS) during epoxy cure to yield a three-phase composition. This new approach to the formation of ternary composites may be broadly applicable to other PIPS systems combined with electrospun webs, blown fibers, or foams. Our study of 4SMC thermomechanical behavior and morphological properties contrasted the new material with binary composite counterparts, revealing three distinct transitions well separated in temperature and promise of quadruple-shape memory. Indeed 4SMC was found to exhibit both bulk and surface shape memory behavior with one permanent shape and three temporary shapes. Such behavior may be useful for a wide range of applications. In addition, the design of these 4SMCs can be easily adapted to other applications by simply selecting different polymers for either the fibers or composite matrix, giving the 4SMCs new functions like drug delivery or reversible

adhesion. Future work could include designing a 4SMC that responds to a variety of stimuli such as light or pH to increase the adaptability of these composites.

## 6.7 Acknowledgments

The authors acknowledge the use of the facilities at the Syracuse Biomaterials Institute and the efforts of Dr. Eric Finkelstein in maintaining them. Partial support from the NSF IGERT (DOE-1068780) and NSF DMREF (1334658) is gratefully acknowledged. The student contributions of Benjamin Posnick and Justine Paul is also gratefully acknowledged.



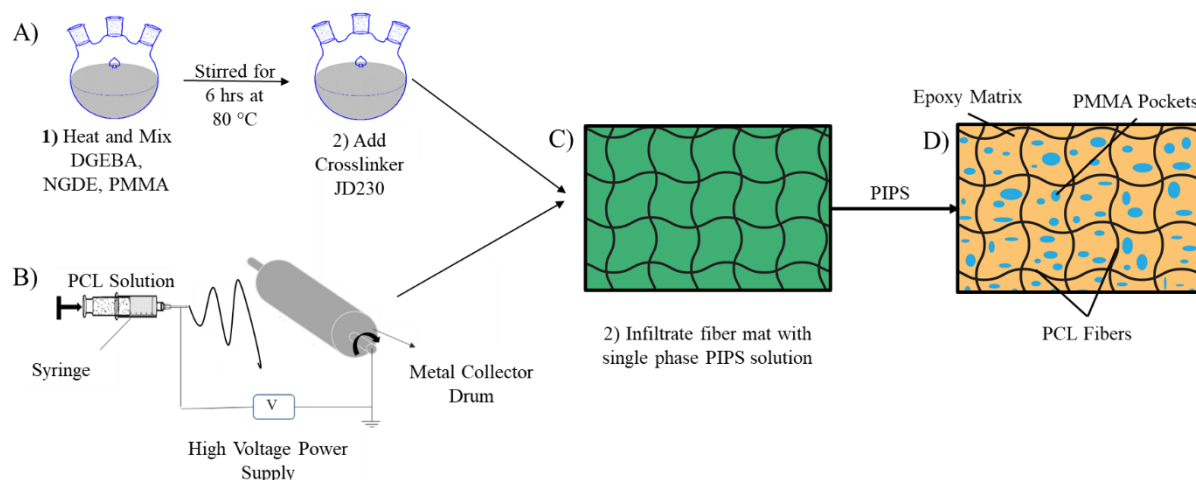
**Table 6-1.** The measured thermal transitions and % compositions of all composite materials.  
[a] °C [b] %.

	Epoxy T <sub>g</sub> <sup>[a]</sup>	Epoxy Incorporation <sup>[b]</sup>	PCL T <sub>m</sub> <sup>[a]</sup>	PCL Incorporation <sup>[b]</sup>	PMMA T <sub>g</sub> <sup>[a]</sup>	PMMA Incorporation <sup>[b]</sup>
TSPC	34.1	91	55.5	9	-	0
PIPS Composite	31.2	75	-	0	101.6	25
4SMC	32.0	79	55.4	9	94.8	12

**Table 6-2.** The fixing and recovery ratios for the 4SM composite cycled through three separate QSMCs.

	<b>Epoxy</b>		<b>PCL</b>		<b>PMMA</b>	
	R <sub>f</sub>	R <sub>r</sub>	R <sub>f</sub>	R <sub>r</sub>	R <sub>f</sub>	R <sub>r</sub>
Equal Strain	94.8	95.7	69.4	111.7	74.8	101.3
More PCL Strain	94.7	96.5	69.2	102.6	77.5	102.0
More PMMA Strain	94.7	96.1	78.1	102.7	68.9	99.2

All listed values are in units of percent.



**Scheme 6-1.** Process to make 4SMCs. 1) PIPS precursor is prepared by heating a solution of NGDE, DGEBA, and PMMA at 80 °C until all materials formed a homogenous solution. 2) JD230 cross-linker is then added and the solution was cooled to 50 °C. 3) PCL web is separately prepared by electrospinning rotating collector drum. 4) The PIPS precursor solution (green) is then imbibed into the web (black). 5) Upon cure, the PMMA and epoxy phase separate, creating a three-phase solid of PMMA, epoxy, and PCL.

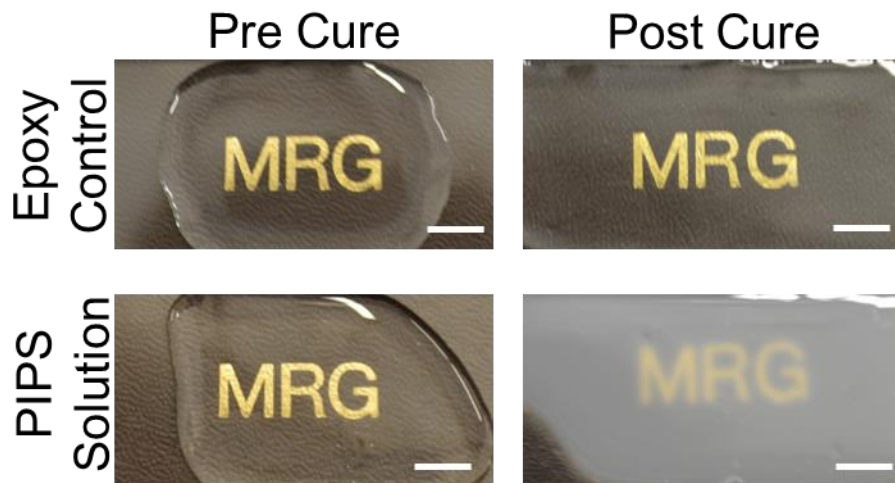


**Figure 6-1.** The images on the left are of epoxy liquids prior to cure. The top image is a pure epoxy resin and the bottom is a PIPS solution. After cure, the epoxy resin remained optically clear (shown top right) and the PIPS precursor solution became optically opaque (bottom right), indicating that phase separation had occurred. Scale Bar is 10 mm.

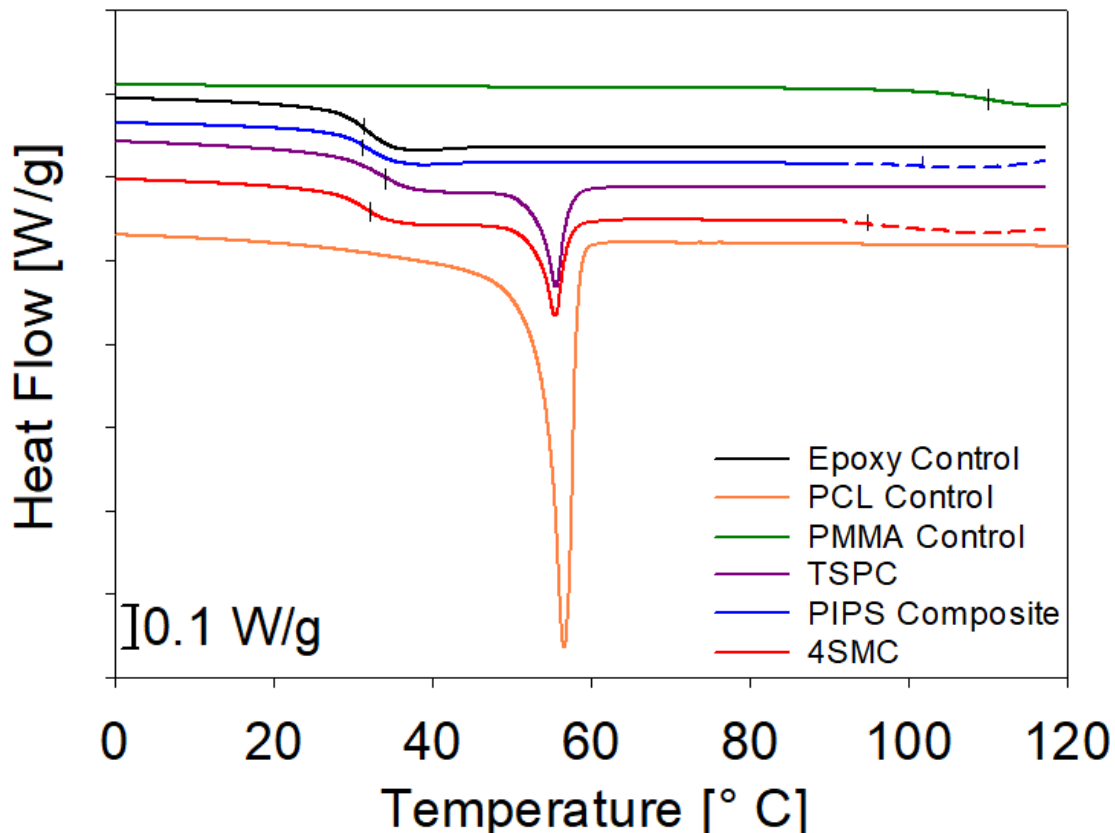


**Figure 6-2.** DSC thermograms (2nd heating) of 4SMCs, triple shape composite controls, and material controls. Epoxy matrix, PCL and PMMA controls are shown in black, red and green respectively. The epoxy/PMMA PIPS composite and epoxy/PCL TSPC controls are shown in blue and purple, respectively. The 4SMC is shown in red. The dashed lines are scaled up by a factor of 7 to make the PMMA T<sub>g</sub> visible in the DSC traces since the corresponding DSC signal was very small compared to the other thermal transitions. The heating rate was 10 °C/min for all samples.

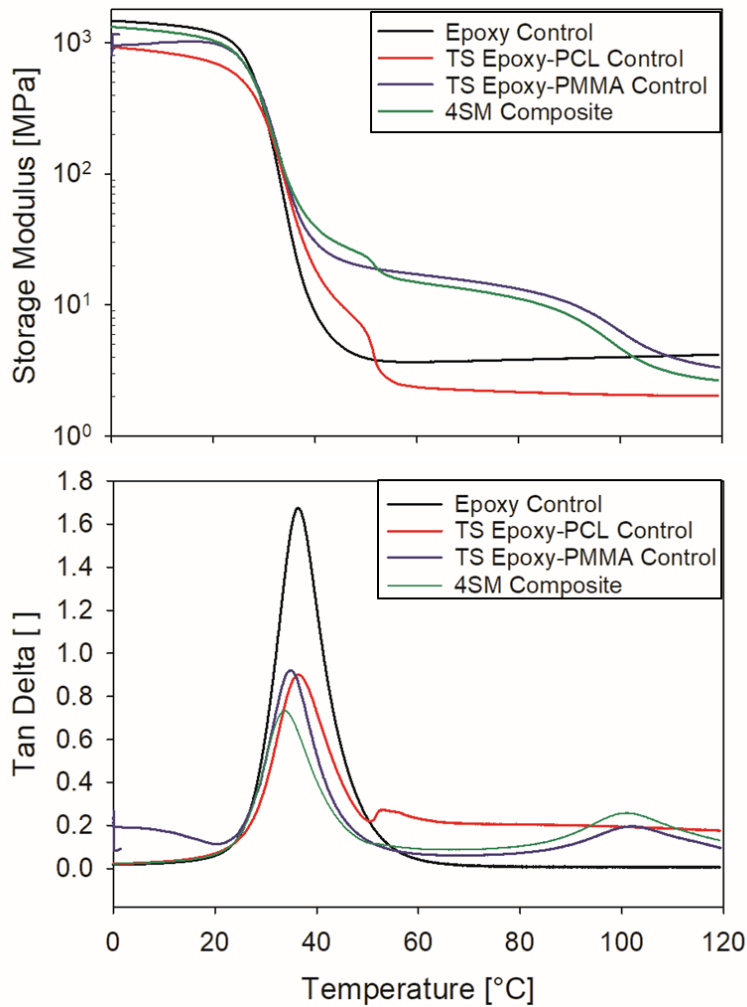


**Figure 6-3.** The DMA results for all material composites and an epoxy control. The top graph shows the temperature dependence of the storage modulus while the bottom shows the loss modulus. The thermal-mechanical transition of the PMMA was clearly visible in PMMA containing composite materials. The heating rate for all tests was 2 °C/min

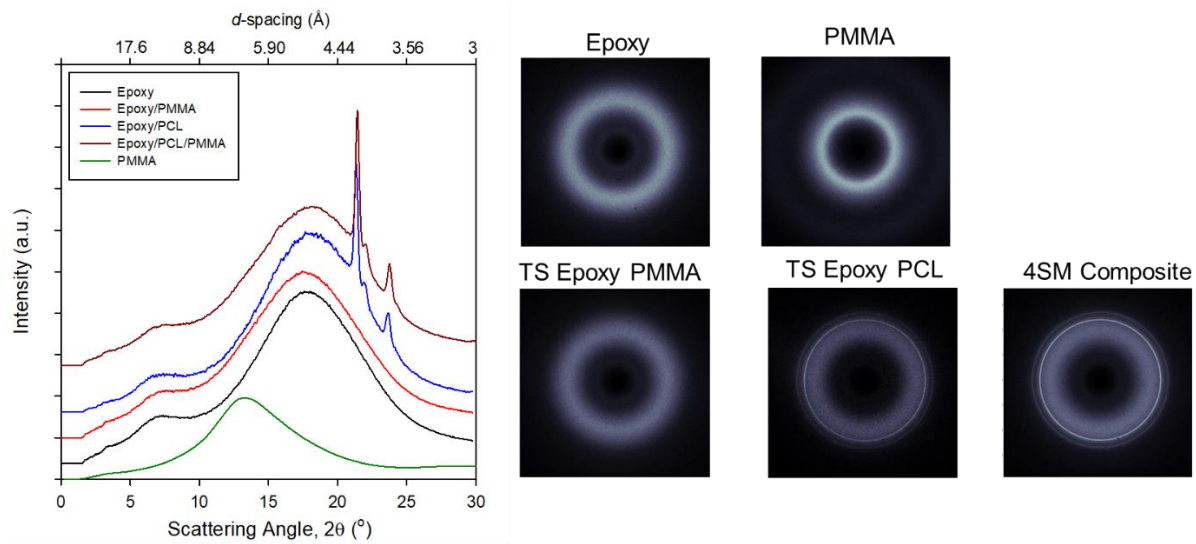


**Figure 6-4.** The Wide-Angle X-ray Diffraction of all control samples and composites. A) The intensity versus diffraction angle for all tested materials B) The WAXS scattering patterns for all materials.

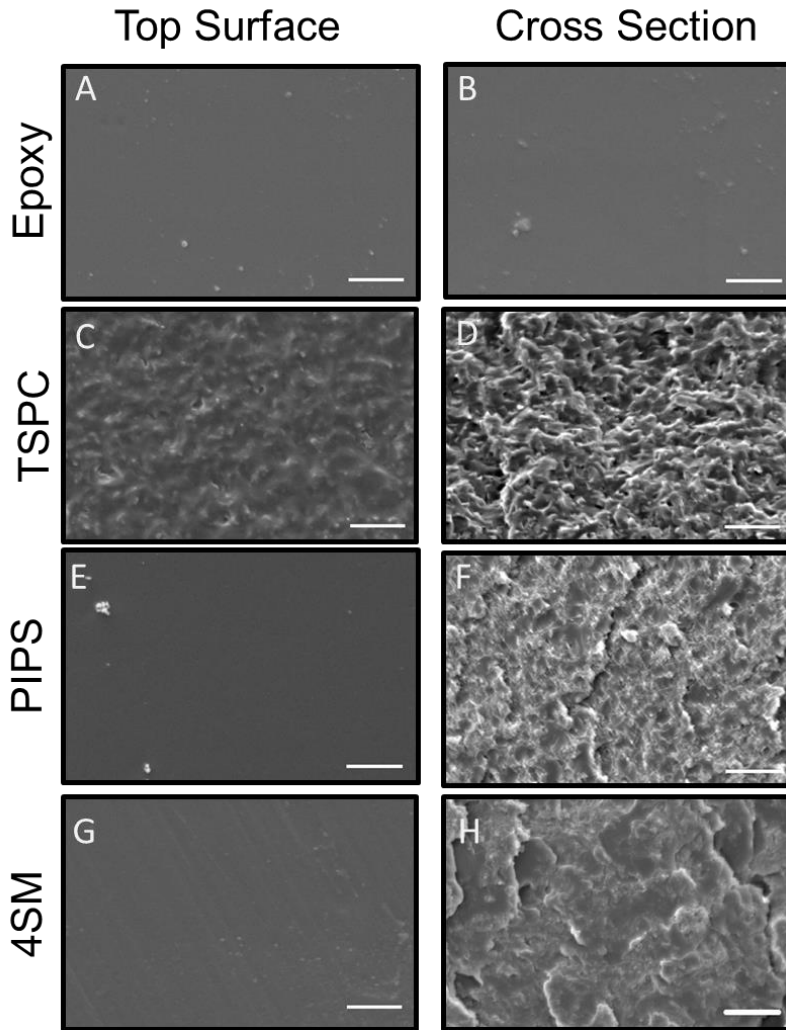


**Figure 6-5.** SEM of the composite materials and epoxy control. Images A, C, E, and G are representative images of the top surfaces of the epoxy control, epoxy/PCL triple shape composite, epoxy/PMMA PIPS composite and 4SMC, respectively. Images B, D, F, H show the cross-section of the epoxy control, epoxy/PCL triple shape composite, epoxy/PMMA PIPS composite and 4SMC, respectively. Scale bar is 10  $\mu\text{m}$ .



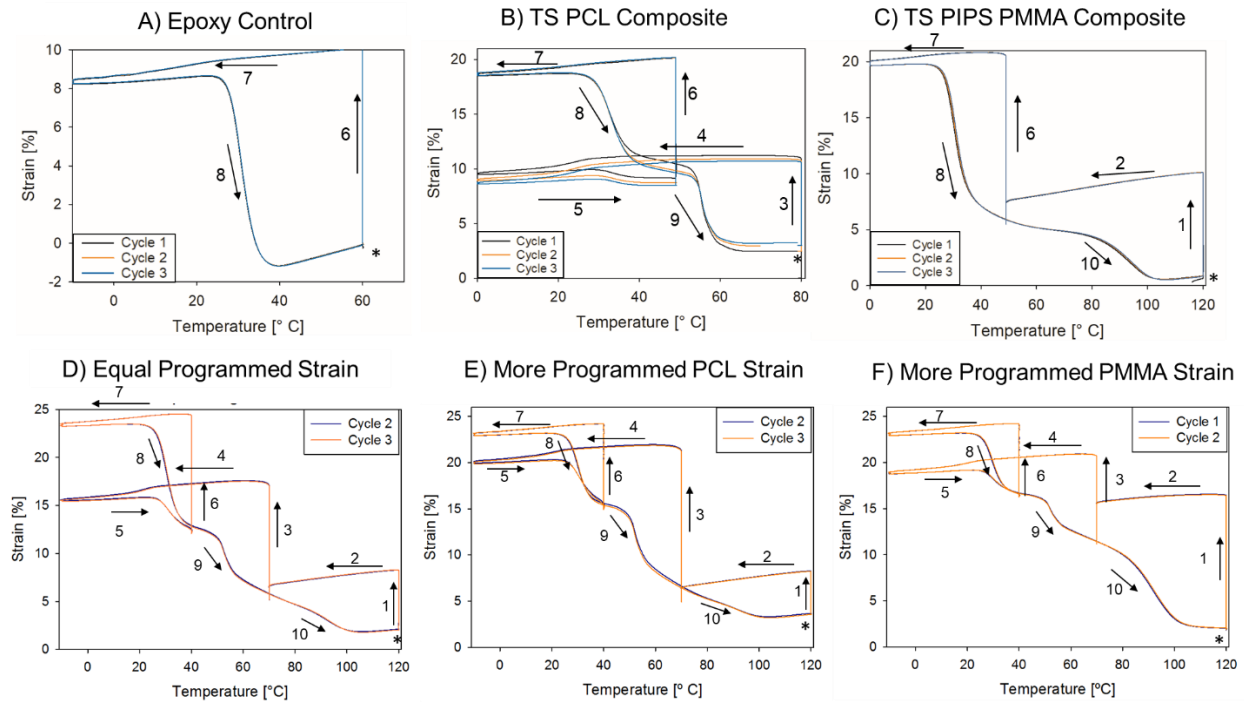


**Figure 6-6.** Shape memory characterization of epoxy matrix control and all composite materials. Graph A shows the 1 WSMC for the epoxy control matrix. In all graphs, the asterisk denotes that starting point. Graph B and C show the triple shape memory cycles for the TSPC control and the PIPS composite control, respectively. Graph D, E, and F are QSMCs programming different amounts of strain into each phase of the material. D: Equal amounts of strain were programmed into the composites and then recovered under continuous heating. E: More strain was programmed into the PCL phase of the material. F: More strain was programmed into the PMMA phase of the material. Step 1, 3, and 6 are stretching and programming strain into the PMMA, PCL and Epoxy phase respectively. Step 2, 4 and 7 were cooling steps with fixing of strain into the PMMA, PCL and epoxy phases, respectively. Steps 8, 9 and 10 show the recovery of the Epoxy, PCL and PMMA phases, respectively, under continuous heating. Step 5 was heating above the glass transition of the epoxy after cooling to a low temperature to fix the strain in the PCL.

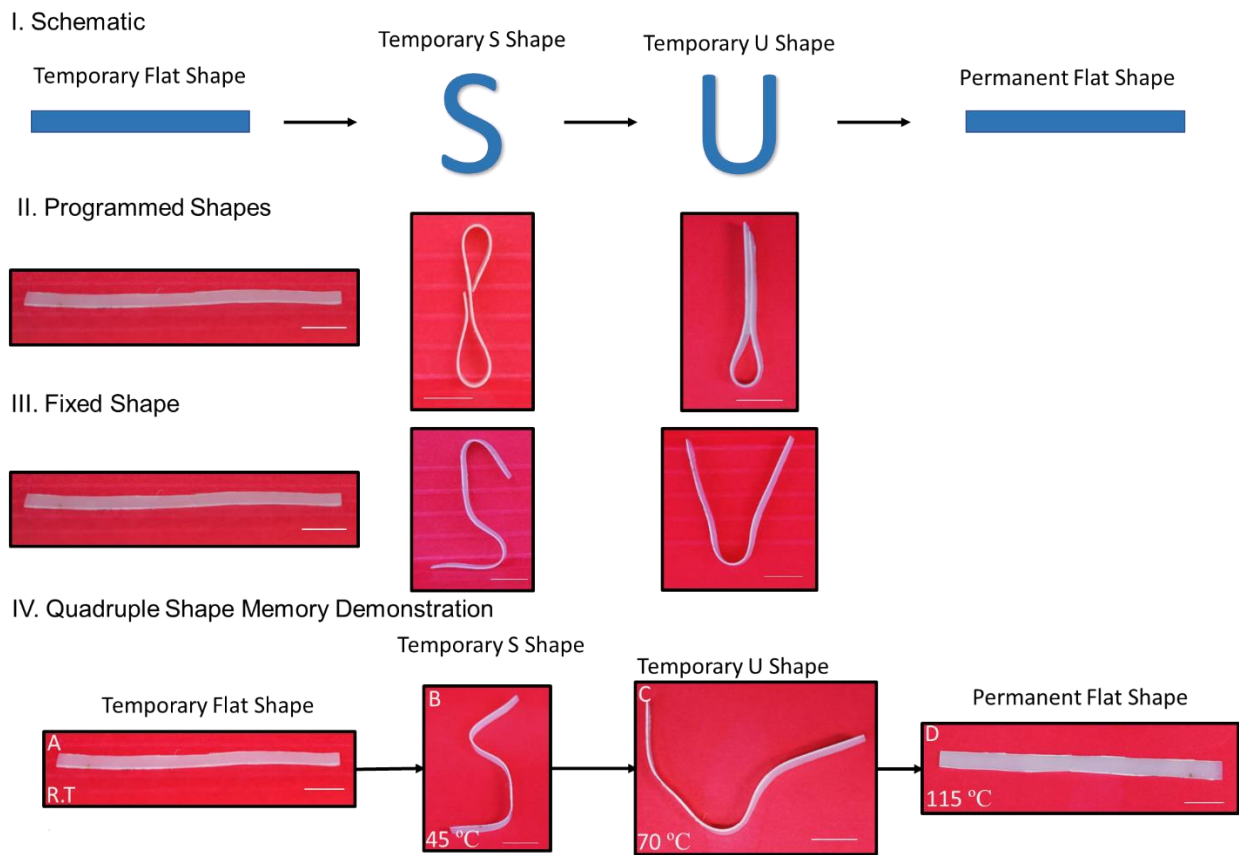


**Figure 6-7.** Macro SM Demonstration. I) shows an animation of the desired programmed shapes. II) Shows the programmed shapes in the 4SMCI. III) Shows the shapes fixed into the material by the desired material phase. IV) Shows the recovery of the 4SMCs the shape transitions from flat, to an S to a U to flat again, effectively demonstrating 4 distinct shapes. The scale bar shown in each image represents 10 mm.

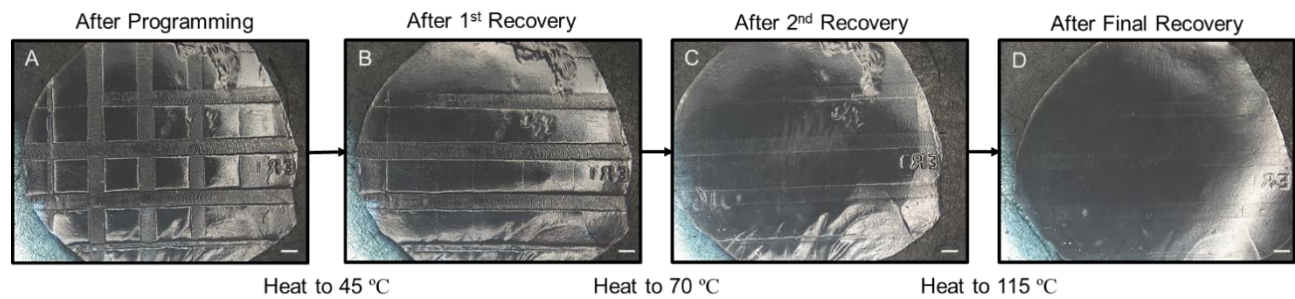


**Figure 6-8.** Surface Shape Memory Demonstration. A) Fully programmed disk with three separate patterns programmed on top of each other in the three separate material phases. B) 4SMC surface after allowing the epoxy to recover and the vertical lines fixed into the matrix recovered. C) 4SMC surface after triggering the PCL phase to recover and the horizontal lines recovered. D) 4SMC surface after triggering the PMMA to recover, returning the disk to its original shape. Scale Bar is 1 mm.

## 6.8 References

1. Luo, X. & Mather, P. T. Triple-Shape Polymeric Composites (TSPCs). *Adv. Funct. Mater.* **20**, 2649–2656 (2010).
2. Torbati, A. H., Nejad, H. B., Ponce, M., Sutton, J. P. & Mather, P. T. Properties of triple shape memory composites prepared via polymerization-induced phase separation. *Soft Matter* **10**, 3112–3121 (2014).
3. Liu, C., Qin, H. & Mather, P. T. Review of progress in shape-memory polymers. *J. Mater. Chem.* **17**, 1543 (2007).
4. Mather, P. T., Luo, X. & Rousseau, I. A. Shape Memory Polymer Research. *Annu. Rev. Mater. Res.* **39**, 445–471 (2009).
5. Hager, M. D., Bode, S., Weber, C. & Schubert, U. S. Shape memory polymers: Past, present and future developments. *Prog. Polym. Sci.* **49–50**, 3–33 (2015).
6. Meng, H. & Li, G. A review of stimuli-responsive shape memory polymer composites. *Polymer (Guildf)*. **54**, 2199–2221 (2013).
7. Liu, T. *et al.* Stimulus methods of multi-functional shape memory polymer nanocomposites: A review. *Compos. Part A Appl. Sci. Manuf.* **100**, 20–30 (2017).
8. Zhao, Q., Behl, M. & Lendlein, A. Shape-memory polymers with multiple transitions: complex actively moving polymers. *Soft Matter* **9**, 1744–1755 (2013).
9. Lendlein, A. Biodegradable, Elastic Shape-Memory Polymers for Potential Biomedical Applications. *Science (80-. )*. **296**, 1673–1676 (2002).
10. Lendlein, A., Jiang, H., Jünger, O. & Langer, R. Light-induced shape-memory polymers.

- Nature* **434**, 879–882 (2005).
11. Jiang, H. Y., Kelch, S. & Lendlein, A. Polymers Move in Response to Light. *Adv. Mater.* **18**, 1471–1475 (2006).
  12. Li, G., Fei, G., Xia, H., Han, J. & Zhao, Y. Spatial and temporal control of shape memory polymers and simultaneous drug release using high intensity focused ultrasound. *J. Mater. Chem.* **22**, 7692 (2012).
  13. Luo, X. & Mather, P. T. Conductive shape memory nanocomposites for high-speed electrical actuation. doi:10.1039/c001295e
  14. Gu, X. & Mather, P. T. Water-triggered shape memory of multiblock thermoplastic polyurethanes (TPUs)<sup>3</sup>. **3**, (2013).
  15. Mendez, J. *et al.* Bioinspired mechanically adaptive polymer nanocomposites with water-activated shape-memory effect. *Macromolecules* **44**, 6827–6835 (2011).
  16. Lv, H., Leng, J., Liu, Y. & Du, S. Shape-Memory Polymer in Response to Solution. *Adv. Eng. Mater.* **10**, 592–595 (2008).
  17. Zhang, F. H. *et al.* Remote, fast actuation of programmable multiple shape memory composites by magnetic fields. *J. Mater. Chem. C* **3**, 11290–11293 (2015).
  18. Mohr, R. *et al.* Initiation of shape-memory effect by inductive heating of magnetic nanoparticles in thermoplastic polymers. *Proc. Natl. Acad. Sci.* **103**, 3540–3545 (2006).
  19. Rodriguez, E. D. *et al.* Anisotropic Shape-Memory Elastomeric Composites: Fabrication and Testing. doi:10.1002/macp.201300086
  20. Torbati, A. H. & Mather, P. T. A hydrogel-forming liquid crystalline elastomer exhibiting

- soft shape memory. *J. Polym. Sci. Part B Polym. Phys.* **54**, 38–52 (2016).
21. Torbati, A. H., Mather, R. T., Reeder, J. E. & Mather, P. T. Fabrication of a light-emitting shape memory polymeric web containing indocyanine green. doi:10.1002/jbm.b.33107
  22. Rodriguez, E. D., Luo, X. & Mather, P. T. Linear/Network Poly( $\epsilon$ -caprolactone) Blends Exhibiting Shape Memory Assisted Self-Healing (SMASH). doi:10.1021/am101012c
  23. Behl, M., Razzaq, M. Y. & Lendlein, A. Multifunctional Shape-Memory Polymers. *Adv. Mater.* **22**, 3388–3410 (2010).
  24. Lawton, M. I. *et al.* Anhydride-Based Reconfigurable Shape Memory Elastomers. *ACS Macro Lett.* **5**, 203–207 (2016).
  25. Inoue, K., Yamashiro, M. & Iji, M. Recyclable shape-memory polymer: Poly(lactic acid) crosslinked by a thermoreversible Diels-Alder reaction. *J. Appl. Polym. Sci.* **112**, 876–885 (2009).
  26. Westbrook, K. K. *et al.* Two-way reversible shape memory effects in a free-standing polymer composite. *Smart Mater. Struct.* **20**, (2011).
  27. Fan, J. & Li, G. High performance and tunable artificial muscle based on two-way shape memory polymer. *RSC Adv.* **7**, 1127–1136 (2017).
  28. Bellin, I., Kelch, S., Langer, R. & Lendlein, A. Polymeric triple-shape materials. *Proc. Natl. Acad. Sci.* **103**, 18043–18047 (2006).
  29. Nejad, H. B., Baker, R. M. & Mather, P. T. Preparation and characterization of triple shape memory composite foams. doi:10.1039/c4sm01379d
  30. Xiao, Y.-Y. *et al.* Light-, pH- and thermal-responsive hydrogels with the triple-shape

- memory effect. *Chem. Commun.* **52**, 10609–10612 (2016).
31. He, Z., Satarkar, N., Xie, T., Cheng, Y. T. & Hilt, J. Z. Remote-controlled multi-shape polymer nanocomposites with selective radiofrequency actuations. *Adv. Mater.* **23**, 3192–3196 (2011).
  32. Li, J. *et al.* A versatile approach to achieve quintuple-shape memory effect by semi-interpenetrating polymer networks containing broadened glass transition and crystalline segments. *J. Mater. Chem.* **21**, 12213 (2011).
  33. Luo, Y., Guo, Y., Gao, X., Li, B. G. & Xie, T. A general approach towards thermoplastic multi-shape-memory polymers via sequence-structure design. *Adv. Mater.* **25**, 743–748 (2013).
  34. Podgórski, M., Wang, C. & Bowman, C. N. Multiple shape memory polymers based on laminates formed from thiol-click chemistry-based polymerizations. *Soft Matter* **11**, 6852–6858 (2015).
  35. Miller, R. L., Boyer, R. F. & Heijboer, J. X-ray scattering from amorphous acrylate and methacrylate polymers: Evidence of local order. *J. Polym. Sci. Polym. Phys. Ed.* **22**, 2021–2041 (1984).
  36. Lovell, R. & Windle, A. H. Determination of the local conformation of PMMA from wide-angle X-ray scattering. *Polymer (Guildf)*. **22**, 175–184 (1981).
  37. Alvarado-Tenorio, B., Romo-Uribe, A. & Mather, P. T. Microstructure and Phase Behavior of POSS/PCL Shape Memory Nanocomposites. (2011). doi:10.1021/ma2005662
  38. Nojima, S., Hashizume, K., Rohadi, A. & Sasaki, S. Crystallization of  $\epsilon$ -caprolactone

- blocks within a crosslinked microdomain structure of poly( $\epsilon$ -caprolactone)-block-polybutadiene. *Polymer (Guildf)*. **38**, 2711–2718 (1997).
39. Chatani, Y., Okita, Y., Tadokoro, H. & Yamashita, Y. Structural Studies of Polyesters. III. Crystal Structure of Poly- $\epsilon$ -caprolactone. *Polym. J.* **1**, 555–562 (1970).
  40. Huber, G., Gorb, S. N., Hosoda, N., Spolenak, R. & Arzt, E. Influence of surface roughness on gecko adhesion. *Acta Biomater.* **3**, 607–610 (2007).
  41. Glinel, K., Thebault, P., Humblot, V., Pradier, C. M. & Jouenne, T. Antibacterial surfaces developed from bio-inspired approaches. *Acta Biomater.* **8**, 1670–1684 (2012).
  42. Teisala, H., Tuominen, M. & Kuusipalo, J. Adhesion Mechanism of Water Droplets on Hierarchically Rough Superhydrophobic Rose Petal Surface. *J. Nanomater.* **2011**, 1–6 (2011).



# Chapter 7: Conclusions and Future Work

## 7.1 Overall Conclusions

This work describes the design and application of novel shape memory polymer (SMPs) for active cell culture experiments. These new isothermal platforms will enable future cell mechanobiological experiments to further understanding of how cells respond to mechanical changes in their environment and may be broadly applicable to tissue engineering applications.

In chapter 2, the design and fabrication of a novel SMP that triggers its material recovery in response to enzymatic degradation is described. This fiber composite was made using two commercially available elastomeric materials poly( $\epsilon$ -caprolactone) and Pellethane™ and is triggered to recover its original shape by the enzymatic degradation of PCL. This shape change was successfully demonstrated in bulk degradation experiments and was shown to be cytocompatible. In addition, when the SMP was triggered to recover, cells dynamically altered their morphology-based on the change in fiber architecture. This sensitivity to enzyme is advantageous over other triggering mechanisms as it has the potential to be tuned to specific cell behavior. For instance, if applied to wound healing we could design a bandage that as cells secrete enzymes to remodel the underlying tissue the material could apply a tensile force to slowly pull the wound closed as healing advances. It additionally adds SMPs to the field of enzyme responsive materials that have already been proposed for applications in drug delivery. Finally, this SMP advances the field of active cell culture platforms by adding a material that can change shape under isothermal conditions and in response to specific cell behavior. This will prove advantageous in active cell culture experiments especially given that enzyme sensitive dynamically stiffening hydrogels are already being used to better model cancer cell

environments. Having an SMP that can dynamically alter its alignment in response to enzyme activity better models the extracellular matrix orientation changes that occur during cancer cell metastasis and is expected to be a powerful experimental platform.

Chapter 3 described the development of a bilayer active cell culture platform that responds to light via the incorporation of methacrylated graphene oxide. Both the modified material chemistry and the process of light-triggered recovery were shown to be cytocompatible and could dynamically alter cell alignment. This work builds on the platform developed by us<sup>1</sup> that has already proven valuable in active cell culture experiments to alter cell morphology<sup>1</sup> and migration behavior.<sup>2-4</sup> By enabling the material to be light-sensitive the SMP platform is now able to recover in response to light during a cell experiment, negating the need for a temperature change to induce material recovery. In addition, light-triggered SMPs were shown to be locally triggered to recover enabling the formation of boundaries as the topography transitioned from flat to wrinkled. This localized recovery could be applied to studying how cell migration behavior changes as they move across topographical boundaries.

Chapter 4 describes the modification of a previously developed post-process cell tracking algorithm, automated contour-based tracking for *in vitro* environments (ACTIVE),<sup>4</sup> into a real-time cell tracking platform. To accomplish this, the  $\mu$ Manger controls for the microscope were ported into MATLAB, enabling ACTIVE to both analyze cell migration behavior and direct the microscope in image acquisition during live-cell experiments. We successfully showed that both the accuracy of cell tracks and subsequent analysis were unaffected by running the code in real-time for multiple positions, by comparing the results to post-analyzed data. In addition, we began the development of a single cell tracking code that could follow a single cell throughout an experiment, an experimental tool that has not been previously demonstrated. Where corrections

to the cell tracks following translation still need to be implemented we expect this will be a useful experimental tool for future cell mechanobiological experiments.

Currently, the majority of active cell culture platforms are only capable of a single mechanical transition. Chapter 5 and chapter 6 discuss applying multi-shape memory materials to generate surfaces capable of multiple topographical transitions. In chapter 5 the same bilayer system used in chapter 3 was applied to a triple shape memory composite (TSMC) and the formation of double or complex wrinkle patterns was observed. The developed wrinkle patterns showed a sensitivity to the strain programmed into the composites, the order of triggered recovery and to the material phase inducing recovery. Chapter 6 discussed the development of a novel quadruple shape memory composite platform that was the first to demonstrate quadruple surface shape memory. Where these two material platforms were not cytocompatible, these two platforms provide insight into the design and implementation of composites capable of multiple surface transitions, thus informing the development of active cell culture platforms capable of similar transitions.

Overall the SMP platforms developed in this dissertation show great potential for use as active cell culture platforms and are expected to be used in future cell mechanobiology experiments. Their sensitivity to different material triggers should enable new experimental designs that were previously impossible. Some suggestions for future work relating to the SMPs developed in this dissertation are discussed below.

## 7.2 Recommendations for Future Work

### 7.2.1 Demonstrating Cell-Triggered Recovery of Enzymatically Triggered SMPs

Were we successfully demonstrated enzymatic shape recovery in the presence of cells, we have not yet shown enzymatic shape recovery due to the enzymatic secretions of cells. To accomplish this task, we have already demonstrated that enzymatic shape recovery can induce changes in fiber morphology (Fig. 7-1) by following programming procedures established by Ling-Fang Tseng.<sup>5</sup> Briefly, an aligned fiber mat is stretched perpendicular to the direction of fiber orientation, creating a temporary strain-unaligned fiber morphology. Upon shape recovery the strain-unaligned morphology transitions back to its aligned morphology causing cells to change their orientation from random to aligned. Initial experiments using the enzymatic SMP and this programming method have shown that it may also be an effective method for re-aligning cells cultured on the enzymatic SMP as well (Fig. 7-1). After seeding cells on the strain-unaligned samples for 3 hours, media containing three separate concentrations of lipase were added to the well plates. The samples were then fixed after incubating for 24 hours in the enzyme-containing media and the cell morphology and number was observed. In this initial experiment, we noted that substrates cultured in 1.5 mg/mL of lipase had not yet recovered but the samples incubated in 3.7 mg/mL and 7.5 mg/mL lipase had recovered. In response, the cells cultured on the recovered materials now showed a more polarized morphology. However, the number of cells attached to the substrate decreased with increasing enzyme concentration indicating that the speed of the enzymatic shape triggering could cause cell detachment. In the future, we plan to continue these experiments using a lipase secreting cell line such as the HepG2 cell line or activated macrophages. We expect that if the cells secrete a high enough concentration of enzyme then the cells themselves could trigger material recovery.

## 7.2.2 Improving the Design of Enzymatically Triggered SMPs

Where there are certainly advantages to the current design of enzymatically triggered SMPs, there are several drawbacks that could be expanded on. First, the current design of enzyme-triggered SMPs would only allow for a tensile force to be applied or only shrinking to occur. An expanding platform, like that capable of SMP foams, may prove interesting for mechanobiological experiments. To design such a platform, we propose designing a custom synthesized SMP following thermoplastic polyurethane chemistry previously developed by the Mather lab and used in some of our past work. This previously used TPU would show extensive shrinking after electrospinning due to residual stress present in the fibers. This residual stress had to be released using a Pluronic™ treatment before deploying the electrospun platform in active cell culture platforms. We believe that this shrinking could instead be used to program an SMP fiber platform that will then expand upon enzymatic degradation of this TPU. To accomplish this, the previously made TPU would first have to be modified to be enzymatically degradable. This can be accomplished by adding caprolactone to the poly-ol during synthesis. The caprolactone content would have to be carefully controlled such that enzymatic degradation resulted in a loss of polymer mechanical integrity and the SMP demonstrated substantial shrinking post electrospinning. This newly designed TPU would then be dual electrospun with an elastomeric material like Pellethane™. After electrospinning, the material would be heated to induce shrinking and the Pellethane would be put under a compressive force. Upon the enzymatic degradation of the TPU, the Pellethane™ would then be allowed to expand back to its original, entropically preferred state.

Second, the current design is not especially sensitive to enzymes. The enzyme used to demonstrate enzymatically-triggered shape recovery (Chapter 2), lipase, generally degrades

polyesters. In addition, the SMP was not very sensitive to the presence of the enzyme and required large concentrations of enzyme to trigger material recovery in the observed experimental time-period. By incorporating naturally occurring peptide sequences in the backbone of the degrading polymer, we can both improve the sensitivity of the SMP to enzyme concentration and increase the number of enzymes that the triggered recovery is sensitive too. Sears and colleagues were able to synthesis a polyurea elastomer with collagen derived peptide incorporated into the polymer backbone that showed tuned enzymatic degradation.<sup>6</sup> If such a platform could be modified for the TPU chemistry, we could synthesize a variety of materials that show enzymatic susceptibility to several enzymes found in the body and tune the enzymatic sensitivity of the material to the current application.

### 7.2.3 Physiologically Relevant Multi-Shape Memory Material

Despite the growing body of SMPs that have been successfully deployed as active cell culture platforms, there is currently no example of a multi-shape memory material capable of undergoing both recoveries during a cell culture experiment. The development of such a material would enable the application of either two precise mechanical stimulations or two topographical transitions during an active cell culture experiment. However, due to the relatively small temperature range that cells are viable at it seems unlikely that such a platform could be triggered by temperature alone. Instead, we believe that a multi-shape memory material capable of multiple shape transitions during cell culture would have to be designed to respond to temperature and light, or just light. We are currently developing a multi-shape memory composite capable of undergoing one shape change due to temperature and a subsequent shape change in response to light. To fabricate this SMP graphene oxide is incorporated into an electrospinning solution of PCL and then electrospun. This results in a fiber mat of PCL that is

dispersed with graphene oxide. The PCL fiber mat is then encased in a matrix to *tert*-butyl acrylate-co-butyl acrylate to create a multi-shape memory composite capable of undergoing two separate shape changes. The glass transition of the matrix is carefully tuned to recover at 37 °C and we have successfully shown that the material is capable of recovering in response to exposure from white light. We believe that these two transitions can be triggered separately during an active cell culture experiment where cells are first seeded on the material and cultured at 30 °C. We can then increase the temperature to 37 °C, which would trigger the first recovery event but would not be enough to melt the PCL fibers and thus trigger the second recovery event. After a set amount of time, we would then expose the sample to light which would be absorbed by the graphene oxide as heat and transferred to the PCL fibers. This would cause the PCL fibers to melt and the matrix to recover the second shape, thus applying the second recovery transition to the cultured cells. To develop a multi-shape memory material that is only light-triggered, one would have to incorporate two different light photo-thermal agents into the two different phases of the composite SMP. This would be possible by taking advantage of the plasmonic resonance of gold and silver nanoparticles where absorb in the red and blue light ranges respectively.

#### 7.2.4 Reversible Light-Triggered SMPs for Active Cell Culture Experiments

Despite interest in developing reversible SMPs that could be applied to biomedical applications, there has not been an example of a reversible SMP applied as an active cell culture platforms. The closest reversible SMP platform developed was by Ashby and colleagues and could reversibly actuate between a flat surface and a patterned surface.<sup>7</sup> However, this actuation was not demonstrated in the presence of cells, likely because of the temperature shifts required to actuate the SMP. In fact, the majority of reversible actuators require large shifts in temperature to show a large shift in shape. However, this limitation can be overcome using photo-thermal

recovery, similar to the strategy used in chapter 3. Previously, Tan *et al.* developed a reversible actuator using the SMP foam developed by Baker et al. and infiltrating it with polydimethylsiloxane.<sup>8</sup> By mixing graphene oxide into the polymer solution during the foam fabrication we can design a reversible SMP that actuates in response to light, thus potentially enabling large strain actuation during active cell culture experiments.



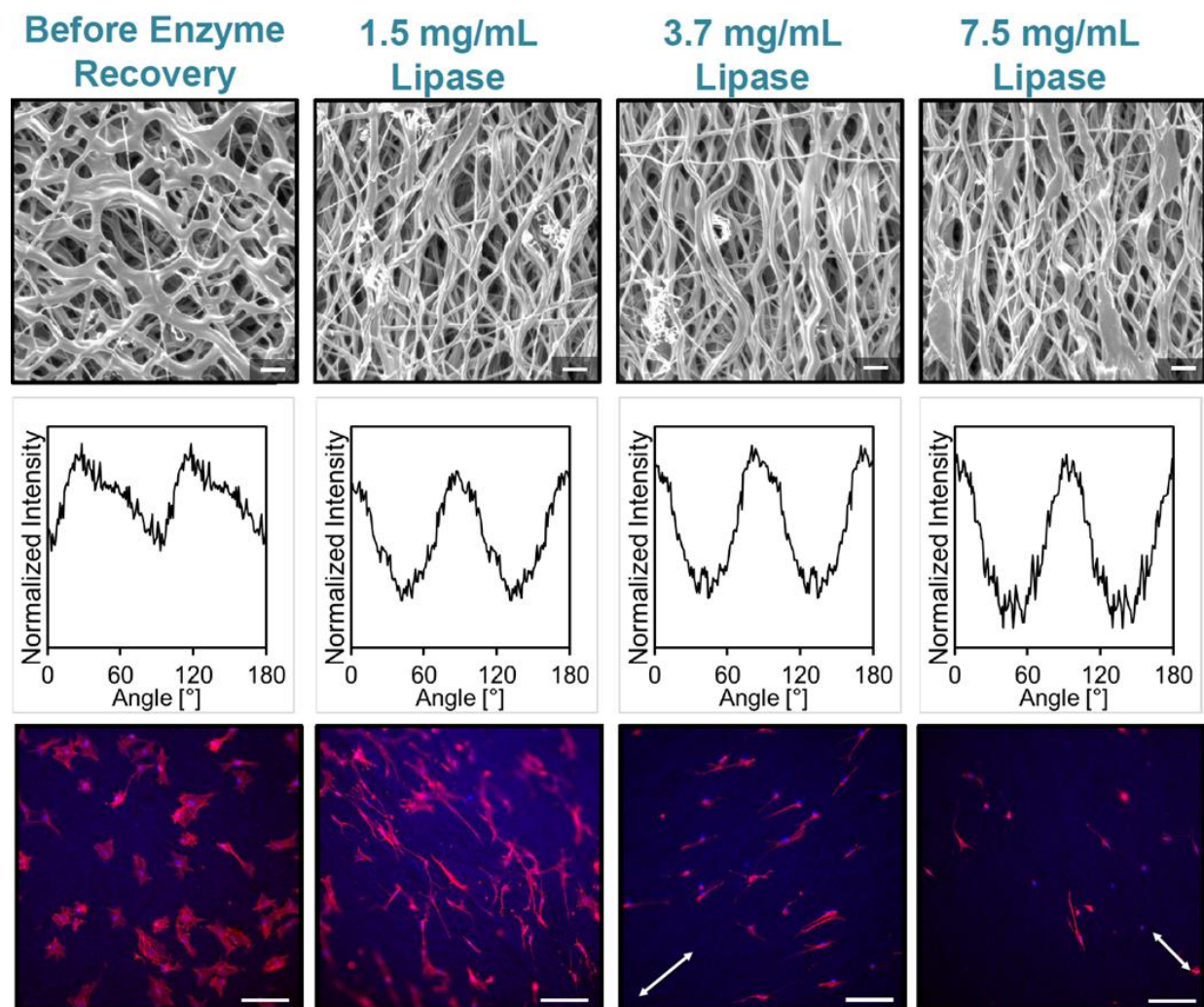


**Figure 7-1.** Top) SEM micrographs of the fiber orientation before triggering and after incubating in a solution of PBS and varying concentrations of lipase for 24 hours. Scale bar 10  $\mu\text{m}$ . Middle) 2DFFT azimuthal scans of the SEM micrographs. As the fibers become for aligned a bimodal distribution becomes apparent indicating fiber alignment. Bottom) Cell micrographs of fixed cells cultured on the surface of enzymatic SMPs while the material recovers its aligned fiber architecture. Scale bar 50  $\mu\text{m}$ .

### 7.3 References

1. Yang, P. *et al.* In vitro wrinkle formation via shape memory dynamically aligns adherent cells. *Soft Matter* **9**, 4705 (2013).
2. Brasch, M. E. *et al.* Nuclear position relative to the Golgi body and nuclear orientation are differentially responsive indicators of cell polarized motility. *PLoS One* (2019).  
doi:10.1371/journal.pone.0211408
3. Passucci, G., Brasch, M. E., Henderson, J. H., Zaburdaev, V. & Manning, M. L. Identifying the mechanism for superdiffusivity in mouse fibroblast motility. *PLoS Comput. Biol.* (2019). doi:10.1371/journal.pcbi.1006732
4. Baker, R. M., Brasch, M. E., Manning, M. L. & Henderson, J. H. Automated, contour-based tracking and analysis of cell behavior over long time scales in environments of varying complexity and cell density. *J. R. Soc. Interface* **11**, 20140386 (2014).
5. Tseng, L.-F., Mather, P. T. & Henderson, J. H. Shape-memory-actuated change in scaffold fiber alignment directs stem cell morphology. *Acta Biomater.* **9**, 8790–8801 (2013).
6. Sears, N. A., Pena-Galea, G., Cereceres, S. N. & Cosgriff-Hernandez, E. Hybrid polyurea elastomers with enzymatic degradation and tunable mechanical properties. *J. Tissue Eng.* **7**, 204173141667936 (2016).
7. Turner, S. A., Zhou, J., Sheiko, S. S. & Ashby, V. S. Switchable Micropatterned Surface Topographies Mediated by Reversible Shape Memory. *ACS Appl. Mater. Interfaces* **6**, 8017–8021 (2014).
8. Tan, C. Soft Reversible Actuator based on Shape Memory Polymer. *Diss. - ALL* (2015).

## VITA

**NAME OF AUTHOR:** Shelby Lois Buffington

**PLACE OF BIRTH:** Merced, CA, USA

**DATE OF BIRTH:** September 19, 1990

### EDUCATION:

B.S. in Bioengineering, Texas A&M University, College Station, 2012

PhD. in Bioengineering, Syracuse University, 2013-present

### PUBLICATIONS:

1. **Buffington SL**, Paul JE, Ali MM, Macios MM, Mather PT, Henderson JH. Enzymatically Triggered Shape Memory Polymers. *Acta Biomaterialia*, 2018, *Accepted*, [10.1016/J.ACTBIO.2018.11.031](https://doi.org/10.1016/j.actbio.2018.11.031)
2. **Buffington SL**, Posnick B, Paul JE, Mather PT. Ternary Polymeric Composites Exhibiting Bulk and Surface Quadruple-Shape Memory Properties. *ChemPhysChem Special Issue: Smart Materials*, 2018 19 (16), 2014-2024
3. **Buffington SL**, Pual JE, Henderson JH, and Mather PT. Strain Stiffening Anisotropic Elastomer Composites. *In Preparation*
4. Gu H, Lee SW, **Buffington SL**, Henderson JH, and Ren D. On-demand removal of bacterial biofilms via shape memory activation. *ACS Applied Materials & Interfaces*, 2016 8 (33), 21140-21144
5. **Buffington SL**, Browning MB, Cosgriff-Hernandez E. Clinically Applied Biomaterials for Soft Tissue Applications. *Biomedical Technology and Devices*, 2nd ed., D. Maitland, J. Moore, CRC Press, February 15, 2013
6. Braun B, **Buffington SL**, Dees M. Performance Evaluation of Process Rheometer on Different Product Families Report I-III. Internal Dow Publication, 2013

### PEER-REVIEWED ABSTRACTS AND CONFERENCE PROCEEDINGS:

1. **Buffington SL**, Macios MM, Lee C, Mather PT, Henderson JH. Enzymatically Triggered Shape Memory Polymers. Oral Presentation, Society for Biomaterials, Atlanta, GA, April 11-13<sup>th</sup> 2018
2. **Buffington SL**, Paul JE, Ali MM, Macios MM, Mather PT, Henderson JH. Enzymatically Triggered Shape Memory Polymers. Poster Presentation NYS Bioengineering Symposium, Syracuse NY, May 17<sup>th</sup>, 2018. **2nd Place Award**
3. **Buffington SL**, Paul JE, Ali MM, Mather PT, and Henderson JH. Enzymatically Triggered Shape Memory Polymers. Poster Presentation, Biomedical Engineering Society Annual Meeting, Atlanta, GA, October 17<sup>th</sup>, 2018

4. **Buffington SL**, Posnick B, Mohun PA, Kotis BM, and Henderson JH. Developing a Real-Time Contour Based Cell Tracking Algorithm. Poster Presentation, Biomedical Engineering Society Annual Meeting, Atlanta, GA, October 17<sup>th</sup>, 2018
5. Mather PT and **Buffington SL**. Ternary Polymer Composites Exhibiting Bulk and Surface Quadruple Shape Memory. XXVII International Materials Research Congress (IMRC), Symposium on New Trends in Polymer Chemistry and Characterization, Cancun, MEXICO. 2018
6. **Buffington SL**, Macios MM, Lee C, Mather PT, Henderson JH. Enzymatically Triggered Shape Memory Polymers. Poster Presentation, Northeast Bioengineering Conference, Philadelphia, PA, March 27<sup>th</sup> – 29<sup>th</sup> 2018
7. Paul JE, **Buffington SL**, Mather PT, and Henderson JH. An Expanding, Enzyme Responsive Shape Memory Polymer. Biomedical Engineering Conference (NEBEC), 44<sup>th</sup> Annual Northeast, IEEE, 2018. In press.
8. Jannini AVS, **Buffington SL**, and Henderson JH. Polymers in the Classroom: Developing a Summer Workshop for High School Science Teachers. Oral Presentation, 2018 ASEE Annual Conference and Exposition, Salt Lake City, UT; June 24-27, 2018
9. **Buffington SL**, Jannin AVS, Johnson AJ, Pieri K, Smith R. Soft Skills Boot Camp: Designing a Three Day Student-Run Seminar and Workshop Series for Graduate Students. Oral Presentation, American Society for Engineering Education Annual Conference and Exposition, Salt Lake City, UT, June 27<sup>th</sup>, 2018
10. Paul JE, **Buffington SL**, Henderson JH, and Mather PT. Biomimetic Rubber: Applications, Structure, and Properties. Biomedical Engineering Society Annual Meeting, Phoenix, AZ; October 11-14, 2017.
11. **Buffington SL**, Henderson JH, Mather PT. Generating Complex Wrinkle Patterns for Active Cell Culture via Shape Memory Polymers. American Chemical Society Annual Meeting, Philadelphia, PA, August 24<sup>th</sup>, 2016
12. Gu H, Lee SW, **Buffington SL**, Henderson JH, and Ren D. On-demand release of bacterial biofilms via shape memory activation. AIChE Annual Meeting, Biomaterials: Faculty Candidates II, San Francisco, CA; November 14, 2016.
13. Benn S., **Buffington SL**, Henderson JH. Incorporation of Silver Nanoparticles in Electrospun Fiber Mat to Increase Antimicrobial Activity. National Society for Black Engineers (NSBE) Technical Research Competition. Niagara Fall, NY; November 18, 2016. Winner, **First Place Prize**.
14. **Buffington SL**, Loh D, Henderson JH, Mather PT, “Generating Complex Wrinkle Patterns for Active Cell Culture via Shape Memory Polymers” Poster Presentation, Materials Research Symposium, Boston, MA, November 30<sup>th</sup> – December 5<sup>th</sup>, 2014. **Biomaterial Science Prize**
15. **Buffington SL**, Braun B, Dees M. Project Review of Process Rheometers. Oral Presentation, Global Characterization, Freeport, TX, June 16<sup>th</sup>, 2013
16. **Buffington SL**, Holm J, Cosgriff-Hernandez E. Characterizing Injectability and Progressing Toward Cell Encapsulation with a Highly Porous Bone Graft. Poster Presentation, SFB-Biomaterials Day, Houston, TX, July 29<sup>th</sup>, 2013.
17. Moglia R, Holm J, **Buffington SL**, Touchet T, Cosgriff-Hernandez E. Fabrication of Injectable and High Porosity PolyMIPE Scaffolds for Soft Tissue Regeneration. Oral Presentation, 245<sup>th</sup> ACS National Meeting, New Orleans, LA April 7-11, 2013

18. Holm J, Moglia R, **Buffington SL**, Munoz-Pinto D, Hahn M, Cosgriff-Hernandez E. High Porosity PolyHIPEs as Injectable Bone Grafts. Oral Presentation, 2011 Biomedical Engineering Society Annual Meeting, Hartford, CT, October 12-15, 2011

#### **LOCAL PRESENTATIONS:**

1. **Buffington SL**, Paul JE, Ali MM, Mather PT, Henderson JH. Development of Novel Smart Materials: Enzymatically Triggered Shape Memory Polymers. Seminar Oral Presentation. Department of Biomedical and Chemical Engineering Seminar Series, Syracuse University. November 30<sup>th</sup>, 2018.
2. **Buffington SL**, Macios MM, Lee C, Mather PT, Henderson JH. Enzymatically Triggered Shape Memory Polymers. Poster Presentation Syracuse Engineering and Computer Science Research Day, Syracuse NY, March 29th. **1st Place Award**
3. Paul JE, **Buffington SL**, Mather PT, and Henderson JH. Expanding, Enzymatic Responsive Shape-Memory Polymer. Poster Presentation, Stevenson Biomaterials Research Poster Session 2018, Syracuse University, Syracuse, NY; April 23, 2018
4. Kotis BM, **Buffington SL**, Mohun PA, and Henderson JH. Automated Cell Tracking. Poster Presentation, Stevenson Biomaterials Research Poster Session 2018, Syracuse University, Syracuse, NY; April 23, 2018.
5. Waimin JF, **Buffington SL**, and Henderson JH. Photothermally Activated Shape Memory Polymers. Poster Presentation, Stevenson Biomaterials Research Poster Session 2018, Syracuse University, Syracuse, NY; April 23, 2018.
6. **Buffington SL**, Macios MM, Lee C, Mather PT, and Henderson JH. Enzymatically Triggered Shape Memory Polymers. Poster Presentation, Stevenson Biomaterials Research Poster Session 2018, Syracuse University, Syracuse, NY; April 23, 2018.
7. Paul JE, **Buffington SL**, Mather PT, and Henderson JH. Expanding, Enzymatic Responsive Shape-Memory Polymer. Poster Presentation, Syracuse Engineering and Computer Science Research Day, Syracuse NY; March 29th, 2018.
8. Waimin JF, **Buffington SL**, and Henderson JH. Photothermally Activated Shape Memory Polymers. Poster Presentation, Syracuse Engineering and Computer Science Research Day, Syracuse NY; March 29th, 2018.
9. Posnick BM, **Buffington SL**, Mohun PA, Kotis BM, and Henderson JH. Real-Time Contour Based Cell Tracking. Poster Presentation, Syracuse Summer Research Symposium, August 8<sup>th</sup>, 2018
10. Agyapong J, **Buffington SL**, and Henderson JH. Localized Photothermal Stimulation of Shape Memory Polymers. Poster Presentation, Syracuse Biomaterials Institute REU Summer Research Poster Session, Syracuse, NY; August 10, 2017.
11. Gu H, Lee SW, **Buffington SL**, Henderson JH, and Ren D. On-Demand Release of Bacterial Biofilms via Shape Memory Activation. Poster Presentation, Stevenson Biomaterials Research Poster Session 2017, Syracuse University, Syracuse, NY; March 3, 2017.
12. Posnick BM, **Buffington SL**, Paul JE, Mather PT, Henderson JH. Video Documentation of Quadruple Shape Memory Polymer (Q-SMP) Behavior. Summer Poster Competition. August 12<sup>th</sup>, 2016 Syracuse University. **Awarded 5th Place Overall**
13. Paul JE, **Buffington SL**, Henderson JH, Mather PT, “Development of Anisotropic Composites and Chiral Elastomers” REU Poster Competition. August 11th, 2016. Syracuse NY
14. **Buffington SL**, Henderson JH, Mather PT. Quadruple Shape Memory: Because 4 is Greater than 3. Poster Presentation, Nunan Engineering Day, March 2016

15. **Buffington SL**, Mather PT, and Henderson JH. Utilizing Shape Memory Polymers to Generate Complex Wrinkle Patterns for Active Cell Culture. Poster Presentation, Stevenson Poster Session, Syracuse University, February 2016
16. Hart L, **Buffington SL**, Mather PT, and Henderson JH. Using Triple Shape Memory Polymers to Generate Complex Wrinkle Patterns. Hampton—Brandeis PREM Research Retreat, Hampton, VA; September 16, 2016.
17. Hart L, **Buffington SL**, Mather PT, and Henderson JH. Using Triple Shape Memory Polymers to Generate Complex Wrinkle Patterns. Syracuse Biomaterials Institute REU Summer Research Poster Session, Syracuse, NY; August 11, 2016.
18. **Buffington SL**, Loh DA, Mather PT, and Henderson JH. Utilizing Shape Memory Polymers to Generate Complex Wrinkle Patterns for Active Cell Culture. Poster Presentation, Nunan Engineering Day, Syracuse University, March 2015
19. **Buffington SL**, Loh DA, Mather PT, and Henderson JH. Utilizing Shape Memory Polymers to Generate Complex Wrinkle Patterns for Active Cell Culture. Poster Presentation, IGERT Retreat, Syracuse University, November 2015
20. Benn S., **Buffington SL**, Henderson JH. Incorporation of Silver Nanoparticles in Electrospun Fiber Mat to Increase Antimicrobial Activity. Syracuse University Symposium for Undergraduate Research. Syracuse, NY; August 7, 2015. Winner, Biological/General Sciences **Third Place Prize.**
21. **Buffington SL**, Mather PT, and Henderson JH. Generating Complex Wrinkle Patterns on Shape Memory Substrates for Directing Cell Function. Oral Presentation, NSF IGERT Retreat, Syracuse University, Syracuse, NY; April 5, 2014.

#### **PATENTS:**

Henderson JH, Mather PT, and **Buffington SL**. Enzyme-Responsive Shape Memory Polymers. U.S. provisional patent application No. 62/649,934 filed March 29, 2018.